

Dissertation zur Erlangung des Doktorgrades  
der Fakultät für Chemie und Pharmazie  
der Ludwig-Maximilians-Universität München

# **Mesoporous Titania Materials**

–

**Tuning and Optimizing Nanostructures and Porous Morphologies**

von

Johann Martin Szeifert

aus

Peißenberg

2011



## **Erklärung**

Diese Dissertation wurde im Sinne von § 13 Abs. 3 bzw. 4 der Promotionsordnung vom 29. Januar 1998 (in der Fassung der sechsten Änderungssatzung vom 16. August 2010) von Herrn Professor Dr. Thomas Bein von der Fakultät für Chemie und Pharmazie betreut.

## **Ehrenwörtliche Versicherung**

Diese Dissertation wurde selbständig, ohne unerlaubte Hilfe erarbeitet.

München, 12.05.2011

.....  
(Unterschrift des Autors)

Dissertation eingereicht am 12.05.2011

1. Gutachter Prof. Dr. Thomas Bein
2. Gutachter Prof. Dr. Lukas Schmidt-Mende

Mündliche Prüfung am 28.06.2011



## **Danksagung**

Zu Beginn möchte ich mich bei meinem Doktorvater Professor Dr. Thomas Bein herzlich bedanken für die freundliche Aufnahme in seine Gruppe, sein Vertrauen mir dieses spannende, für diese Gruppe recht neue Thema zu geben, die große Freiheit zu eigenverantwortlicher Forschungsarbeit und die vielen richtungsweisenden Ratschläge.

Dr. Dina Fattakhova-Rohlfing möchte ich ebenfalls sehr herzlich danken für ihre intensive und sehr freundschaftliche Art der Betreuung während der Master-Arbeit, für die vielen kreativen Diskussionen und Ideen während der Doktorarbeit und für ihre großartige Hilfe beim Schreiben und Korrigieren der Veröffentlichungen.

Professor Dr. Lukas Schmidt-Mende möchte ich danken, dass er nicht nur als Zweitbetreuer im IDK, als Zweitgutachter für diese Arbeit, sondern auch sonst immer für Fragen zur Verfügung stand und so gute Evaluierungen meiner IDK-Jahresberichte geschrieben hat.

Ich möchte mich auch bei meinen Kooperationspartnern aus Lausanne bedanken: Herrn Professor Dr. Michael Grätzel für die Möglichkeit direkt vor Ort in der Gruppe des Erfinders die Grätzel-Zelle kennen zu lernen und später weiter zusammen arbeiten zu dürfen, Dr. Shaik M. Zakeeruddin für die Koordination der Kooperation und die äußerst wertvollen Diskussionen, Dr. Daibin Kuang, Dr. Sophie Wenger und Magdalena Marszalek für die vielen Experimente, deren Auswertung und Aufbereitung. Der zweiten zentralen Kooperation gebührt ebenso großer Dank für die vielen Krypton Sorptions-Messungen und Experimente zur Photokatalyse, sowie die exzellente Zusammenarbeit beim Schreiben der gemeinsamen Veröffentlichungen: Dr. Jiri Rathousky und Vit Kalousek vom J. Heyrovsky Institut in Prag.

IDK und CeNS möchte ich danken für die finanzielle Unterstützung meiner Forschung.

Aus der Bein-Gruppe möchte ich mich insbesondere bei den Photovoltaik-Experten und Kollegen bedanken: Norma Minar und Hans Feckl für ihre geduldige Art mit ihrem Diplomarbeitbetreuer zusammen zu arbeiten, und dafür nicht nur mit mir sondern auch

untereinander derart gut zu kooperieren, Benni Mandlmeier für die gute Zeit und Atmosphäre im gemeinsamen Büro (sogar ohne Paravent), und Benni, Dr. Valentina Cauda, und Yujing Liu für die genialen Kooperationen und gemeinsamen Projekte. Ebenfalls großartige PV-Experten und -Kollegen waren Florian Auras, Alesja Ivanova, Dr. Mihaela Nedelcu, und Askhat Jumabekov.

Das angenehme Arbeitsklima im AK Bein ist natürlich den netten Kollegen zu verdanken, allen voran waren hier Jörg Schuster (der mich das ganze Studium begleitet hat – war eine geile Zeit auf den Konferenzen und am Elettra!), Mirjam Dogru, Dr. Axel Schloßbauer, Dr. Andreas Keilbach, Stefan Niedermayer, Doro Wichmann und Dr. Ralf Köhn. Auch in den anderen Subgroups gibt es äußerst nette Kollegen: Basti, Christian, Alex, Fabian, Vesna, Yan, Karin, Flo HiHo, und Kun (und alle die ich hier vergessen habe). Danke euch für die zahlreichen schönen Kaffeepausen und Konferenzen! Beruflich bereits weg, aber ebenfalls sehr nette Kollegen waren Johann, Hendrik, Johannes, Camilla, Anderl, Lea, Monika und Olivier (Badminton am Freitagmorgen – Hammer!), die stets mit Rat und Tat zur Seite standen.

Besonderen Dank an Tina Reuther für zahllose Messungen und Hilfen bei allen möglichen Dingen, Dr. Steffen Schmidt für viele viele TEM- und SEM-Sessions und seine große Ruhe auch bei schwierigen weil schlechten Proben, und an Dr. Markus Döblinger für TEM-Untersuchungen und seine große Geduld wenn es um meine unglaubliche Ahnungslosigkeit bei Beugungs-Fragen ging. Großen Dank auch an Regina Huber für ihre nahezu mütterliche Fürsorge in allen organisatorischen und motivatorischen Angelegenheiten, und für ein immer offenes Ohr wenn etwas besonders gut oder schlecht lief.

Der größte Dank gilt meiner Familie, für ihre großartige Unterstützung während des Studiums und der Doktorarbeit. Ohne Euch wäre all dies niemals möglich gewesen!

## **Abstract**

This thesis aims at extending the applicability of surfactant-based mesoporous titanium dioxide materials to photovoltaic, photocatalytic and energy storage devices, and to exploit their advantages of high surface area, tuneable pore size and periodic porosity in these applications. The major limitation of the established procedures for preparing surfactant-templated mesoporous titania is the low degree of crystallinity of its walls, and the resulting negative effect on the material's electronic and semiconductor properties. Furthermore, in thin films the significant density changes accompanying the condensation and crystallization of initially amorphous titania walls lead to mechanical stress upon heating, deterioration of film quality and cracking or delamination when stacking several layers.

One strategy to overcome these drawbacks is based on introducing preformed nanocrystalline precursors into the walls of the mesoporous framework in a novel "brick and mortar" approach for creating highly crystalline transparent TiO<sub>2</sub> coatings. In this way, preformed titania nanocrystalline "bricks" are fused with surfactant-templated sol-gel titania "mortar", which acts as a structure-directing matrix and as a chemical glue. The interaction of crystalline and amorphous components leads to a striking synergy, such that a rapid increase in crystallinity occurs upon thermal treatment and highly porous and highly crystalline structures are formed at very mild conditions. Coatings with a broad variety of periodic mesostructures and thicknesses ranging from few nanometers to several micrometers are accessible using the same organic template, and the final structures are tunable by varying the fraction of the "bricks". The beneficial combination of crystallinity and porosity leads to greatly enhanced activity of the films in photocatalytic and photovoltaic processes, and a performance optimum concerning the nanoparticle content is found to be around 70 % (Cooperations with the groups of Dr. J. Rathouský, J. Heyrovský Institute, Prague, and Prof. M. Grätzel, EPF Lausanne).

The potential of the “brick and mortar” approach to synthesize thick mesoporous titania films of up to 10  $\mu\text{m}$  thickness by multilayer deposition was specifically investigated. The as-produced films exhibit very high surface area, which scales linearly with the thickness, and roughness factors of up to 1600  $\text{cm}^2/\text{cm}^2$  can be reached. This is the first time that surfactant-derived mesoporous titanium dioxide films of such a high thickness and surface area can be prepared without serious cracking, delamination, or deterioration of the porous structure. In dye-sensitized solar cells (DSCs) using a volatile electrolyte, the films feature a remarkably high performance level of over 7 % already at thicknesses below 4  $\mu\text{m}$  due to their high surface area and dye adsorption. Thicker “brick and mortar” films reach up to 8.1 % efficiency, which is until today the highest DSC performance of a surfactant-derived mesoporous material.

The advantages of such high surface area mesoporous films can best be exploited in photovoltaic systems which are based on more stable but diffusion-length limited electrolytes, for example room temperature ionic liquids (RTIL, cooperation with the group of Prof. M. Grätzel, EPF Lausanne). DSCs employing RTILs, a high-extinction coefficient organic dye and “brick and mortar” electrodes exhibit very high conversion efficiencies above 6.2 % at low film thicknesses of only 2  $\mu\text{m}$ . This is a very promising performance for such thin films compared to the record for this system (8.2 % efficiency, electrode consisting of 20 nm nanoparticles, thickness 7  $\mu\text{m}$ ), and considering significant losses due to insufficient light absorption. Thicker films (> 2  $\mu\text{m}$ ), however, proved to be not as efficient due to charge transport-limitations, and further thickness and pore size optimization are supposed to increase the maximum performance of “brick and mortar” electrodes in RTIL-based DSCs.

The scope of general strategies employing crystalline titania nanoparticles can be extended, when the dimensions of the nanocrystalline building blocks are further down-sized. A new non-aqueous sol-gel protocol using *tert*-butanol as reaction medium widens the available size

range of TiO<sub>2</sub> nanoparticles at its lower end by producing ultrasmall and highly soluble anatase nanoparticles of around 3 nm employing fast and low-temperature microwave heating. The extremely small size of the nanoparticles and their dispersibility make it possible to use commercial Pluronic surfactants for self-assembly of the nanoparticulate building blocks to form periodic mesoporous structures with a high surface area ranging up to 300 m<sup>2</sup>/g. The advantages of the retention of the mesoporous order with extremely thin nanocrystalline walls were shown by electrochemical lithium insertion, in which films made using microwave-treated nanoparticles showed fast insertion behaviour with high maximum capacity due to quantitative lithiation with a 10-fold increase of charging rates compared to a standard reference electrode made from 20 nm anatase particles.

The use of preformed titania nanocrystals (“bricks”) as precursors for surfactant-templated mesoporous materials can also be extended to titania-silica composite materials. In combination with silica sol-gel precursors as “mortar”, films with a high fraction of crystalline titania particles finely dispersed in periodic silica mesostructures were obtained at temperatures as low as 100 °C, and employed as active layers for the photooxidation of NO (cooperation with Dr. J. Rathouský, J. Heyrovský Institute, Prague). For this material system, the “brick and mortar” approach results in periodic mesoporous nanocomposites with photocatalytically active sites leading to functional coatings which can be processed at low temperatures on a wide range of substrates.

In a second strategy towards titania-silica composites with control over the crystalline properties of the porous system, colloidal mesoporous silica (CMS) nanoparticles with a thin titania-enriched outer shell showing a spatially resolved functionality were synthesized by a delayed co-condensation approach (joint project with Dr. Valentina Cauda, LMU Munich). The titania shell can serve as a selective nucleation site for the growth of nanocrystalline anatase clusters. These fully inorganic pure silica-core titania-enriched shell mesoporous nanoparticles show orthogonal functionality, demonstrated through the selective adsorption of

a carboxylate-containing ruthenium N3-dye. UV-Vis and fluorescence spectroscopy indicate the strong interaction of the N3-dye with the titania-phase at the outer shell of the CMS nanoparticles. This selectivity is strongly enhanced when anatase nanocrystallites are nucleated at the titania-enriched shell surface.

In conclusion, the introduction of crystalline titania nanoparticles to the synthesis of mesostructures based on surfactants and sol-gel precursors allowed to improve the applicability of the resulting pure titania or silica-titania composite materials. This measure provides the possibility to exploit the attractive porous characteristics and versatile chemistry of templated metal oxides, and led to coatings exhibiting very promising performance in photovoltaics and photocatalysis, and bulk materials with orthogonal functional properties.

# Table of Contents

<b>1. Introduction to Titanium Dioxide Nanomaterials.....</b>	<b>1</b>
1.1 Titania Nanoparticles and Sol-gel Chemistry .....	2
1.2 Mesoporous Titania Films.....	7
1.3 Dye-sensitized Solar Cells (DSCs) .....	13
1.4.1 Operational Principle of the DSC.....	14
1.4.2 Physics of the DSC.....	17
1.4.3 DSC Assembly .....	19
1.4.4 DSC Materials .....	21
1.5 References .....	26
<b>2 Characterization.....</b>	<b>31</b>
2.1 X-ray Diffraction (XRD).....	31
2.2 Electron Microscopy .....	33
2.3 Raman Spectroscopy .....	36
2.4 UV/Vis Spectroscopy .....	38
2.5 Fluorescence Spectroscopy .....	39
2.6 Sorption .....	41
2.7 Quartz Crystal Microbalance (QCM).....	43
2.8 Dynamic Light Scattering (DLS) .....	45
2.9 Zeta Potential Measurements .....	47
2.10 Thermogravimetric Analysis (TGA).....	48
2.11 Photocatalytic Activity (PA) .....	50
2.12 Electrochemical Lithium Insertion.....	52
2.13 Photovoltaic Characterization .....	54
2.14 References .....	59
<b>3. “Brick and Mortar” Strategy for the Formation of Highly Crystalline Mesoporous Titania Films from Nanocrystalline Building Blocks.....</b>	<b>63</b>
3.1 Introduction .....	63
3.2 Results and Discussion.....	65
3.3 Experimental Section .....	77
3.4 References .....	80
<b>4. Multilayered High Surface Area “Brick and Mortar” Mesoporous Titania Films as Efficient Anodes in Dye-Sensitized Solar Cells.....</b>	<b>83</b>
4.1 Introduction .....	83
4.2 Results and Discussion.....	86
4.3 Conclusion.....	95
4.4 Experimental Section .....	96
4.5 References .....	98

<b>5. High Surface Area “Brick and Mortar” Films for Ionic Liquid Dye-Sensitized Solar Cells .....</b>	<b>101</b>
5.1 Introduction .....	101
5.2 Results and Discussion.....	103
5.3 Conclusion and Outlook.....	110
5.4 Experimental Section .....	111
5.5 References .....	113
<b>6. Ultrasmall Titania Nanocrystals and their Direct Assembly into Mesoporous Structures showing fast Lithium Insertion .....</b>	<b>115</b>
6.1 Introduction .....	115
6.2 Results and Discussion.....	117
6.3 Conclusion.....	131
6.4 Experimental Section .....	132
6.5 References .....	134
<b>7. Low-Temperature Synthesis of Mesoporous Titania-Silica Films with preformed Anatase Nanocrystals .....</b>	<b>139</b>
7.1 Introduction .....	139
7.2 Results and Discussion.....	142
7.2.1 Films templated with Pluronic P123 .....	144
7.2.2 Films templated with Pluronic F127 .....	147
7.3 Conclusion.....	156
7.4 Experimental Section .....	157
7.5 References .....	160
<b>8. All-Inorganic Core-Shell Silica-Titania Mesoporous Colloidal Nanoparticles Showing Orthogonal Functionality.....</b>	<b>163</b>
8.1 Introduction .....	163
8.2 Results and Discussion.....	167
8.3 Conclusion.....	178
8.4 Experimental Section .....	179
8.5 References .....	183
<b>9. Conclusion and Outlook .....</b>	<b>187</b>
<b>10. Curriculum Vitae .....</b>	<b>191</b>
<b>11. Publications and Presentations .....</b>	<b>193</b>
11.1 Publications .....	193
11.2 Poster Presentations.....	194
11.3 Oral Presentations .....	194

# 1. Introduction to Titanium Dioxide Nanomaterials

Titanium dioxide is a semiconductor material with great potential in the fields of photovoltaics,<sup>1,2</sup> energy storage<sup>3,4</sup> and photocatalysis<sup>5</sup>. Examples for such titania-based applications are dye-sensitized solar cells, lithium-ion batteries, and self-cleaning coatings for glass windows. In recent years, especially the new energy technologies have become extremely important, since global warming and the scarcity of raw materials demand a more efficient and ideally sustainable conversion of natural resources.<sup>6</sup>

The working principles in all of these energy conversion or storage devices involve charge transfer reactions and accompanying transport processes. Therefore, large interfaces and free accessibility for diffusion are crucial for the usability and efficiency of active materials.<sup>7,8</sup>

These essential requirements are exclusively met by nanostructured materials, which feature repeating structural elements with length scales in the nanometer range.<sup>9-11</sup> In order to achieve fast and unhindered diffusion, most often these materials are highly porous, and the size of the pores is also on a nanoscale dimension. In particular, materials with pore diameters in the range of 2 – 50 nm are specified as mesoporous (IUPAC classification).<sup>12</sup>

Mesoporous titania materials offer advantages in many technological fields due to their unique electronic, chemical and optical properties such as transparency for visible light, low toxicity, conductivity, and chemical and structural versatility.<sup>9</sup> The performance of mesoporous titania in energy applications depends strongly on its surface area, porosity and morphology, but also to a large extent on the control over the crystalline nature of titanium dioxide.<sup>13,14</sup>

TiO<sub>2</sub> naturally occurs in amorphous or crystalline phases, the crystalline ones being anatase, rutile, and brookite.<sup>15</sup> Anatase is usually the desired phase for photovoltaic applications due to its electronic characteristics, but also other synthetic phases and mixed metal oxides have

interesting physical properties, for example the layered  $\text{TiO}_2(\text{B})$  as supercapacitor material in lithium insertion experiments.<sup>16,17</sup>

In order to be applicable in technological devices, in most cases titania nanostructures have to be prepared as films on conductive substrates, and tuneable film thicknesses in a narrow range of a few micrometers in combination with high optical quality of the coatings are required.

Due to its practical importance, the elaboration of mesoporous titanium dioxide has been intensively investigated. Nowadays, numerous synthetic strategies are described for the fabrication of mesoporous titania materials. The most basic strategy towards mesoporous  $\text{TiO}_2$  is the sintering of preformed nanoparticles.<sup>18</sup> Other more sophisticated approaches use organic templates or employ electrochemical methods.<sup>10,19</sup>

In the following, different strategies for preparing titanium dioxide nanostructures will be introduced, starting with the most basic one, the synthesis of nanoparticles.

### 1.1 Titania Nanoparticles and Sol-gel Chemistry

There are many different ways of synthesizing titanium dioxide particles with defined properties on the nanoscale. The most important characteristics of nanoparticles for their use in fabrication of mesoporous films are particle size and size distribution, crystallinity, and agglomeration/dispersibility.<sup>9-11,20,21</sup> There are few synthetic procedures that provide particles with the desired characteristics, and are also effective concerning their cost, effort and yield. The most important ones are the commercial products from flame hydrolysis, and the wet-chemistry approaches employing sol-gel, hydrothermal, or solvothermal processes.

For the commercial production of  $\text{TiO}_2$  nanoparticles, **flame hydrolysis** is probably the most important technique.<sup>22,23</sup> A prominent example of a product synthesized using this technique

## 1. Introduction to Titanium Dioxide Nanomaterials

---

is Aeroxide P25 by Degussa.<sup>23</sup> By reaction of vaporized titanium tetrachloride ( $\text{TiCl}_4$ ) with oxygen and hydrogen in the gas phase at high temperatures of over 1000 °C, highly crystalline titanium dioxide nanoparticles can be obtained, which have an average diameter of approximately 21 nm, and consist of a mixture of anatase (~ 80 %) and rutile (~ 20 %).

This technique is advantageous for experiments on a large scale and is employed in industrial production. Major drawbacks for application in the production of mesoporous materials are the coexistence of two crystalline phases, the limitation to rather large particle sizes, and the low redispersibility.

Wet-chemistry approaches in general are very versatile and by choosing the right protocol, a product with the desired characteristics can be obtained.<sup>21</sup> They are based on a combination of hydrolysis and condensation reactions of metal halide or alkoxide precursors in water or oxygen-containing organic solvents. Depending on the degree of condensation, these reactions can lead to molecular nanoclusters, nanoparticles, or polymer-like metal oxide networks. This sequence of reactions is traditionally called **sol-gel process**.<sup>24,25</sup> The underlying principle of this technique has already been utilized since 1848 and the enormous amount of literature on this topic reflects its diversity and usefulness.

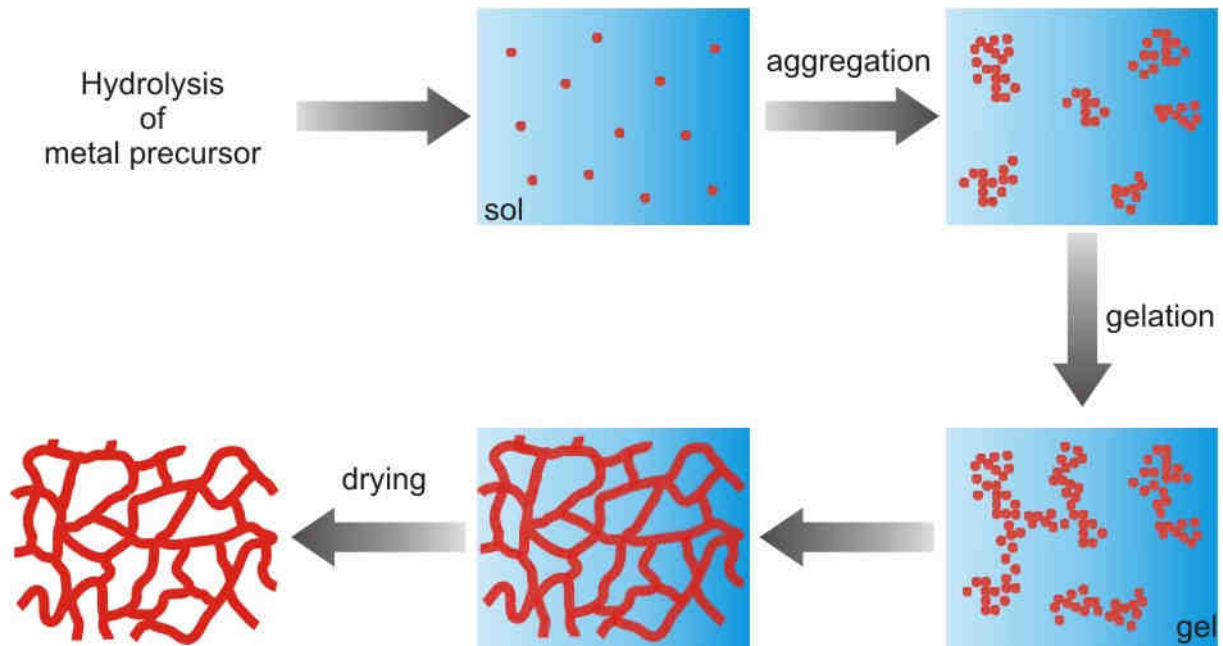
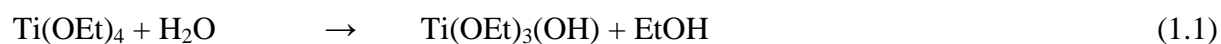


**Figure 1.1.** Reaction steps of the sol-gel process leading to a condensed inorganic network.

The classical sol-gel process can be divided into five characteristic steps (Figure 1.1):<sup>21</sup>

- 1) Generation of a stable solution of molecular metal precursors (the *sol*).
- 2) Formation of a bridged network by condensation reactions, gelation with increasing viscosity (the *gel*).
- 3) Ageing of the gel with ongoing condensation. Formation of a solid mass and expulsion of solvents.
- 4) Drying of the gel, removal of water and solvents by thermal treatment (*xerogel*) or by extraction at super-critical conditions (*aerogel*).
- 5) Dehydration and removal of surface-bound hydroxy-groups by calcination, in some cases, densification and removal of remaining organics at higher temperatures ( $> 800\text{ }^{\circ}\text{C}$ ).

Hydrolysis of titanium species is very fast, as with most transition metals, compared to their silicon analogues. Examples for the reactions occurring during the hydrolysis of  $\text{Ti}(\text{OEt})_4$  (1) – (4) and for condensation (5) are the following:



The degree of hydrolysis and the organic leaving groups attached to titanium strongly influence the particle formation in the gel. Addition of ligands as further modifications of the precursors can also control the structure or morphology of the condensation products.

Sol-gel syntheses of titania particles enable the control of particle size, crystallinity and morphology by changing reaction parameters, such as water/alkoxide ratio, pH, and temperature. The dimension of the particles which can be obtained by altering these parameters ranges from 4 nm up to about 1  $\mu\text{m}$  and is finely tuneable.<sup>26</sup>

The major disadvantage of aqueous sol-gel derived  $\text{TiO}_2$  is that its products are mostly amorphous and need hydrothermal treatment (aerogels, see below) or calcination (xerogels) for crystallization.

Non-aqueous sol-gel processes for the synthesis of titania particles offer attractive alternatives to their aqueous analogues. In general, two different approaches can be distinguished: one enabling the control over the particle size and morphology via surfactant (surfactant control) and one via solvent (solvent control).<sup>27</sup>

## 1. Introduction to Titanium Dioxide Nanomaterials

---

The so-called hot injection technique is characterized by addition of a solution of metal precursor into hot solvent containing surfactants. The surfactants coordinate to the precursors and prevent agglomeration.<sup>27</sup> This method has been successfully used in the synthesis of many materials such as cadmium chalcogenide quantum dots and, also for titania, nanorods of 3.3 nm in diameter and 25 nm in length have been reported.<sup>28</sup>

Another example is the hydrolysis of titanium butoxide in the presence of acetylacetone and para-toluenesulfonic acid at 60 °C. This reaction leads to pure-phase anatase particles and their size could be tuned from 1 – 5 nm by adjusting the synthetic conditions.<sup>29</sup>

Solvent control can be explained by a small number of reactants in solution leading to simpler and fewer possible reaction pathways. The main advantage of this method is the increased purity of the products due to the limited number of compounds in solution.<sup>30</sup>

Recently, Niederberger and co-workers reported a non-aqueous system using dry benzyl alcohol as a solvent, titanium tetrachloride as a metal precursor and low to medium temperatures of 40 to 150 °C.<sup>31</sup> The resulting TiO<sub>2</sub> particles were 4 – 8 nm in size and consisted of pure anatase.<sup>32</sup>

In this way, calcination or hydrothermal treatment and consequent agglomeration can be avoided. The organic solvents give access to a wide field of possible modifications by organic molecules which can lead to beneficial chemical properties.<sup>33</sup>

**Hydrothermal or solvothermal processes** are characterized by hydrolysis and condensation reactions in solutions at high pressures and temperatures above their boiling point in sealed vessels. In some cases, the conditions are even above the critical point of a solvent and the special properties of supercritical solvents such as the lack of surface tension and low viscosity are exploited. In general, these processes benefit from the improved solubility and reactivity of reactants at elevated temperatures.

The synthesis of nanocrystalline titania by hydrothermal techniques has already been introduced in 1988. The reaction of  $\text{Ti}(\text{OEt})_4$  and water in ethanol at room temperature yielded amorphous titanium dioxide, and subsequent hydrothermal processing led to crystallization of these particles. Pure, crystalline anatase could be obtained as agglomerates of 600 – 700 nm in diameter with a crystallite size of about 10 – 20 nm, after processing at 200 – 280 °C at pressures of 16 – 66 MPa.<sup>34,35</sup>

Other approaches have used  $\text{TiCl}_4$  in water and hydrothermal treatment at various temperatures, pressures, ratios and in some cases with additives. The products exhibited great diversity of particle size, morphology, and agglomeration. Pure-phase crystalline titania could be obtained as well under certain conditions.<sup>36</sup>

Non-aqueous solvothermal systems have been reported, for example employing *n*-butanol and titanium butoxide at 200 °C. These reactions were also performed utilizing different ligands and crystalline anatase nanoparticles of 7 – 16 nm in size were produced.<sup>37</sup>

In general, this technique offers good control on the various physical parameters, however, the degree of redispersibility and the possibility of chemical modification of the particles at high temperatures might be limiting for their applicability. Furthermore, the reaction conditions are normally far above the boiling point of the solvent, require special technical equipment and are thus rather expensive.

### 1.2 Mesoporous Titania Films

The titanium dioxide layers in photovoltaic or energy storage applications consist of mesoporous  $\text{TiO}_2$  films, because of their huge surface area and good accessibility of the pores. There are numerous reports on the synthesis of mesoporous titania films with different

structures, morphologies and degrees of crystallinity.<sup>38</sup> In general, two strategies for preparing such films have been established:

The first is based on preformed nanocrystalline titanium dioxide particles which are deposited from a paste or solution and sintered by calcination. Some recipes additionally employ polymeric binders, and the film preparation is usually done by a screen-printing or doctor-blade technique. This approach is commonly used for many applications, because the manufacturing of such films is very straightforward when the particulate precursors are available. The resulting layers are highly crystalline and show low intrinsic electric resistance.<sup>18</sup> Recent examples of TiO<sub>2</sub> films employed in dye-sensitized solar cells exhibit surface areas of about 80 – 90 m<sup>2</sup>g<sup>-1</sup>, and roughness factors of about 120 – 150 in films of one micrometer thickness.<sup>39</sup> These films do not feature periodically porous structures, but their film thickness can be easily adjusted over a wide range from few nanometers to hundreds of micrometers.

The second preparation method utilizes molecular sol-gel precursors and surfactants as stabilizing and structure directing agents (SDA) in an evaporation-induced self-assembly (EISA, see below) process. In thin films, these mixtures can form highly ordered mesostructures in various morphologies, with very high specific surface area values of up to over 200 m<sup>2</sup>g<sup>-1</sup>.<sup>40</sup> Disadvantages of the sol-gel approach for mesoporous film preparation are the lower crystallinity compared to particle based alternatives, and the extremely thin film thicknesses (usually below one micrometer).<sup>41</sup> Furthermore, due to strong structural contraction upon condensation of the network, the possibilities of increasing the thickness to more applicable values are restricted by crack formation and even delamination of the films.<sup>42</sup>

### *Evaporation-induced self-assembly (EISA)*

Evaporation-induced self-assembly is a process which allows the rapid production of periodically structured porous or nanocomposite materials in form of films, fibers or powders.<sup>43-45</sup> Self-assembly denotes the spontaneous organization of materials without external influence. Amphiphilic surfactants dissolved in solvents are known for their ability to self-organize as soon as they reach a critical concentration into micellar aggregates of different shapes, which can take the form of lamellar, cubic or hexagonal mesophases, among others. The relationship between surfactant concentration, temperature and resulting mesophase can be summarized in a phase diagram.

In the presence of dissolved metal oxide precursors, the surfactants lead to spontaneous co-assembly of both materials in a mesostructured phase.<sup>43</sup> The liquid crystal templating (LCT) theory explains this process with a stabilized surfactant mesophase which is acting as a template for the condensation of the inorganic phase. Another mechanism proposed in this context is called cooperative self-assembly (CSA) mechanism, in which surfactant and inorganic precursor form a combined intermediate phase which behaves as an independent surfactant species and builds up a hybrid structure. The nature of the process is strongly dependent on the chemical composition of the system. For non-ionic templates, the LCT theory is supposed to be applicable, but in most cases the process is likely to follow a combination of both mechanisms.<sup>44</sup>

The main periodic structures which are accessible in this way are hexagonal, cubic, lamellar and wormhole-like mesophases. A schematic overview is illustrated in Figure 1.2.

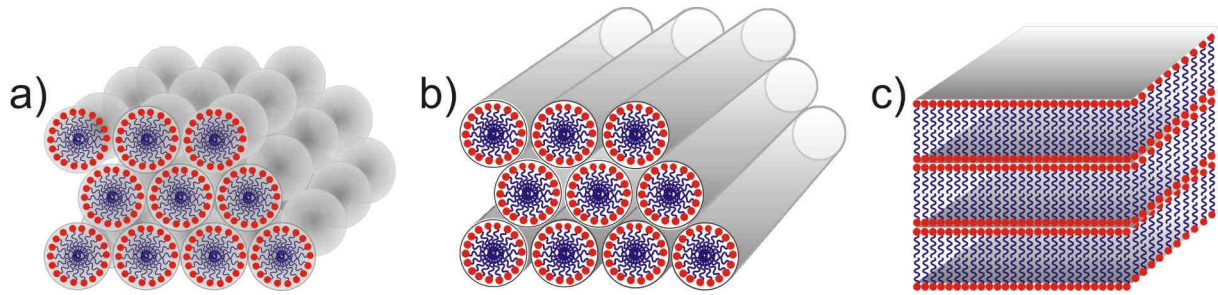


**Figure 1.2.** Highly organized mesostructures: a) Cubic. b) Hexagonal. c) Lamellar.

For the preparation of thin mesoporous films, the evaporation-induced self-assembly method offers control over the final structure. It is very important to record and control the parameters which can influence the process to achieve satisfying reproducibility, namely, the chemical factors responsible for the condensation reactions (concentrations of surfactant and inorganic precursor) and the processing conditions, which govern the diffusion of the volatile fraction.

After deposition of a certain amount of solution on a substrate, the EISA process can be divided into the following steps as shown in Figure 1.3:<sup>45</sup>

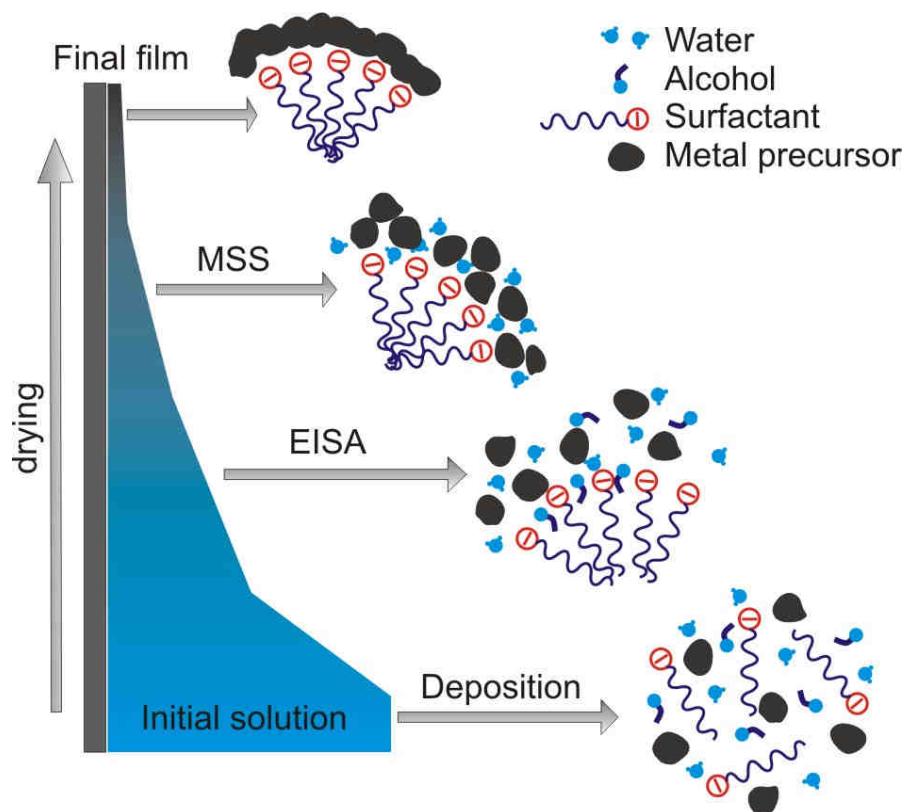


**Figure 1.3.** Film formation using an evaporation-induced self-assembly (EISA) process by dip coating. MSS: Modulable steady state. Figure adapted from ref. 45.

Starting point for the film formation is the initial sol. The chemical composition of this sol-gel system has to be adjusted to achieve the desired rates of hydrolysis and condensation reactions and to match the chemical nature of the substrate. Important parameters are for instance concentration of surfactant and metal precursor, choice of solvent, pH, dilution, water content, and ageing time. For many metal oxides, the pH of the precursor solutions is kept rather low in order to stop hydrolysis reactions in an early stage forming small oligomers and preventing condensation during the deposition process.

The next step is the deposition. The volatile components evaporate very rapidly and the concentrations of metal oligomers and surfactant molecules rise simultaneously. Above the critical micellar concentration, micelles start to form due to hydrophobic interaction of the

alkyl chains, and the self-assembly processes can begin. After the drying line, the mesostructure can still be influenced by changing external parameters such as relative humidity and temperature. This intermediate equilibrium is called modifiable steady state (MSS). When self-organization and condensation are completed, the final mesostructure is formed.

In the following treatment step, further condensation of the inorganic network can be induced for example by calcination to increase its stability and to remove the template to free the pores. This process is usually accompanied by contraction of the network in a direction perpendicular to the substrate plane resulting in the unidimensional shrinkage of the pores. In transition metal oxide films, the temperature of calcination plays an important role on further crystallization of the network, because it can lead to Ostwald ripening and the destruction of the periodic mesophase.

### 1.3 Dye-sensitized Solar Cells (DSCs)

Sun light provides an enormous amount of clean and practically inexhaustible energy. Per year,  $3 \times 10^{24}$  J are supplied to the earth, which is about 10.000 times more than all countries are currently consuming.<sup>46</sup> However, this energy remains mostly unconverted contributing only to an extremely small extent to the total energy generation. In the United States, for example, in 2006 only about 0.08 % of the total energy was produced by conversion of sun light. The predominant photovoltaic devices are based on typical semiconductor p-n-junction cells, with silicon being the major component.<sup>47</sup> In order to increase this level, more solar cells need to be built and set up. However, their production is rather expensive concerning cost and energy, and especially shortage of raw materials must be avoided. On this account, it is very important that aside from the established systems new technologies are further developed and included into the existing portfolio of photovoltaic devices.<sup>48</sup> Photoelectrochemical cells are based on different materials than their semiconductor analogues and therefore offer a great opportunity to exploit a bigger part of this huge amount of energy.<sup>6</sup>

In 1991, Grätzel et al. reported a solar cell based on dye-sensitized colloidal TiO<sub>2</sub> films (dye-sensitized solar cell, DSC).<sup>49</sup> Current is generated by absorption of photons by dye molecules, charge injection into the TiO<sub>2</sub> conduction band and subsequent transfer of separated electrons from the dye-titania interface to an electrode. The circuit is completed by a redox electrolyte which is reduced at the counter electrode and regenerates the dyes. Solar cells with conversion efficiencies of 11 % have been attained so far and further efforts to optimize their efficiency and stability are underway.<sup>50</sup> The major advantages of this solar cell are the low cost and the good availability and variability of the materials needed. Especially, semiconducting porous

titanium dioxide can be obtained in various ways, and as titanium is one of the most common elements on earth, supply with titania is abundant.<sup>15</sup>

### 1.4.1 Operational Principle of the DSC

A schematic overview of the operational principle is shown in Figure 1.4.

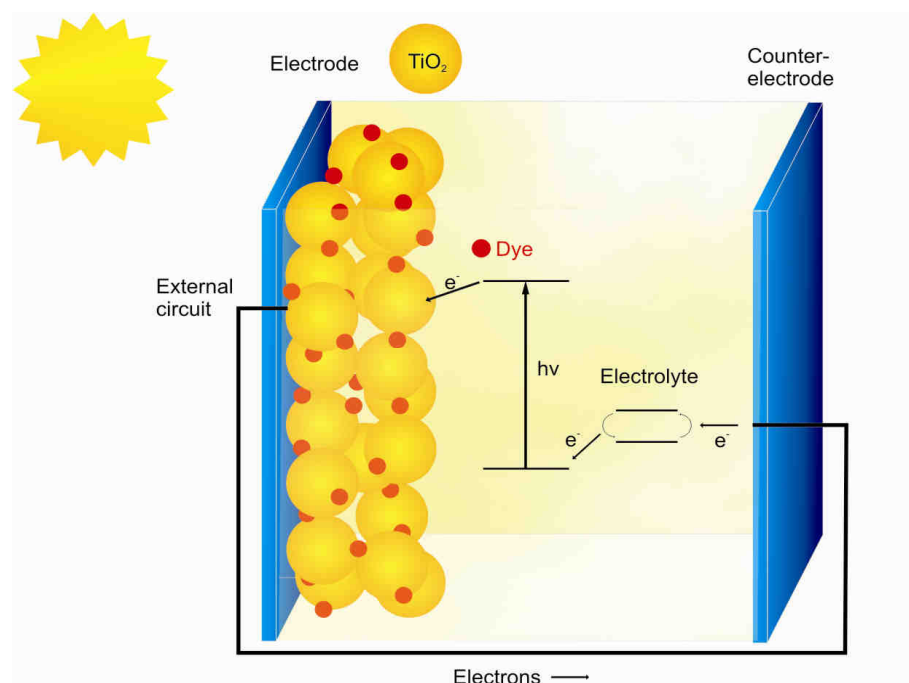


**Figure 1.4.** Operational principle of the DSC. Figure adapted from ref. 50.

A mesostructured semiconductor oxide film on conducting glass is in contact with a redox electrolyte or an organic hole conductor. The semiconductor is sensitized on its surface by a monolayer of a dye. The oxide consists normally of anatase ( $\text{TiO}_2$ ), but other materials like  $\text{ZnO}$ ,  $\text{SnO}_2$  or  $\text{Nb}_2\text{O}_3$  can also be employed.<sup>51,52</sup> The photosensitizer is in most cases a Ru-centered polypyridyl complex. Other examples for suitable dyes are zinc porphyrins or indoline based organic molecules.<sup>53</sup> Excitation of the dye by absorption of a photon leads to

an excited state, from where an electron can be injected into the conduction band of the oxide. Regeneration of the dye is done by an electrolyte, usually a redox system such as the iodide/triiodide couple in an organic solvent. The sensitizer is reduced by iodide and triiodide is formed. At the cathode, triiodide is reduced to regenerate iodide. Under illumination, the cell is generating voltage. The maximum voltage arises from the difference of energies between the quasi-Fermi level of the semiconductor and the redox potential of the electrolyte.<sup>50</sup>

In the dark, a solar cell displays the same electrical characteristics as a diode. When a voltage is applied, the current rises exponentially. This dark current is based on the voltage-dependent reduction of the electrolyte at the titania surface. Under illumination, the dye molecules can absorb light, and inject electrons into the conduction band of  $\text{TiO}_2$ . In this way, charge separation occurs and an electrical field is built up. The charges are transported to the electrodes and a photocurrent is generated, whose direction is opposing the dark current. The current-voltage characteristics of an idealized solar cell under illumination are shown in Figure 1.5.

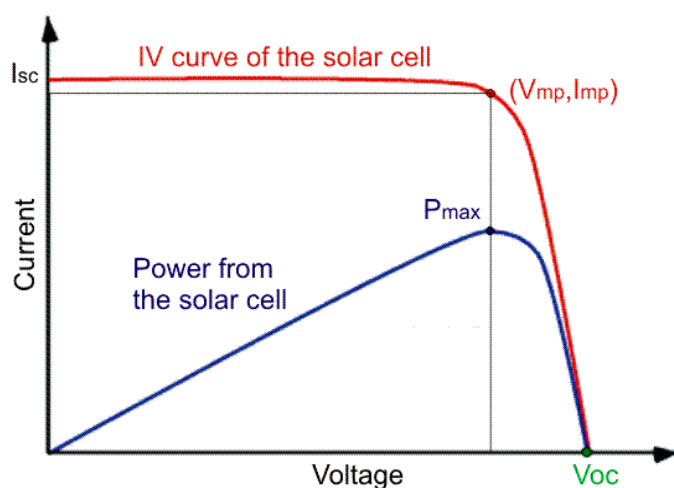


**Figure 1.5.** Idealized I-V-characteristics of a solar cell under illumination.

Under short-circuit conditions, the so called short-circuit current  $I_{SC}$  passes the electrodes. In an ideal solar cell, this point marks the current's maximum and neither voltage nor power is generated. In the DSC, the  $I_{SC}$  corresponds to the number of dye molecules which can simultaneously absorb photons and generate charge carriers. The maximum potential available from a solar cell is called the open circuit voltage  $V_{OC}$ , and for DSCs it is dependent on the energy difference of the quasi-Fermi level and the redox potential of the redox electrolyte. This voltage is reached at the maximum charge separation point at zero current.

The electrical power which can be generated within a solar cell is determined by the product of current and voltage. Therefore, at each point in the I-V curve, the power corresponds to the area of a rectangle. The power curve has a maximum at  $P_{max}$ , with the current  $I_{mp}$  and the voltage  $V_{mp}$ . The fill factor (ff) is a measure for the power of a solar cell and refers to the ratio of maximum power to the product of maximum current and maximum voltage:

$$ff = \frac{V_{mp} I_{mp}}{V_{oc} I_{sc}} = \frac{P_{max}}{V_{oc} I_{sc}} . \quad (1.6)$$

The overall conversion efficiency  $\eta_{global}$  is the light-to-energy conversion yield of a solar cell. It is determined by the ratio of converted, electrical power to incident power, or in another form by the photocurrent density at short circuit  $I_{SC}$ , the open-circuit photovoltage  $V_{OC}$ , the fill factor ff of the cell and the intensity of the incident light I:

$$\eta_{global} = \frac{P_{max}}{P_{in}} = \frac{V_{oc} I_{sc} (ff)}{I} . \quad (1.7)$$

For dye-sensitized solar cells, certified conversion efficiencies of about 11 % have been reported. Other single-junction, solid-state devices exhibit much higher efficiencies, the highest being crystalline GaAs and crystalline silicon both at about 25 %, which is already close to the upper maximum of 33 % for single-junction solar cells.

The record is held by multi-junction devices, which combine several materials and exploit their different absorption behaviour. Their efficiencies currently range up to 34 % under one sun illumination, and can reach over 40 % when light concentrator systems are used to increase the light intensity. However, these values are still relatively low, compared to the thermodynamic Carnot limit of 93 %, leaving great potential for further development.<sup>54</sup>

### 1.4.2 Physics of the DSC

The crucial physical processes in dye-sensitized solar cells which mainly affect their efficiency are:<sup>50</sup>

- (1) Absorption of incident light in a chromophore,
- (2) heterogeneous electron injection from the dye to the semiconductor and charge separation,
- (3) electron percolation over the mesoporous network to the electrode, and
- (4) charge diffusion through the electrolyte/hole transporter (HTM) and regeneration of the dye.

Absorption of the photon energy (1) is the starting point of the cycle for power generation. The charge transport processes (2) and (3) are of great importance, because they compete with the thermodynamically favoured back reaction of the electron with the oxidized sensitizer. This recombination is the main loss process and produces heat instead of electrical current. The kinetics of step (4) affect this main recombination pathway only if the life-times of the injected electrons in the semiconductor are on the same timescale as diffusion through the electrolyte/HTM.

The efficiency of these processes can be expressed in the incident photon to current conversion efficiency (IPCE, also external quantum efficiency EQE). It corresponds to the

number of electrons that are converted into photocurrent divided by the photon flux striking the cell. The IPCE is dependent on the wavelength and can be obtained by

$$\text{IPCE}(\lambda) = \text{LHE}(\lambda) \Phi_{\text{inj}} \eta_{\text{coll}} . \quad (1.8)$$

Here, absorption is represented by the light-harvesting efficiency for photons of wavelength  $\lambda$ ,  $\text{LHE}(\lambda)$ . Injection processes are combined in the quantum yield for electron injection  $\Phi_{\text{inj}}$ . The electron collection efficiency  $\eta_{\text{coll}}$  denotes the influence of charge carrier percolation through the semiconductor.

The  $\text{LHE}(\lambda)$  can be explained as the probability of absorption of an incident photon in the film. It can be calculated from the thickness of the film  $d$  and the reciprocal absorption length  $\alpha$  of the sensitizer, which depends on the dye's extinction coefficient  $\epsilon$  and the concentration of the dye in the film:

$$\text{LHE}(\lambda) = 1 - 10^{-\alpha d} . \quad (1.9)$$

The quantum yield for electron injection  $\Phi_{\text{inj}}$  depicts the fraction of absorbed photons which are converted into conduction band electrons. There are several deactivation channels competing with the injection to the semiconductor and the sum of rate constants for these non-productive channels is taken into account for  $\Phi_{\text{inj}}$ :

$$\Phi_{\text{inj}} = k_{\text{inj}} / (k_{\text{inj}} + k_{\text{deact}}) . \quad (1.10)$$

Absorption of a photon on a ruthenium polypyridyl complex leads at first to a metal-to-ligand charge transfer transition. From the ligand, injection to the semiconductor occurs within pico- to femtoseconds. This injection time is typically several orders of magnitude shorter than the time spans of deactivating processes, which are in the range of milliseconds to nanoseconds. Hence, a high quantum yield for electron injection can be achieved.

The last variable, the electron collection efficiency  $\eta_{\text{coll}}$ , is dependent on various factors, such as the electron diffusion coefficient and specific conductivity of the semiconductor or

interfacial electron-transfer reactions such as loss of electrons to the electrolyte. A key parameter for quantitative collection of charge carriers is the electron diffusion length  $L_n$ , which is given by

$$L_n = \sqrt{D_e \tau_r}, \quad (1.11)$$

where  $D_e$  and  $\tau_r$  are diffusion coefficient and lifetime of the electron.

Hence, complete collection of all photogenerated carriers can only be achieved if the electron diffusion length is greater than the film thickness. However, the film needs to be thicker than the light absorption length for guaranteeing quantitative harvesting of light. The thickness of the semiconductive layer likewise has an optimum, at which the positive effect of additional charge carriers due to higher absorption in thicker films is counterbalanced by increased recombination caused by the longer diffusion length in the thicker semiconductor layer. This optimum is strongly dependent on the choice of materials. For liquid-electrolyte DSCs with standard Ruthenium polypyridyl dyes it is typically about 6 to 12 micrometers.<sup>50</sup>

### 1.4.3 DSC Assembly

The choice of materials and the optimal cell design strongly affect the efficiency and lifetime of the solar cell, and are subject to constant improvement. Figure 1.6 shows the details of one of the latest configurations of the DSC.<sup>39</sup>

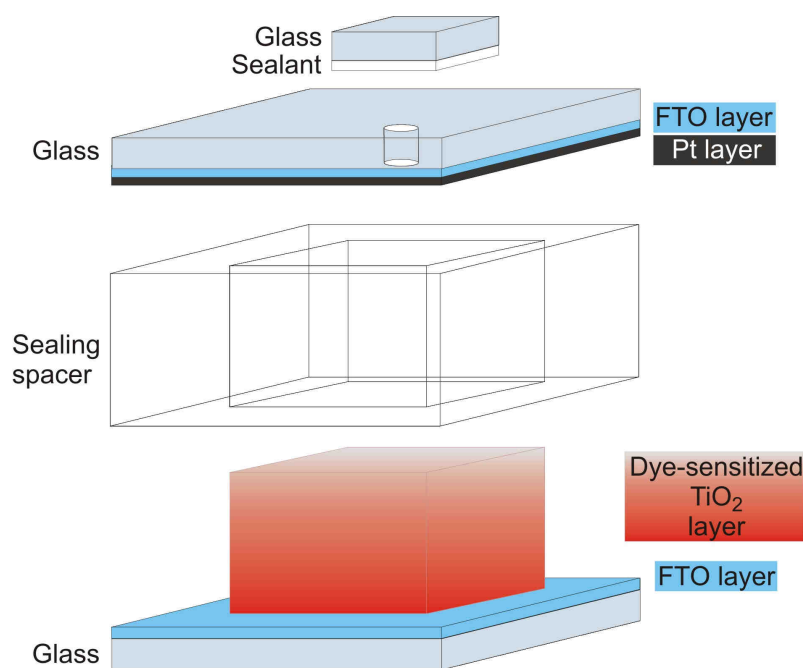


**Figure 1.6.** Sandwich-type configuration of the DSC.

The two electrodes, one coated with a sensitized, nanocrystalline titania film, the other covered by a platinum layer, are assembled in a sandwich-type cell. A light scattering layer of submicron-sized crystalline anatase on top of the nanocrystalline film is in some cases used both as a photon-trap and as a second active layer for the generation of photocurrent. A thermoplastic frame is used as a sealing spacer (e.g. Surlyn polymer foil of 20 to 60  $\mu\text{m}$  thickness) and encloses the electrolyte.

The electrolyte is filled in through the hole in the counter electrode by vacuum-backfilling. Therefore, a small amount of electrolyte is dropped on the hole and vacuum is applied. Upon exposing to normal pressure again, the electrolyte is driven into the cell. The small hole is finally sealed with a thermoplastic film and a thin cover glass.

The FTO-covered glass slides are coated with solder or silver lacquer in short distance to the plastic frame in order to improve the electrical contact to the external circuit, and to reduce the total resistance of the cell.

### 1.4.4 DSC Materials

There are various materials with specific properties which have been used and tested with regard to their performance in the DSC. In the following, an overview of common materials for the several parts of the DSC is shown.

#### *Electrodes*

The electrodes for the DSC consist of glass which is coated with a transparent conductive layer, such as fluorine-doped tin oxide (FTO) or tin-doped indium oxide (ITO). FTO is the most commonly employed conductor, because of its lower resistance after heating to high temperatures which are necessary for calcination and sintering of the titania or platinum layer (for ITO, the resistance increases threefold after heating to temperatures of 300 °C or higher due to a reduction of oxygen vacancies).<sup>55</sup> For the counter electrode, a catalytic layer of platinum is deposited on top of this oxide layer. This can be achieved by dropping a solution of a platinum precursor ( $\text{H}_2\text{PtCl}_6$ ) on the electrode with subsequent heat treatment to 400 °C to reduce the Pt, and to obtain finely spread nanoparticles of platinum.<sup>39,56</sup>

#### *Semiconductive mesostructured layer*

To obtain an acceptable photovoltaic efficiency, light must cross hundreds of adsorbed dye monolayers, because the area occupied by one dye molecule is much larger than its optical cross section.<sup>46</sup> On this account, the semiconductive layer consists of a mesoporous material with an extremely high surface area, which is able to take up a large number of sensitizing molecules. Anatase (titanium dioxide) is the most widely used oxide for the semiconductive layer. Other wide-band-gap materials such as ZnO,  $\text{SnO}_2$ ,<sup>51</sup>  $\text{Nb}_2\text{O}_3$ <sup>51</sup> or  $\text{CeO}_2$ <sup>52</sup> have also been

employed, but due to various reasons (electric conductivity, electronic band structure, electrolyte recombination rates, stability) have not reached the performance level of TiO<sub>2</sub>.

In the established standard procedure for nanocrystalline titania electrodes, the mesoporous films consist of hydrothermally prepared nanoparticles, which have a spherical or pyramidal shape and an average size of about 20 nm.<sup>18</sup> These particles are dispersed in a paste, in most cases in combination with a cellulose binder, and are coated on FTO glass, for example by screen printing or doctor-blading. Usually, the particle films are subject to a short sintering process at about 450 – 500 °C to combust remaining organic compounds, to establish interconnections between the particles and to improve the conductivity within the film.

Some additional measures are beneficial to the efficiency of the cell. First, the FTO electrode is treated with TiCl<sub>4</sub> before coating with the particle paste, which forms a dense layer of TiO<sub>2</sub>. This leads to a reduction of losses due to charge recombination via direct contact of the electrolyte with the FTO layer and enhances the connectivity of the titanium dioxide layers with the FTO. Second, after screen printing and sintering, the mesoporous layer is again soaked with a TiCl<sub>4</sub> solution to increase both the contact area between particles and the roughness of the titania surface. Depending on the dye's extinction coefficient and the electrolyte or hole conductor, the optimal thickness of the nanocrystalline, transparent TiO<sub>2</sub> layer is usually in the range of several micrometers and has a strong influence on the conversion efficiency. For a typical DSC system with a performance of over 10 % employing a Ru-dye and a volatile iodide-based electrolyte, an efficiency maximum can be reached for a layer thickness of about 12 – 14 μm.<sup>39</sup>

Further improvements can be achieved by using a light-scattering layer of large, microcrystalline anatase particles on top of the nanocrystalline layer. These particles of approximately 100 – 400 nm reflect the light which has not been absorbed in the nanocrystalline layer, and help increasing the total level of absorption. Furthermore, they also act as active sites for photovoltaic power generation.

### Dyes

For application in a DSC, a dye has to fulfil several requirements:<sup>56,57</sup>

- It should absorb all visible and near infrared light below a wavelength of about 920 nm.
- Adequate functional groups for grafting the dye onto the oxide surface must be present.
- Absorption of light should lead to electron injection into the solid with a quantum yield of unity.
- The energy level of the dye's excited state is supposed to be just slightly above the lower bound of the conduction band of the semiconductor and
- The redox potential of the dye should be adequately high, such that it can be reduced by the redox electrolyte.
- It must be stable to exposure of light and temperature fluctuations and be able to endure  $10^8$  turnovers or 20 years of life-time.

The best match for all of these requirements has so far been reached by ruthenium-centered polypyridyl complexes, and they are most commonly employed in DSCs nowadays. Some examples for dyes with excellent properties for DSCs are shown in Figure 1.7.

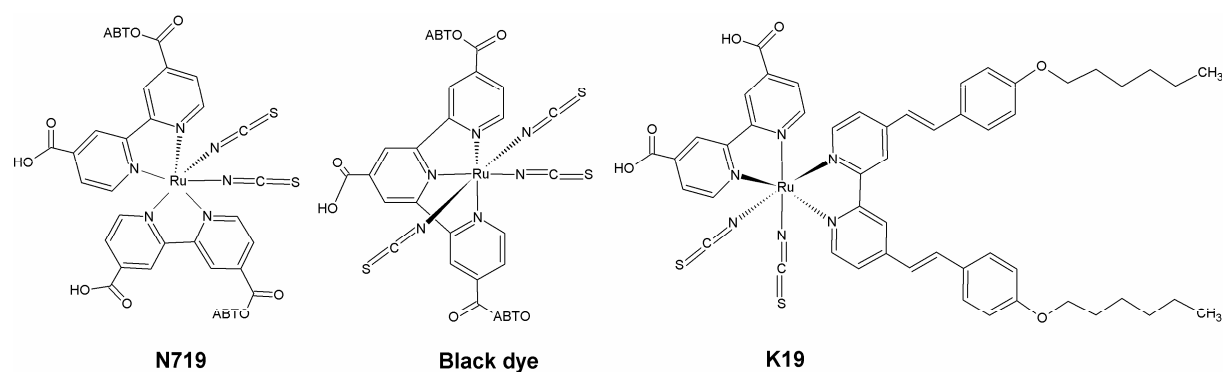


**Figure 1.7.** Examples for dyes with excellent efficiency and stability in DSCs: N719, black dye and K19. ABTO: tetrabutylammonium  $[N(C_4H_9)_4]^+$  salt.

The *cis*-RuL<sub>2</sub>(NCS)<sub>2</sub> complex named N3, or as the corresponding bis-tetrabutylammonium salt N719 is probably the most renowned and it was the first dye which in 1993 could reach an overall efficiency of 10 % employed in a DSC.<sup>58</sup> Other dyes such as the “black dye” slightly exceeded the performance of N3 a few years later.<sup>59</sup> Recently, new compounds were developed, for example K19, which feature improved light harvesting also in the near infrared region and superior long-term stability due to electron donating alkoxy groups.<sup>60</sup> Extended  $\pi$ -conjugation chains with a third organic redox participant were introduced to enable control over the charge-recombination dynamics and by this means electrically improve the interface of the chromophore and the electrolyte.<sup>61</sup>

Further research aims at replacing ruthenium dyes by other less expensive but stable and efficient materials. First results involve porphyrins, indolines, phthalocyanines or coumarine type sensitizers and efficiencies of up to 7.7 % have been reached.<sup>53</sup> One promising characteristic of many of the all-organic sensitizers is their extremely high extinction coefficient (for example, D205 indoline dye: 53 000 M<sup>-1</sup> cm<sup>-1</sup> at  $\lambda$  = 532 nm measured in tetrahydrofurane, whereas N3 Ru-dye: 14 000 M<sup>-1</sup> cm<sup>-1</sup> at  $\lambda$  = 538 nm in ethanol).<sup>62,63</sup>

Another attractive alternative to dyes as sensitizers is the use of quantum dots. Many types of semiconductor particles have been described, which are small enough to produce quantum confinement effects and their absorption spectrum can be adjusted by altering the particle size. So far, there are several limits to their application in DSCs, one important being photo-corrosion with the liquid redox electrolyte. However, once these difficulties can be overcome, quantum dots are supposed to exhibit great stability combined with a very high extinction coefficient, and they are therefore promising candidates for DSCs.<sup>64</sup>

### *Electrolyte or hole conductor*

In general, electrolytes are liquid solutions of charged molecules, and in case of the DSC of a redox-active species in a solvent. Hole conductors are mostly p-type semiconductors and can

be liquid or solid, for example the polymers spiro-MeOTAD, or P3HT, and the inorganic CuSCN.<sup>65-67</sup> The choice of the electrolyte or hole conductor strongly affects the performance of the solar cell. The maximum photovoltage corresponds to the difference of the Nernst potential of the redox system and the quasi-Fermi level of the semiconductor. The diffusion constant of the electrolyte can also be a limiting factor for the photocurrent. Other important requirements to the electrolyte are reversibility of the redox reaction, slow recombination rates with the semiconducting titania electrode, thermal stability, and low light absorption.<sup>57</sup>

Typical electrolytes for the DSC employ the iodide/triiodide redox couple due to its excellent redox potential, kinetics and stability, and solvents mixtures such as acetonitrile with *tert*-butanol or methoxypropionitrile.<sup>39,56</sup> Additives such as alkylimidazolium iodides, guanidium thiocyanate and *tert*-butyl pyridine are used for adjusting the potential of both the redox couple and the surface of TiO<sub>2</sub>, and for screening the charge of excited electrons to avoid reduction of the electrolyte at the titanium dioxide layer.<sup>50</sup> A key role for stability of DSCs is the volatility and viscosity of the electrolyte, because one of the major problems for future outdoor applications is leakage of the electrolyte under thermal stress. Recently, polymeric or gel materials incorporating the redox couple have been reported, which show enhanced stability in combination with non-hindered diffusion of the electrolyte.<sup>68</sup>

Ionic liquids have also been intensively investigated as a replacement for volatile solvents. These materials usually consist of a eutectic melt of imidazolium salts, which are liquid at room temperatures and have an extremely low vapour pressure. Despite a lower charge diffusion length their efficiency is at a respectable maximum level of over 8 % with cell lifetimes of many thousand hours even at elevated temperatures of 80 °C.<sup>69</sup>

The use of solid hole transporting materials (HTMs) is supposed to further increase the long-term and thermal stability of the devices. In these cells, a solution of the HTM is spin-coated on the sensitized titania layer. The counter electrode is replaced by a metallic layer of for example gold, silver or aluminium, which is sputtered or thermally evaporated on top of the

solid HTM. Until today, the major drawback of this setup is the drastically reduced diffusion length, which limits the titania electrode thickness from which charges can be extracted to about below 2  $\mu\text{m}$ . This thickness is not sufficient for complete light absorption and on this account the maximum efficiencies of solid DSCs have been below 5 %.<sup>70,71</sup> New titania nanostructures are investigated to improve the penetration and charge extraction of the HTM, and to increase the accessible surface area.

### 1.5 References

1. Hagfeldt, A.; Grätzel, M. *Acc. Chem. Res.* **2000**, *33*, 269-277.
2. Hagfeldt, A.; Grätzel, M. *Chem. Rev.* **1995**, *95*, 49-68.
3. Wagemaker, M.; Kentgens, A. P. M.; Mulder, F. M. *Nature* **2002**, *418*, 397-399.
4. Poizot, P.; Laruelle, S.; Grugeon, S.; Dupont, L.; Tarascon, J. M. *Nature* **2000**, *407*, 496-499.
5. Linsebigler, A. L.; Lu, G.; Yates, J. T. *Chem. Rev.* **1995**, *95*, 735-758.
6. Dresselhaus, M. S.; Thomas, I. L. *Nature* **2001**, *414*, 332-337.
7. O'Regan, B. C.; Durrant, J. R. *Acc. Chem. Res.* **2009**, *42*, 1799-1808.
8. Peter, L. *Acc. Chem. Res.* **2009**, *42*, 1839-1847.
9. Bartl, M. H.; Boettcher, S. W.; Frindell, K. L.; Stucky, G. D. *Acc. Chem. Res.* **2005**, *38*, 263-271.
10. Yang, P.; Zhao, D.; Margolese, D. I.; Chmelka, B. F.; Stucky, G. D. *Nature* **1998**, *396*, 152-155.
11. Yang, P.; Deng, T.; Zhao, D.; Feng, P.; Pine, D.; Chmelka, B. F.; Whitesides, G. M.; Stucky, G. D. *Science* **1998**, *282*, 2244-2246.
12. McCusker, L. B.; Liebau, F.; Engelhardt, G. *Pure Appl. Chem.* **2001**, *73*, 381-394.

13. Zhang, Y.; Xie, Z.; Wang, J. *ACS Appl. Mater. Interfaces* **2009**, *1*, 2789-2795.
14. Rajeshwar, K.; de Tacconi, N. R.; Chenthamarakshan, C. R. *Chem. Mater.* **2001**, *13*, 2765-2782.
15. Holleman, A. F.; Wiberg, N. *Lehrbuch der Anorganischen Chemie*; 102 ed.; de Gruyter: Berlin, 2007.
16. Hoffmann, M. R.; Martin, S. T.; Choi, W.; Bahnemann, D. W. *Chem. Rev.* **1995**, *95*, 69-96.
17. Armstrong, A. R.; Armstrong, G.; Canales, J.; Bruce, P. G. *Angew. Chem. Int. Ed.* **2004**, *43*, 2286-2288.
18. Barbé, C. J.; Arendse, F.; Comte, P.; Jirousek, M.; Lenzmann, F.; Shklover, V.; Grätzel, M. *J. Am. Ceram. Soc.* **1997**, *80*, 3157-3171.
19. Zhu, K.; Neale, N. R.; Miedaner, A.; Frank, A. J. *Nano Lett.* **2007**, *7*, 69-74.
20. Lee, J.; Orilall, C. M.; Warren, S. C.; Kamperman, M.; DiSalvo, F. J.; Wiesner, U. *Nature Mater.* **2008**, *7*, 222-228.
21. Cushing, B. L.; Kolesnichenko, V. L.; O'Connor, C. J. *Chem. Rev.* **2004**, *104*, 3893-3946.
22. Kriechbaum, G. W.; Kleinschmit, P. *Angew. Chem.* **1989**, *101*, 1446-1453.
23. Degussa; DE762723 **1942**.
24. Hench, L. L.; West, J. K. *Chem. Rev.* **1990**, *90*, 33-72.
25. Boettcher, S. W.; Fan, J.; Tsung, C.-K.; Shi, Q.; Stucky, G. D. *Acc. Chem. Res.* **2007**, *40*, 784-792.
26. Hsu, J.-P.; Nacu, A. *Langmuir* **2003**, *19*, 4448-4454.
27. Niederberger, M. *Acc. Chem. Res.* **2007**, *40*, 793-800.
28. Li, X.-L.; Peng, Q.; Yi, J.-X.; Wang, X.; Li, Y. *Chem. Eur. J.* **2006**, *12*, 2383-2391.
29. Scolan, E.; Sanchez, C. *Chem. Mater.* **1998**, *10*, 3217-3223.
30. Pinna, N.; Niederberger, M. *Angew. Chem. Int. Ed.* **2008**, *47*, 5292-5304.

31. Niederberger, M.; Bartl, M. H.; Stucky, G. D. *J. Am. Chem. Soc.* **2002**, *124*, 13642-13643.
32. Niederberger, M.; Bartl, M. H.; Stucky, G. D. *Chem. Mater.* **2002**, *14*, 4364-4370.
33. Niederberger, M.; Garnweitner, G. *Chem. Eur. J.* **2006**, *12*, 7282-7302.
34. Oguri, Y.; Riman, R. E.; Bowen, H. K. *J. Mater. Sci.* **1988**, *23*, 2897-2904.
35. Kondo, M.; Shinozaki, K.; Ooki, R.; Mizutani, N. *J. Ceram. Soc. Jpn.* **1994**, *102*, 742-746.
36. Cheng, H.; Ma, J.; Zhao, Z.; Qi, L. *Chem. Mater.* **1995**, *7*, 663-671.
37. Yang, X.; Konishi, H.; Xu, H.; Wu, M. *Eur. J. Inorg. Chem.* **2006**, *2006*, 2229-2235.
38. Sanchez, C.; Boissière, C.; Grosso, D.; Laberty, C.; Nicole, L. *Chem. Mater.* **2008**, *20*, 682-737.
39. Ito, S.; Murakami, T. N.; Comte, P.; Liska, P.; Grätzel, C.; Nazeeruddin, M. K.; Grätzel, M. *Thin Solid Films* **2008**, *516*, 4613-4619.
40. Choi, S. Y.; Mamak, M.; Coombs, N.; Chopra, N.; Ozin, G. A. *Adv. Funct. Mater.* **2004**, *14*, 335-344.
41. Fattakhova-Rohlfing, D.; Wark, M.; Brezesinski, T.; Smarsly, B. M.; Rathouský, J. *Adv. Funct. Mater.* **2007**, *17*, 123-132.
42. Zukalova, M.; Zukal, A.; Kavan, L.; Nazeeruddin, M. K.; Liska, P.; Graetzel, M. *Nano Lett.* **2005**, *5*, 1789-1792.
43. Kresge, C. T.; Leonowicz, M. E.; Roth, W. J.; Vartuli, J. C.; Beck, J. S. *Nature* **1992**, *359*, 710-712.
44. Brinker, C. J.; Lu, Y.; Sellinger, A.; Fan, H. *Adv. Mater.* **1999**, *11*, 579-585.
45. Grosso, D.; Cagnol, F.; Soler-Illia, G. J. de A. A.; Crepaldi, E. L.; Amenitsch, H.; Brunet-Bruneau, A.; Bourgeois, A.; Sanchez, C. *Adv. Funct. Mater.* **2004**, *14*, 309-322.
46. Gratzel, M. *Nature* **2001**, *414*, 338-344.

47. "Annual Energy Review 2006", Energy Information Administration Office of Energy Markets and End Use, US Department of Energy, Washington DC, <http://www.eia.doe.gov/aer>, 2006.
48. Barnham, K. W. J.; Mazzer, M.; Clive, B. *Nat. Mater.* **2006**, *5*, 161-164.
49. O'Regan, B.; Grätzel, M. *Nature* **1991**, *353*, 737-740.
50. Grätzel, M. *Inorg. Chem.* **2005**, *44*, 6841-6851.
51. Tennakone, K.; R. R. A. Kumara, G.; R. M. Kottegoda, I.; P. S. Perera, V. *Chem. Commun.* **1999**, 15-16.
52. Corma, A.; Atienzar, P.; Garcia, H.; Chane-Ching, J.-Y. *Nat. Mater.* **2004**, *3*, 394-397.
53. Grätzel, M. *J. Photochem. Photobiol. A-Chem.* **2004**, *164*, 3-14.
54. Green, M. A. *Prog. Photovoltaics* **2001**, *9*, 123-135.
55. Kawashima, T.; Ezure, T.; Okada, K.; Matsui, H.; Goto, K.; Tanabe, N. *J. Photochem. Photobiol. A-Chem.* **2004**, *164*, 199-202.
56. Kroon, J. M.; Bakker, N. J.; Smit, H. J. P.; Liska, P.; Thampi, K. R.; Wang, P.; Zakeeruddin, S. M.; Grätzel, M.; Hirsch, A.; Hore, S.; Würfel, U.; Sastrawan, R.; Durrant, J. R.; Palomares, E.; Pettersson, H.; Gruszecki, T.; Walter, J.; Skupien, K.; Tulloch, G. E. *Prog. Photovoltaics* **2007**, *15*, 1-18.
57. Grätzel, M. *Prog. Photovoltaics* **2000**, *8*, 171-185.
58. Nazeeruddin, M. K.; Kay, A.; Rodicio, I.; Humphry-Baker, R.; Mueller, E.; Liska, P.; Vlachopoulos, N.; Graetzel, M. *J. Am. Chem. Soc.* **1993**, *115*, 6382-6390.
59. Nazeeruddin, M. K.; Péchy, P.; Renouard, T.; Zakeeruddin, S. M.; Humphry-Baker, R.; Comte, P.; Liska, P.; Cevey, L.; Costa, E.; Shklover, V.; Spiccia, L.; Deacon, G. B.; Bignozzi, C. A.; Grätzel, M. *J. Am. Chem. Soc.* **2001**, *123*, 1613-1624.
60. Wang, P.; Klein, C.; Humphry-Baker, R.; Zakeeruddin, S. M.; Grätzel, M. *Appl. Phys. Lett.* **2005**, *86*, 123508.
61. Moser, J.-E. *Nat. Mater.* **2005**, *4*, 723-724.

62. Zakeeruddin, S. M.; Nazeeruddin, M. K.; Humphry-Baker, R.; Pechy, P.; Quagliotto, P.; Barolo, C.; Viscardi, G.; Grätzel, M. *Langmuir* **2002**, *18*, 952-954.
63. Wang, P.; Klein, C.; Humphry-Baker, R.; Zakeeruddin, S. M.; Grätzel, M. *J. Am. Chem. Soc.* **2004**, *127*, 808-809.
64. Plass, R.; Pelet, S.; Krueger, J.; Grätzel, M.; Bach, U. *J. Phys. Chem. B* **2002**, *106*, 7578-7580.
65. Bach, U.; Lupo, D.; Comte, P.; Moser, J. E.; Weissortel, F.; Salbeck, J.; Spreitzer, H.; Gratzel, M. *Nature* **1998**, *395*, 583-585.
66. Chang, J. A.; Rhee, J. H.; Im, S. H.; Lee, Y. H.; Kim, H.-j.; Seok, S. I.; Nazeeruddin, M. K.; Gratzel, M. *Nano Lett.*, *10*, 2609-2612.
67. Hodes, G. *J. Phys. Chem. C* **2008**, *112*, 17778-17787.
68. Wang, P.; Zakeeruddin, S. M.; Moser, J. E.; Nazeeruddin, M. K.; Sekiguchi, T.; Gratzel, M. *Nat. Mater.* **2003**, *2*, 402-407.
69. Shi, D.; Pootrakulchote, N.; Li, R.; Guo, J.; Wang, Y.; Zakeeruddin, S. M.; Graetzel, M.; Wang, P. *J. Phys. Chem. C* **2008**, *112*, 17046-17050.
70. Wang, M.; Moon, S.-J.; Zhou, D.; Le Formal, F.; Cevey-Ha, N.-L.; Humphry-Baker, R.; Grätzel, C.; Wang, P.; Zakeeruddin, S. M.; Grätzel, M. *Adv. Funct. Mater.*, *20*, 1821-1826.
71. Wang, M.; Xu, M.; Shi, D.; Li, R.; Gao, F.; Zhang, G.; Yi, Z.; Humphry-Baker, R.; Wang, P.; Zakeeruddin, S. M.; Grätzel, M. *Adv. Mater.* **2008**, *20*, 4460-4463.

## 2 Characterization

### 2.1 X-ray Diffraction (XRD)

X-ray diffraction (XRD) is a very useful characterization method, because it can determine and distinguish crystalline phases in a sample and can also provide information on organized porosity.<sup>1</sup> The principle of XRD is based on scattering of X-rays with wavelengths in the range of only a few Ångströms on structures which have about the same physical dimension. Constructive interference of an incident beam can occur only on periodic lattices of matter and leads to diffraction patterns (see Figure 2.1).

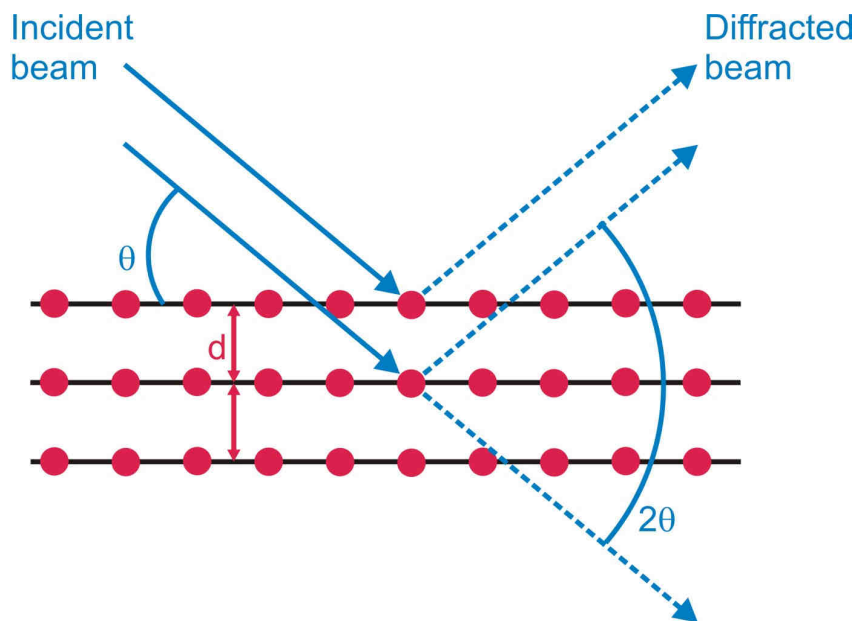


**Figure 2.1.** Diffraction of X-rays on a periodic lattice illustrating the Bragg condition for constructive interference.

Bragg's law gives the relationship between the angle of constructive interference and the distance of lattice planes:

$$n\lambda = 2d \sin\theta, \quad (2.1)$$

where  $n$  is the order of interference,  $\lambda$  is the wavelength of X-rays (usually Cu  $K_{\alpha}$ :  $\lambda = 1.540562 \text{ \AA}$ ),  $d$  is the lattice spacing and  $\theta$  is the angle of incidence. The dimension of structures which can be resolved is in a range of about 20 nm to 0.1 nm, if angles from  $0.5^{\circ} 2\theta$  to  $100^{\circ} 2\theta$  are considered.

Furthermore, the widths of the reflexes are dependent on the size of the crystalline domains which are responsible for constructive interference. The peak broadening is measured as full width at half maximum and relates to the crystalline domain size  $D$  according to the Scherrer equation:<sup>2</sup>

$$D = \frac{k\lambda}{\beta \cos \theta}. \quad (2.2)$$

Here,  $k$  is a factor depending on the crystals' shape and is usually 0.9,  $\lambda$  is the wavelength of X-rays,  $\beta$  is the full width at half maximum precorrected for instrumental peak broadening in  $^{\circ} 2\theta$ , and  $\theta$  is the angle of incidence. The intensity of the diffraction reflexes is dependent on the scattering volume, and the intensity for small domains is rather low. Therefore, for size determination of crystalline domains in nanosized materials, either a large amount of material has to be available for the measurement, or the exposure times have to be rather long.

Traditionally, measurements at angles below  $10^{\circ} 2\theta$  are called small angle X-ray scattering (SAXS) and diffraction at angles above that angle up to about  $100$  to  $140^{\circ} 2\theta$  are referred to as wide angle X-ray scattering (WAXS).

In SAXS, two-dimensional detectors can be used to obtain orientational information of the reflections. With the resulting data, it is in some cases possible to index the reflections of highly periodic and oriented mesoporous structures, and to assign the mesostructure with a space group. 2D-SAXS can be performed in transmission mode on thin membranes or using

grazing incidence geometry with thin films on a substrate (GISAXS). Since these experiments typically need very bright X-ray sources, 2D-GISAXS was performed with mesoporous titanium dioxide thin films at the SAXS beamline at the ELETTRA Synchrotron in Trieste (Italy). The wavelength of the incident beam was 0.15498 nm (8 keV), and the sample-detector distance was set to 1430 mm. The detector was a two-dimensional image intensified CCD detector (Model CV 12, Photonic Science Ltd., Millham, UK). In-situ heating was done using a DHS-1100 heating stage from Anton Paar, and the development of structural parameters from the diffraction patterns was evaluated using the Bragg equation.

For quantitative X-ray diffraction measurements, in order to determine the content of crystalline titanium dioxide material, calcium fluoride was chosen as an internal standard because of its high crystallinity and its diffraction peak close to the (101) anatase peak. Evaluation of the diffraction patterns was done by normalizing the integrals of the (101) anatase peaks to the integral of the standard, taking into account its exact content in the sample.<sup>3,4</sup>

X-ray diffraction analysis was carried out in reflection mode using a Scintag XDS 2000 (Scintag Inc.) and a Bruker D8 Discover with Ni-filtered CuK $\alpha$ -radiation and a position-sensitive detector (Vantec). The thermal development of the XRD diffraction patterns was monitored either by ex situ heating or in in-situ measurements using a DHS-1100 heating chamber with a graphite dome (Anton Paar).

### **2.2 Electron Microscopy**

Electron microscopy is a powerful technique to obtain structural and compositional information on the nanoscale. Similar to XRD, it is in principle a scattering technique, but instead of light with wavelengths of hundreds of nanometers as in optical microscopy or a few

## 2. Characterization

---

Ångströms in XRD, electrons are used with wavelengths in the range of picometers. The resolution of structures thus increases substantially and images of structures of only a few nanometers in size can be obtained.<sup>1</sup>

The interaction of electrons with matter is much stronger than that of light or X-rays and the signals emanating from a sample upon irradiation with a beam of high energy, primary electrons can be classified as shown in Figure 2.2.<sup>1</sup>

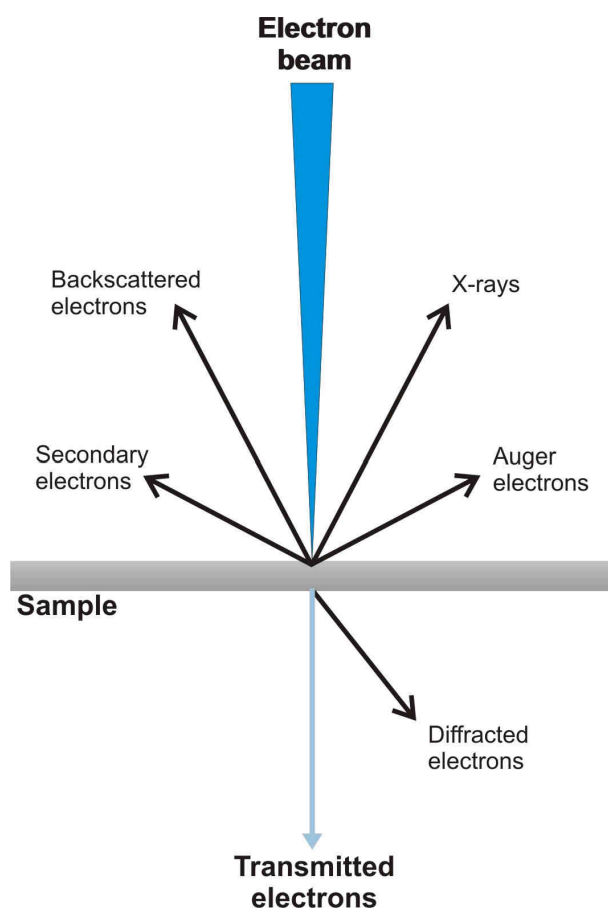


**Figure 2.2.** Signals emanating from a sample in electron microscopy.

Transmitted electrons are not influenced by the specimen and do not suffer from energy loss or a change in direction. The fraction of transmitted electrons is mainly dependent on the thickness of a sample (which for imaging needs to be below about 100 nm), the chemical composition, and its periodic structure. Elastically scattered electrons include diffracted

## 2. Characterization

---

electrons and backscattered electrons. Both have high energy, but the angle of diffraction can be different. Secondary electrons are emitted when high-energy primary electrons strike other electrons in the specimen such that they emerge from the sample. Their energy is rather low and they can only leave the specimen when they originate from within a volume close to the surface.

Auger electrons or characteristic X-rays are generated when an electron from an inner shell is removed by the beam. Another electron from a higher shell must fill the vacancy and the energy difference is either released by emission of characteristic X-rays or of an Auger electron from an outer shell.

Electron microscopy can be divided into three basic techniques: Scanning electron microscopy (SEM), transmission electron microscopy (TEM) and scanning transmission electron microscopy (STEM). In all cases, the electron beam is produced with an electron gun, usually consisting of a heated tungsten filament or a field emission gun, which is put under high tension to extract the electrons. These electrons are focussed and accelerated. The beam is directed into an optical system of condenser lenses and onto the specimen, and the latter is imaged by objective lenses.

In **SEM**, the surface of a sample is investigated and usually only secondary electrons are detected. The high voltage is normally in a range of 4 – 30 keV. The beam can be moved over the specimen by a set of coils and follows a grid pattern. On each spot, the interaction is detected and in the end put together into a final image.

**TEM** in contrast is designed to obtain information on the internal structure of a sample. It detects transmitted and scattered electrons and because the intensity of the signal is a very important factor, the specimen has to be very thin (below 100 nm). Microscopes for TEM are

run at high voltages of typically 100 – 300 keV and the transmitted electrons are detected by a fluorescent screen or by a CCD camera.

**STEM** is a special mode of TEM, in which a strongly focussed beam scans the sample in a grid-like pattern and an image is built up of these pixels. High mass contrasts can be obtained by using high angle annular diffraction, in which a detector is arranged in a circular fashion around the optical axis of the microscope and thus only the electrons diffracted at higher angles are detected.

In this work, scanning electron microscopy (SEM) was performed on a JEOL JSM-6500F scanning electron microscope equipped with a field emission gun, at 4 kV. High Resolution Transmission Electron Microscopy (HRTEM) and Scanning Transmission Electron Microscopy in High Angle Annular Dark Field mode (STEM-HAADF) were performed using a FEI Titan 80-300 equipped with a field emission gun operated at 300 kV.

### **2.3 Raman Spectroscopy**

Raman spectroscopy is a valuable method for characterization, because it offers information on for example chemical composition and crystallinity of a sample and is a non-destructive and quantitative technique.

In Raman spectroscopy, usually a monochromatic laser irradiates a specimen and the scattered light is examined at wavelengths different from the excitation light. These shifts of frequency correspond to specific energy levels of the sample and can be assigned to a specific material.<sup>5</sup>

The possible kinds of scattering upon excitation are summarized in Figure 2.3.

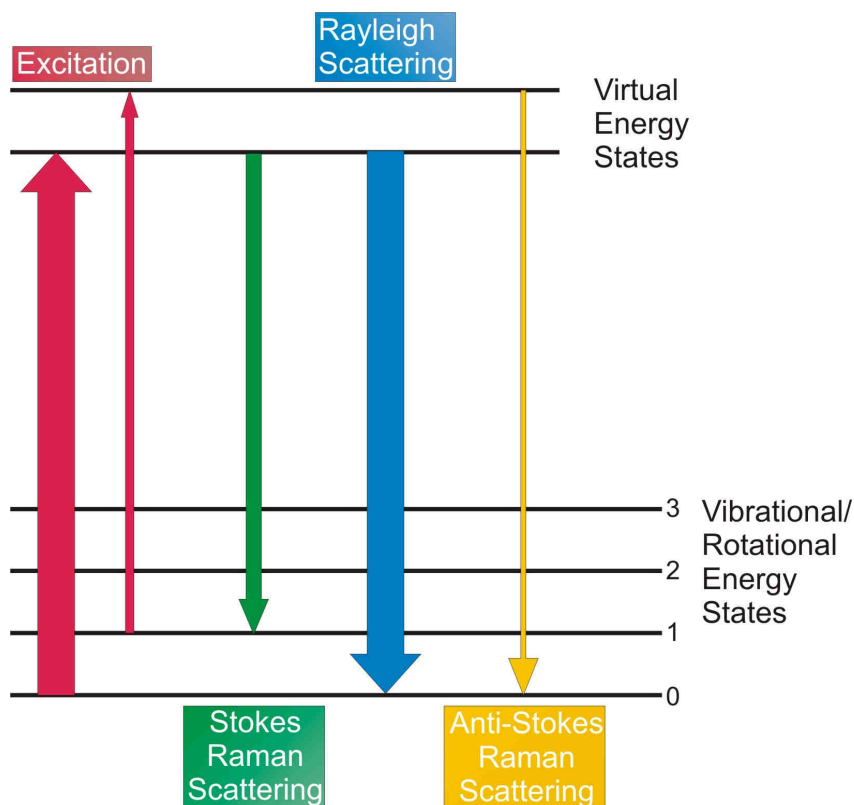


**Figure 2.3.** Energy levels and transitions in Raman spectroscopy.

The reason for these shifts is the so called Raman effect. A molecule is at first excited to a virtual energy state. From there it can relax to the same state (Rayleigh scattering) or a vibrational/rotational state different to the initial one. These inelastic scattering effects can start from the ground state and end in an excited state, emitting light of less energy. This phenomenon is also called Stokes Raman scattering. If the molecule was originally in an excited vibrational state, anti-Stokes Raman scattering leads to relaxation back to an energetically lower state than the initial one, and to emission of light with shorter wavelength. Generally, Stokes lines are much more intensive, because usually most molecules of an ensemble are in the vibrational ground state.

In general, Raman-active molecules must feature vibrational modes in which the electron cloud can be polarized by irradiation. The intensity of the Stokes and Anti-Stokes lines is

mainly dependent on the degree of polarizability, and on various other factors such as the amount of material and temperature.

Raman spectroscopy affords mainly vibrational information and likewise a chemical fingerprint of the compounds in a specimen. In addition, when the laser is coupled to a confocal microscope, a very small volume can be examined and information on differences of composition within one sample can be obtained.

Raman spectra were recorded with a LabRAM HR UV-VIS (Horiba Jobin Yvon) Raman microscope (Olympus BX41) with a Symphony CCD detection system using a HeNe laser at 632.8 nm.

### 2.4 UV/Vis Spectroscopy

Spectroscopy using ultraviolet to near infrared light is commonly employed for quantitative determination of compounds which can absorb light in this range. The amount or concentration of an absorbing species can be derived from the Beer-Lambert law:<sup>5</sup>

$$A = -\log \frac{I}{I_0} = \epsilon c L, \quad (2.3)$$

where A is the measured absorbance,  $I_0$  the intensity of the incident light at a given wavelength, I is the transmitted intensity, L the pathlength through the sample, and c the concentration of the absorbing species. The ratio of I and  $I_0$  is called transmittance.

An UV/Vis spectrophotometer generally consists of a light source (for example a light bulb or a deuterium arc lamp), a sample holder, a diffraction grating or a monochromator for separating light of different wavelengths and a detector (typically a photodiode or a CCD).

UV/Vis spectroscopy can be performed both in solution or using thin films.

In this work, UV-Vis measurements were done in transmission mode using a UV-Vis spectrophotometer (Hitachi U-3501).

### **2.5 Fluorescence Spectroscopy**

In fluorescence spectroscopy, the existence and nature of excited electronic states is investigated. In general, the instant, radiative decay of such states is called fluorescence. The mechanism of fluorescence spectroscopy starts with the absorption of light in a molecule, and the generation of an excited electronic state (Figure 2.4). The excited state is influenced by collisions with other molecules and some part of its energy is lost via non-radiative dissipation until the excited molecule has reached its vibrational ground state. However, the environment is unable to absorb such a high amount of energy that the excited molecule could reach its electronic ground state. On this account, the molecule can relax to its ground state by spontaneous emission of a photon, which has a different wavelength than the initial excitation light.<sup>6</sup>

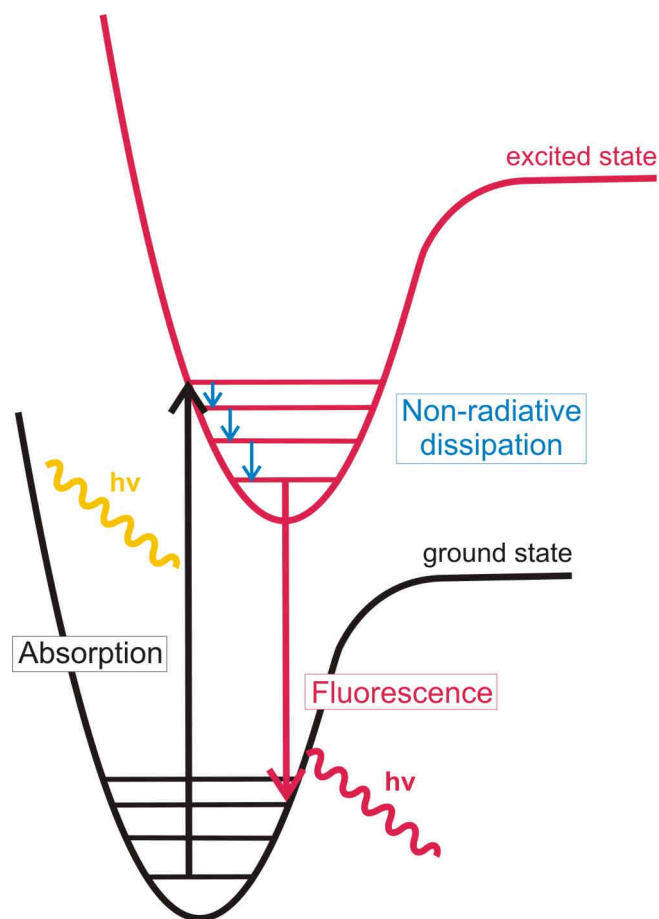


**Figure 2.4.** Energy levels and transitions in fluorescence spectroscopy.<sup>6</sup>

In this work, fluorescence spectroscopy was employed to study dye molecules and their attachment to titanium dioxide surfaces. Dissolved in a solution, most standard ruthenium metal complexes used for the DSC feature a specific fluorescent emission. Surface-bound dyes, in contrast, can inject their excited electrons into the conduction band of the titania semiconductor, and do no longer exhibit any fluorescence signal. Fluorescence spectroscopy was performed on a PTI spectrofluorometer with a photomultiplier detection system (model 810/814) and a xenon short arc lamp (UXL-75XE USHIO).

## 2.6 Sorption

Sorption measurements examine the interactions of an adsorptive species (typically gas molecules) on an adsorbent surface, which allows deriving information about important properties of the adsorbent such as its structure and porosity. The interactions involve mainly physisorption, which is a rather weak bonding based on, for example, van-der-Waals forces. During the measurement, the relative vapour pressure of the adsorptive is slowly increased and the amount of adsorbate, i.e. the adsorbed adsorptive, is monitored. The resulting curve is called isotherm, as it is obtained at a constant temperature.<sup>7</sup>

There are various theories for interpreting these isotherms. One very common is the Brunauer-Emmett-Teller (BET) theory, which is based on the following two assumptions: There is, first, no interaction between particles in a layer and, second, the adsorption enthalpy for the first monolayer is different from those for all the other layers, because of adsorptive-adsorbent interactions.<sup>8</sup> Using this theory, the surface area of a sample can be estimated through the number of adsorbed molecules in the first monolayer.

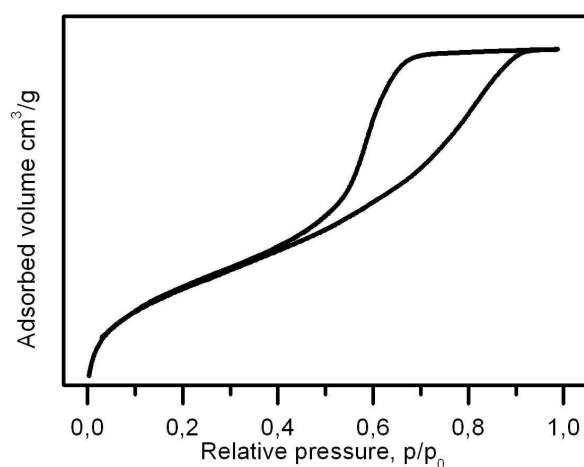


**Figure 2.5.** Typical example of an isotherm of a mesoporous material.

## 2. Characterization

---

In general, six basic types of isotherms are classified, which can be obtained from different materials.<sup>7,9</sup> The shape of isotherms differs for different pore structures and is also dependent on the type and strength of interaction between adsorptive and adsorbent. Mesoporous samples usually exhibit a so-called type IV isotherm. A typical example is shown in Figure 2.5. From such sorption measurements, sample characteristics such as the specific surface area, pore radius and pore volume can be obtained.

A typical feature of a type IV isotherm is the hysteresis loop of the adsorption and desorption branch, which can be explained by capillary condensation of adsorptive in mesopores. After filling these pores, the curve typically reaches a plateau or a region with a smaller slope due to further adsorption at the external surface or in textural porosity. The initial part at low values of  $p/p_0$  is characterized by the adsorption of a monolayer at low pressures and the following multilayer condensation.

Sorption measurements of porous powder samples are usually performed using nitrogen ( $N_2$ ) as adsorptive and are carried out at its boiling point of 77 K. Physical data such as specific surface area and pore volume can be obtained with classical thermodynamic calculations. For the evaluation of the pore size distribution, in addition to the classical Barrett-Joyner-Halenda (BJH) theory, approaches such as non-local density functional theory (NLDFT) or Monte-Carlo simulations (MC) are employed.

In case of particulate  $TiO_2$  samples, the specific surface area from sorption measurements can be used to estimate the size of the particles. Based on the assumption that the specimen consists only of ideal spheres without any connection points, the ratio of the particle surface area and their mass is constant and equals the specific surface area. Thus, the hypothetical particle size can be calculated as

$$r = \frac{6}{\rho S_{BET}}, \quad (2.4)$$

where  $\rho$  is the density of the material ( $3.88 \text{ g cm}^{-3}$  for anatase), and  $S_{\text{BET}}$  the specific surface area derived from the linearized part of the isotherm using BET theory.

Thin mesoporous films and other materials having a very small specific surface area are measured utilizing an adsorptive with lower saturation vapour pressure than nitrogen. Krypton sorption at 77 K is commonly employed and enables determination of surface areas down to a few  $\text{cm}^2$ . There are, however, drawbacks of this method: Since Kr is solid at this temperature, the theory for other sorptives cannot be easily transferred, and quantitative evaluation of surface area and pore size is usually done indirectly after calibration measurements using standards.

In the present work, all Kr sorption measurements were performed and evaluated by Dr. Jiri Rathouský at the J. Heyrovský Institute of Physical Chemistry in Prague. The porosity of thin films was determined by the analysis of adsorption isotherms of Kr at the boiling point of liquid nitrogen (approx. 77 K) using an ASAP 2010 apparatus (Micromeritics). Textural data are obtained from comparing the shape of the hysteresis loop and the limiting adsorption at saturation pressure of the krypton sorption isotherms with reference materials (anatase powders) characterized by nitrogen sorption. Comparison plots were constructed for each sample, and the differentiation of these plots provided the basis for the pore size distribution.

### 2.7 Quartz Crystal Microbalance (QCM)

A quartz crystal microbalance (QCM) measures mass differences through the change in frequency of a piezoelectric quartz crystal. These measurements of frequency can be performed precisely, and using the direct proportionality of mass and frequency change  $\Delta f$  described by the Sauerbrey equation, even tiny mass changes  $\Delta m$  can be determined (Equation 12).<sup>10</sup> This sensitivity can be exploited for measuring sorption isotherms using

## 2. Characterization

---

solvent molecules such as toluene or ethanol as adsorptives. For obtaining isotherms using QCM, a porous sample is deposited on the QCM chip, consisting of a piezoelectric quartz crystal sandwiched between two gold electrodes. After determining the resonant frequency of the fundamental mode of the crystal chip,  $f_0$ , the liquid adsorptive is vaporized and led on the specimen. The resulting mass change corresponds to the amount of adsorbate.

$$\Delta f = -\frac{2f_0^2 \Delta m}{A\sqrt{\rho_q \mu_q}} \quad (2.5)$$

A: Active area of the crystal.

$\rho_q$ : Density of quartz.

$\mu_q$ : Shear modulus of quartz.

The choice of the solvent as sorptive is crucial, since the size of the molecule and the philicity of both surface and solvent molecule are decisive for the sorptive's ability to enter the porous system. Moreover, the strength of the interaction between sorptive and surface can vary strongly and can have a major influence on the shape of an isotherm.

A major advantage of QCM is that it can be performed with metal oxide films that are deposited on one side of the chip (usually by spin-coating). The resulting porous characteristics are always normalized to the weight of the deposited material, which can be initially determined with a high accuracy even for small amounts of material. Furthermore, the method is sensitive enough even for small specific surface areas and is therefore especially suitable for thin films. A disadvantage of this method is the fact that physical models for adsorption are not easily adaptable to the interaction of solvent molecules with surfaces, and that for this reason the determination of porous characteristics from QCM measurements employing such adsorptives is an indirect method that needs other standardized procedures for calibration.

Adsorption measurements employing the QCM were carried out using a self-built Quartz Crystal Microbalance (QCM) system. For this purpose, the mesoporous films were produced by spin-coating of a precursor solution on KVG 10 MHz QCM devices with gold electrodes (from Quartz Crystal Technology GmbH) and subsequent calcination. Toluene was used as an adsorptive and the measurements were performed at 25 °C.

### 2.8 Dynamic Light Scattering (DLS)

Dynamic light scattering (DLS, also known as photon correlation spectroscopy, PCS) is a very useful, fast and non-destructive technique for obtaining information on the size and agglomeration of nanoparticles dispersed in a solvent.<sup>11,12</sup> It is based on monitoring the Brownian motion of particles in solution and relating it with the particles' size and size distribution. The resulting sizes are always the hydrodynamic dimensions of dissolved particles, because they include shells of solvent molecules or other species which diffuse alongside the particles.

The measurement is done by illuminating a sample with a laser beam, and observing the scattered light. Since the particles are moving through the solution, the scattering pattern is fluctuating, and the time evolution of this pattern can be recorded. A digital correlator can then perform a similarity analysis of the individual patterns at different points of time. The fluctuations in intensity  $I$  are correlated across time by a second order autocorrelation function  $g^2$ :<sup>11</sup>

$$g^2(\mathbf{q};\tau) = \frac{\langle I(t)I(t+\tau) \rangle}{\langle I(\tau) \rangle^2}, \quad (2.6)$$

## 2. Characterization

---

with the wave vector  $q$ , time  $t$ , and the delay time  $\tau$ . This correlation shows an exponential decay towards long delay times, and can be related to the first order autocorrelation function  $g^1$ :

$$g^2(q;\tau) = 1 + \beta [g^1(q;\tau)]^2 \quad (2.7)$$

( $\beta$ : constant, “coherence factor”). Employing this correlation function  $g^1$  and assuming dilute solutions of monodisperse nanoparticles, the diffusion coefficient  $D$  can be obtained from a single exponential function:

$$g^1(q;\tau) = \exp(-q^2 D \tau). \quad (2.8)$$

For spherical particles in a dilute solution the relation between diffusion coefficient  $D$  and the hydrodynamic diameter  $d$  is given by the Stokes-Einstein equation:

$$D = \frac{kT}{3\pi\eta d}, \quad (2.9)$$

with the Boltzmann constant  $k$ , temperature  $T$ , and solvent viscosity  $\eta$ .

Since this assumption of monodisperse particles in most cases is a simplistic model, size distribution effects can be taken into account by using Rayleigh scattering or Mie theory. Rayleigh scattering describes the elastic interaction of light with objects which are much smaller than the wavelength of the light, such as for example nanoparticles. The intensity of Rayleigh scattering  $I$  is given as:

$$I = I_0 \frac{1 + \cos^2 \theta}{2R^2} \left( \frac{2\pi}{\lambda} \right)^4 \left( \frac{n^2 - 1}{n^2 + 2} \right)^2 \left( \frac{d}{2} \right)^6. \quad (2.10)$$

$I_0$ : Intensity of the incoming light;  $\theta$ : Scattering angle;  $\lambda$ : Wavelength of the light;  $n$ : Refractive index of the nanoparticle;  $d$ : Particle diameter.

Thus, the scattering intensity is proportional to  $d^6$ , resulting in an enormous scattering contribution of large particles compared to smaller ones. Especially for polydisperse samples,

this effect needs to be considered and further mathematical treatment of the intensity-based results of DLS leading to volume-weighted ( $d^3$ ) or number-weighted ( $d$ ) distributions can be more significant.

Dynamic light scattering (DLS) measurements were carried out on diluted suspensions using a Malvern Zetasizer-Nano instrument with a 4 mW He-Ne laser ( $\lambda = 633$  nm) and an avalanche photo detector.

### 2.9 Zeta Potential Measurements

The potential due to the existence of an electrical double layer at a virtual boundary at the interface of a particle dispersed in a liquid is called the zeta potential.<sup>13</sup> This boundary is located outside the Stern layer, in a diffuse region, in which ions are still attached when the particle is moving, for example due to gravity or an applied electrical field. The zeta potential can be considered a stability indicator for the colloidal system, because high positive (or negative) zeta potential values are equivalent to a large number of positive (negative) charges which will lead to a strong repulsive force between particles and in this way prevent agglomeration and flocculation. The main factor influencing the zeta potential besides the chemical composition of liquid and solid is the pH of the solution. For this reason, zeta potential data are usually displayed as a function of pH, and the point in which the curve passes through zero (least stable colloidal system) is called the isoelectric point.<sup>14</sup>

The zeta potential of particles in a medium is usually obtained by measuring the electrophoretic mobility, which is the movement of the particle upon application of an electrical field. The relationship between zeta potential  $\zeta$  and electrophoretic mobility  $U_E$  is given by the Henry equation:

$$U_E = \frac{2\varepsilon z f(Ka)}{3\eta}, \quad (2.11)$$

where  $\varepsilon$  is the dielectric constant,  $\eta$  the viscosity and  $f(Ka)$  Henry's function, which can be approximated for aqueous systems and rather large particles ( $> 200$  nm) as 1.5 (Smoluchowski approximation), or for smaller particles and low dielectric media as 1.0 (Hückel approximation).<sup>14,15</sup>

The electrophoretic mobility can be obtained by the Laser Doppler Velocimetry (LDV) technique.<sup>13,14</sup> It relies on measuring the speed of the particles in a medium when a potential is applied. The moving particles scatter incident laser light, resulting in an intensity fluctuation when compared to a reference beam. The frequency of this fluctuating signal is proportional to the velocity of the particles, and by modulating one of the laser beams the sign of the zeta potential can be extracted.

Zeta potential measurements were performed and evaluated by Dr. Valentina Cauda on a Zetasizer-Nano (Malvern Instruments) equipped with a 4 mW He-Ne laser of 633 nm wavelength and an avalanche photo detector.

### **2.10 Thermogravimetric Analysis (TGA)**

Thermogravimetric analysis (TGA) is a method for characterizing the composition of a sample and its decomposition behaviour under thermal treatment. This is done by measuring weight losses at different temperatures, which can occur due to desorption of adsorbed molecules, evaporation of volatile compounds and decomposition of materials. Additionally, differential scanning calorimetry (DSC) can determine the enthalpy and thus the thermodynamic nature of a weight loss, by measuring the different amounts of energy needed for heating the sample compared to a reference.

TGA data of particulate metal oxide samples bearing organic ligands can be evaluated by calculating the theoretical weight loss upon removal of the organic compounds. Therefore, the amount of metal surface sites on the outside of the spheres has to be estimated. This is possible taking into account the average volume and surface areas of each TiO<sub>2</sub> in the anatase unit cell, which can be calculated based on the number density of Ti on different lattice planes and an assumed equal probability of surface exposure for (110), (101), and (011) planes. The amount of Ti surface sites can thus be estimated by:<sup>16</sup>

$$\% \text{ surface sites} = \frac{1250}{d}, \quad (2.12)$$

where  $d$  is the diameter of the particles in nanometer. Based on this ratio, and assuming that one surface site binds to one ligand, the theoretical weight loss can be estimated by

$$\text{Theoretical weight loss \%} = \frac{M(\text{Particle}) - M(\text{Metal oxide})}{M(\text{Particle})}. \quad (2.13)$$

Here,  $M(\text{Particle})$  denotes the total molar mass of particles with ligands attached to the surface and  $M(\text{Metal oxide})$  the molar mass of the pure metal oxide.

In this work, thermogravimetric analyses and digital scanning calorimetry measurements were performed using a Netzsch STA 440 C TG/DSC.

### 2.11 Photocatalytic Activity (PA)

The principle of catalysis was first brought up by Berzelius, who in 1835 found that certain chemicals influence the kinetics of chemical reactions. In general, materials which are able to act as catalysts can even in small amounts accelerate the speed of a specific reaction by lowering the energy of a transition state. Regarding the reaction equations in catalytic equilibria, catalysts are either not participating or are regenerated. Catalysis can be performed either in the same phase as the reaction mixture (homogeneous) or in a different phase (heterogeneous).<sup>5,17</sup>

The acceleration of a photoreaction by a catalyst is called photocatalysis.<sup>18</sup> This is achieved through absorption of light by the catalyst, which creates electron-hole pairs. The theoretical principle for a semiconducting catalyst, for example titanium dioxide, is shown in Figure 2.6. After illumination and absorption of a photon, an electron from the valence band is excited to the conducting band and can from there undergo an electron transfer to an acceptor molecule which is reduced. The remaining electron hole in the catalyst oxidizes a donor molecule and is by this means regenerated.

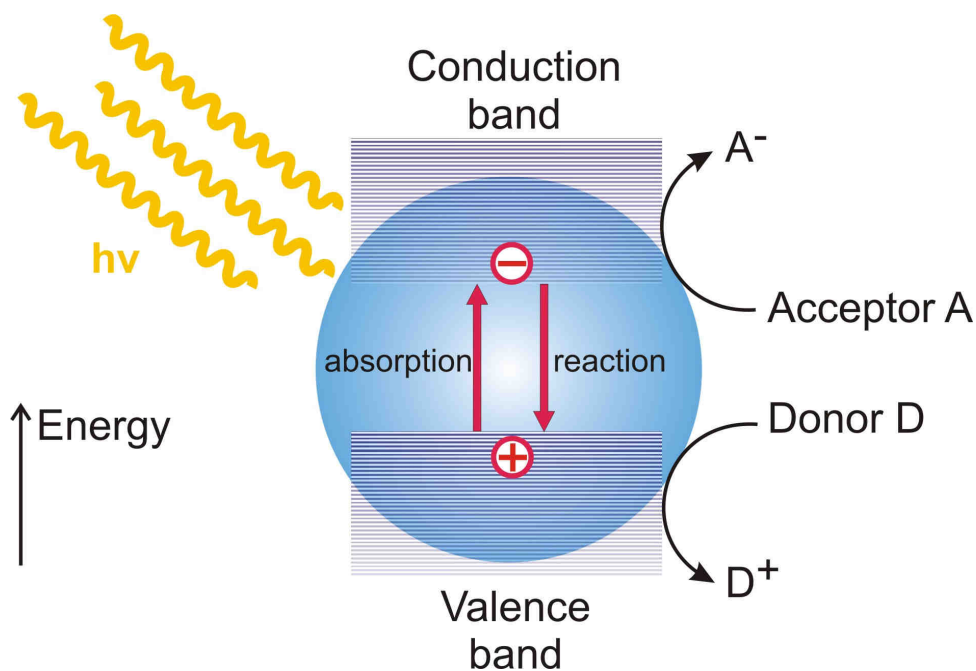


**Figure 2.6.** Principle of photocatalysis.

Photocatalytic activity (PA) is a quantitative measure for the photocatalytic properties of a catalyst and is dependent on its ability to create electron-hole pairs by absorption of light, the efficiency and kinetics of the transfer and regeneration reactions and its specific surface area, i.e. the amount of sites available for reactants.<sup>17-19</sup>

There are several ways of quantifying the photocatalytic activity, including the photocatalytic decomposition of dyes (for example methylene blue), the oxidation of gaseous species (for instance NO), or the decomposition of thin layers of liquid or solid substances (e.g. oleic acid, self-cleaning effect).<sup>20</sup>

In this work, photocatalytic decomposition of oleic acid was employed for measurement of the PA of titania thin films as it is a technically inexpensive and reliable technique, which has also been suggested as an ISO standard. The measurements were performed by J. Rathouský at the J. Heyrovský Institute of Physical Chemistry, Prague. TiO<sub>2</sub> films were covered with a layer of oleic acid and illuminated with UV-light. Oleic acid transforms into more hydrophilic

compounds, such as acids with shorter alkyl chains, aldehydes, alcohols, or gaseous products like CO<sub>2</sub> and likewise leads to the exposure of the hydrophilic TiO<sub>2</sub> surface. The degradation of the oleic acid was monitored by measuring its contact angle for water, as a decrease in the contact angle for water is proportional to the degree of degradation.

### 2.12 Electrochemical Lithium Insertion

In recent years, rechargeable lithium-ion batteries have proven their attractivity as power sources, especially for portable electronic applications.<sup>21,22</sup> Electrochemical insertion of lithium is the central process in these batteries, and both anode and cathode materials have been intensively investigated.<sup>23,24</sup> Nanostructured titanium dioxide can be used as cathode material, and especially TiO<sub>2</sub>(B) and the spinel-type lithium titanate Li<sub>4</sub>Ti<sub>5</sub>O<sub>12</sub> feature highly interesting energy densities, insertion kinetics and cycling stability.<sup>25-28</sup>

In this work, electrochemical lithium insertion is employed as a characterization technique for titanium dioxide materials, and information about the phase composition, crystallinity, the electrochemical accessibility of the titania material related to its porosity, and the suitability of the nanostructure for efficient lithium insertion and charge storage can be obtained.<sup>29,30</sup>

The method is based on the following reaction:



in which titanium ions are reduced to Ti(III) and Li<sup>+</sup> ions are inserted into the lattice. Depending on the crystalline phase, TiO<sub>2</sub> is able to take up different amounts of Li (from x = 0 to 0.96), at different potentials, and with varying kinetics due to the corresponding insertion mechanism. For example, the electrochemical lithium insertion into anatase takes place at a

## 2. Characterization

---

formal potential of about 1.85 V, and the maximum theoretical insertion capacity is 168 mAh g<sup>-1</sup>, which corresponds to a chemical composition of about Li<sub>0.5</sub>TiO<sub>2</sub> (further intercalation leads to a phase transition to an orthorhombic phase). Figure 2.7 shows a typical cyclic voltammogram (CV) from a mesoporous titania electrode consisting of mainly anatase with traces of TiO<sub>2</sub>(B).

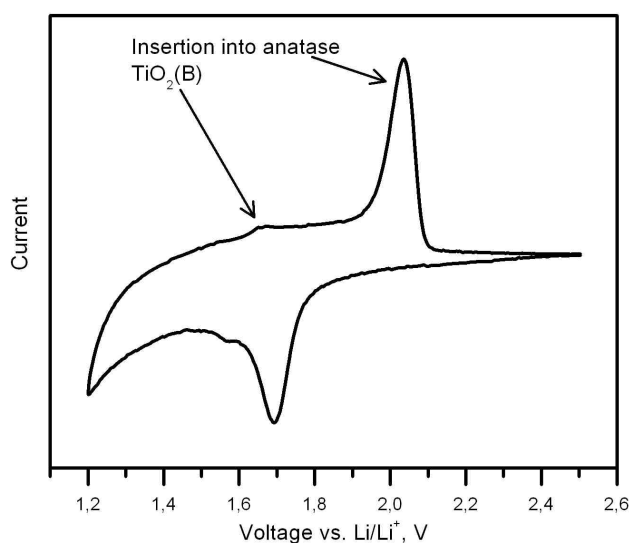


**Figure 2.7.** Cyclic voltammogram (CV) of an electrochemical lithium insertion experiment with a mesoporous titanium dioxide cathode material. The distinct peaks denote the contributions of intercalation into anatase and TiO<sub>2</sub>(B). The broad hysteresis of the baseline curve is mainly due to capacitive (faradaic and non-faradaic) charging as well as electrochemical reduction/oxidation of the amorphous titania phases.

The total charge storage in titania materials can be separated into two components: a faradaic contribution from intercalation of lithium into the bulk of TiO<sub>2</sub>, and capacitive charge transfer processes at the surface of titania nanoparticles (faradaic/pseudocapacitive or non-faradaic/capacitive). The kinetics of the intercalation and capacitive charging are rather

different, and their contributions can be extrapolated by determining the current response on different potential scan rates in cyclic voltammetry.<sup>30</sup>

In our experiments, the total gravimetric insertion capacity of lithium into titania was determined by integrating the area under the CV curve upon reduction (forward process) and oxidation (reverse process), respectively, and normalizing it with the active electrode's mass. The fraction of crystalline anatase could be evaluated by analyzing the integral of the anatase insertion peak and comparing it with the theoretical capacity of fully lithiated anatase. Furthermore, cyclic voltammetry experiments were performed at different scan rates to get insight on how different nanostructures influence the kinetics of lithium insertion by amplifying pseudocapacitive processes.

Cyclic voltammetry was performed in a three-electrode cell using porous titanium dioxide on FTO conductive glass as a working electrode, Li wire as both the auxiliary and the reference electrodes, and an electrolyte composed of  $\text{LiN}(\text{SO}_2\text{CF}_3)_2$  in a mixture of ethylenecarbonate and 1,2-dimethoxyethane (1:1 v/v). Electrochemical measurements were performed in a potential range from 3.0 to 1.3 V using a Parstat 2273 potentiostat (Princeton Applied Research).

### 2.13 Photovoltaic Characterization

Mesoporous titanium dioxide coatings have been examined regarding their performance as active electrodes in dye-sensitized solar cells. For this purpose, **current-voltage (I-V) curves** were recorded by varying an applied external voltage and monitoring the current response of solar cells both under illumination and in the dark. In order to obtain the steady-state current response of the cells, the scan rate was chosen to be sufficiently slow to avoid capacitive charging at the large interface of the cells.<sup>31</sup> The I-V curves are used to extract the typical

## 2. Characterization

---

characteristics of a solar cell: short-circuit current  $I_{sc}$ , open circuit potential  $V_{oc}$ , Fill Factor FF, and power conversion efficiency  $\eta$  (see Introduction, section 1.4).

By varying the light intensity used for illumination, the so-called “linearity” of the photovoltaic performance can be investigated. Typical experiments are run at illumination levels of 1 %, 10 % and 100 % sun (1, 10 and 100 mW/cm<sup>2</sup>, respectively), and use neutral grey filters of different density to adjust the light intensity. Under these conditions, the overall conversion efficiency is supposed to be constant, whereas the individual parameters vary. Thus,  $I_{sc}$  rises linearly with increasing photon flux due to higher absorption and charge generation.<sup>32</sup>  $V_{oc}$  shows a linear dependence on the logarithm of the light intensity, which can be explained by the difference in occupancy of electronic states under illumination and in the dark, or employing a different theoretical model by an decreased contribution of shunt current to recombination at high light intensities.<sup>33,34</sup> As a result of the combination of the dependencies of  $I_{sc}$  and  $V_{oc}$ , the fill factor values decrease slightly with increasing light intensity because of the higher slope of the current-intensity curve.<sup>31,35</sup> This “linearity” of the photovoltaic performance generally applies only for DSCs which are not limited by charge transport or diffusion (i.e. when volatile liquid electrolytes and sufficiently accessible porous electrodes are employed). For DSCs employing more viscous electrolytes or solid hole transporters, the investigation of performance at low light intensities can provide indications for the existence of such transport or diffusion limitations.<sup>36</sup>

Another characterization technique to elucidate the transport and diffusion behavior of DSCs is the recording of **transient current decays**. Instead of measuring the steady-state current response of solar cells under illumination, a flash of light of defined intensity and length is used and the generated photocurrent is monitored at short-circuit conditions with special focus on its time-dependence. The photocurrent arises shortly after the light pulse, and in an ideal DSC it should be constant at the same level as in steady-state conditions. Transport limitations

## 2. Characterization

---

can be clearly identified when the time-resolved current response exhibits an exponential decay from a high first value to a lower steady-state level. Current decay measurements are usually also performed at different light intensities in order to obtain information on the significance and nature of the restrictions of the cells' charge transport.<sup>31,37</sup>

The spectral current response of solar cells can be examined by measuring the **internal photon to current efficiency (IPCE)** at different wavelengths (see Introduction, section 1.4).

The IPCE can be obtained at low light intensities, when the cells are illuminated by light of only one wavelength, or under full sun illumination by superimposing additional photons of a certain wavelength on the standard AM 1.5 simulated sunlight. IPCE measurements can be run under short-circuit conditions or with an external bias. In the first case, the product of the IPCE values with the spectral energy characteristics of an AM 1.5 spectrum equals the short-circuit current, in the latter the current value on the I-V curve at the applied potential, respectively. For DSCs, the IPCE curves are generally mainly dependent on the chemical nature of the dye (i.e. its absorption characteristics) and its concentration in the path of the incident light.<sup>38</sup>

Apart from these photoelectrochemical measurements, established electrochemical methods can also be used to individually characterize the components of DSCs.<sup>31</sup> In particular, **electrochemical impedance spectroscopy (EIS)** has proven to be a powerful tool to study the influence of various parameters, such as the series resistance of the complete cell, capacitance or resistance of charge transfer, charge transport and diffusion of the individual components of the solar cells (FTO electrode, titania layer, electrolyte, and platinum-loaded counter electrode).<sup>39</sup> EIS is based on the perturbation of an externally applied potential by a small ac sine wave modulation ( $\Delta U$ ), and the measurement of the resulting sinusoidal current signal ( $\Delta I$ ) as a function of its frequency (amplitude and phase shift  $\phi$ ). The impedance  $Z_{\text{EIS}}$  is then given by:<sup>40</sup>

$$Z_{\text{EIS}} = \frac{\Delta U}{\Delta I} e^{i\varphi}. \quad (2.15)$$

Shown in a Nyquist plot, the impedance of a DSC typically exhibits three semicircles of increasing frequency, which correspond to the individual contributions of Nernst diffusion in the electrolyte, electron transfer at the interface of titania and electrolyte, and the redox reaction at the counter electrode, respectively.<sup>39</sup> Theoretical models to evaluate the frequency response of DSCs have been developed, and the impedance can be interpreted as a transmission line using an equivalent circuit for modelling the important parameters.<sup>41</sup> In this equivalent circuit model, the interfacial reactions are each represented as a combination of double-layer capacitor and resistance.<sup>42</sup> Figure 2.8 illustrates the components of such an equivalent circuit and the parameters which can be obtained from EIS analysis.

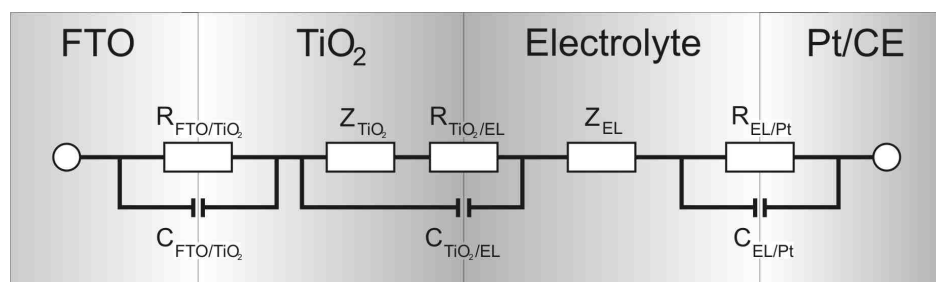


**Figure 2.8.** Equivalent circuit of a DSC. Parallel resistors  $R$  and capacitances  $C$  represent the charge transfer interfaces between FTO-TiO<sub>2</sub>-Electrolyte-Pt/CounterElectrode. Additional diffusion elements  $Z$  correspond to resistance of charge transport. Figure adapted from ref. 39.

In this way, EIS can be employed to derive the intrinsic charge transfer and transport properties of a DSC. Combined with photovoltaic characterization, it allows important insights into the underlying physical processes defining the performance of solar cells.

**Dye-sensitized solar cells** were prepared following a reported procedure.<sup>43</sup> In short, conductive glass (fluorine-doped tin dioxide layer, FTO on glass) was thoroughly cleaned (washing and ultrasonication steps with water and detergent, water, and ethanol; subsequent

## 2. Characterization

---

drying in air and plasma-cleaning), and coated with a dense blocking layer made from a dilute solution of prehydrolyzed tetraethyl orthotitanate and hydrochloric acid in tetrahydrofuran. On top of this dense titania layer, a mesoporous film of varying composition, morphology and thickness was deposited. The titania layers were usually calcined to temperatures above 300 or 450 °C for complete combustion of organic residues and crystallization of the porous network, then cooled to ca. 80 °C and immersed into a dye solution at room temperature, and kept there for at least 16 h. A typical dye solution contained 0.5 mM of the dye N719 in acetonitrile and *tert*-butyl alcohol (volume ratio 1:1). Dye-coated mesoporous TiO<sub>2</sub> films were assembled in a dry-chamber (below 15 % relative humidity), and sealed with a transparent hot-melt 60 µm thick surlyn ring to the counter electrodes (Pt on FTO glass, chemical deposition from 0.01 M hexachloroplatinic acid in ethanol heated at 400 °C for 15 min). The active cell area was usually about 0.196 cm<sup>2</sup>. The electrolyte was injected into the inner electrode space by vacuum back-filling from the counter electrode side through a pre-drilled hole, and then the hole was sealed with a surlyn sheet and a thin glass cover slide by heating to 120 °C. For the electrolyte, either volatile mixtures based on acetonitrile and valeronitrile, non-volatile solvents such as methoxypropionitrile, or room-temperature ionic-liquids were employed. Further additives are BMII (butylmethylimidazolium iodide), iodine, GuNCS (guanidinium thiocyanate), and *tert*-butyl pyridine. For the characterization of solar cells, an AM 1.5 solar simulator (Solar light Co.) was used. The light intensity was monitored by a pyranometer (PMA2100, Solar light Co.). Current density-voltage measurements were performed with a Zahner IM6ex impedance measurement unit. The scan speed was set to 10 mV/s.

Experiments using non-volatile and ionic liquid electrolytes in DSCs, their I-V testing, electrochemical impedance spectroscopy, transient current and IPCE measurements were

performed in cooperation with the group of Prof. Michael Grätzel, EPF Lausanne (Switzerland).

### 2.14 References

1. Vainshtein, B. K. *Fundamentals of Crystals*; Springer-Verlag: Berlin, 1994; Vol. 1.
2. Patterson, A. L. *Phys. Rev.* **1939**, *56*, 978.
3. Klug, H. P.; Alexander, L. E. *X-ray Diffraction Procedures*; 2nd ed.; Wiley: New York, 1974.
4. Laskowski, J. J.; Young, J.; Gray, R.; Acheson, R.; Forder, S. D. *Anal. Chim. Act.* **1994**, *286*, 9-23.
5. Wedler, G. *Lehrbuch der Physikalischen Chemie*; 5. ed.; Wiley-VCH: Weinheim, 2004.
6. Atkins, P. W. *Physikalische Chemie*; 3. ed.; Wiley-VCH: Weinheim, 2001.
7. Lowell, S.; Shields, J.; Thomas, M. A.; Thommes, M. *Characterization of Porous Solids and Powders: Surface Area, Porosity and Density*; **Springer**: Dordrecht, 2006.
8. Brunauer, S.; Emmett, P. H.; Teller, E. *J. Am. Chem. Soc.* **1938**, *60*, 309-319.
9. Sing, K. S. W.; Everett, D. H.; Haul, R. A. W.; Moscou, L.; Pierotti, R. A.; Rouquerol, J.; Siemieniewska, T. *Pure Appl. Chem.* **1985**, *57*, 603.
10. Sauerbrey, G. *Zeitschrift für Physik A Hadrons and Nuclei* **1959**, *155*, 206-222.
11. Pecora, R. *J. Nanopart. Res.* **2000**, *2*, 123-131.
12. Murphy, R. J.; Pristinski, D.; Migler, K.; Douglas, J. F.; Prabhu, V. M. *J. Chem. Phys.*, *132*, 194903-6.
13. Jiang, J.; Oberdörster, G.; Biswas, P. *J. Nanopart. Res.* **2009**, *11*, 77-89.
14. Malvern Instruments, *Zetasizer Nano Series - User Manual*, **2003**.

15. Teubner, M. *J. Chem. Phys.* **1982**, *76*, 5564-5573.
16. Chen, L. X.; Rajh, T.; Wang, Z.; Thurnauer, M. C. *J. Phys. Chem. B* **1997**, *101*, 10688-10697.
17. Fox, M. A.; Dulay, M. T. *Chem. Rev.* **1993**, *93*, 341-357.
18. Linsebigler, A. L.; Lu, G.; Yates, J. T. *Chem. Rev.* **1995**, *95*, 735-758.
19. Hoffmann, M. R.; Martin, S. T.; Choi, W.; Bahnemann, D. W. *Chem. Rev.* **1995**, *95*, 69-96.
20. Wang, R.; Hashimoto, K.; Fujishima, A.; Chikuni, M.; Kojima, E.; Kitamura, A.; Shimohigoshi, M.; Watanabe, T. *Nature* **1997**, *388*, 431-432.
21. Poizot, P.; Laruelle, S.; Grugeon, S.; Dupont, L.; Tarascon, J. M. *Nature* **2000**, *407*, 496-499.
22. Winter, M.; Brodd, R. J. *Chem. Rev.* **2004**, *104*, 4245-4270.
23. Tarascon, J. M.; Armand, M. *Nature* **2001**, *414*, 359-367.
24. Whittingham, M. S. *Chem. Rev.* **2004**, *104*, 4271-4302.
25. Arico, A. S.; Bruce, P.; Scrosati, B.; Tarascon, J.-M.; van Schalkwijk, W. *Nat. Mater.* **2005**, *4*, 366-377.
26. Ren, Y.; Hardwick, L. J.; Bruce, P. G. *Angew. Chem. Int. Ed.* **2010**, *49*, 2570-2574.
27. Zukalova, M.; Kalbac, M.; Kavan, L.; Exnar, I.; Graetzel, M. *Chem. Mater.* **2005**, *17*, 1248-1255.
28. Kavan, L.; Prochazka, J.; Spitler, T. M.; Kalbac, M.; Zukalova, M.; Drezen, T.; Gratzel, M. *J. Electrochem. Soc.* **2003**, *150*, A1000-A1007.
29. Fattakhova-Rohlfing, D.; Wark, M.; Brezesinski, T.; Smarsly, B. M.; Rathouský, J. *Adv. Funct. Mater.* **2007**, *17*, 123-132.
30. Brezesinski, T.; Wang, J.; Polleux, J.; Dunn, B.; Tolbert, S. H. *J. Am. Chem. Soc.* **2009**, *131*, 1802-1809.

## 2. Characterization

---

31. Hagfeldt, A.; Boschloo, G.; Sun, L.; Kloo, L.; Pettersson, H. *Chem. Rev.* **2010**, *110*, 6595-6663.
32. Cao, F.; Oskam, G.; Meyer, G. J.; Searson, P. C. *The Journal of Physical Chemistry* **1996**, *100*, 17021-17027.
33. Peter, L. M. *J. Phys. Chem. C* **2007**, *111*, 6601-6612.
34. Halme, J.; Vahermaa, P.; Miettunen, K.; Lund, P. *Adv. Mater.* **2010**, *22*, E210-E234.
35. Fisher, A. C.; Peter, L. M.; Ponomarev, E. A.; Walker, A. B.; Wijayantha, K. G. U. *J. Phys. Chem. B* **2000**, *104*, 949-958.
36. Zakeeruddin, S. M.; Grätzel, M. *Adv. Funct. Mater.* **2009**, *19*, 2187-2202.
37. Nakade, S.; Kanzaki, T.; Wada, Y.; Yanagida, S. *Langmuir* **2005**, *21*, 10803-10807.
38. Kalyanasundaram, K. *Dye-sensitized solar cells*; 1. ed.; EPFL Press: Lausanne, 2010.
39. Wang, Q.; Moser, J.-E.; Grätzel, M. *J. Phys. Chem. B* **2005**, *109*, 14945-14953.
40. Kern, R.; Sastrawan, R.; Ferber, J.; Stangl, R.; Luther, J. *Electrochimica Acta* **2002**, *47*, 4213-4225.
41. Bisquert, J. *J. Phys. Chem. B* **2001**, *106*, 325-333.
42. Grätzel, M. *Inorg. Chem.* **2005**, *44*, 6841-6851.
43. Ito, S.; Murakami, T. N.; Comte, P.; Liska, P.; Grätzel, C.; Nazeeruddin, M. K.; Grätzel, M. *Thin Solid Films* **2008**, *516*, 4613-4619.



### **3. “Brick and Mortar” Strategy for the Formation of Highly Crystalline Mesoporous Titania Films from Nanocrystalline Building Blocks**

*This chapter is based on the following publication:*

Johann M. Szeifert, Dina Fattakhova-Rohlfing, Dimitra Georgiadou, Vit Kalousek, Jiri Rathouský, Daibin Kuang, Sophie Wenger, Shaik M. Zakeeruddin, Michael Grätzel and Thomas Bein, *Chemistry of Materials* **2010**, *21* (7), 1260-1265.

#### **3.1 Introduction**

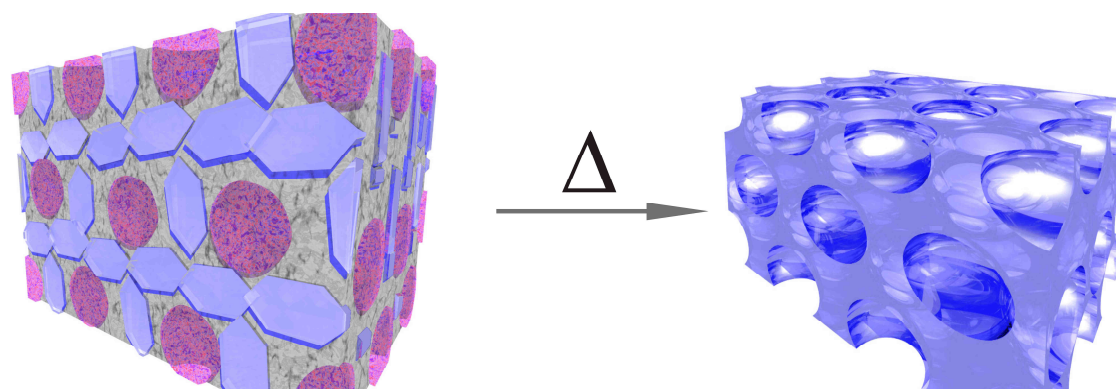
Nanostructured films of TiO<sub>2</sub> have an enormous potential for applications in photocatalysis, solar cells, sensors, and energy storage.<sup>1</sup> However, reaching this potential often requires films that simultaneously feature both large and easily accessible surface area and highly crystalline pore walls. Crystalline titania layers are most commonly assembled from crystalline particles by sintering.<sup>2, 3</sup> This approach offers very good control over the phase composition and the degree of crystallinity, but lacks the possibility to tune the structure and the porosity. In order to overcome these shortcomings molecular/oligomeric precursors (sols) are employed in a templated sol-gel process.<sup>4-6</sup> Thus, precise control over the porosity by using structure directing agents<sup>7-10</sup> can be achieved, but the crystallinity of the resulting TiO<sub>2</sub> frameworks is usually only moderate and high calcination temperatures are needed for further crystallization. Here we present a novel preparation strategy that not only combines the strong points of both above-mentioned techniques, but also extends the material's functionality by introducing

### 3. “Brick and Mortar” Mesoporous Titania Films

---

further control over physical properties beyond the scope of the classical techniques. This is achieved by the fusion of preformed titania nanocrystals with surfactant-templated sol-gel titania, which acts as a structure-directing matrix and as a chemical glue. This technique can be described as a "brick and mortar" approach, a term which has been introduced for the preparation of composite materials.<sup>11-14</sup> The uniqueness of our approach consists in the similar chemical composition of both the "bricks" and the "mortar", such that the latter acts as a reactive precursor for the further growth of the crystalline phase seeded by the nanocrystals. This synergy leads to a drastically lowered temperature needed for crystallization (Scheme 3.1). Moreover, the films exhibit high transparency, tunable thickness over a wide range from tens of nanometers to several micrometers, and strong adhesion to the substrate.

The following experiments have been performed as a joint project: The “brick and mortar” films were synthesized and characterized by Johann M. Szeifert. Krypton sorption and photocatalytic experiments were performed and evaluated by Vit Kalousek and Dr. Jiri Rathouský at the J. Heyrovský Institute in Prague. Investigation of the photovoltaic performance in dye-sensitized solar cells was done by Dr. Sophie Wenger and Dr. Daibin Kuang in the group of Dr. S. M. Zakeeruddin and Prof. Dr. Michael Grätzel at the EPF Lausanne.



**Scheme 3.1.** Scheme of formation of crystalline mesoporous titania films (right side) via the “brick and mortar” approach. The nanocrystalline titania “bricks” (light blue, left side) are

dispersed in amorphous titania “mortar” (grey), which is periodically self-assembled around the micelles of the polymer template (magenta).

## 3.2 Results and Discussion

The synthesis of the titania nanocrystalline “bricks” was inspired by a non-aqueous route originally developed by M. Niederberger et al.<sup>15, 16</sup> Completely crystalline particles of 4-5 nm in size are formed by the reaction of titanium tetrachloride with benzyl alcohol at low temperatures (Figure 3.1).

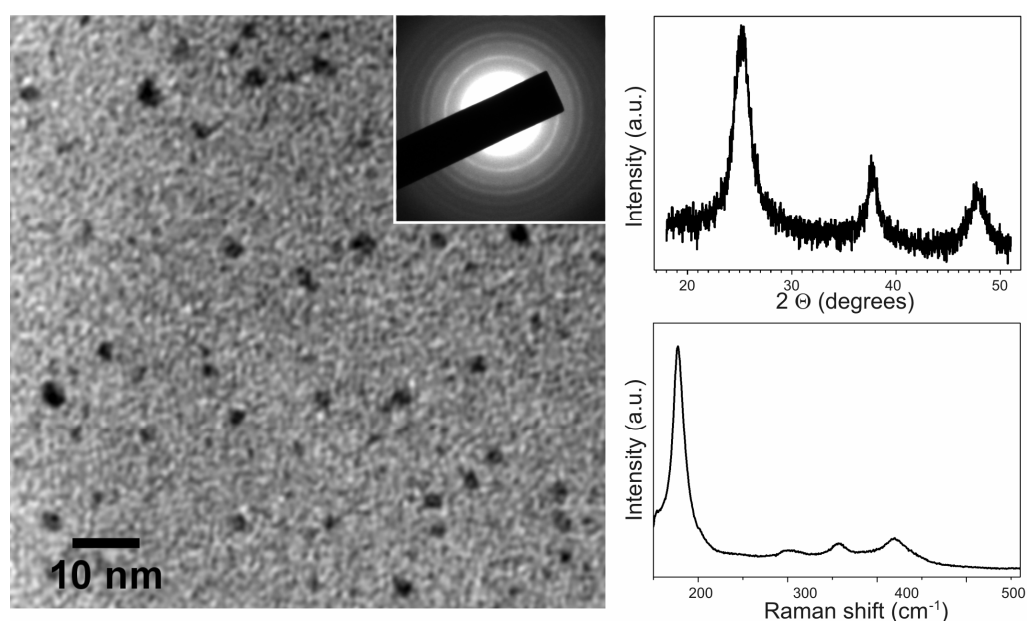


**Figure 3.1.** TEM image of titania nanoparticles used for film preparation with their selected area electron diffraction (SAED) pattern in the inset (a), their powder XRD pattern (b) and Raman spectrum (c).

We found that the resulting particles redisperse easily in tetrahydrofuran (THF) at high concentrations exceeding 5 wt% in the presence of the Pluronic 123 block-copolymer (PEO<sub>20</sub>-

### 3. “Brick and Mortar” Mesoporous Titania Films

---

PPO<sub>70</sub>-PEO<sub>20</sub>). The latter promotes stabilization of the particles and acts as a structure directing agent in the film assembly. The sol of titania “mortar” was prepared by the hydrolysis of tetraethyl orthotitanate catalyzed by hydrochloric acid.<sup>17</sup> For the preparation of the nanocomposite films, the “mortar” was added to the colloidal solution of “bricks” at ratios ranging from 0 wt% to 100 wt% (related to the total mass of TiO<sub>2</sub> formed after calcination). The dip-coated titania films were calcined at 300 °C in order to induce further crystal growth and to remove the copolymer.

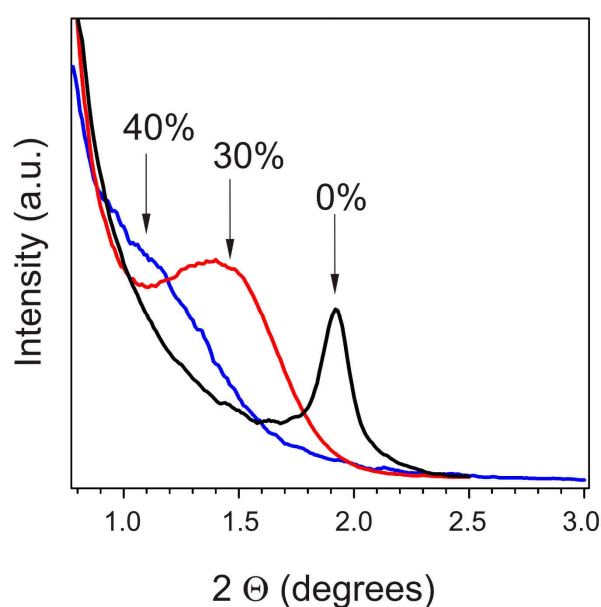


**Figure 3.2.** SAXS patterns of titania films prepared from solutions containing various amounts of titania nanoparticles.

The results of transmission electron microscopy (TEM), small-angle X-ray scattering (SAXS, Figure 3.2), scanning electron microscopy (SEM) images and physical sorption experiments clearly show that the introduction of crystalline titania nanoparticles into surfactant-templated titania precursor sols has a dramatic influence on the porous structure and crystallinity of the calcined films. While the pure sol-gel derived amorphous films exhibit a well-defined 3D-cubic arrangement of mesopores of 7 nm in size with a periodicity of 14 nm (Figure 3.3a),

### 3. “Brick and Mortar” Mesoporous Titania Films

---

deterioration of the mesostructure occurs upon addition of small amounts of particles, accompanied by some increase in the crystallinity (Figure 3.3b).

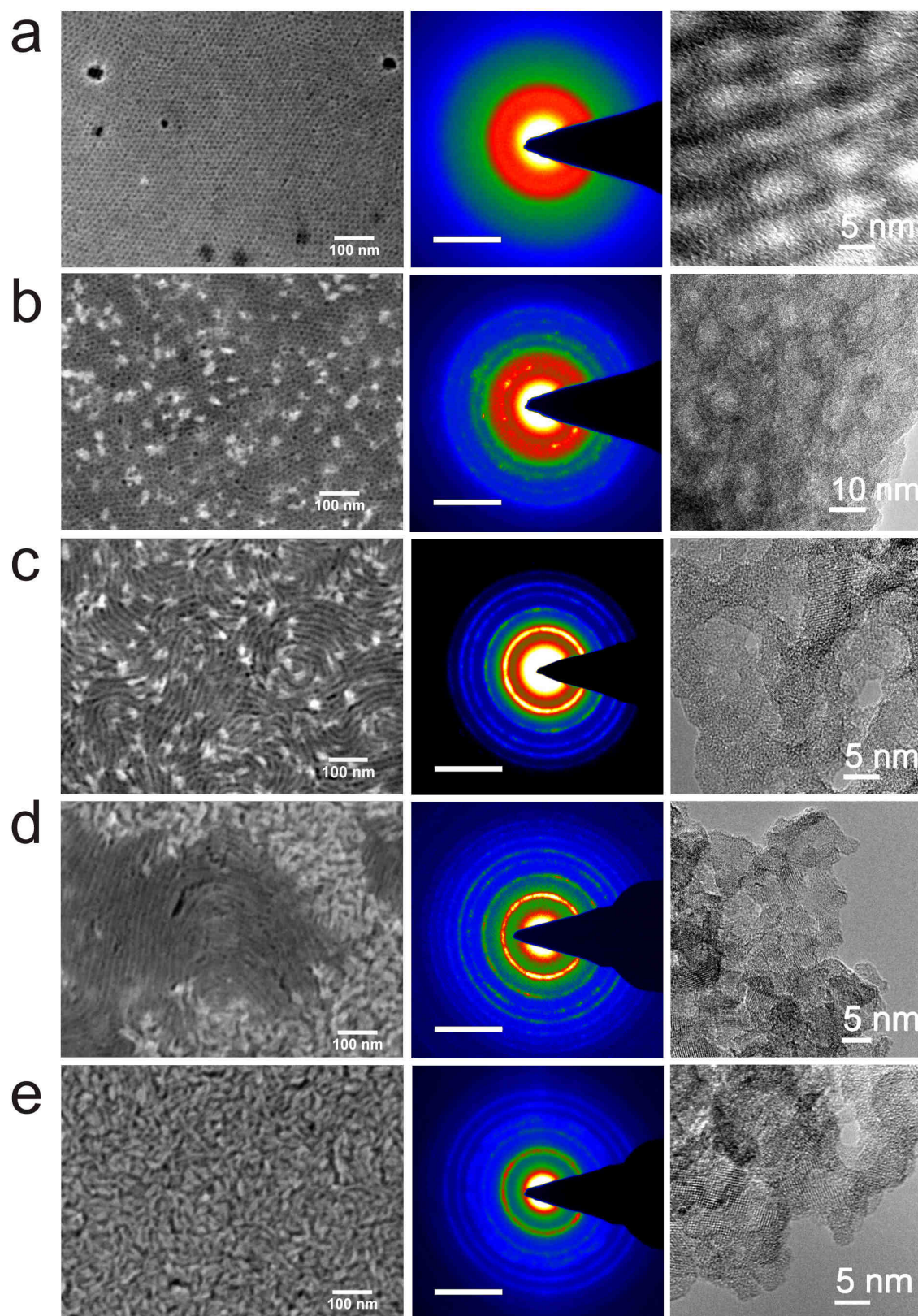


**Figure 3.3.** SEM images on silicon substrate (first column), HRTEM images (third column) and the corresponding SAED patterns (second column) of the composite titania films containing 0 % (a), 10 % (b), 15 % (c), 30 % (d) and 100 % (e) of titania nanoparticles.

### 3. “Brick and Mortar” Mesoporous Titania Films

When the fraction of the titania nanoparticles exceeds a critical value of 15 wt%, a channeled, fingerprint-like structure is formed with greatly increased crystallinity (Figure 3.3c). A further increase in the concentration of nanoparticles leads to a phase separation and coexistence of a channeled structure and domains of a particulate phase having a different mesoporous structure (Figure 3.3d). The latter phase becomes dominant when the particle fraction exceeds 50 %.

Addition of different amounts of titania nanoparticles also changes the character of porosity (Table 3.1 and Figure 3.4). In pure sol-gel films the spherical pores are connected with each other via openings of the ink-bottle type<sup>18</sup> with restricted accessibility. Addition of titania nanoparticles at 15 or more wt% induces an increase in pore size and pore volume and an opening of the pore system. Higher concentrations of anatase particles lead to the creation of roughly cylindrical mesopores with a substantially increased size, and the complete removal of pore blocking.

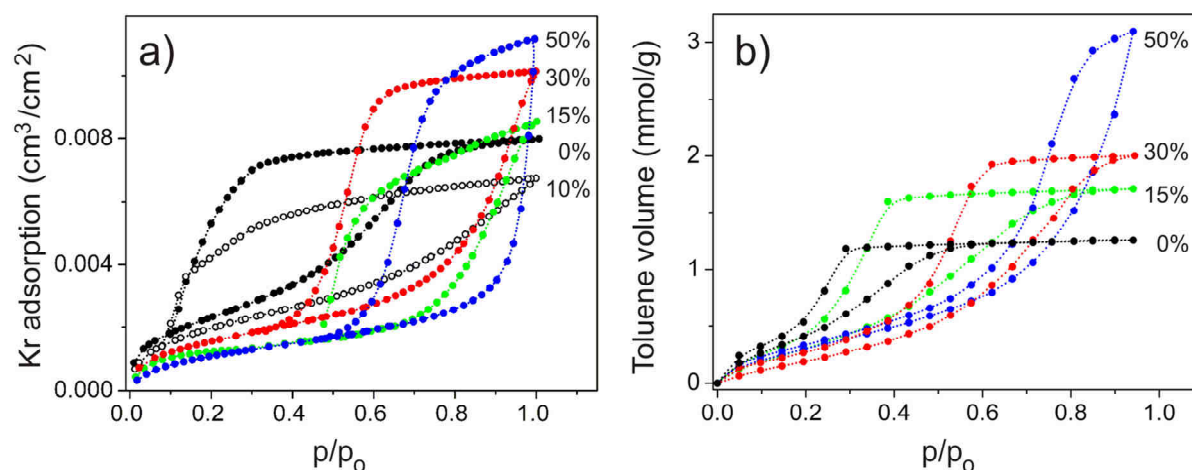


**Figure 3.4.** Adsorption isotherms of krypton at 77 K (a) and toluene at 298 K (b) on “brick and mortar” titania films calcined at 300 °C. The labels indicate the particle content in the initial solution.

### 3. “Brick and Mortar” Mesoporous Titania Films

Percentage of nanoparticles, %	$S_{\text{BET}}^{\text{a}}$ , m <sup>2</sup> /g	$S_{\text{BET}}^{\text{b}}$ , cm <sup>2</sup> /cm <sup>2</sup>	$V_{\text{TOT}}^{\text{c}}$ , cm <sup>3</sup> /g	$V_{\text{TOT}}^{\text{d}}$ , mm <sup>3</sup> /cm <sup>2</sup>	D, nm
0	89	118	0.132	0.010	3-4
10	-	98	-	0.0086	3-4
15	71	110	0.180	0.0107	7.5
30	52	77	0.210	0.013	6-7
50	62	57	0.325	0.0142	10
100	-	68	-	-*	-*

**Table 3.1.** Texture data of mesoporous titania films

a from adsorption isotherms of toluene at 25 °C, using the cross-sectional area of toluene of 0.314 nm<sup>2</sup> calculated from the density of the liquid adsorptive in the bulk liquid state.

b from adsorption isotherms of krypton at 77 K, using the cross-sectional area of krypton of 0.210 nm<sup>2</sup>.

c from adsorption isotherms of toluene at 25 °C, using the molar volume of liquid toluene.

d from adsorption isotherms of krypton at 77 K, using the molar volume of solid krypton.

e average value for a bimodal texture (wider cavities with narrow necks).

\* Isotherm of a macroporous material. Pore size and volume are not determinable from Kr sorption experiments. D = pore diameter.

The crystallinity of the films prepared by the “brick and mortar” approach was found to increase dramatically upon calcination at the relatively low temperature of only 300 °C. This development of crystallinity was demonstrated by quantitative X-ray diffraction using a crystalline standard as a reference and comparing the (101) anatase peak integral (Figure 3.5). As the crystallinity increases much faster than the percentage of added crystalline particles, the crystalline building blocks must have induced the crystallization of the surrounding sol-

### 3. “Brick and Mortar” Mesoporous Titania Films

gel matrix and acted as seeds for the crystallization of amorphous titania. Above a percentage of approximately 50 %, the crystallinity reaches a plateau which corresponds to the maximum value of crystallinity.

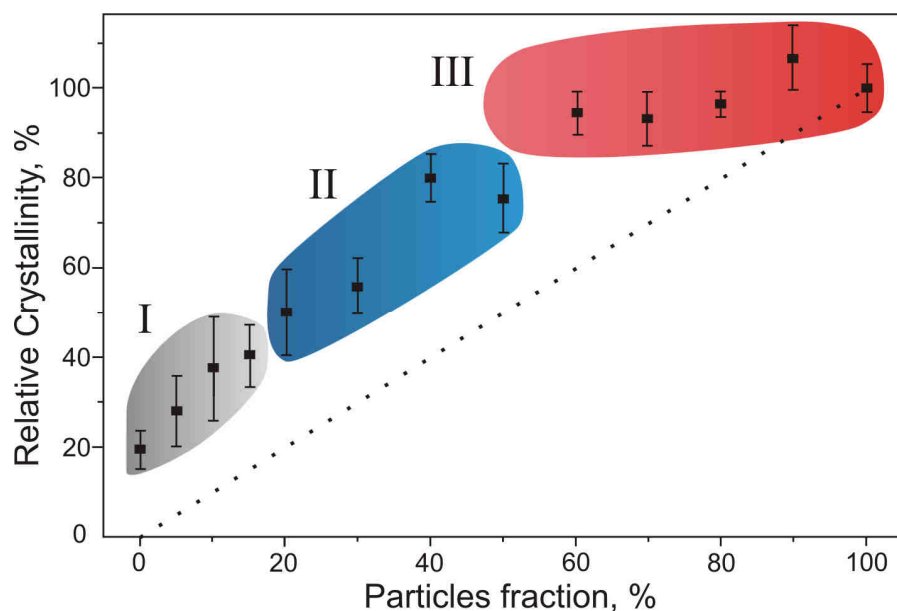


**Figure 3.5.** A diagram showing the development of crystallinity in samples from cast solutions after calcination at 300 °C as a function of the fraction of nanoparticles in the precursor solution. The data points (average of 3 experiments) were calculated using the internal standard method (see experimental section).<sup>19, 20</sup> In short, the integral of (101) anatase was divided by that of the standard (111) fluorite, and normalized to the value of the samples which contains 100 % crystalline particles; the error bars indicate the standard deviation. This is correlated to the formation of different mesoporous structures as observed by electron microscopy and sorption methods: distorted cubic mesophase (I), channeled structure (II), and particulate phase (III). The dotted line shows the theoretical crystallinity of the films before calcination.

### 3. “Brick and Mortar” Mesoporous Titania Films

---

The titania films prepared by the “brick and mortar” approach were investigated in some of their most important applications, namely in photocatalysis and in dye-sensitized solar cells (DSC).

The photooxidation of NO was selected as a suitable photocatalytic reaction because of its environmental importance.<sup>21</sup> Low concentrations of nitrogen oxides remaining in atmosphere after the burning of fuels present a major environmental risk in cities. Highly crystalline mesoporous films of TiO<sub>2</sub> are especially suitable for the removal of NO due to their large surface area, as the heterogeneous photodecomposition processes are dependent on the amount of surface-adsorbed reactants. The studied films can be roughly divided into three groups according to their photoactivity (Figure 3.6a). The films with a nanoparticle content of 50-70 % are the most active ones, the stationary (steady state) photoconversion reaching about 9 %. Those prepared without nanocrystals are much less active – the stationary conversion being only about 4 %. Interestingly, the films prepared exclusively from nanocrystals without any sol-gel “mortar” addition also exhibit low conversion efficiency, most probably due to the lower surface area and less favorable pore structure. Thus, the “brick and mortar” layers are very promising materials for photocatalytic applications due to their high efficiency in the degradation of NO. The additional advantages of “brick and mortar” layers in this context are high transparency and excellent optical qualities in combination with strong adhesion to the substrate. This makes them attractive candidates for large-area coatings on glass panels and windows in buildings, where mechanical stability and transparency are essential.

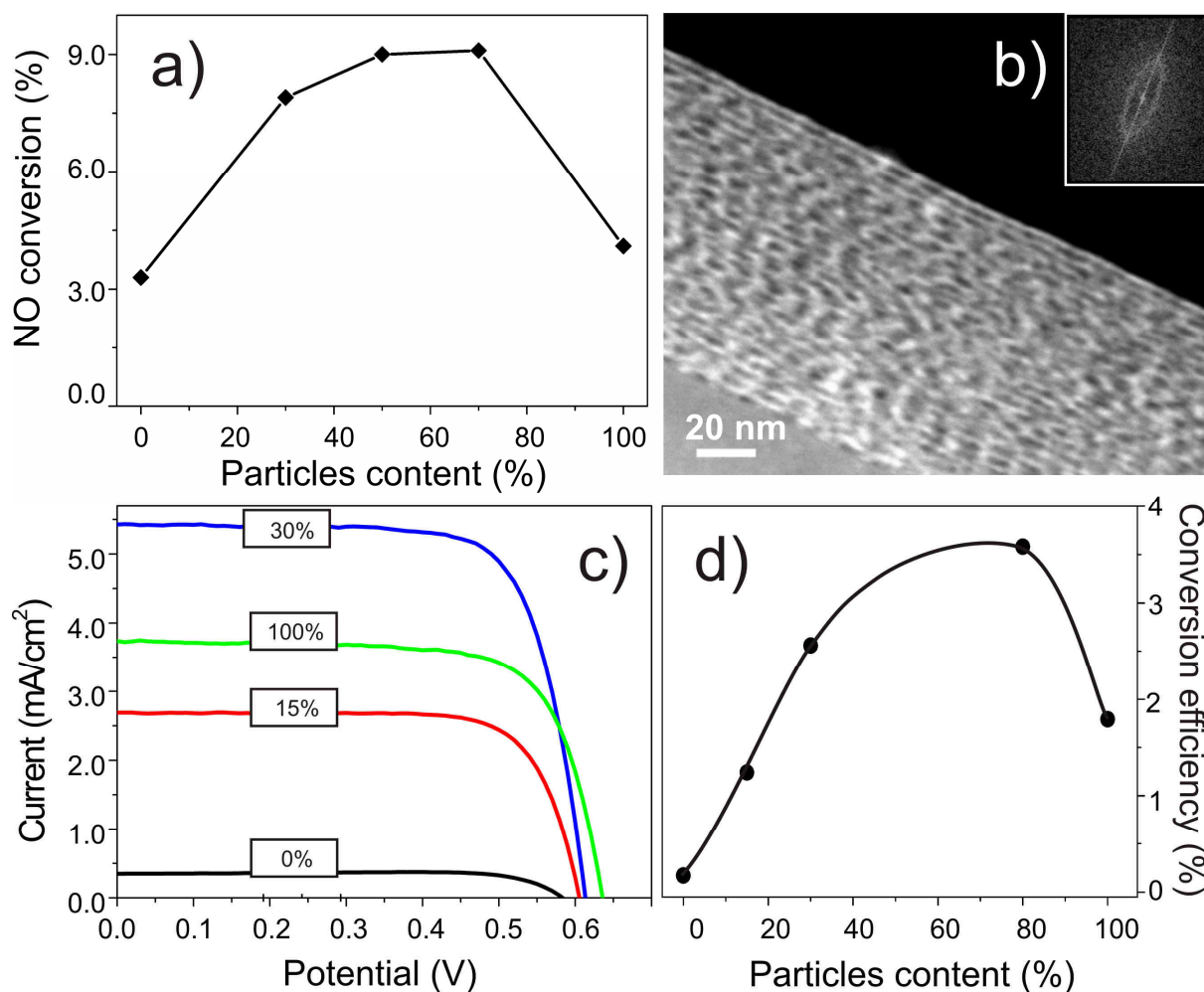


**Figure 3.6.** Photocatalytic degradation of NO on titania films with different particle content: steady-state conversion efficiency (a) and cross-sectional STEM-HAADF image of one of the highly photoactive films containing 50 % of titania particles (Phase III from Figure 3) (b). Inset: Fourier transform of the picture revealing the periodic pore shape. Photocurrent-voltage curve (c) and dependence of conversion efficiency (d) of DSC devices based on the “brick and mortar” titania layers with a nanoparticle content ranging from 0 to 100 wt%, D205 sensitizer and Z646 electrolyte.<sup>22</sup> The titania layer thickness was ca. 1.0  $\mu\text{m}$ . The photovoltaic performance was measured at air mass 1.5 (100  $\text{mW}/\text{cm}^2$ ) full sunlight illumination. The active cell area was 0.158  $\text{cm}^2$ .

### 3. “Brick and Mortar” Mesoporous Titania Films

---

A similar non-linear change in performance was also observed for photovoltaic cells fabricated from films with different particle content (Figure 3.6 c,d and Table 3.2). The films prepared from a sol-gel precursor without particles exhibit very low photocurrent and conversion efficiency. The performance increases more than 7-fold when 15 wt% of nanocrystals are added to the initial solution, and still improves with a further increase in particle content. This effect, similar to that observed for the photocatalytic performance, clearly reflects the drastic changes in the degree of crystallinity of the titania material.

Nanoparticle content in the titania precursor, wt%	$J_{sc}$ , mA/cm <sup>2</sup>	$V_{oc}$ , mV	FF	$\eta$ , %
0	0.355	593	0.75	0.16
15	2.68	615	0.75	1.24
30	5.54	632	0.74	2.56
80	6.34	742	0.75	3.58
100	3.83	645	0.73	1.79

**Table 3.2.** Photovoltaic parameters of DSC devices based on “brick and mortar” titania layers of about 1.0  $\mu\text{m}$  thickness with varying nanoparticle concentration, in combination with D205 sensitizer and Z646 electrolyte under AM 1.5 sunlight at 100 mW/cm<sup>2</sup> full sun irradiation.

It is supported also by the photocurrent transient studies (Figure 3.7), which indicate electron collection problems due to the insufficient crystallinity of titania layers containing less than 30 % of particles. We note that TiO<sub>2</sub> films prepared from 100 % nanoparticles exhibit much worse photovoltaic properties in spite of their complete crystallinity, which are about 45 % lower than the values for the films containing 30 % of nanocrystals. The mild calcination temperature of 300 °C is apparently not sufficient for sintering the particles *via* solid-state diffusion. In contrast, the fast viscous sintering of the amorphous sol-gel (mortar) component

### 3. “Brick and Mortar” Mesoporous Titania Films

---

followed by its crystallization enables efficient fusion of the particles and provides the necessary electrical contact. The binding role of the sol-gel component also becomes evident in the obvious difference in the mechanical stability of the nanocomposite films. While the 100 % particulate films are rather fragile and easily scratched off the substrate, films containing the sol-gel precursor are much more robust and mechanically stable.

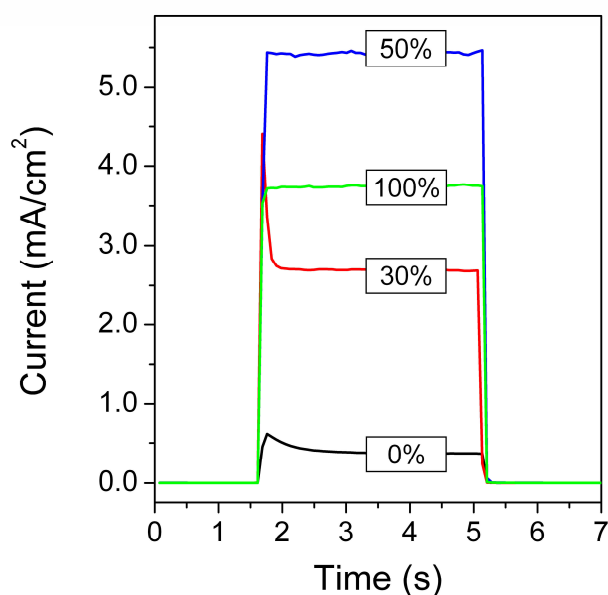


**Figure 3.7.** Photocurrent-time dependence of DSC devices based on the “brick and mortar” titania layers with a nanoparticle content ranging from 0 to 100 wt%, D205 sensitizer and Z646 electrolyte. The titania layer thickness was ca. 0.9  $\mu\text{m}$ . The photovoltaic performance was measured at air mass 1.5 ( $100 \text{ mW}/\text{cm}^2$ ) full sunlight illumination. The active cell area was  $0.158 \text{ cm}^2$ .

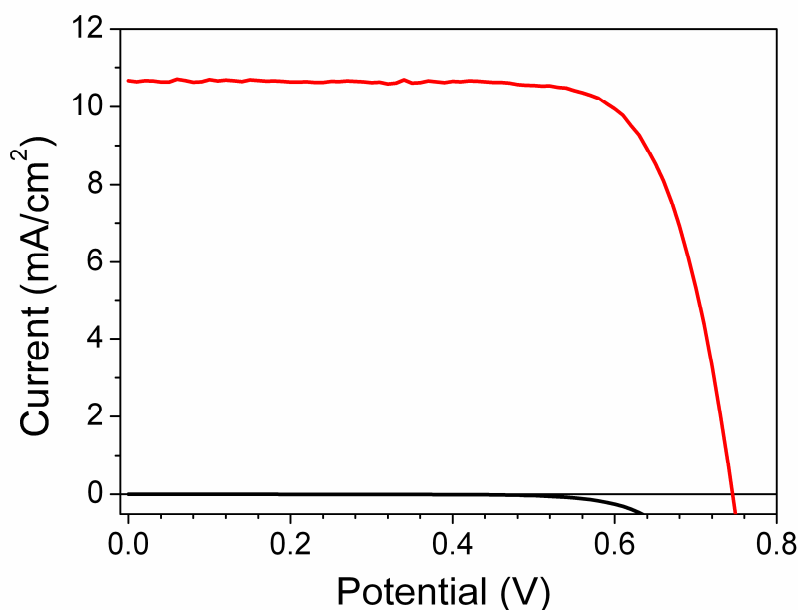


**Figure 3.8.** Photocurrent-voltage curve of DSC devices based on the “brick and mortar” titania layers with a nanoparticle content of 80 wt%, D205 sensitizer and Z646 electrolyte. The titania layer thickness was ca. 2.7  $\mu\text{m}$ . The photovoltaic performance was measured at air mass 1.5 (100  $\text{mW}/\text{cm}^2$ ) full sunlight illumination. The active cell area was 0.158  $\text{cm}^2$ .

The films prepared by the “brick and mortar” approach are very versatile with respect to the thickness of the finally obtained films. The coating procedure can be repeated several times leading to a linear increase in thickness, surface area and pore volume without any significant change in the nature of the porosity. This feature is drastically different from the classical sol-gel template films. For the latter, the surface area and pore volume can be increased at maximum by 4-5 times compared to a single coating, while further coating/calcination cycles lead to a degradation of the porous system.<sup>23</sup>

As expected, the photovoltaic efficiency is improved after increasing the thickness of the titania layer. The optimum performance was found for films prepared using 80 wt% of anatase nanoparticles. The cell based on such a film with 2.7  $\mu\text{m}$  in thickness gives, under standard global AM 1.5 full sunlight (100  $\text{mW}/\text{cm}^2$ ) illumination, a short circuit photocurrent density ( $J_{\text{sc}}$ ) of 10.7  $\text{mA}/\text{cm}^2$ , an open circuit potential ( $V_{\text{oc}}$ ) of 745 mV and a fill factor (FF)

### 3. “Brick and Mortar” Mesoporous Titania Films

---

of 0.75, yielding a total conversion efficiency of 6.0 % (Figure 3.8). This is impressively high for such thin films in combination with a non-volatile electrolyte, and makes them serious candidates for photoanodes in dye-sensitized solar cells.

In conclusion, the “brick and mortar” approach for the formation of mesoporous crystalline materials shows a striking synergy in the interactions of crystalline and amorphous components. The distinctive feature of this approach is the ability to create highly porous and highly crystalline structures at very mild conditions. A broad variety of mesostructures is accessible using the same organic template, and the final structures are tunable by varying the fraction of the “bricks”. This attractive strategy offers new opportunities for the design of nanostructured materials with enhanced functionality through various architectures with large accessible porosity and high crystallinity.

### 3.3 Experimental Section

Titanium dioxide nanoparticles were synthesized following a modified procedure by Niederberger et al.<sup>16</sup> Titanium tetrachloride (1.5 mL, 13.7 mmol) was dissolved in toluene (10 mL) and added to benzyl alcohol (30 mL, 290.8 mmol) under continuous stirring. The solution was kept at 60 °C for 20 h, then cooled down to room temperature. The particles were separated by centrifugation at 50000 rcf for 30 minutes and used without further treatment. As such, the particles contain about 55 wt% of benzyl alcohol according to thermogravimetric analysis; this was taken into account for the adjustment of the TiO<sub>2</sub>-content.

In a typical synthesis, a solution of Pluronic P123 (0.2 g, 0.04 mmol) in THF (4 mL) was added to non-washed particles (0.2 g, 1.1 mmol of TiO<sub>2</sub>, previously separated by centrifugation) and stirred overnight until the particles were homogeneously redispersed.

### 3. “Brick and Mortar” Mesoporous Titania Films

---

Subsequently, the desired amount of sol-gel (SG, see below) solution (for example, 0.9 mL, with 2.51 mmol of TiO<sub>2</sub>, for the solution containing 30 % particles) was added followed by stirring for several minutes. The final solutions were transparent or translucent, being of yellow to orange color. The SG solution was prepared by adding hydrochloric acid (37 %, 5.1 mL, 62.1 mmol) to tetraethyl orthotitanate (7.2 mL, 34.3 mmol) at room temperature under continuous stirring.

The mass-ratio of nanoparticles to the sol-gel precursor was varied, but the total amount of TiO<sub>2</sub> was kept at 0.4 g (5.01 mmol). The Pluronic P123 content in the dip-coating solution was 50 wt % with respect to the total mass of TiO<sub>2</sub>. As an example, the amount of TiO<sub>2</sub> in the solution containing 50 % particles was 8.1 wt %. The films were prepared by dip-coating at  $23 \pm 2$  °C and a relative humidity of  $45 \pm 10$  % at a withdrawal rate of 1.8 mm/s, and calcined at 300 °C (with a ramp of  $0.6$  °C min<sup>-1</sup>) for 30 minutes.

Scanning electron microscopy (SEM) was performed on a JEOL JSM-6500F scanning electron microscope equipped with a field emission gun, at 4 kV. High Resolution Transmission Electron Microscopy (HRTEM) and Scanning Transmission Electron Microscopy in High Angle Annular Dark Field mode (STEM-HAADF) was performed using a FEI Titan 80-300 equipped with a field emission gun operated at 300 kV. The particulate samples were prepared by evaporating a drop of a diluted solution of particles with small amounts of Pluronic P123 in THF on a Plano holey carbon coated copper grid. HRTEM of films was carried out by scraping the thin-film samples off the substrate onto a holey carbon coated copper grid. The film thickness was measured by profilometry (Dektak), ellipsometry using a Woolam ESM-300, and SEM. The porosity of the films was determined by the analysis of adsorption isotherms of Kr at the boiling point of liquid nitrogen (approx. 77 K) using an ASAP 2010 apparatus (Micromeritics). Krypton sorption was performed and evaluated by Dr. J. Rathouský and V. Kalousek at the J. Heyrovský Institute, Prague. The toluene adsorption was carried out using a self-built Quartz Crystal Microbalance (QCM)

### 3. “Brick and Mortar” Mesoporous Titania Films

---

system. For this purpose, the precursor solutions were spin-coated (3000 rpm, 30 s) on KVG 10 MHz QCM devices with gold electrodes (from Quartz Crystal Technology GmbH) and calcined at 300 °C. Toluene was used as an adsorptive and the measurements were performed at 25 °C. Raman spectra were recorded with a LabRAM HR UV-VIS (Horiba Jobin Yvon) Raman microscope (Olympus BX41) with a Symphony CCD detection system using a HeNe laser at 632.8 nm. The spectra were taken from material removed from the substrate. X-ray diffraction analysis was carried out in reflection mode using a Scintag XDS 2000 (Scintag Inc.) with Ni-filtered  $\text{CuK}\alpha$ -radiation.

The quantitative crystallinity measurements were performed using the internal standard method with fluorite,  $\text{CaF}_2$ , as internal standard.<sup>19,20</sup> For this purpose, the dip-coating solutions were cast into a wide calcination vessel, dried over night at 60 °C, and calcined at 300 °C (with a ramp of 0.6 °C  $\text{min}^{-1}$ ) for 30 minutes. The resulting film or powder was ground and thoroughly mixed with 10 wt% of fluorite. X-ray diffraction patterns were recorded using a STOE STADI P COMBI diffractometer. The diffraction peaks of (101) anatase and (111) fluorite were fitted with a Gaussian peak shape and integrated. The integral of (101) anatase was divided by that of (111) fluorite. This crystallinity value was normalized to that of the 100 % particles sample, which after calcination is considered to be completely crystalline. The data points correspond to an average of three samples. The error bars indicate the standard deviation from the average.

The experimental set-up for the photocatalytic tests consisted of a gas supply part, the photoreactor, and a chemiluminiscent NO-NO<sub>x</sub> gas analyzer. (Horiba ambient monitor APNA-360). The gaseous reaction mixture was prepared by mixing streams of dry air (1500 mL/min), wet air (1500 mL/min, relative humidity of 100 %) and 50 ppm NO/N<sub>2</sub> (approx. 60 mL/min), in order to obtain a final concentration of NO of 1 ppm at a relative humidity of 50 %. The photoreactor was illuminated by four 8 W black lights, thus achieving a UV light intensity of 1  $\text{mW/cm}^2$ . Prior to the photocatalytic tests, the photoreactor was purged with the

### 3. “Brick and Mortar” Mesoporous Titania Films

---

NO/water vapor/air mixture without illumination until a steady NO concentration was achieved at the outlet. 100% NO conversion is equivalent to a photonic efficiency of  $\xi=0.14$  % assuming a mean irradiation wavelength of 350 nm. The photocatalytic experiments were performed and evaluated by Dr. J. Rathouský at the J. Heyrovský Institute, Prague.

For photovoltaic measurements, the mesoporous TiO<sub>2</sub> films on FTO-coated glass substrates were heated at 200 °C for 30 min, then cooled to ca. 80 °C and immersed into the dye solution at room temperature, and kept there for 16 h. The dye solution containing 0.3 mM of the indoline dye D205 (molar extinction coefficient of 53000 at 532 nm) in acetonitrile and *tert*-butyl alcohol (volume ratio: 1:1) was used to sensitize the photoanode.<sup>24</sup> Dye-coated mesoporous TiO<sub>2</sub> films were assembled and sealed with a thin transparent hot-melt 25  $\mu$ m thick surlyn ring (DuPont) to the counter electrodes (Pt on FTO glass, chemical deposition from 0.005 M hexachloroplatinic acid in isopropanol per cm<sup>2</sup> surface area, heated at 400 °C for 15 min). The electrolyte was injected into the inner electrode space from the counter electrode side through a pre-drilled hole, and then the hole was sealed with a Bynel sheet and a thin glass cover slide by heating. The non-volatile electrolyte (Z646) contains 1.0 M PMII (propylmethylimidazolium iodide), 0.15 M iodine, 0.1 M GuNCS (guanidinium thiocyanate), and 0.5 M N-butyl benzimidazole (NBB) in 3-methoxypropionitrile.<sup>22</sup> The device assembly, the characterization of current density-voltage and incident photon to current conversion efficiency (IPCE) of the DSCs were performed by Dr. S. Wenger, and Dr. D. Kuang in the group of Dr. S. M. Zakeeruddin, and Prof. Dr. M. Grätzel at the EPF Lausanne, Switzerland, and are described in detail elsewhere.<sup>22</sup>

### 3.4 References

1. Linsebigler, A. L.; Lu, G.; Yates, J. T. *Chem. Rev.* **1995**, *95*, 735-758.

### 3. “Brick and Mortar” Mesoporous Titania Films

---

2. O'Regan, B.; Gratzel, M. *Nature* **1991**, *353*, 737-740.
3. Kavan, L.; Gratzel, M.; Rathouský, J.; Zukal, A. *J. Electrochem. Soc.* **1996**, *143*, 394-400.
4. Choi, S. Y.; Lee, B.; Carew, D. B.; Mamak, M.; Peiris, F. C.; Speakman, S.; Chopra, N.; Ozin, G. A. *Adv. Funct. Mater.* **2006**, *16*, 1731-1738.
5. Crepaldi, E. L.; Soler-Illia, G.; Grosso, D.; Cagnol, F.; Ribot, F.; Sanchez, C. *J. Am. Chem. Soc.* **2003**, *125*, 9770-9786.
6. Sanchez, C.; Boissiere, C.; Grosso, D.; Laberty, C.; Nicole, L. *Chem. Mater.* **2008**, *20*, 682-737.
7. Brinker, C. J.; Lu, Y. F.; Sellinger, A.; Fan, H. Y. *Adv. Mater.* **1999**, *11*, 579-585.
8. Yang, P. D.; Zhao, D. Y.; Margolese, D. I.; Chmelka, B. F.; Stucky, G. D. *Chem. Mater.* **1999**, *11*, 2813-2826.
9. Grosso, D.; Boissiere, C.; Smarsly, B.; Brezesinski, T.; Pinna, N.; Albouy, P. A.; Amenitsch, H.; Antonietti, M.; Sanchez, C. *Nature Mater.* **2004**, *3*, 787-792.
10. Sel, O.; Kuang, D. B.; Thommes, M.; Smarsly, B. *Langmuir* **2006**, *22*, 2311-2322.
11. Boal, A. K.; Ilhan, F.; DeRouchey, J. E.; Thurn-Albrecht, T.; Russell, T. P.; Rotello, V. M. *Nature* **2000**, *404*, 746-748.
12. Arumugam, P.; Xu, H.; Srivastava, S.; Rotello, V. M. *Polymer Int.* **2007**, *56*, 461-466.
13. Liu, R.; Ren, Y.; Shi, Y.; Zhang, F.; Zhang, L.; Tu, B.; Zhao, D. *Chem. Mater.* **2008**, *20*, 1140-1146.
14. Peng, T. Y.; Zhao, D.; Dai, K.; Shi, W.; Hirao, K. *J. Phys. Chem. B* **2005**, *109*, 4947-4952.
15. Niederberger, M.; Garnweitner, G.; Pinna, N.; Neri, G. *Progress Solid State Chem.* **2005**, *33*, 59-70.
16. Niederberger, M.; Bartl, M. H.; Stucky, G. D. *Chem. Mater.* **2002**, *14*, 4364-4370.

### 3. "Brick and Mortar" Mesoporous Titania Films

---

17. Alberius, P. C. A.; Frindell, K. L.; Hayward, R. C.; Kramer, E. J.; Stucky, G. D.; Chmelka, B. F. *Chem. Mater.* **2002**, *14*, 3284-3294.
18. Ravikovitch, P. I.; Vishnyakov, A.; Neimark, A. V.; Carrott, M.; Russo, P. A.; Carrott, P. J. *Langmuir* **2006**, *22*, 513-516.
19. Klug, H. P.; Alexander, L. E., X-ray Diffraction Procedures, Wiley, New York, 2nd edn., 1974.
20. Laskowski, J. J.; Young, J.; Gray, R.; Acheson, R.; Forder, S. D., *Anal. Chim. Acta* **1994**, *286*, 9-23.
21. Galloway, J. N.; Townsend, A. R.; Erisman, J. W.; Bekunda, M.; Cai, Z.; Freney, J. R.; Martinelli, L. A.; Seitzinger, S. P.; Sutton, M. A. *Science* **2008**, *320*, 889-892.
22. Kuang, D. B.; Klein, C.; Ito, S.; Moser, J. E.; Humphry-Baker, R.; Evans, N.; Duriaux, F.; Graetzel, C.; Zakeeruddin, S. M.; Graetzel, M. *Adv. Mater.* **2007**, *19*, 1133-1137.
23. Zúkalová, M.; Procházka, J.; Zúkal, A.; Yum, J. H.; Kavan, L. *Inorg. Chim. Acta* **2007**, *361*, 656-662.
24. Kuang, D. B.; Wang, P.; Ito, S.; Zakeeruddin, S. M.; Gratzel, M. *J. Am. Chem. Soc.* **2006**, *128*, 7732-7733.

## **4. Multilayered High Surface Area “Brick and Mortar” Mesoporous Titania Films as Efficient Anodes in Dye- Sensitized Solar Cells**

*This chapter is based on the following publication:*

Johann M. Szeifert, Dina Fattakhova-Rohlfing, Jiri Rathouský, Thomas Bein, *Advanced Functional Materials*, submitted.

### **4.1 Introduction**

In 1991, a new type of highly efficient photoelectrochemical device based on mesoporous titanium dioxide covered with a photosensitizing dye and a redox electrolyte, the so called dye-sensitized solar cell (DSC), was reported.<sup>1</sup> Since the DSC's discovery, research has focused most intensively on developing new dyes to increase the amount of absorbed light and thus the conversion efficiency, and on new electrolytes and hole-transporters to significantly enhance the cells' long-term stability.<sup>2</sup> Concerning the electrodes, nanocrystalline mesoporous titania layers featuring a high and accessible surface area for maximum dye loading are the most frequently used anodes in the DSCs. In combination with a scattering layer of larger particles on top, this architecture is the only electrode system until today that can reach the maximum performance of up to 11.2 % using volatile electrolytes.<sup>3,4</sup> The common TiO<sub>2</sub> electrodes are prepared by sintering anatase nanoparticles about 20 nm in size. The resulting nanocrystalline layers are mesoporous due to voids between the nanoparticles, with typical values for pore size and roughness factor being 18 nm and 780,

#### 4. Multilayer “Brick and Mortar“ Titania Films in Dye-Sensitized Solar Cells

---

respectively, for a layer with a typical thickness of 10  $\mu\text{m}$ .<sup>1,5</sup> This design of the double layer electrodes has been the basis for all record efficiencies reported with liquid electrolyte DSCs. However, when more viscous electrolytes such as ionic liquids or solid hole transporters are employed, the relatively high thickness of such electrodes can become a limiting factor in the cell performance.<sup>6</sup> In the above systems, the diffusion length of excited electrons becomes shorter than the necessary film thickness to harvest all photons. This leads to an increased probability for recombination and lowers the maximum efficiency.<sup>3,7,8</sup>

In order to improve the performance of DSCs, it is desirable to further optimize the electrode's nanostructure.<sup>9</sup> One synthetic strategy is based on the use of block copolymer templates for obtaining periodic porous structures with very high surface areas, usually employing sol-gel derived amorphous species as metal oxide precursors.<sup>10</sup> This alternative route enables the fabrication of titania layers which feature one of the highest volumetric efficiencies reported so far. Thus, layers of only 2  $\mu\text{m}$  in thickness can reach impressively high efficiencies of up to over 5 %.<sup>10-12</sup> However, attempts to further improve the cell efficiency by a corresponding increase in electrode thickness prove to be difficult. The major problem is that only relatively thin films of up to about 2  $\mu\text{m}$  can be fabricated by this approach, which is still below the optimum thickness required for efficient photon absorption.<sup>13,14</sup> The main reason for this limitation is a drastic change in density upon transformation of an initially amorphous mesostructured framework into a crystalline phase upon calcination. As a result, the porous structure shrinks significantly, with destructive consequences of cracking or delamination of the films, and can even totally collapse into dense material. Thicker films are accessible with this approach by sequential deposition of thin layers.<sup>10,11,13-17</sup> Although the efficiency of such films can be partially improved, the increase in the film thickness does not lead to the expected linear increase in surface area and pore volume because of the progressing deterioration of the first layers upon multiple thermal treatment.<sup>11,15,16</sup>

#### 4. Multilayer “Brick and Mortar” Titania Films in Dye-Sensitized Solar Cells

---

We have recently demonstrated an alternative strategy for obtaining regular surfactant-based mesoporous films.<sup>18,19</sup> Titanium dioxide layers were produced by using a combination of pre-formed nanocrystals with surfactant-templated amorphous sol-gel. We called this a “brick and mortar” approach, because the nanoparticles act as “bricks” assembling around the surfactant, and are fused by the amorphous sol-gel (“mortar”). Upon thermal treatment, the “bricks” act as crystal seeds for the further crystallization of the mesoporous framework, and the final thin films exhibit high surface area, porosity, and transparency in combination with a tunable porous morphology. Due to the intrinsic crystallinity of the nanoparticle precursors, the volume and density changes upon heating are drastically reduced. On that account, this combination enables the production of multilayers of several micrometers thickness without influencing the bottom layers. The resulting layers have shown to act as very efficient anodes in DSCs, exhibiting a conversion efficiency of 6.0 % for films of only 2.7  $\mu\text{m}$  in thickness.<sup>18</sup> Such a high performance of “brick and mortar” layers has led us to further investigate the possibility of maximizing the cells’ efficiency by optimizing the titania layer thickness and morphology.

Here we report the fabrication of thick “brick and mortar” titania films by sequential deposition of several layers, focusing on the effect of stacking multiple layers on the films’ physical properties such as nanostructure morphology, surface area, pore size and dye adsorption, and the corresponding performance as anodes in DSCs. We find that even relatively thin films of few micrometers show remarkable light absorption and photovoltaic performance in liquid DSCs. In this way, the high volumetric efficiencies of films obtained with this synthetic strategy open perspectives for electrode materials in DSCs made with diffusion-limited hole transporting materials to achieve good performance and long solar cell lifetimes.

## 4.2 Results and Discussion

The “brick and mortar” mesoporous titania layers were synthesized as described previously.<sup>18</sup> In short, anatase nanocrystals are prepared in a non-aqueous sol-gel process using benzyl alcohol and titanium tetrachloride at elevated temperatures. The nanoparticles of about 4-5 nm are separated by centrifugation, and are redispersed using a PEO-PPO-PEO block copolymer (Pluronic P123 or F127) in tetrahydrofuran. After adding a pre-hydrolyzed molecular sol-gel precursor (obtained from tetraethyl orthotitanate and hydrochloric acid), the colloidal dispersions are used for spin- or dip-coating on flat substrates. Since a nanoparticle to sol-gel ratio of 70 wt % nanoparticles (fraction of nanoparticles based on the total mass of TiO<sub>2</sub> precursors in solution) proved to be optimal for photovoltaic applications,<sup>18</sup> all layers were prepared with this ratio. Using a typical coating solution with a total titanium dioxide content of 7 wt % and spin-coating on glass or FTO substrates, homogeneous, crack-free and transparent films can be made. After calcination above 300 °C, the films are mesoporous due to the combustion of the polymer template. The thickness of the films obtained after a single coating is usually about 1 μm depending on the polymer used, and can reach at maximum 1.5 to 1.8 μm without cracking and delamination. To obtain the thicker films required in many applications, multiple “brick and mortar” layers can be sequentially deposited on the top of the previous ones. Between each coating, a calcination step to 300 °C has to be performed in order to reduce the mechanical stress due to the template removal in lower layers. The film thickness rises linearly with the number of coatings (Figure 4.1), and with the employed conditions an average thickness per layer of about 0.6 μm for P123- and 0.85 μm for F127-containing precursor solutions is obtained, respectively.

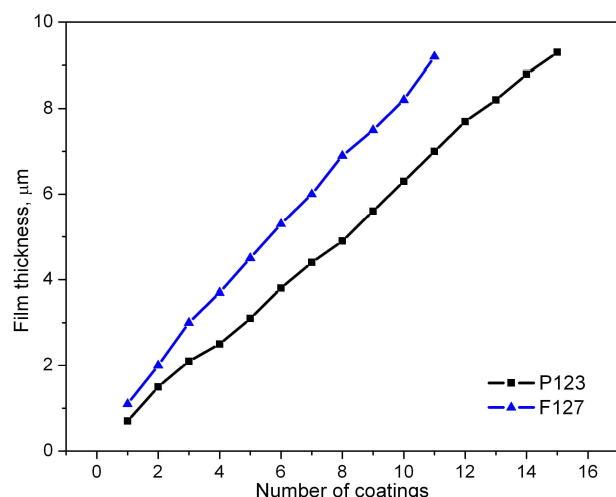


**Figure 4.1.** Development of film thickness with multiple coating cycles for P123- and F127-templated “brick and mortar” titania films. The films were calcined at 300 °C between each coating.

With this method, it is now possible to prepare surfactant-templated mesoporous films of up to 10 μm in thickness without cracking and delamination. As can be seen from cross-sectional SEM images (Figure 4.2), all layers have a very homogeneous and flat surface (for example, compared to the rough FTO surface in Figure 4.2b), allowing us to tune the film thickness in a wide range. The porous structure (Figure 4.2c) exhibits no periodic order over large domains; no characteristic small-angle X-ray scattering peak is observed. This non-periodic porous structure appears to be consistent throughout the whole film and no drastic structural differences between the top and bottom layers are visible.

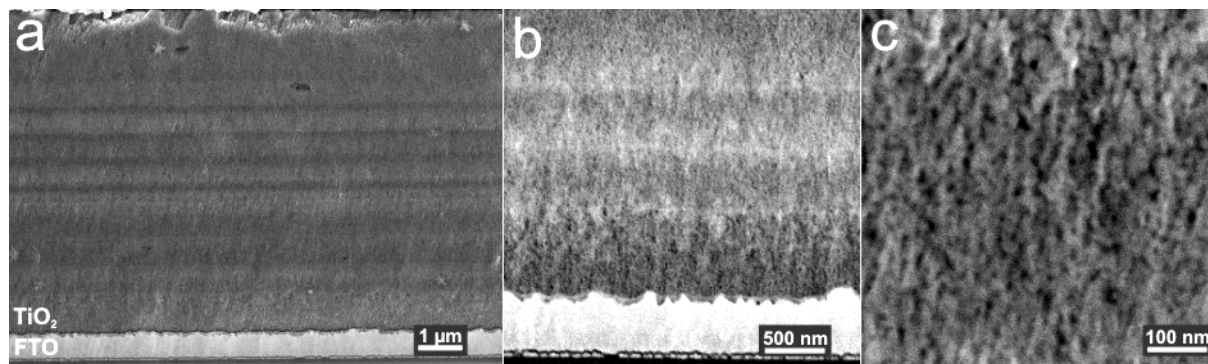


**Figure 4.2.** Cross-sectional SEM images of a multilayer “brick and mortar” film. Overview on the whole film with a thickness of 7.5  $\mu\text{m}$  prepared by a sequential deposition of 12 layers (a). Magnification of the first four layers at the interface with the FTO substrate (b), and of the mesostructure in a middle layer (c).

Krypton and dye adsorption studies were performed to gain further information about the pore system. Special attention was focused on the accessibility of the lower layers in thick films. For this purpose, films of different thicknesses were examined using Kr sorption at 77 K. The films exhibit type IV isotherms of mesoporous materials (Figure 4.3). Since the isotherms do not exhibit a saturation plateau at high partial pressures due to full condensation in the pores, the pore volumes of the films are somewhat underestimated. The development of the surface area upon sequential coating of multiple layers is shown in Figure 3c. The roughness factor rises linearly with the film thickness, proving the unhindered accessibility of the bottom layers in the thick multilayer film, and the thickest layers exhibit roughness factors of up to 1600  $\text{cm}^2/\text{cm}^2$ . This linearity demonstrates the advantage of the “brick and mortar” approach for the fabrication of thick mesoporous films compared to strategies based on only sol-gel derived titania precursors. For the latter ones, an increase in surface area and pore volume upon deposition of additional layers is usually observed merely for the very first layers reaching up to about 2  $\mu\text{m}$  total film thickness. Beyond this thickness a plateau in surface area is reached due to progressive densification of the bottom layers, and the porous characteristics

#### 4. Multilayer “Brick and Mortar” Titania Films in Dye-Sensitized Solar Cells

only deteriorate with increasing film thickness.<sup>13,14</sup> The “brick and mortar” strategy, however, can overcome this disadvantage, most probably because already at the relatively low temperatures of 300 °C necessary for template removal, the films are completely crystalline,<sup>18</sup> providing sufficient stability against further condensation and densification.

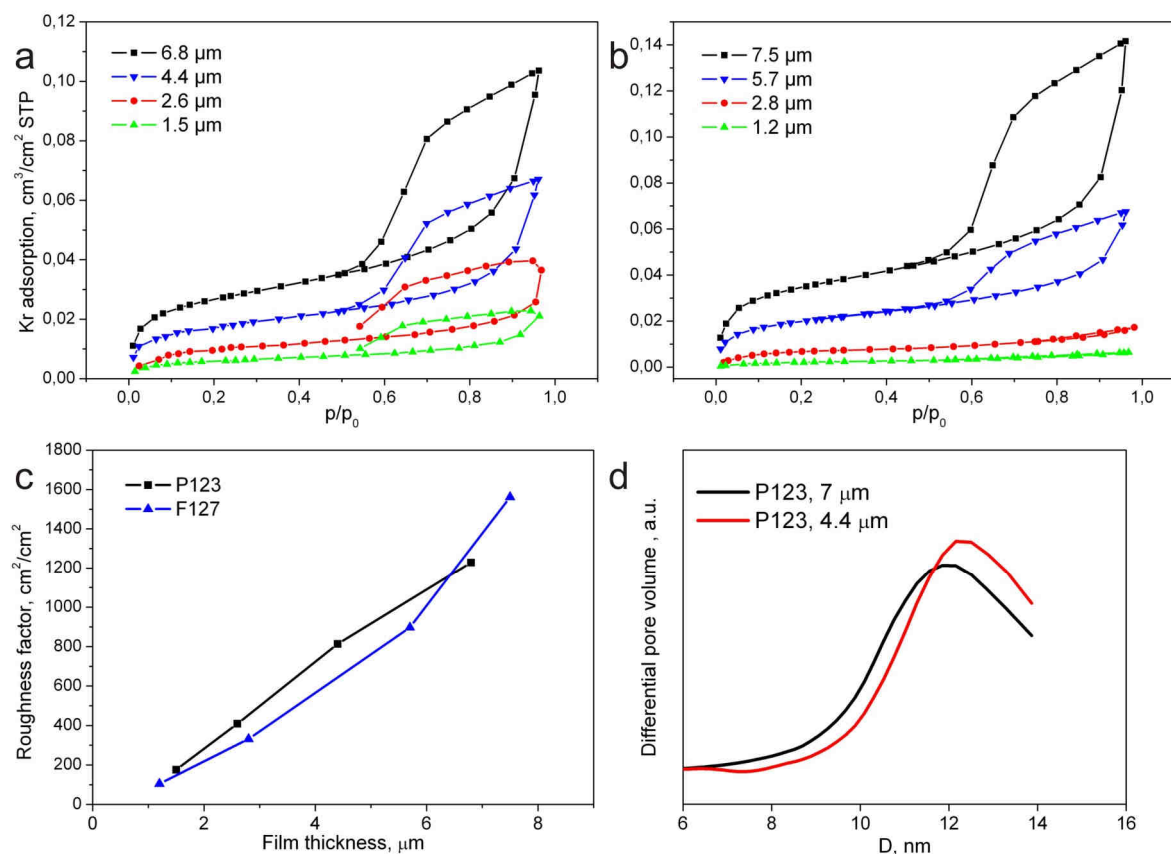


**Figure 4.3.** Krypton sorption isotherms of Pluronic P123 (a) and F127 (b) templated mesoporous “brick and mortar” titanium dioxide films of varying thickness after calcination at 450 °C. (c) Development of surface area (given as roughness factor) depending on the film thickness derived from Kr sorption on multilayer “brick and mortar” mesoporous TiO<sub>2</sub> employing the templates Pluronic P123 (black squares) or F127 (blue triangles). (d) Pore size distribution for two films composed of different numbers of layers.

The pore size of the P123-templated “brick and mortar” films is found to be about 12 nm and is thus very large for mesostructures using this polymer. Additional nitrogen sorption

measurements are in close agreement with the above results (Figure 4.4). The pore size is rather independent of the film thickness, which is shown by pore-size distributions of two films of 4.4 and 7  $\mu\text{m}$  thickness, respectively (Figure 4.3c). The pores in the lower layers are not filled up with precursor solution by coating additional films using the same precursor solution. This effect for multiple coatings of surfactant-containing solutions has been explained by surfactant molecules plugging the open pores at the surface, thus limiting the diffusion of precursor solution into lower layers.<sup>13</sup>

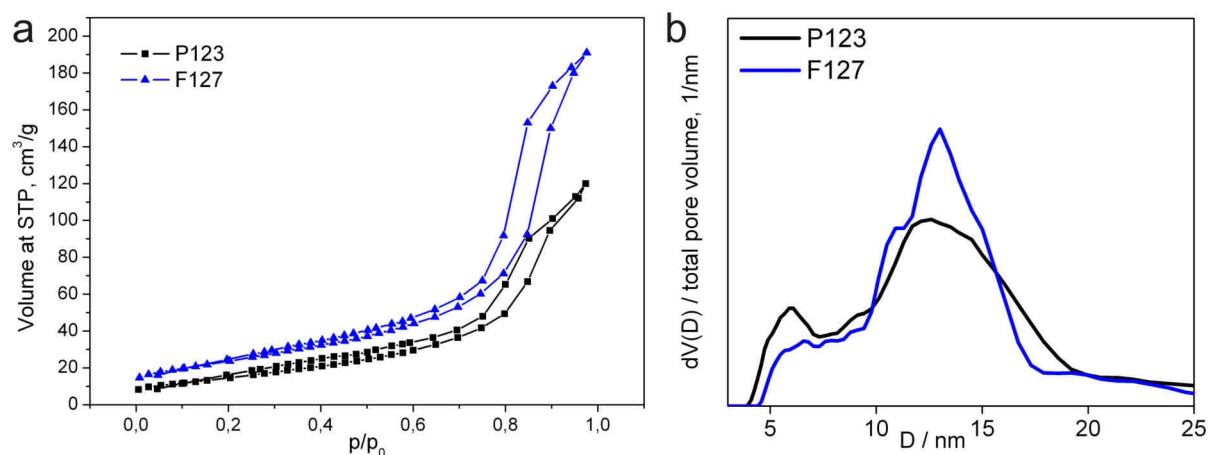


**Figure 4.4.** (a) Nitrogen sorption isotherms of Pluronic P123 and F127 templated mesoporous “brick and mortar” titanium dioxide films after calcination at 450 °C. To obtain sufficient amounts of porous material for N<sub>2</sub> sorption, 20 one-layer films of about 1  $\mu\text{m}$  thickness were scratched off the substrate after calcination and measured as powders. (b) Comparison of pore-size distributions derived from the isotherms. The maxima correspond to 12.1 nm (P123) and 13.5 nm (F127).

In order to exploit the structural features of the multilayered “brick and mortar” films in the DSC, we investigated the accessibility of the mesopores for dye molecules used in DSCs and the dye loading in the films composed of several layers. Absorption data obtained from UV-Vis spectroscopy of films after staining with a N719 dye solution are shown in Figure 4.5.

#### 4. Multilayer “Brick and Mortar“ Titania Films in Dye-Sensitized Solar Cells

The spectra show the typical absorption features of the dye bound to titanium dioxide,<sup>4,20</sup> and the absorbance both at the absorption maximum at 520 nm and the mean absorbance over the whole visible spectrum rises linearly with high film thicknesses of over 7  $\mu\text{m}$ . This indicates a constant accessible surface area per thickness throughout the whole film. The surface areas are very high, since at film thicknesses of about 4  $\mu\text{m}$  already over 90 % of the incoming light is absorbed at the absorption maximum (Figure 4.5b).

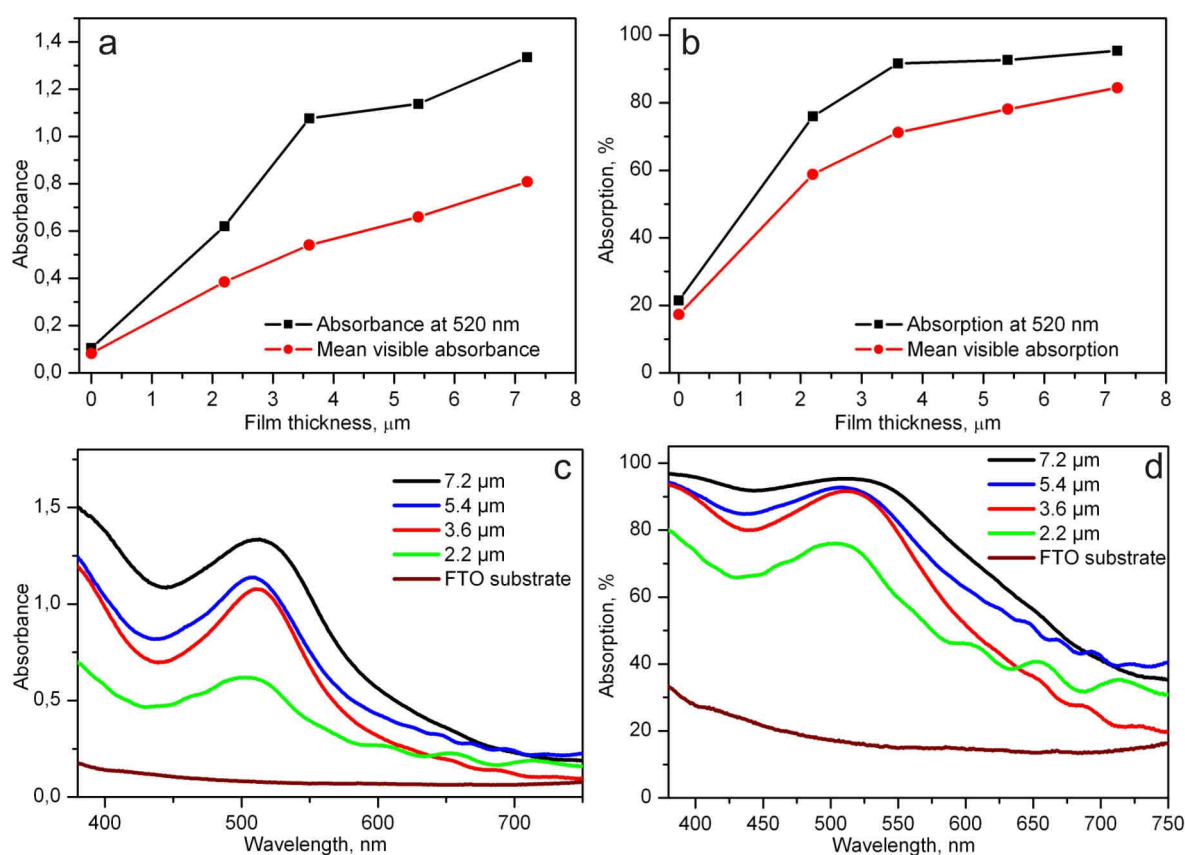


**Figure 4.5.** Absorption behaviour of N719 dye molecules adsorbed onto the P123-templated mesoporous films of varying thickness on FTO substrates. (a), (c) Absorbance (optical density) values obtained from UV-Vis spectra measured in transmission. Note that scattering and reflection are not taken into account. (b), (d) Calculated absorption values in % of incident light intensity, with  $(\text{absorption } \%) = (1 - 10^{(-\text{absorbance})}) * 100$ . Squares: mean absorption in the visible spectrum; circles: absorption at the absorption maximum. (a),(b) The first value (zero film thickness) corresponds to the blank FTO substrate.

These high values for light absorption in relatively thin films could be very useful in dye-sensitized solar cells because in thin films the charges can be transported efficiently due to low resistance. “Brick and mortar” films of varying thickness were examined in DSCs using N719 dye and a typical volatile iodine-containing electrolyte, and Figure 4.6 shows the photovoltaic characteristics.

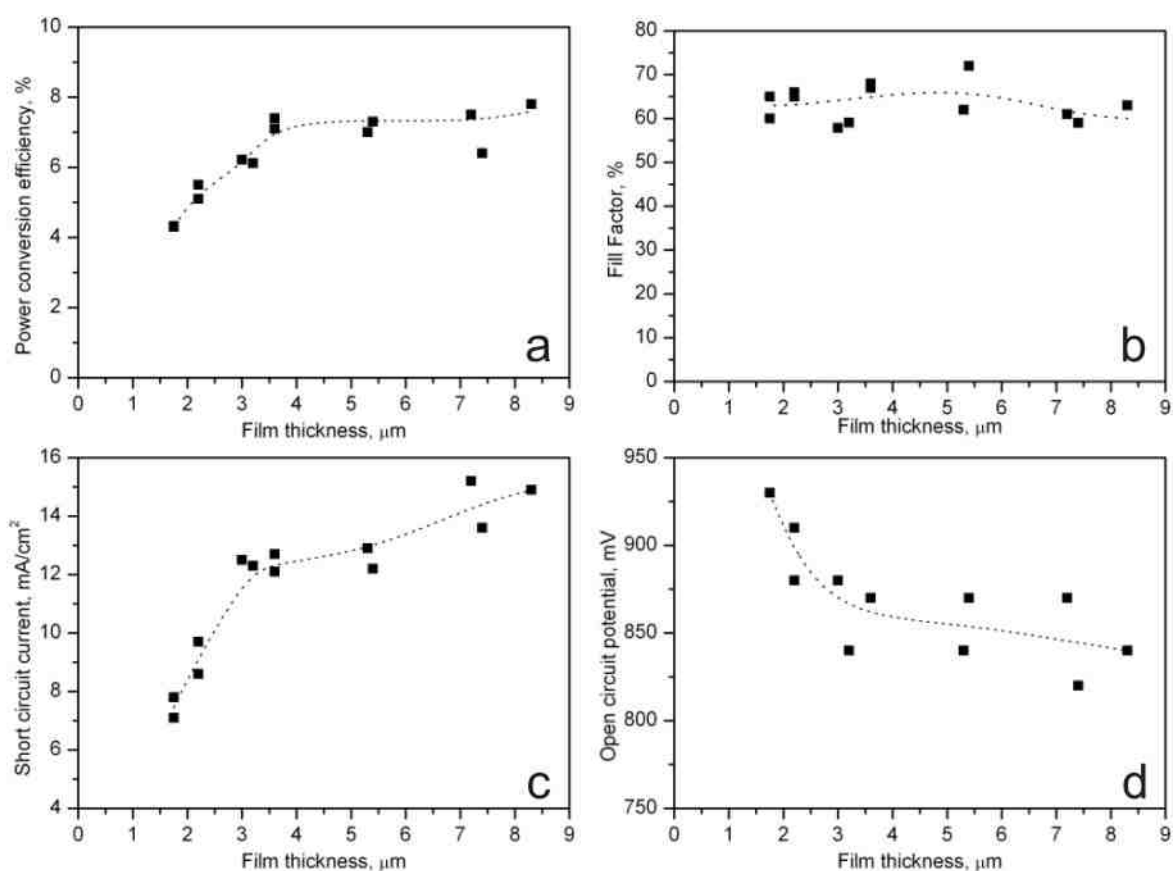


**Figure 4.6.** Photovoltaic performance of DSCs made using Pluronic P123 templated “brick and mortar” mesoporous  $\text{TiO}_2$  electrodes with varying thickness, and employing N719 dye with a volatile electrolyte under 1 sun illumination: Power conversion efficiency (a), fill factor (b), short circuit current (c), and open circuit potential (d), versus the film thickness. The dotted lines indicate fits of the development of mean values.

The power conversion efficiency of a series of P123-templated electrodes with varying thickness rises quickly to reach a plateau of over 7 % for films of less than 4 μm thickness,

mainly due to a fast increase in photo- and short circuit current for low film thicknesses. This can be correlated with the mean visible absorption of the films, which shows a similar behaviour (Figure 4.6b). Above 4  $\mu\text{m}$  film thickness, despite a higher absorption, the additionally generated charges contribute less to the total power resulting in a slower increase in conversion efficiency. This can be explained mainly by the thickness-dependent reduction of open circuit potential from over 900 mV for films of less than 2  $\mu\text{m}$  to less than 800 mV for films above 8  $\mu\text{m}$  (Figure 4.6d). We attribute this lower potential to the increase in the number of recombination sites and the dark current (Figure 4.7) due to the higher surface area in thick films.<sup>8,21,22</sup>

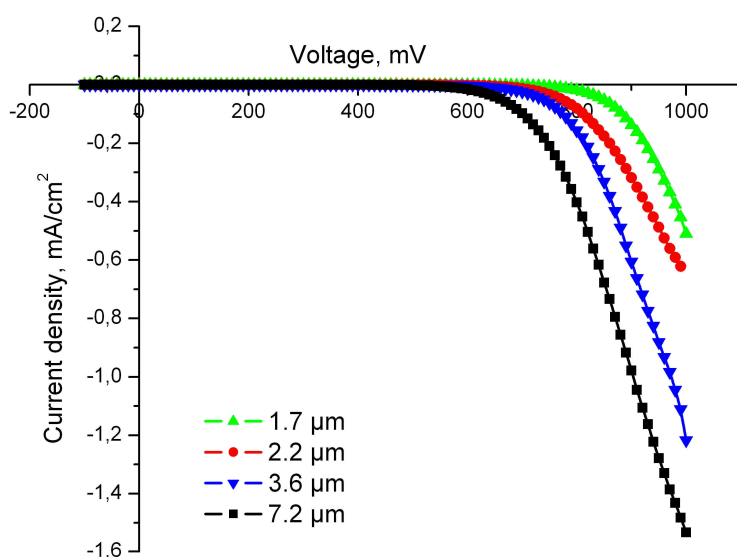


**Figure 4.7.** Dark current measurements of DSCs made using Pluronic P123 templated “brick and mortar” mesoporous  $\text{TiO}_2$  electrodes of varying thickness.

The maximum performance obtained with Pluronic P123 templated “brick and mortar” films was found to be 7.8 % ( $V_{oc}$ : 840 mV,  $I_{sc}$ : 14.9  $\text{mA}/\text{cm}^2$ , FF: 0.63, 1 sun illumination, film thickness 8.5  $\mu\text{m}$ ), and 8.1 % for a film made using the slightly larger polymer Pluronic F127 ( $V_{oc}$ : 820 mV,  $I_{sc}$ : 15.1  $\text{mA}/\text{cm}^2$ , FF: 0.65, 1 sun illumination, film thickness 10  $\mu\text{m}$ , Figure

4.8). These conversion efficiencies are rather similar for the two polymers, which reflects the similar pore size distributions in the titania films (Figure 4.9). This indicates that despite having smaller pores than the standard nanocrystalline electrodes (18 nm average pore size), the pore size and the charge collection by the volatile electrolyte are not the major performance-limiting factors.<sup>23,24</sup> In fact, these conversion efficiencies are the highest that have been reported for surfactant-templated mesoporous films, and since no backscattering layer was applied, even compared to the standard electrodes these values are quite high.

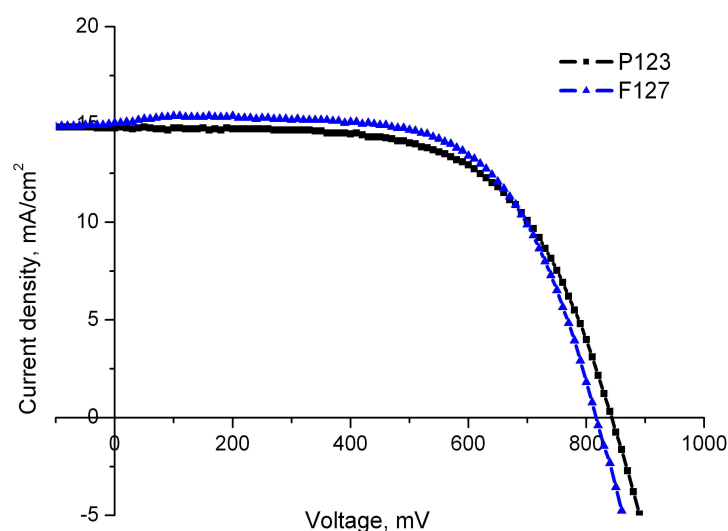


**Figure 4.8.** Current density – voltage curves of the most efficient DSCs assembled from titania layers made using Pluronic P123 or F127 as templates (active area: 0.196 cm<sup>2</sup>; 1 sun illumination). Black squares: P123-templated electrode, efficiency: 7.8 %,  $V_{oc}$ : 840 mV,  $I_{sc}$ : 14.9 mA/cm<sup>2</sup>, FF: 0.63, film thickness 8.5  $\mu$ m. Blue triangles: F127-templated electrode, efficiency: 8.1 %,  $V_{oc}$ : 820 mV,  $I_{sc}$ : 15.1 mA/cm<sup>2</sup>, FF: 0.65, film thickness 10  $\mu$ m.

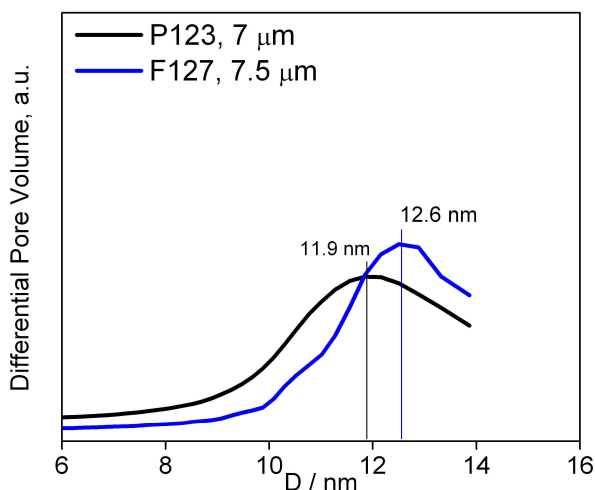


**Figure 4.9.** Comparison of pore-size distributions for multilayer “brick and mortar” films templated with P123 (film thickness 7  $\mu\text{m}$ ) or F127 (7.5  $\mu\text{m}$ ) derived from Kr sorption.

### 4.3 Conclusion

In conclusion, the “brick and mortar” synthetic strategy was used to prepare up to 10  $\mu\text{m}$  thick multilayer mesoporous titanium dioxide films. The multilayers exhibit a very high surface area, which scales linearly with the film thickness when multiple coatings are stacked. In this way, roughness factors of up to 1600  $\text{cm}^2/\text{cm}^2$  can be reached, without serious cracking, delamination, or deterioration of the porous structure. These high surface areas and film thicknesses are a new record for surfactant-derived mesoporous titanium dioxide films. The mesopores prepared by using the commercial block copolymers Pluronic P123 and F127 are rather large, and despite stacking many layers they do not shrink and remain accessible, which could be proven by dye adsorption experiments. Applied in dye-sensitized solar cells, the multilayered “brick and mortar” films feature a remarkably high performance level of over 7 % already at film thicknesses below 4  $\mu\text{m}$ , which is attributed to their large surface area and the consequently high amount of adsorbed dye molecules. This makes them interesting candidates for solid-state solar cells employing diffusion-limited hole transporting materials.

### 4.4 Experimental Section

Titanium dioxide nanoparticles were prepared using a modified procedure developed by Niederberger et al.<sup>25</sup> Titanium tetrachloride (1.5 mL, 13.7 mmol) was dissolved in toluene (10 mL) and added to benzyl alcohol (30 mL, 291 mmol) under continuous stirring. The solution was kept at 60 °C for 20 h, then cooled down to room temperature. The particles were separated by centrifugation at 50 000 rcf for 30 minutes and used without further treatment. The centrifuged particles (without being subjected to washing procedures) contain about 45 wt% of benzyl alcohol according to thermogravimetric analysis; this was taken into account for the adjustment of the TiO<sub>2</sub>-content.

To obtain a coating solution with 70 wt % TiO<sub>2</sub> nanoparticles and 30 wt % sol-gel titania precursors (based on Ti-content), a solution of Pluronic P123 (0.2 g, 0.04 mmol) or F127 (0.3 g, 0.02 mmol) in tetrahydrofurane (4 mL) was added to centrifuged, unwashed particles (0.4 g, 2.2 mmol of TiO<sub>2</sub>), ultrasonicated and stirred overnight until the particles were homogeneously redispersed. Subsequently, 0.4 mL (corresponding to 1.1 mmol TiO<sub>2</sub>) of a prehydrolyzed sol-gel solution was added (sol-gel solution, see below), and the mixture was stirred for several minutes. The final solutions were transparent or translucent, being of a yellow to orange color. The sol-gel solution was prepared by adding hydrochloric acid (37 %, 5.1 mL, 62.1 mmol) to tetraethyl orthotitanate (7.2 mL, 34.3 mmol) under continuous stirring for about 10 min. The films were prepared on FTO-coated glass (TEC-7 from Pilkington) by spin-coating (150 - 180 μL per 1 cm<sup>2</sup> substrate area) at 800 rpm for 30 seconds and calcined at 450 °C (with a ramp of 0.6 °C min<sup>-1</sup>) for 30 minutes.

Scanning electron microscopy (SEM) was performed on a JEOL JSM-6500F scanning electron microscope equipped with a field emission gun, at 4 kV. The film thickness was measured by profilometry (Dektak). The porosity of the films was determined by the analysis

#### 4. Multilayer “Brick and Mortar“ Titania Films in Dye-Sensitized Solar Cells

---

of adsorption isotherms of Kr at the boiling point of liquid nitrogen (approx. 77 K) using an ASAP 2010 apparatus (Micromeritics). All krypton sorption experiments were performed and evaluated by Dr. Jiri Rathouský at the J. Heyrovský Institute in Prague. Textural information is obtained by comparing the Krypton sorption isotherms and their limiting adsorption at saturation pressure with reference materials (anatase powders) characterized by Nitrogen sorption. Comparison plots were constructed for each sample, and the differentiation of these plots provided the basis for the pore size distribution. Nitrogen sorption measurements were performed with a NOVA 4000e (Quantachrome Instruments) at 77 K. To obtain sufficient amounts of porous material for N<sub>2</sub> sorption, 20 one-layer films of about 1 μm thickness were scratched off the substrate after calcination and measured as powders. Pore size distributions were calculated using a NLDFT equilibrium model of N<sub>2</sub> on silica assuming cylindrical pores. UV-Vis measurements of mesoporous titania films were performed in transmission using a UV-Vis spectrophotometer (Hitachi U-3501). Scattering or reflection from the FTO substrates were not taken into account. Absorption values in % were calculated from the corresponding absorbance values by the formula: (absorption %) =  $(1 - 10^{(-\text{absorbance})}) * 100$ .

For photovoltaic measurements, the mesoporous TiO<sub>2</sub> films on FTO-coated glass substrates were heated at 450 °C for 30 min, then cooled to ca. 80 °C and immersed into the dye solution at room temperature, and kept there for 16 h. A dye solution containing 0.5 mM of the dye N719 in acetonitrile and *tert*-butyl alcohol (volume ratio 1:1) was used to sensitize the photoanodes. Dye-coated mesoporous TiO<sub>2</sub> films were assembled and sealed with a transparent hot-melt 60 μm thick surlyn ring to the counter electrodes (Pt on FTO glass, chemical deposition from 0.01 M hexachloroplatinic acid in ethanol heated at 400 °C for 15 min). The active cell area in all samples was about 0.196 cm<sup>2</sup>. The electrolyte was injected into the inner electrode space by vacuum back-filling from the counter electrode side through a pre-drilled hole, and then the hole was sealed with a surlyn sheet and a thin glass cover slide

by heating to 120 °C. The volatile electrolyte contains 0.6 M BMII (butylmethylimidazolium iodide), 0.03 M iodine, 0.1 M GuNCS (guanidinium thiocyanate), and 0.5 M tert-butyl pyridine in acetonitrile and valeronitrile (volume ratio 1:1). For the characterization of solar cells, an AM 1.5 solar simulator (Solar light Co.) was used. The photovoltaic measurements have been performed under one sun illumination, and the light intensity was monitored by a pyranometer (PMA2100, Solar light Co.). Current density-voltage measurements were performed with a Zahner IM6ex impedance measurement unit.

#### 4.5 References

1. O'Regan, B.; Grätzel, M. *Nature* **1991**, *353*, 737-740.
2. Grätzel, M. *Acc. Chem. Res.* **2009**, *42*, 1788-1798.
3. Wang, P.; Zakeeruddin, S. M.; Comte, P.; Charvet, R.; Humphry-Baker, R.; Grätzel, M. *J. Phys. Chem. B* **2003**, *107*, 14336-14341.
4. Nazeeruddin, M. K.; De Angelis, F.; Fantacci, S.; Selloni, A.; Viscardi, G.; Liska, P.; Ito, S.; Takeru, B.; Grätzel, M. *J. Amer. Chem. Soc.* **2005**, *127*, 16835-16847.
5. Ito, S.; Murakami, T. N.; Comte, P.; Liska, P.; Grätzel, C.; Nazeeruddin, M. K.; Grätzel, M. *Thin Solid Films* **2008**, *516*, 4613-4619.
6. O'Regan, B. C.; Durrant, J. R. *Acc. Chem. Res.* **2009**, *42*, 1799-1808.
7. Docampo, P.; Guldin, S.; Stefiik, M.; Tiwana, P.; Orilall, M. C.; Hüttner, S.; Sai, H.; Wiesner, U.; Steiner, U.; Snaith, H. J. *Adv. Funct. Mater.* **2010**, *20*, 1787-1796.
8. Ito, S.; Zakeeruddin, S.; Humphry-Baker, R.; Liska, P.; Charvet, R.; Comte, P.; Nazeeruddin, M.; Péchy, P.; Takata, M.; Miura, H.; Uchida, S.; Grätzel, M. *Adv. Mater.* **2006**, *18*, 1202-1205.

9. Kim, D.; Lee, K.; Roy, P.; Birajdar, B.; Spiecker, E.; Schmuki, P. *Angew. Chem. Int. Ed.* **2009**, *48*, 9326-9329.
10. Zukalova, M.; Zukal, A.; Kavan, L.; Nazeeruddin, M. K.; Liska, P.; Grätzel, M. *Nano Lett.* **2005**, *5*, 1789-1792.
11. Prochazka, J.; Kavan, L.; Zukalova, M.; Frank, O.; Kalbac, M.; Zukal, A.; Klementova, M.; Carbone, D.; Grätzel, M. *Chem. Mater.* **2009**, *21*, 1457-1464.
12. Hou, K.; Tian, B.; Li, F.; Bian, Z.; Zhao, D.; Huang, C. *J. Mater. Chem.* **2005**, *15*, 2414-2420.
13. Prochazka, J.; Kavan, L.; Shklover, V.; Zukalova, M.; Frank, O.; Kalbac, M.; Zukal, A.; Pelouchova, H.; Janda, P.; Mocek, K.; Klementova, M.; Carbone, D. *Chem. Mater.* **2008**, *20*, 2985-2993.
14. Zukalova, M.; Prochazka, J.; Zukal, A.; Yum, J. H.; Kavan, L.; Grätzel, M. *J. Electrochem. Soc.* **2010**, *157*, H99-H103.
15. Zhang, Y.; Xie, Z. B.; Wang, J. *Nanotechnology* **2009**, *20*, 505602.
16. Zhang, Y.; Xie, Z.; Wang, J. *ACS Appl. Mater. Interfaces* **2009**, *1*, 2789-2795.
17. Zukalová, M.; Procházka, J.; Zukal, A.; Yum, J. H.; Kavan, L. *Inorg. Chim. Acta* **2008**, *361*, 656-662.
18. Szeifert, J. M.; Fattakhova-Rohlfing, D.; Georgiadou, D.; Kalousek, V.; Rathouský, J.; Kuang, D.; Wenger, S.; Zakeeruddin, S. M.; Grätzel, M.; Bein, T. *Chem. Mater.* **2009**, *21*, 1260-1265.
19. Fattakhova-Rohlfing, D.; Szeifert, J. M.; Yu, Q.; Kalousek, V.; Rathouský, J.; Bein, T. *Chem. Mater.* **2009**, *21*, 2410-2417.
20. Nazeeruddin, M. K.; Zakeeruddin, S. M.; Humphry-Baker, R.; Jirousek, M.; Liska, P.; Vlachopoulos, N.; Shklover, V.; Fischer, C.-H.; Grätzel, M. *Inorg. Chem.* **1999**, *38*, 6298-6305.

#### 4. Multilayer “Brick and Mortar“ Titania Films in Dye-Sensitized Solar Cells

---

21. Zhu, K.; Kopidakis, N.; Neale, N. R.; van de Lagemaat, J.; Frank, A. J. *J. Phys. Chem. B* **2006**, *110*, 25174-25180.
22. Wang, Q.; Ito, S.; Grätzel, M.; Fabregat-Santiago, F.; Mora-Sera, I.; Bisquert, J.; Bessho, T.; Imai, H. *J. Phys. Chem. B* **2006**, *110*, 25210-25221.
23. Chou, T. P.; Zhang, Q.; Russo, B.; Fryxell, G. E.; Cao, G. *J. Phys. Chem. C* **2007**, *111*, 6296-6302.
24. Barbé, C. J.; Arendse, F.; Comte, P.; Jirousek, M.; Lenzenmann, F.; Shklover, V.; Grätzel, M. *J. Amer. Chem. Soc.* **1997**, *80*, 3157-3171.
25. Niederberger, M.; Bartl, M. H.; Stucky, G. D. *Chem. Mater.* **2002**, *14*, 4364-4370.

## **5. High Surface Area “Brick and Mortar” Films for Ionic Liquid Dye-Sensitized Solar Cells**

### **5.1 Introduction**

In the past two decades, dye-sensitized solar cells (DSCs) have demonstrated their potential as alternative technology to conventional photovoltaic devices, and maximum efficiencies of over 11 % have been attained.<sup>1-3</sup> Substantial progress has been made in solving the problem of achieving both long-term stability and at the same time high efficiency of the cells by the introduction of solid hole transporters or room-temperature ionic liquids (RTILs).<sup>4-6</sup> Especially the latter exhibit acceptable performance levels; their efficiency record is currently reaching 8.5 %, with excellent stability over thousands of hours even at elevated temperatures.<sup>7</sup> In general, the photovoltaic systems employing more stable electrolytes or hole transporters have the drawback of a low electron diffusion length leading to increased recombination.<sup>8-10</sup> As a result, the maximum film thickness from which charges can be extracted is reduced to less than about 5 (solid) or 10  $\mu\text{m}$  (ionic liquid hole transporters), respectively, which is below the optimum thickness required for complete light absorption.<sup>8,11</sup> In order to improve the performance of these types of cells, new titania electrode morphologies are needed which feature an optimal combination of high accessible surface area, pore size, and electron conductivity.<sup>12</sup> In our previous publications, we have introduced a new concept enabling the use of surfactant-derived mesoporous titanium dioxide films for application in DSCs by integrating preformed nanocrystalline seeds into the walls of a mesostructure.<sup>13,14</sup> This so called “brick and mortar” approach leads to highly crystalline films with very high surface area and large, accessible mesopores of over 12 nm in size. The

## 5. High Surface Area “Brick and Mortar“ Films for Ionic Liquid Dye-Sensitized Solar Cells

electrode thickness can be precisely tuned by deposition of multiple layers. Applied in solvent-based DSCs, these layers exhibited a maximum efficiency of over 8 % with the standard ruthenium dye N719 and a film thickness of about 10  $\mu\text{m}$ . The most intriguing feature of cells fabricated using this method, however, is the remarkable performance of rather thin layers: An efficiency plateau of over 7 % can already be reached with layer thicknesses of only 4  $\mu\text{m}$ . In this way, the combination of high accessible surface area in thin films offers a significant advantage for photovoltaic systems with low electron diffusion lengths.

Here we report on the investigation of “brick and mortar” titanium dioxide films as anodes in DSCs based on high molar extinction coefficient sensitizers and room temperature ionic liquid electrolytes. The mesoporous films can reach the performance level of the reference nanocrystalline electrode when employing similar electrode thicknesses. However, the rather small pore size of the “brick and mortar” mesostructures is shown to be affecting the photovoltaic characteristics in thicker films ( $> 6 \mu\text{m}$ ). The advantages of the high surface area in “brick and mortar” films can be best exploited when thin electrodes are used. DSCs made using such layers exhibit a maximum in efficiency of over 6 % at film thicknesses as low as 2  $\mu\text{m}$ .

The following experiments have been performed as a joint project: The “brick and mortar” films were synthesized and characterized by Johann M. Szeifert. Testing of the photovoltaic performance in ionic liquid dye-sensitized solar cells was done by M. Marszalek in the group of Dr. S. M. Zakeeruddin and Prof. Dr. Michael Grätzel at the EPF Lausanne.

## 5.2 Results and Discussion

The “brick and mortar” mesoporous titania layers were prepared following a reported procedure.<sup>13</sup> In brief, anatase nanocrystals of about 4-5 nm are synthesized using a non-aqueous sol-gel protocol using benzyl alcohol and  $\text{TiCl}_4$  at 60 °C. After centrifugation, the nanoparticles are redispersed using a solution of a PEO-PPO-PEO block copolymer (Pluronic P123 or F127) in tetrahydrofuran. A pre-hydrolyzed sol-gel precursor (obtained from tetraethyl orthotitanate and hydrochloric acid) is added, and the colloidal dispersions are employed for spin-coating on flat substrates. Since a high ratio of nanoparticles to sol-gel titanium dioxide precursors proved to be optimal for photovoltaic applications,<sup>13</sup> all samples were prepared using this basic recipe (see experimental section). The thickness of the homogeneous and transparent films obtained after a single coating procedure on FTO-coated glass is usually about 1  $\mu\text{m}$  after calcination, and can reach at maximum 1.5 to 1.8  $\mu\text{m}$  without cracking and delamination. Sequential coating steps allow the preparation of thicker films, with the total thickness rising linearly up to 10  $\mu\text{m}$ . Between coating steps, for condensation and stabilization of the lower layers, a calcination step to 300 °C has to be performed. For application in DSCs, the final films are heated to 500 °C prior to immersion into a dye solution to remove organic residues. In the following, “brick and mortar” films which were made employing the polymer Pluronic P123 are denoted **BM-P**, those using Pluronic F127 **BM-F**, respectively. The standard reference electrode with which the highest efficiency has been reported is abbreviated **NP-Ref**, and was prepared by screen-printing a paste of nanoparticles of 20 nm in size with cellulose binders. In some cases, a scattering layer of 400 nm anatase particles is deposited on top of the NP-Ref layer (double layer reference, **DL-Ref**). Since the large crystals hardly contribute to the active surface area of an

## 5. High Surface Area “Brick and Mortar“ Films for Ionic Liquid Dye-Sensitized Solar Cells

---

electrode, their thickness contribution is not taken into account when comparing different cells, and the thickness values correspond to the underlying nanoparticle layer only.

For an optimal cell performance employing ionic liquids and thin TiO<sub>2</sub> electrodes, it is crucial to choose a high molar extinction coefficient dye and a matching RTIL electrolyte. The organic dye D205 offers acceptable characteristics, because of its molar extinction coefficient of 53 000 M<sup>-1</sup> cm<sup>-1</sup>, and also quite high maximum efficiencies in ionic liquid DSCs (7.2 %).<sup>9</sup> Imidazolium salt based iodine containing ionic liquids are currently the best performing RTIL low viscosity electrolytes.<sup>12</sup> Examples are iodine-containing electrolyte mixtures consisting of 1-methyl-3-propylimidazolium iodide (PMII) and 1-methyl-3-ethylimidazolium tetracyanoborate (EMITCB), denoted as **IL-A**, or 1-ethyl-3-methylimidazolium iodide (EMII), 1,3-dimethylimidazolium iodide (DMII) and EMITCB, referred to as **IL-B**, respectively. For optimal performance of the solar cells, guanidinium thiocyanate (GuNCS) and N-methylbenzimidazole (nMBI) are added to the electrolytes.<sup>9</sup> The low viscosity of the two ionic liquid mixtures leads to a rather high triiodide diffusion coefficient in the RTIL electrolytes of 5.9 10<sup>-7</sup> cm<sup>2</sup>/s and 5.8 10<sup>-7</sup> cm<sup>2</sup>/s at room temperature for IL-A and IL-B, respectively.<sup>5,12,15</sup>

These materials were employed in first DSC tests using the “brick and mortar” titania layers of about 5 to 10 μm thickness. The main photovoltaic parameters are summarized in Figure 1. The reference cells exhibited high power conversion efficiencies of 6.5 % (5 μm, NP-Ref) and 6.7 % (8 μm, DL-Ref). “Brick and mortar” electrodes made using the smaller polymer Pluronic P123 (BM-P) resulted in cells with significantly lower performance. The main reason for this effect is a decrease in open circuit potential of about 50 mV. This can be attributed to drastically increased recombination, and is probably caused by charge transport limitations due to the small pore size. The limited transport also leads to lower short circuit current values comparing to reference cells.

## 5. High Surface Area “Brick and Mortar“ Films for Ionic Liquid Dye-Sensitized Solar Cells

The BM-F layers made using the slightly larger polymer F127 exhibit much better charge transport behaviour resulting at maximum in very good performance, reaching the level of the reference cells DL-Ref at 6.7 % for films of about 6.5  $\mu\text{m}$  (BM-F). Interestingly, both the power conversion and the short circuit current curves for BM-F show increasing trends towards lower film thicknesses, indicating that a performance maximum might exist at film thicknesses below 6  $\mu\text{m}$ . Regarding the open circuit potential and the fill factor, the BM-F cells exhibit rather little variation and are at the same level as the reference electrodes.

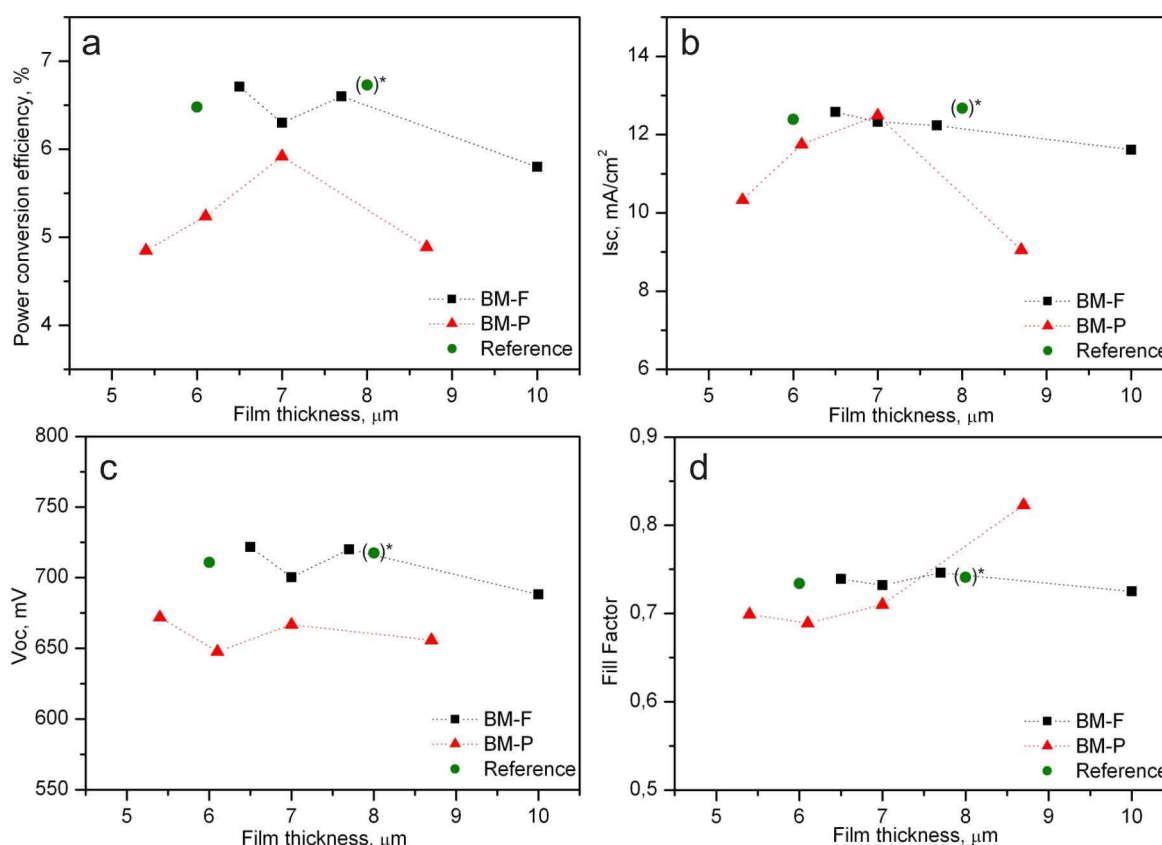


**Figure 5.1.** Thickness dependence of the photovoltaic parameters of DSCs made using “brick and mortar” electrodes with the templates Pluronic F127 (BM-F) and P123 (BM-P), dye D205 and RTIL electrolyte IL-A. (a) Power conversion efficiency. (b) Short circuit current,  $I_{sc}$ . (c) Open circuit potential,  $V_{oc}$ . (d) Fill factor.

\* Double layer reference electrode: 8  $\mu\text{m}$  nanoparticulate layer and a scattering layer of 5  $\mu\text{m}$  on top consisting of 400 nm titania particles.

The action spectrum of the best cell (BM-F, 6.5  $\mu\text{m}$ ) exhibits very high internal photon to current efficiencies reaching about 75 % at the absorption maximum of the dye (Figure 5.2a). However, time-resolved photocurrent measurements of this device indicate that at high levels of illumination the charge transport is slightly hindered, and the steady-state current is reduced (Figure 5.2b, 0.5 and 1.0 sun illumination). This fact is also in agreement with the observation that the short circuit current curve rises towards lower film thicknesses despite the lower dye loading and absorption, because the transport limitations are supposed to be decreasing with lower film thicknesses. It also indicates that the measured efficiency is transport-limited, and by overcoming this restriction a higher performance might be obtainable.

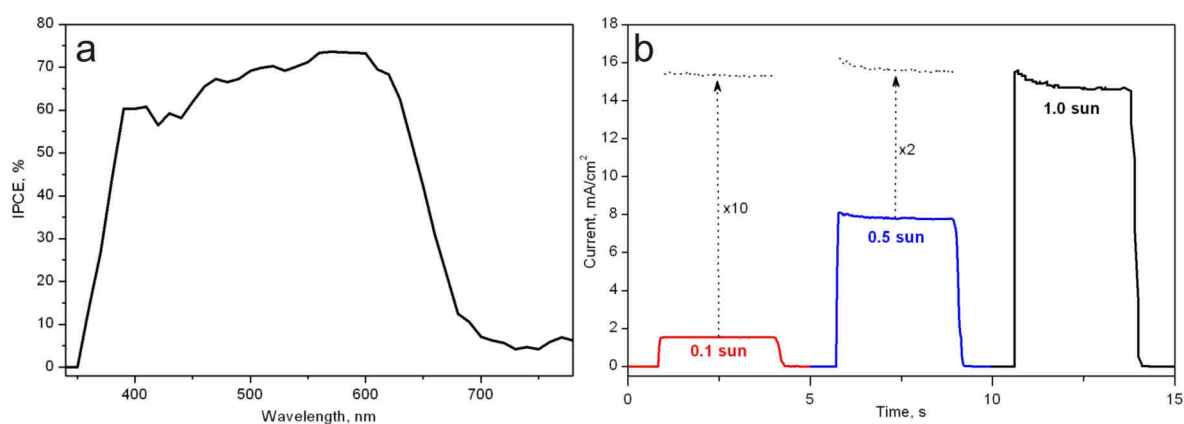


**Figure 5.2.** (a) IPCE spectrum of the best cell BM-F (layer thickness of 6.5  $\mu\text{m}$ , 6.7 % efficiency). (b) Time-resolved photocurrent measurements of the same cell under different levels of illumination. For 0.1 and 0.5 sun photocurrent data: Extrapolation of theoretical current values under full sun illumination.

## 5. High Surface Area “Brick and Mortar“ Films for Ionic Liquid Dye-Sensitized Solar Cells

In this way, these initial results of “brick and mortar” layers in RTIL-based DSCs show the potential of this alternative porous morphology, and further tests with lower film thicknesses could lead to even higher performance levels surpassing that of reference films.

On this account, BM-F films with thicknesses ranging from 2 to 8  $\mu\text{m}$  were prepared, and subjected to testing in DSCs. This time a different organic dye was employed (Y123), because it features a similarly high molar extinction coefficient, but at the same time photovoltaic characteristics superior to D205. In combination with the low viscosity ionic liquid electrolyte **IL-B** maximum efficiencies of 8 % could be achieved in a 8  $\mu\text{m}$  reference film (DL-Ref,  $I_{\text{sc}}$ : 14.3  $\text{mA}/\text{cm}^2$ ,  $V_{\text{oc}}$ : 763 mV, FF: 0.72). The results of the BM-F layers as active electrodes in Y123-sensitized DSCs are summarized in Figure 3. Surprisingly, the thinnest layer of only 2  $\mu\text{m}$  exhibited the highest conversion efficiency reaching 6.2 %, 11.3  $\text{mA}/\text{cm}^2$  short circuit current, and a fill factor of 0.74.

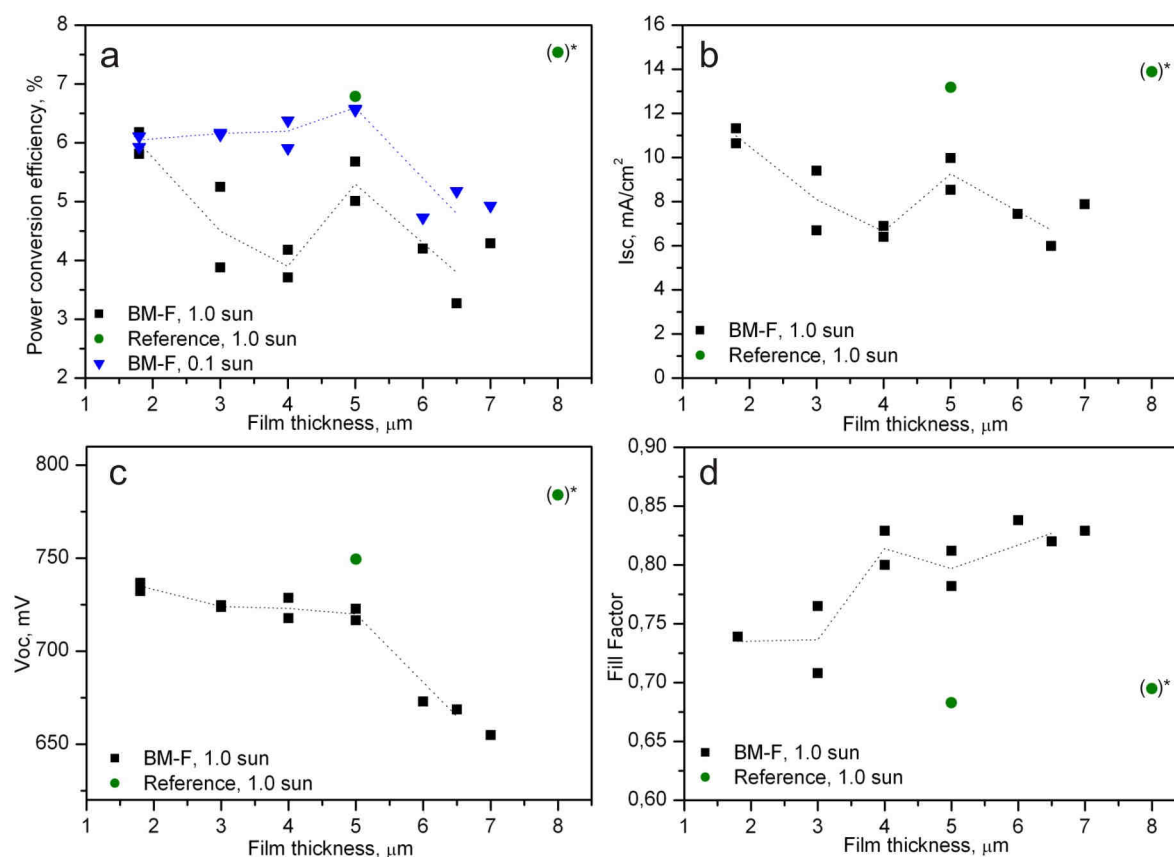


**Figure 5.3.** Thickness dependence of photovoltaic parameters of DSCs made using BM-F electrodes, dye Y123 and RTIL electrolyte IL-B. (a) Power conversion efficiency. Black squares, green circles: Full sun illumination. Blue triangles: Behaviour of BM-F DSCs under 0.1 % sun illumination (data not displayed for the other parameters (b)-(d) for clarity). (b) Short circuit current,  $I_{sc}$ . (c) Open circuit potential,  $V_{oc}$ . (d) Fill factor.

\* Double layer reference electrode: 8  $\mu\text{m}$  nanoparticulate layer and a scattering layer of 5  $\mu\text{m}$  on top consisting of 400 nm titania particles.

The fill factor values (Figure 5.3c) are generally very high, reaching 0.85, and the open circuit potentials (Figure 5.3d) decrease with increasing film thicknesses. Thus, thin BM-F films appear to be rather promising for application in these devices. Already this thinnest sample, however, features a slightly reduced open circuit potential of only 737 mV (compared to the reference electrodes), which could be an indication of some recombination due to transport

## 5. High Surface Area “Brick and Mortar“ Films for Ionic Liquid Dye-Sensitized Solar Cells

limitations. This constriction can be more clearly observed when testing BM-F cells of higher film thickness. Whereas the efficiency under low illumination levels of 0.1 sun ( $1 \text{ mW/cm}^2$ , Figure 5.3a) increases with electrode thickness (mainly because of increasing current values), in full sun the transport is hindered and both efficiency and short circuit current decrease significantly. Furthermore, the existence of a transport problem can be proven by current transient measurements (Figure 5.4). The lowest film thickness of  $1.8 \mu\text{m}$  shows negligible current transients, however, already at  $3 \mu\text{m}$  and more dramatically for thicker films photocurrent decay occurs. This indicates that at first a higher amount of charge carriers are generated, but cannot be extracted from the porous electrode. As a result, the steady-state current is reduced (Figure 5.4, 25 % loss from the initial peak value for the cell BM-F  $3 \mu\text{m}$ , 46 % for BM-F  $4 \mu\text{m}$ , respectively), and consequently the efficiency level for these cells is much lower.

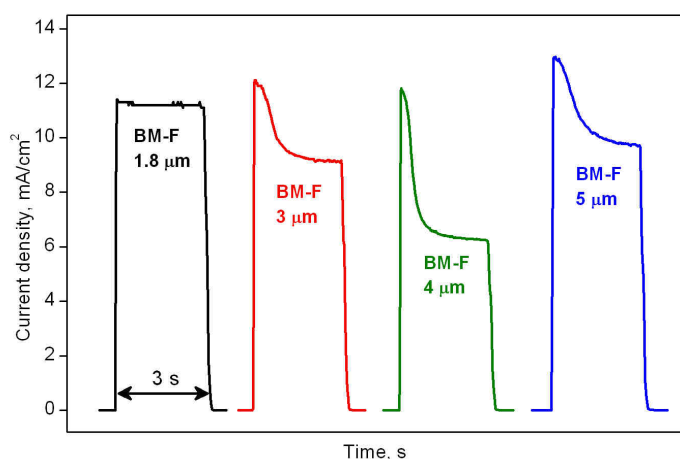


**Figure 5.4.** Current decay measurements of BM-F samples of varying electrode thickness (1.8, 3, 4, and  $5 \mu\text{m}$  thick titania layers) under full sun illumination.

### 5.3 Conclusion and Outlook

In conclusion, the “brick and mortar” approach has proven to be a promising alternative synthesis strategy for the preparation of active electrodes for RTIL-based DSCs. Rather than coatings of TiO<sub>2</sub> have achieved very high efficiency values, but increasing the thickness resulted in deteriorating photovoltaic characteristics. Comparing the experiments made using thin films of BM-F with Y123 and IL-B with the initial results obtained from thicker layers of BM-F with D205 and IL-A, gives rise to several questions: Why do such drastic transport limitations (reduced voltage and current) occur in thinner BM-F films, whereas the restrictions were found to be much less pronounced in thicker BM-F electrodes (despite the similar viscosity of the electrolytes IL-A and IL-B)? What is the statistical significance of these results? What measures can be taken to overcome the transport problems? Can the total performance be improved by achieving higher absorption due to a large surface area in close vicinity to the FTO electrode?

Future experiments are necessary to address these questions. They involve the improvement of the statistical quality of the data, electrochemical characterization of the best cells using impedance spectroscopy, and the testing of even thinner films. Furthermore, it could be tried to increase the pore size by using slightly larger polymers or by adding swelling agents to enlarge the surfactant micelles with the same polymers. Finally, varying the size of the nanocrystalline titania precursor in the “brick and mortar” approach might affect the pore size and the transport properties of the titania walls, and optimizing this parameter could lead to an improvement of the transport characteristics of RTIL-based DSCs.

## 5.4 Experimental Section

Nanoparticles of titanium dioxide were synthesized by a modified non-aqueous sol-gel protocol reported by Niederberger *et al.*<sup>16</sup> A solution of  $\text{TiCl}_4$  (1.5 mL, 13.7 mmol) in toluene (10 mL) was added to benzyl alcohol (30 mL, 291 mmol) under continuous stirring. The reaction mixture was heated to 60 °C and kept there for 20 h. After cooling, the particles were centrifuged for 30 minutes at 50 000 rcf. The as-synthesized particles contain about 55 wt% of titania according to thermogravimetric analysis, and were used without further purification. Since in previous publications, coating solutions with a content of 70 wt %  $\text{TiO}_2$  nanoparticles and 30 wt % sol-gel titania precursors (based on Ti-content) proved best for photovoltaic applications, this ratio was employed for all samples in this chapter. Solutions of Pluronic P123 (0.2 g, 0.04 mmol, **BM-P**) or F127 (0.3 g, 0.02 mmol, **BM-F**) in tetrahydrofurane (4 mL) were added to titania nanoparticles (0.4 g of crude nanoparticles, 2.2 mmol of  $\text{TiO}_2$ ), subjected to ultrasonic treatment for 20 minutes and stirred until a homogeneous dispersion formed. Subsequently, a prehydrolyzed titania sol-gel solution (0.4 mL, corresponding to 1.1 mmol  $\text{TiO}_2$ ) was added (sol-gel solution, see below), and stirred for several minutes. The final solutions were of a yellow to orange color, and transparent or translucent. The sol-gel solution was obtained by slowly adding hydrochloric acid (37 %, 5.1 mL, 62.1 mmol) to tetraethyl orthotitanate (7.2 mL, 34.3 mmol) under continuous stirring. Mesoporous titania films on FTO-coated glass (TEC-7 from Pilkington) were prepared by a spin-coating process (150 - 180  $\mu\text{L}$  per 1  $\text{cm}^2$  substrate area, 800 rpm for 30 seconds) and calcined at 450 °C (with a ramp of 0.6 °C  $\text{min}^{-1}$ ) for 30 minutes.

Scanning electron microscopy (SEM) was performed on a JEOL JSM-6500F scanning electron microscope equipped with a field emission gun, at 4 kV. The film thickness was measured by profilometry (Dektak). Nitrogen sorption measurements were performed with a

## 5. High Surface Area “Brick and Mortar“ Films for Ionic Liquid Dye-Sensitized Solar Cells

---

NOVA 4000e (Quantachrome Instruments) at 77 K. To obtain sufficient amounts of porous material for N<sub>2</sub> sorption, 20 one-layer films of about 1 μm thickness were scratched off the substrate after calcination and measured as powders. Pore size distributions were calculated using a NLDFT equilibrium model of N<sub>2</sub> on silica assuming cylindrical pores.

For photovoltaic measurements, the mesoporous TiO<sub>2</sub> films on FTO-coated glass substrates were heated at 500 °C for 30 min, then cooled to ca. 80 °C and immersed into the dye solution at room temperature, and kept there for 16 h. Dye solutions of the dye Y123 or D205 (0.3 mM in 1:1 volume ratio of acetonitrile/*tert*-butanol) were used to sensitize the photoanodes. Dye-coated mesoporous TiO<sub>2</sub> films were assembled and sealed with a transparent hot-melt 25 μm thick surlyn ring to the counter electrodes (Pt on FTO glass, chemical deposition from 0.01 M hexachloroplatinic acid in ethanol heated at 400 °C for 15 min). The active cell area in all samples was about 0.185 cm<sup>2</sup>. The electrolyte was injected into the inner electrode space by vacuum back-filling from the counter electrode side through a pre-drilled hole, and then the hole was sealed with a surlyn sheet and a thin glass cover slide by heating to 120 °C. The electrolyte mixtures IL-A and IL-B contain 0.5 M NMBI (N-methylbenzimidazole), 0.2 M iodine, 0.1 M GuNCS (guanidinium thiocyanate), in RTIL mixtures of either PMII/EMITCB (**IL-A**, 65:35 volume ratio, PMII: 1-propyl-3-methylimidazolium iodide, EMITCB: 1-ethyl-3-methyl) or DMII/EMII/EMITCB (**IL-B**, 12:12:16 molar ratio, DMII: 1,3-dimethylimidazolium iodide, EMII: 1-ethyl-3-methylimidazolium iodide). The device assembly, the characterization of current density-voltage, time-resolved photocurrent and incident photon to current conversion efficiency (IPCE) of the DSCs were performed by M. Marszalek in the group of Dr. S. M. Zakeeruddin, and Prof. Dr. M. Grätzel at the EPF Lausanne, Switzerland, are described in detail elsewhere.<sup>17</sup>

## 5.5 References

- (1) O'Regan, B.; Gratzel, M. *Nature* **1991**, *353*, 737-740.
- (2) Nazeeruddin, M. K.; De Angelis, F.; Fantacci, S.; Selloni, A.; Viscardi, G.; Liska, P.; Ito, S.; Takeru, B.; Graetzel, M. *J. Am. Chem. Soc.* **2005**, *127*, 16835-16847.
- (3) Nazeeruddin, M. K.; Péchy, P.; Renouard, T.; Zakeeruddin, S. M.; Humphry-Baker, R.; Comte, P.; Liska, P.; Cevey, L.; Costa, E.; Shklover, V.; Spiccia, L.; Deacon, G. B.; Bignozzi, C. A.; Grätzel, M. *J. Am. Chem. Soc.* **2001**, *123*, 1613-1624.
- (4) Bach, U.; Lupo, D.; Comte, P.; Moser, J. E.; Weissortel, F.; Salbeck, J.; Spreitzer, H.; Gratzel, M. *Nature* **1998**, *395*, 583-585.
- (5) Bai, Y.; Cao, Y.; Zhang, J.; Wang, M.; Li, R.; Wang, P.; Zakeeruddin, S. M.; Gratzel, M. *Nat. Mater.* **2008**, *7*, 626-630.
- (6) Ito, S.; Zakeeruddin, S. M.; Comte, P.; Liska, P.; Kuang, D.; Gratzel, M. *Nat Photon* **2008**, *2*, 693-698.
- (7) Shi, D.; Pootrakulchote, N.; Li, R.; Guo, J.; Wang, Y.; Zakeeruddin, S. M.; Graetzel, M.; Wang, P. *J. Phys. Chem. C* **2008**, *112*, 17046-17050.
- (8) Ito, S.; Zakeeruddin, S.; Humphry-Baker, R.; Liska, P.; Charvet, R.; Comte, P.; Nazeeruddin, M.; Péchy, P.; Takata, M.; Miura, H.; Uchida, S.; Grätzel, M. *Adv. Mater.* **2006**, *18*, 1202-1205.
- (9) Kuang, D.; Uchida, S.; Humphry-Baker, R.; Zakeeruddin, S. M.; Grätzel, M. *Angew. Chem. Int. Ed.* **2008**, *47*, 1923-1927.
- (10) Fabregat-Santiago, F.; Bisquert, J.; Cevey, L.; Chen, P.; Wang, M.; Zakeeruddin, S. M.; Grätzel, M. *J. Am. Chem. Soc.* **2008**, *131*, 558-562.
- (11) Snaith, H. J.; Humphry-Baker, R.; Chen, P.; Cesar, I.; Zakeeruddin, S. M.; Grätzel, M. *Nanotechnology* **2008**, *19*, 424003.

## 5. High Surface Area “Brick and Mortar“ Films for Ionic Liquid Dye-Sensitized Solar Cells

---

- (12) Zakeeruddin, S. M.; Grätzel, M. *Adv. Funct. Mater.* **2009**, *19*, 2187-2202.
- (13) Szeifert, J. M.; Fattakhova-Rohlfing, D.; Georgiadou, D.; Kalousek, V.; Rathouský, J.; Kuang, D.; Wenger, S.; Zakeeruddin, S. M.; Gratzel, M.; Bein, T. *Chem. Mater.* **2009**, *21*, 1260-1265.
- (14) Fattakhova-Rohlfing, D.; Szeifert, J. M.; Yu, Q.; Kalousek, V.; Rathouský, J.; Bein, T. *Chem. Mater.* **2009**, *21*, 2410-2417.
- (15) Kuang, D.; Klein, C.; Zhang, Z.; Ito, S.; Moser, J.-E.; Zakeeruddin, S. M.; Grätzel, M. *Small* **2007**, *3*, 2094-2102.
- (16) Niederberger, M.; Bartl, M. H.; Stucky, G. D. *Chem. Mater.* **2002**, *14*, 4364-4370.
- (17) Kuang, D.; Klein, C.; Ito, S.; Moser, J. E.; Humphry-Baker, R.; Evans, N.; Duriaux, F.; Grätzel, C.; Zakeeruddin, S. M.; Grätzel, M. *Adv. Mater.* **2007**, *19*, 1133-1137.

## **6. Ultrasmall Titania Nanocrystals and their Direct Assembly into Mesoporous Structures showing fast Lithium Insertion**

*This chapter is based on the following publication:*

Johann M. Szeifert, Johann M. Feckl, Dina Fattakhova-Rohlfing, Yujing Liu, Vit Kalousek, Jiri Rathouský, Thomas Bein, *Journal of the American Chemical Society* **2010**, *132*, 12605-12611.

### **6.1 Introduction**

Mesoporous crystalline metal oxide layers have been in the focus of extensive research activities in the last decade.<sup>1-5</sup> The crystallinity of a metal oxide scaffold in combination with a high interfacial surface area and a periodic ordering on the nanoscale are of special interest in applications involving interfacial charge transfer and bulk charge transport processes such as solar cells,<sup>6-8</sup> sensors<sup>9</sup> and energy storage devices.<sup>10,11</sup> The basic approach to manufacturing such layers is the self-assembly of metal oxide building units assisted by a suitable structure-directing agent.<sup>1,12</sup> The critical point here is the amorphous character of the common metal oxide precursors, which usually emanate from sol-gel synthesis and require crystallization at elevated temperatures, often resulting in the collapse of the mesostructure.<sup>13</sup> This limitation motivates the search for largely crystalline building units that could convert to the final crystalline periodic scaffolds at mild conditions and low temperatures.<sup>14</sup> To make such an approach successful, the building blocks need to be extremely small in order to be compatible with the size of the structure-directing agents, and they should be dispersible in the required

solvents without agglomeration.<sup>15</sup> Hydrothermal synthesis methods are often unsuitable for this purpose due to the fast reaction rates, resulting in highly agglomerated nanoparticles with a wide distribution of particle size and shape. On the contrary, non-aqueous solvothermal routes usually provide much better control over the size, crystallinity and agglomeration behavior of the nanoparticles.<sup>16</sup> Among the large number of organic solvents examined in this context, benzyl alcohol has received much attention, as it enables the synthesis of a large variety of metal oxide nanoparticles with high crystallinity, a low degree of agglomeration and tunable particle size.<sup>17,18</sup> However, it is difficult to prepare extremely small particles with this approach, and surface-modifying ligands are needed for stabilization. Another issue with the benzyl alcohol synthesis is the presence of benzyl alcoholate residues on the particles' surface, which influence physical and chemical properties of the interface and can be removed only by harsh oxidative treatment or at temperatures above 450 °C.<sup>19,20</sup> An accessible and ligand-free surface is, however, of great importance for charge transfer processes across the interfaces. This issue can be solved when non-aromatic solvents are used as reaction medium.<sup>21</sup> Thus, polyols enable the preparation of monodisperse crystalline nanoparticles with good interface properties, however, again it is difficult to prepare very small nanoparticles with this approach.<sup>22,23</sup> Aliphatic alcohols usually require higher reaction temperatures and typically do not provide homodispersed non-agglomerated nanocrystals.<sup>24-27</sup> Crystalline nanoparticles can also be prepared in other non-aqueous solvents such as ketones or aldehydes.<sup>28</sup>

Aiming to prepare metal oxide nanoparticles of small size, enhanced crystallinity and good dispersibility without the need of additional stabilizing ligands, we explored *tert*-butanol as a novel reaction medium. Similar to other small aliphatic alcohols, this solvent can be easily removed due to its low boiling point of 83 °C. The unique reactivity of *tert*-butanol resulting from a strong inductive stabilization of an intermediate carbocation is supposed to result in a different mechanism of particle formation compared to that of other aliphatic alcohols, thus

leading to particles with different properties and morphology.<sup>29</sup> As a metal oxide system we selected titanium dioxide, which is of great interest for applications in solar cells, catalysis and energy storage.<sup>30</sup>

Here we describe the use of *tert*-butanol as a new solvent and reactant in a non-aqueous sol-gel protocol leading to highly dispersible and nanocrystalline titania particles without the need for additional ligands or surfactants. Ultrasmall anatase nanoparticles of high crystallinity were obtained by a special microwave-based heating procedure that allows the crystal formation within several minutes. Additionally, this new approach permits the direct application of the as-synthesized particles in combination with a commercial polymer template for the preparation of mesoporous titanium dioxide films without the need for particle separation or chemical processing. The crystalline nature of the films and their use as electrode material for Li-ion batteries is shown by electrochemical lithium insertion. Here, the high surface to bulk ratio of the nanocrystals, and the easily accessible mesoporous structures with extremely thin walls lead to a drastic acceleration of the Li insertion and high maximum capacitance. Our synthetic strategy leading to highly dispersible and crystalline nanoparticles represents a versatile alternative for the preparation of periodically ordered mesostructures, and should be applicable to other metal oxides and mixed oxides.

The following experiments have been performed by Johann M. Feckl and Johann M. Szeifert in the group of Prof. Dr. Thomas Bein. Vit Kalousek and Dr. Jiri Rathouský contributed by measuring and evaluating krypton sorption isotherms.

### 6.2 Results and Discussion

In a typical procedure for the preparation of titanium dioxide nanoparticles, a solution of titanium tetrachloride in toluene was added to water-free *tert*-butanol at 25 °C and subjected

to different temperature treatments. In a conventional synthesis, the reaction mixture was put into an oven at 60 °C for 24 hours until it turned into a colourless but turbid and highly viscous suspension (assigned further as T60). After cooling to room temperature, the nanoparticles were separated by centrifugation for further characterization. The particles were highly dispersible in ethanol, and wide-angle X-ray scattering (WAXS) of the material showed the formation of partially crystalline TiO<sub>2</sub> anatase particles of about 4 nm in size and the presence of a relatively large amount of amorphous phase (Figure 6.1a).

In an attempt to shorten the reaction time, microwave-based heating was examined for this reaction mixture, as it had been reported for other systems to significantly accelerate certain reactions.<sup>31</sup> After only one hour at 50 °C under microwave irradiation, the solution turned colourless and transparent, and formation of anatase particles of only 3.1 nm was observed by dynamic light scattering (DLS) and WAXS (Sample MW50, Figure 6.1a). The broad background in the WAXS pattern still indicates the presence of amorphous material, but at much lower relative ratios than for samples prepared by conventional heating. Microwave syntheses at higher temperatures led to a significant increase in crystallinity, but also to larger particle sizes and precipitation of the particles from the solution, thus decreasing their dispersibility.

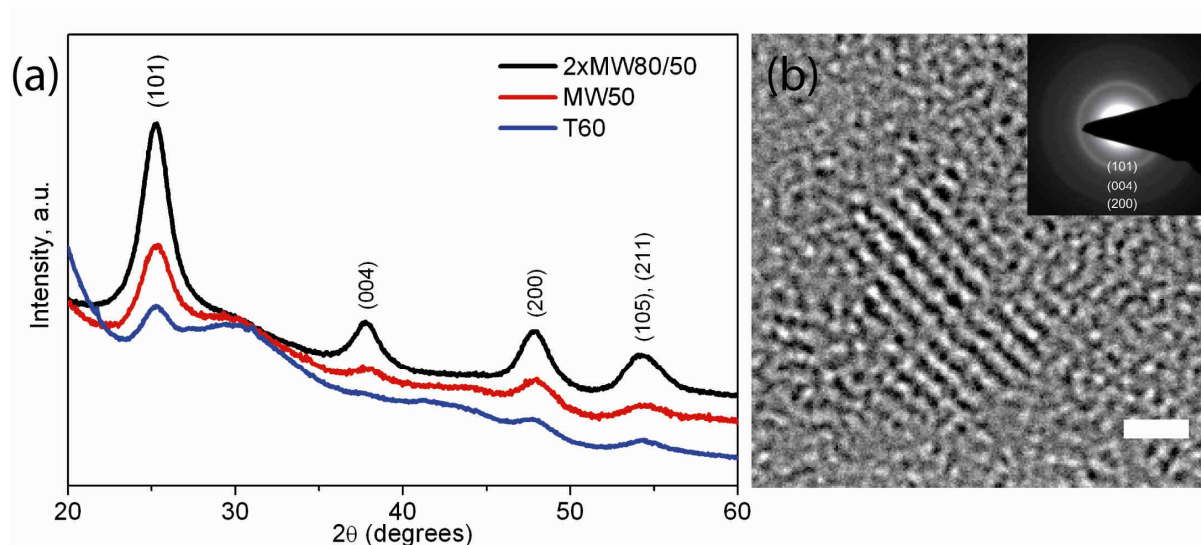


**Figure 6.1.** Crystallinity and morphology of the  $\text{TiO}_2$  nanoparticles obtained using *tert*-BuOH as the reaction medium after different synthesis conditions: WAXS patterns of samples T60 (blue), MW50 (red) and 2xMW80/50 (black) (a); high resolution TEM image (HRTEM) and SAED pattern (inset) of the MW50 particles (b). The scale bar corresponds to a distance of 1.0 nm.

Using microwave irradiation, we aimed to maximize the yield of crystalline material in the product and simultaneously to prevent further particle growth and agglomeration. For this purpose, we combined a fast ramp to a higher temperature such as 80 °C for an initial burst of nucleation, directly followed by a cooling period and a longer dwell time at lower temperatures (50 °C) for subsequent particle growth (sample MW80/50). This procedure leads to the formation of very small and crystalline particles without visible agglomeration, as demonstrated by the DLS data of the particles in solution (Figure 6.3), and the transmission electron microscopy (TEM) images of dried particles on a carbon-coated copper grid (Figure 6.1b). Although DLS data show the formation of small particles of less than 3 nm in size, the yellow color of the reaction solution still indicates the presence of titanium-chloro complexes and thus incompletely reacted molecular precursors. It was found that after two cycles of this heat treatment a colourless and slightly turbid solution can be obtained (sample 2xMW80/50),

## 6. Mesoporous Titania Structures from Ultrasmall Nanoparticles

---

from which nanoscale titanium dioxide could be flocculated using n-heptane. TGA data of this sample show weight loss to above 400 °C, suggesting the presence of organic material on the surface of the nanoparticles (Figure 6.2). The WAXS pattern of particles made this way shows much reduced amorphous phase, and the peak broadening corresponds to nanocrystals of 3.8 nm in size (Figure 6.1a). This is in good agreement with the HRTEM micrographs (Figure 6.1b) that show particles of the same size exhibiting lattice fringes and the typical d-spacings and electron diffraction pattern of anatase.

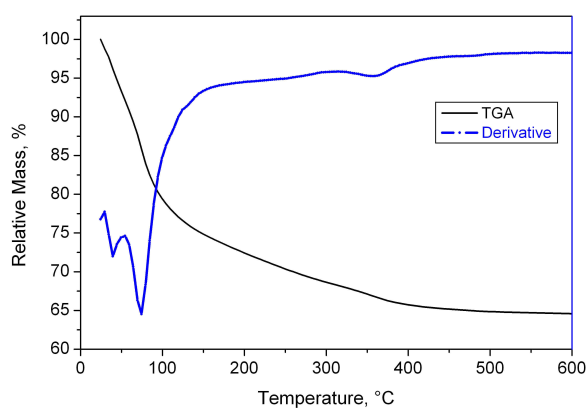


**Figure 6.2.** TGA of TiO<sub>2</sub> nanoparticles from a *tert*-BuOH synthesis (sample 2xMW80/50, prior to measurement powder was dried at 60 °C over night). The initial weight losses below 100 °C correspond to the evaporation of remaining solvent molecules.

The dispersibility of the particles in *tert*-butanol and ethanol was proven by DLS, showing monodisperse particles with hydrodynamic radii of about 3 to 4 nm (Figure 6.3).

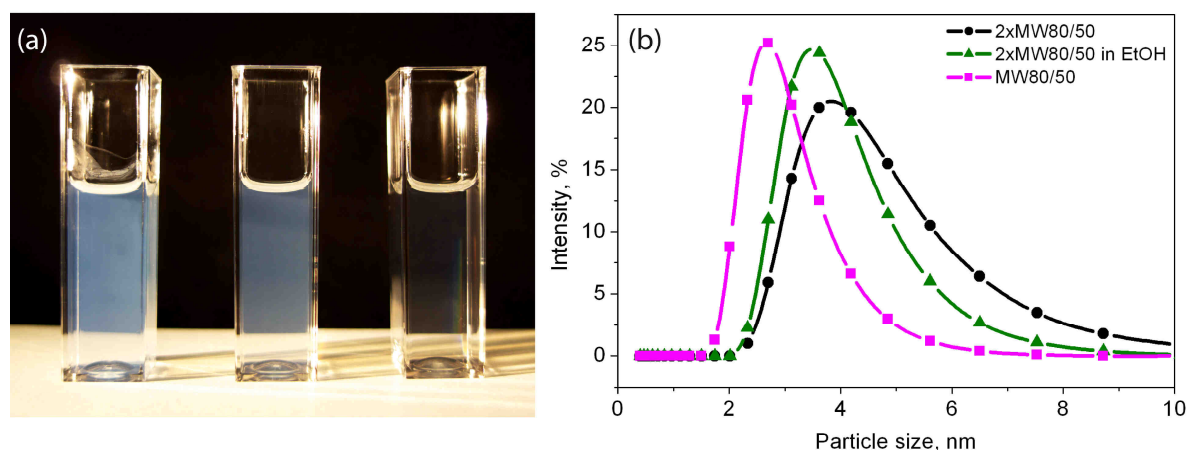


**Figure 6.3.** (a) Picture of 2xMW80/50 particle solutions: in *tert*-butanol/toluene (3:1 volume ratio, 3.3 wt% TiO<sub>2</sub>, left), after flocculation with heptane, centrifugation and redispersion in ethanol (3.3 wt%, middle), and further diluted in ethanol (0.7 wt%, right). (b) DLS data of dispersions of particles prepared by microwave treatment in *t*BuOH (magenta: MW80/50, black: 2xMW80/50), and of 2xMW80/50 in EtOH (green).

The excellent dispersibility of the *tert*-butanol-based nanoparticles in both ethanol and *tert*-butanol can be exploited for the preparation of mesoporous films using the as-synthesized nanocrystals as metal oxide building blocks. The special advantages of *tert*-butanol are, first, that due to its low boiling point of only 83 °C, unlike benzyl alcohol, it is a suitably volatile solvent for evaporation-induced self-assembly (EISA) in thin films. Second, it is a good solvent for the polymers of the Pluronic family, which are commonly used as templates for mesostructure formation.<sup>3,30</sup> Therefore, the reaction mixture containing the nanoparticles can be used directly, and the effort needed for the additional steps of particle separation and redispersion in other solvents suitable for the EISA process can be avoided. Using this direct coating technique, mesoporous titanium dioxide films were produced from solutions containing Pluronic P123 in *tert*-butanol that were treated with either one cycle of microwave irradiation, or two microwave cycles and thus containing fully crystalline titania particles. For

comparison, films were also prepared without any heat treatment of the coating solution from a sol-gel precursor in *tert*-butanol (sample tBuOH-SG).

A TEM investigation of very thin films was performed to get insights into how the particles arrange around the pores forming the network. The contrast variations in the walls around the mesopores in Figure 6.4b and 6.4c prove that for both microwave-heated samples, the pore walls consist of many small particles, whereas for the untreated solution, the walls surrounding the pores show uniform density which indicates the presence of homogeneous but amorphous titanium dioxide (Figure 6.4a). The tBuOH-SG sample also exhibits a worm-like pore structure, which only converts to an open porous phase at higher temperatures as observed by SEM after calcination at 300 °C (Figure 6.4d).

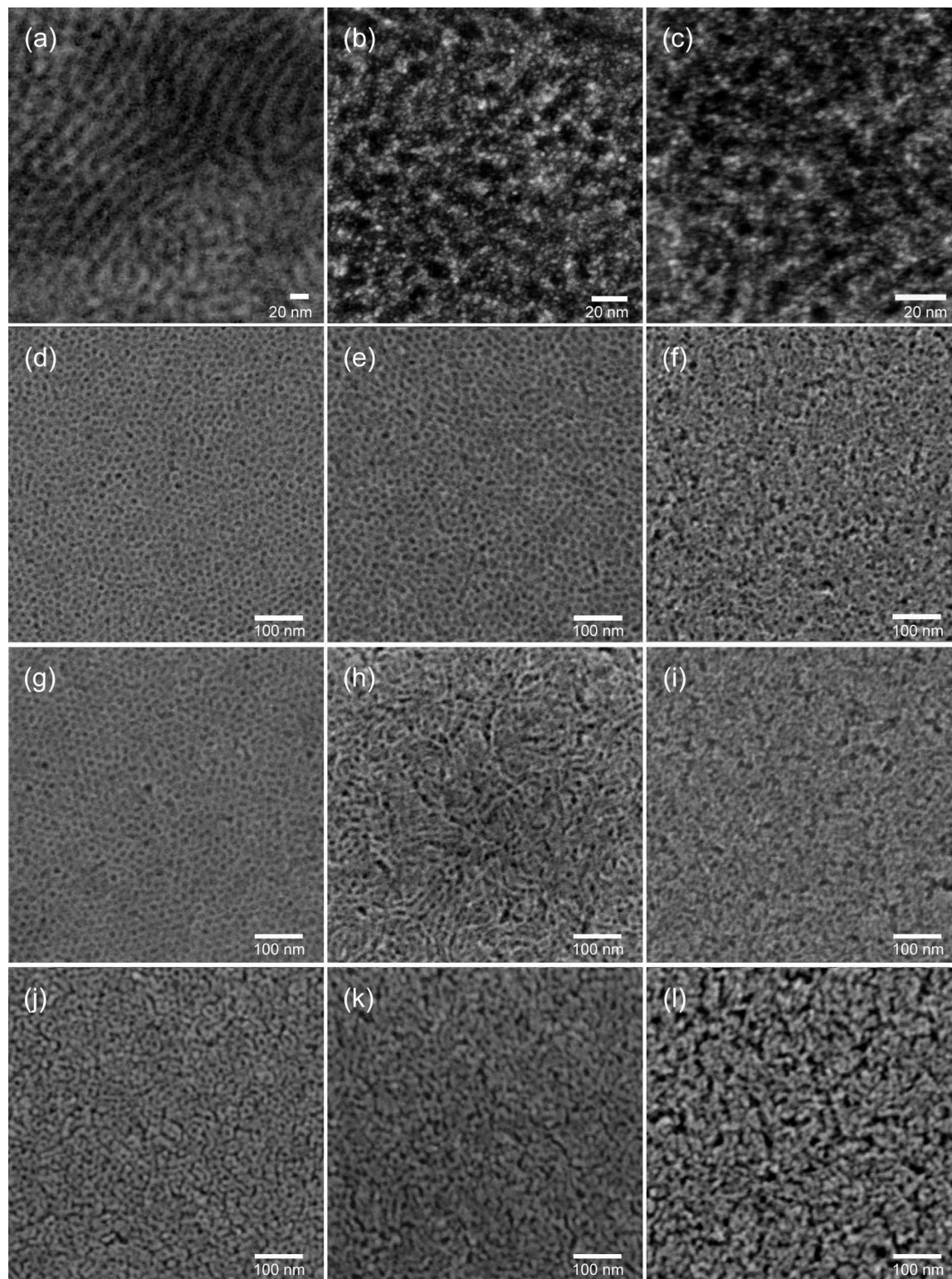


**Figure 6.4.** Mesoporous titanium dioxide films assembled from different building blocks: *tert*-butanol titania sol-gel (tBuOH-SG) (a, d), MW80/50 (b, e) and 2xMW80/50 (c, f). The first row (a-c) shows STEM-HAADF images of the films directly after coating, and the

second row (d-f) SEM images (top view) of the same films after calcination at 300 °C, 450 °C (g-i), and 600 °C (j-l).

All of the layers prepared from different types of reaction mixtures and calcined at 300 °C show mesoporous structures with a regular, wormlike pore system. The reference sample prepared from non-treated sol-gel titania precursor (Figure 6.4d) exhibits the highest degree of periodicity, the biggest size of periodic domains and the smallest mesostructure spacing of 14 nm. The MW80/50 particle solution results in a structure with slightly smaller periodic domains and a larger pore spacing of about 20 nm (Figure 6.4e), while the use of a solution with the more crystalline 2xMW80/50 particles leads to a much less periodic structure on the film surface (Figure 6.4f). Still, pores of the same size that are open to the surface can be observed.

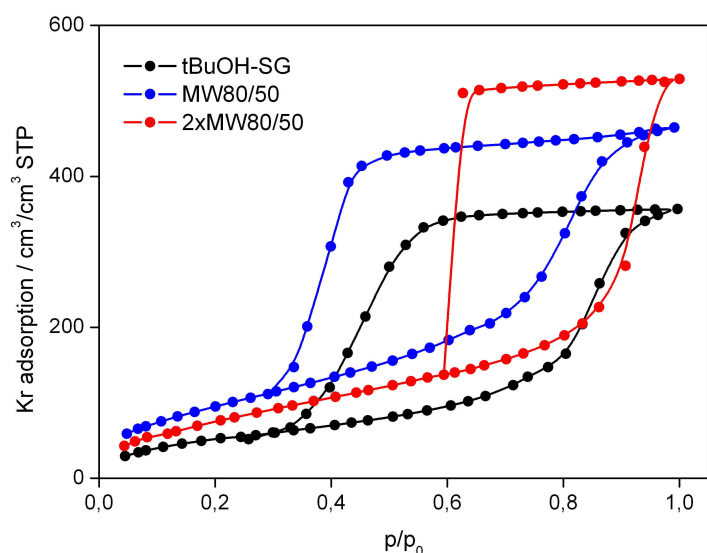


**Figure 6.5.** Isotherms of Krypton adsorption on the titania layers assembled from different building blocks: tBuOH-SG (black), MW80/50 (blue), 2xMW80/50 (red). The BET surface areas of these films are 116 m<sup>2</sup>/g (tBuOH-SG), 294 m<sup>2</sup>/g (MW80/50), and 297 m<sup>2</sup>/g (2xMW80/50). The films were calcined at 300 °C.

The mesoporous nature of the pore system after the template combustion was also investigated using Kr adsorption (Figure 6.5 and 6.6). The isotherms of all layers exhibit the typical shape of mesoporous materials with a large surface area, high pore volume and the open and accessible character of porosity. The highest surface area of about 300 m<sup>2</sup>/g is exhibited by the layers assembled from the MW80/50 and 2xMW80/50 particles. The use of more crystalline 2xMW80/50 particles leads to mesoporous layers with increased pore size and pore volume.

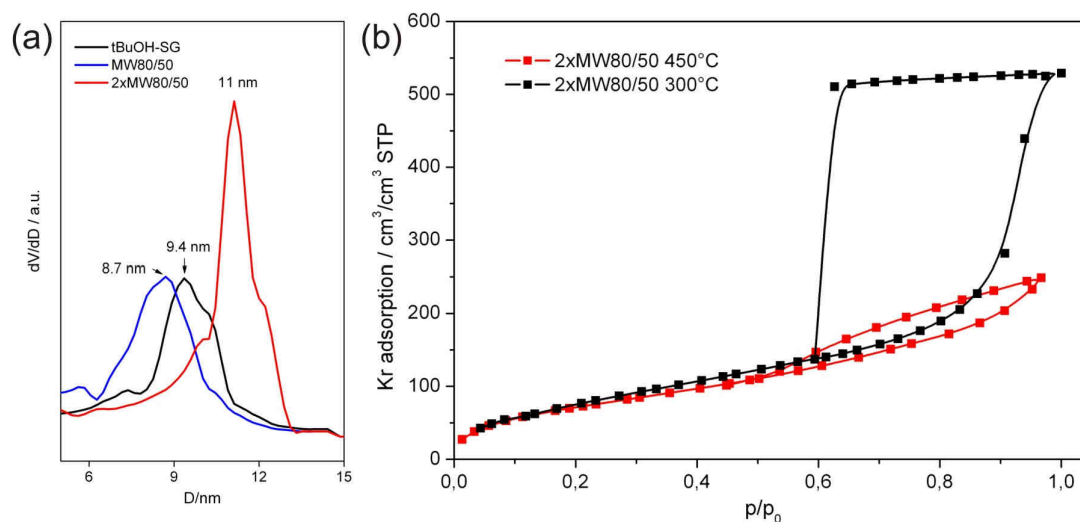


**Figure 6.6.** Textural properties from Kr sorption of samples after calcination at different temperatures. (a): Pore diameters for samples after calcination at 300 °C for samples tBuOH-SG, MW80/50, and 2xMW80/50 (sample names given in the figure). (b): Comparison of isotherms of sample 2xMW80/50 after calcination at 300 °C and 450 °C; these data show the preservation of the surface area (228 m<sup>2</sup>/g for the sample 2xMW80/50 after calcination at 450 °C) and a change in the textural porosity upon heating to the higher temperature.

The periodicity of the mesostructure after treatment at high temperatures was confirmed by the existence of reflections in small angle X-ray scattering (SAXS, Figure 6.7) from samples

## 6. Mesoporous Titania Structures from Ultrasmall Nanoparticles

calcined at different temperatures. At room temperature, the samples exhibited the typical reflection of Pluronic P123-templated titania corresponding to d-spacings of 10 to 12 nm. After calcination at 450 °C, this peak was shifted to higher angles and gradually disappeared at higher temperatures due to rather strong contraction of the mesostructure in the direction perpendicular to the substrate.<sup>32,33</sup> At the same time, other reflections became visible close to the lower detection limit of the SAXS at 0.6 to 0.7 ° 2 $\theta$  and remained at the same position upon further heating. This proves the existence of periodically repeating structural features after heating up to 600 °C, and indicates structural changes upon thermal treatment.

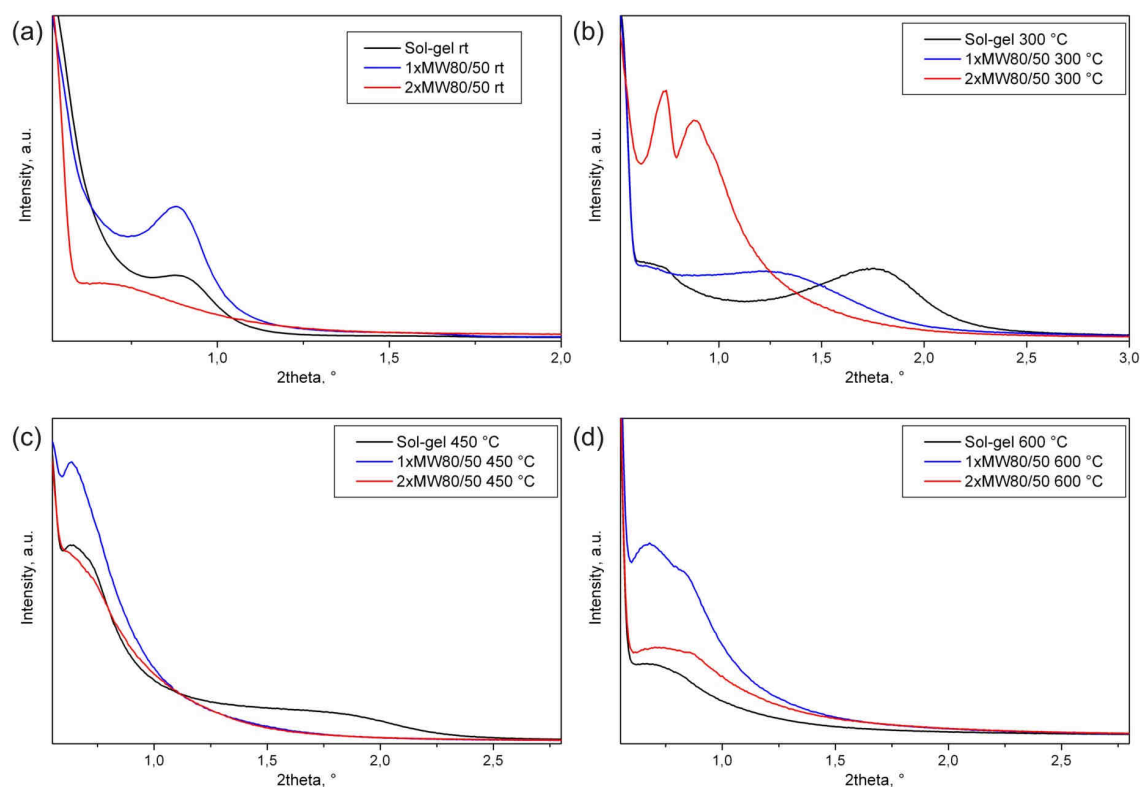


**Figure 6.7.** SAXS patterns of films before and after calcination at different temperatures (a): room temperature, (b): 300 °C, (c): 450 °C, (d): 600 °C. Black: *t*BuOH-SG, blue: MW80/50, red: 2xMW80/50.

The crystallization behavior upon heating was also monitored by evaluating the peak broadening in wide angle X-ray scattering (WAXS). In the sol-gel sample (*t*BuOH-SG), first

traces of anatase nanoparticles of about 4.7 nm could be detected only after heating to 450 °C (Figure 6.8).<sup>33,34</sup> At even higher temperatures, the nanocrystals in the *tert*-butanol sol-gel sample grow rapidly and almost triple their size when heated to 600 °C. The microwave-treated nanoparticulate precursor, however, exhibits a more steady, controllable crystallization, and the particles of originally 4 nm grow to only about 6 nm at 300 °C, to 8 nm at 500 °C, and finally to 11 to 13 nm at 600 °C. Summarizing, at 450 °C the nanoparticulate systems show both crystallinity and templated mesoporosity, while the sol-gel derived systems show only low crystallinity with templated mesoporosity. On heating to 600 °C, both systems have lost the templated mesoporosity due to further crystal growth.

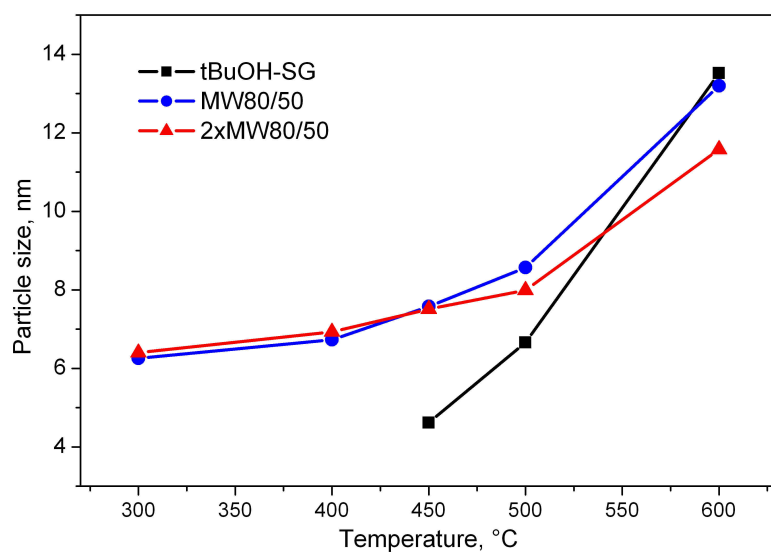


**Figure 6.8.** Development of crystal size from broadening of the (101) anatase reflection in wide-angle X-ray scattering upon heating. Black: tBuOH-SG, blue: MW80/50, red: 2xMW80/50 (film data below 300 °C were not recorded due to their low scattering intensity).

Electrochemical lithium insertion was performed for the determination of the relative amounts of crystalline and amorphous phase in the films assembled from different precursors, and to examine their applicability as electrode materials for Li-ion batteries.<sup>35,36</sup> The layers were

## 6. Mesoporous Titania Structures from Ultrasmall Nanoparticles

calcined at 300 °C in order to combust the template and to open the pores, and at 450 °C to induce further crystallization of the networks. Cyclic voltammograms of the films prepared from the untreated solution exhibit only the broad insertion/extraction features of the amorphous phase even after calcination at 450 °C (Figure 6.9). The films prepared from the MW80/50 nanoparticles show the insertion behavior of an amorphous titania phase after calcination at 300 °C and, after calcination at 450 °C, clearly feature the characteristic quasireversible insertion/extraction anatase-based peaks around 1.85 V vs. Li. Finally, the films assembled from 2xMW80/50 particles show the presence of anatase already after calcination at 300 °C. The amount of crystalline anatase phase doubles after heating the films at 450 °C, and only small traces of TiO<sub>2</sub>(B) (around 1.6 V) are observable.

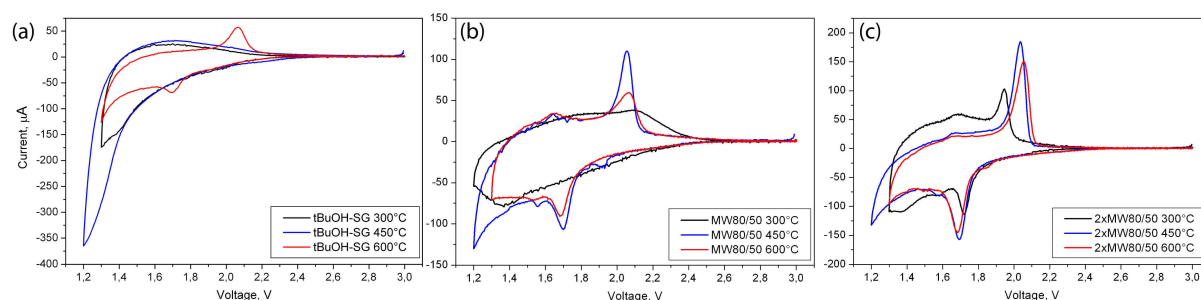


**Figure 6.9.** Cyclic voltammograms (scan rate 0.5 mV/s) from Li insertion of the mesoporous TiO<sub>2</sub> films after calcination at different temperatures: tBuOH-SG (a), MW80/50 (b), and 2xMW80/50 (c). Black: 300 °C; blue: 450 °C; red: 600 °C.

The above evidence shows that the microwave irradiation of the titanium tetrachloride solution in *tert*-butanol leads to the formation of ultrasmall crystalline nanoparticulate seeds, which after film preparation can induce crystallization of the surrounding network at elevated temperatures by lowering the activation energy.

The films from solutions employing two cycles of the burst of nucleation profile (sample 2xMW80/50) show a capacity for lithium insertion at 1.7 V (end of the first plateau

## 6. Mesoporous Titania Structures from Ultrasmall Nanoparticles

---

corresponding to insertion into anatase) of 143 mAh/g after calcination at 450 °C, which is a high level for this temperature considering the maximum theoretical Li insertion capacity of anatase of 167 mAh/g.<sup>35</sup> Furthermore, the material shows good cycling stability, which is comparable to other recently reported nanostructured titania systems (Figure 6.10).<sup>36,37</sup>

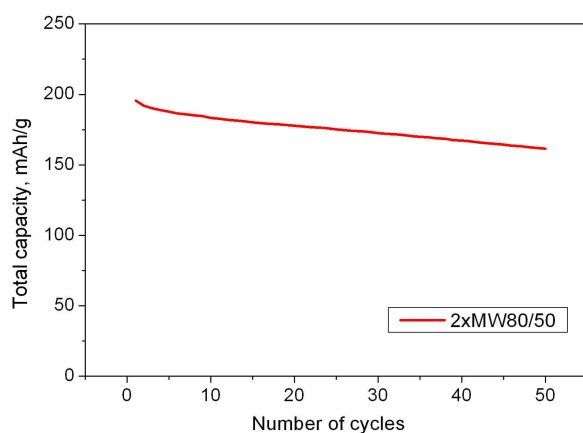


**Figure 6.10.** Total discharge capacity of the sample 2xMW80/50 after calcination at 450 °C upon multiple lithium insertion cycles in the potential range from 3.0 to 1.3 V vs. Li (scan rate 10 mV/s).

Besides the high capacitance, the nanocrystalline and mesoporous nature of the films also leads to a significant increase in the insertion/extraction rate of Li ions (Figure 6.11, and Figure 6.12). During a charging time of only 150 s, the microwave treated samples reach over 80 % of their maximum insertion capacity, whereas reference films assembled from 20 nm anatase particles take approximately 10 times longer to reach that level. Similar accelerated kinetics were also described for films assembled from crystalline anatase nanoparticles<sup>36,38</sup> and were attributed to a significant contribution of pseudocapacitive processes in the total electrochemical Li insertion due to the large surface area of the nanoparticles. The small crystal size comparable to a maximum penetration depth for Li ions, the good connectivity of the crystals providing a continuous pathway for the ion/electron diffusion in the titania

## 6. Mesoporous Titania Structures from Ultrasmall Nanoparticles

scaffold, and the excellent accessibility of the pore system for the Li ions in the electrolyte also contribute to fast insertion kinetics of the prepared films.<sup>38</sup> The high insertion capacity and fast insertion kinetics in combination with a fast and facile preparation procedure make the described mesoporous films promising electrode materials for thin layer Li ion batteries and supercapacitors.

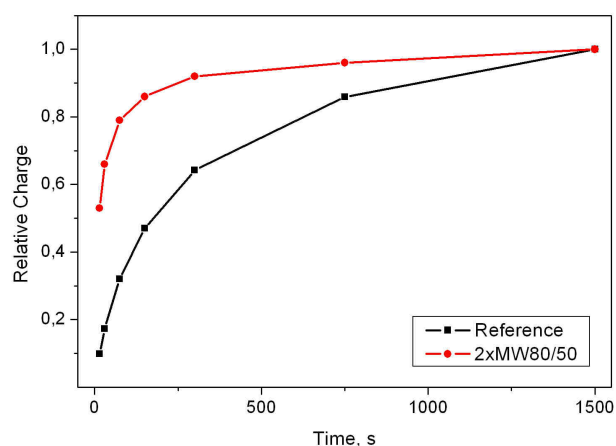


**Figure 6.11.** Comparison of charging rates for reaching maximum Li insertion into  $\text{TiO}_2$  films assembled from different titania precursors. The relative charge was calculated as the ratio of measured charge over the maximum charge at the lowest scan rate. Black: Standard reference film made from 20 nm anatase particles, red: 2xMW80/50.

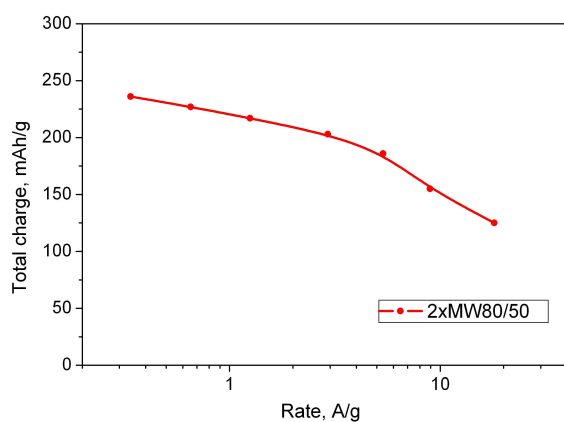


**Figure 6.12.** Rate dependence of the total charge in Li insertion experiments of the sample 2xMW80/50 after calcination at 450 °C in the potential range from 3.0 to 1.3 V vs. Li.

### 6.3 Conclusion

Non-aqueous sol-gel procedures using benzyl alcohol have been successfully employed for the preparation of crystalline metal oxide nanoparticles. However, for titania nanoparticles obtained with this method the dispersibility in organic solvents is limited and very small particle sizes are not accessible. Here we show that the combination of the new reaction medium *tert*-butanol and microwave irradiation using very short reaction times provides an effective synthesis protocol for the preparation of stable, soluble, and ultrasmall anatase nanoparticles. Additionally, due to the low boiling point of *tert*-butanol and the high solubility of Pluronic templates in this solvent, it was possible to develop a direct coating technique for the preparation of mesoporous films from nanocrystalline particles, omitting the time-consuming steps of centrifugation and redispersion of nanoparticles in a different solvent. The use of these ultrasmall and highly soluble particles allowed the production of mesoporous layers from nanoparticulate precursors using commercial Pluronic templates in an efficient one-pot procedure, and the films exhibit uniform mesoporous networks with a very high surface area. The microwave-treated titanium dioxide films can be converted, contrary to untreated *tert*-butanol sol-gel derived films, into anatase upon calcination at 450 °C due to a seeding effect of the previously formed crystalline nanoparticles. Finally, electrochemical lithium insertion in these films shows the advantages of the microwave treatment regarding the retention of mesoporosity and crystallinity, leading to high insertion capacities and remarkably fast charging rates. The efficient preparation of the ultrasmall nanoparticles and their applicability in the direct preparation of mesoporous titanium dioxide make this *tert*-butanol system an attractive alternative to other non-aqueous sol-gel strategies.

### 6.4 Experimental Section

Titanium dioxide nanoparticles were synthesized using a non-aqueous sol-gel route in *tert*-butyl alcohol under microwave irradiation. All chemicals were purchased from Sigma-Aldrich and used as received. *tert*-Butyl alcohol was dried over 4 Å molecular sieve at 28 °C and filtered prior to use.

For all syntheses, titanium tetrachloride (1.5 mL, 13.7 mmol) was dissolved in toluene (10 mL) and added to *tert*-butyl alcohol (30 mL, 320 mmol) under continuous stirring. This solution was directly used as metal oxide precursor for the sample tBuOH-SG. For the sample T60, this solution was kept at 60 °C for 24 hours. Microwave heating was performed in microwave autoclaves with an initial heating power of 1200 W (Synthos 3000, Anton Paar). MW50 was heated to 50 °C within one minute and kept at this temperature for one hour. MW80/50 was heated to 80 °C within one minute, and then kept at 50 °C for 20 minutes resulting in a slightly yellow, transparent solution of nanoparticles.

To obtain the fully crystalline nanoparticles, this heating procedure had to be repeated one more time after a cooling period to room temperature (2xMW80/50). The solution was then colorless, and titanium dioxide could be flocculated by the addition of n-heptane (n-heptane:*t*-butanol/toluene 1:1 volume ratio) and separated by centrifugation at 50000 rcf for 15 minutes. The content of TiO<sub>2</sub> of the resulting solid was determined to be 73 wt% by thermogravimetric analysis (Netzsch STA 440 C TG/DSC).

One-pot coating solutions were made by mixing the reaction mixtures with Pluronic P123 (1.4 g, 0.24 mmol) after microwave heating. Coatings with the nanocrystalline solid as TiO<sub>2</sub> source were made by dissolving the amount of 0.2 g nanoparticles in ethanol (2 mL) and mixing this solution with Pluronic P123 (0.2 g, 0.04 mmol) in THF (2 mL). Films of mesoporous TiO<sub>2</sub>

## 6. Mesoporous Titania Structures from Ultrasmall Nanoparticles

---

were prepared on glass, FTO, or silicon by spin-coating with 1000 rpm at  $23 \pm 2$  °C and a relative humidity of  $45 \pm 10$  %.

Scanning electron microscopy (SEM) was performed on a JEOL JSM-6500F scanning electron microscope equipped with a field emission gun, at 4 kV. High Resolution Transmission Electron Microscopy (HRTEM) and Scanning Transmission Electron Microscopy in High Angle Annular Dark Field mode (STEM-HAADF) were performed using a FEI Titan 80-300 equipped with a field emission gun operated at 300 kV. The particulate samples were prepared by evaporating a drop of a diluted solution of particles with small amounts of Pluronic P123 in THF on a Plano holey carbon coated copper grid. HRTEM of films was carried out by scraping the thin-film samples off the substrate onto a holey carbon coated copper grid or by direct spin-coating of the dilute solution on a non-holey carbon coated copper grid.

The porosity of the films was determined by the analysis of adsorption isotherms of Kr at the boiling point of liquid nitrogen (approx. 77 K) using an ASAP 2010 apparatus (Micromeritics). Textural data is drawn from comparing the shape of the hysteresis loop and the limiting adsorption at saturation pressure of the Krypton sorption isotherms with reference materials (anatase powders) characterized by Nitrogen sorption. Comparison plots were constructed for each sample, and the differentiation of these plots provided the basis for the pore size distribution.

X-ray diffraction analysis was carried out in reflection mode using a Scintag XDS 2000 (Scintag Inc.) and a Bruker D8 Discover with Ni-filtered  $\text{CuK}_\alpha$ -radiation and a position-sensitive detector (Vantec). The thermal development of the XRD diffraction patterns was monitored either by ex situ heating or in in-situ measurements using a DHS-1100 heating chamber with a graphite dome (Anton Parr).

Dynamic light scattering (DLS) was performed using a Malvern Zetasizer-Nano equipped with a 4 mW He-Ne laser (633 nm) and an avalanche photodiode detector. The scattering data

were weighted based on particle number. Prior to DLS measurements, the viscosity of the solvent mixture was measured using a Bohlin rotational rheometer (Malvern).

For lithium insertion, the mesoporous films were coated on conductive ITO glass and subjected to cyclic voltammetry using a Parstat 2273 potentiostat (Princeton Applied Research). The measurements were performed in a 1 M solution of  $\text{LiN}(\text{SO}_2\text{CF}_3)_2$  in a 1:1 w/w mixture of ethylenecarbonate and 1,2-dimethoxyethane. The solution preparation and cell assembly were carried out in an Ar-filled glove box with a water and oxygen content of less than 20 ppm. The electrolyte solution was dried over 4 Å molecular sieve. Li wire was used as both the auxiliary and the reference electrode. The working electrode was masked with a silicone resin to precisely define the exposed surface area. Electrochemical measurements were taken in a potential range from 3.0 to 1.3 V vs. Li. The scan rates in cyclic voltammetry measurements were varied from 0.5 to 100 mV s<sup>-1</sup>. The weight of the titania layers was calculated using the thickness of the films and their density, which can be obtained by multiplying the density of anatase (3.9 g/cm<sup>3</sup>) with the porosity determined by Kr sorption experiments. The accuracy of this method was confirmed by weighing 10 films of the same samples on larger substrates with similar film thicknesses. The reference sample for Li insertion was made as described elsewhere.<sup>39</sup> In brief, anatase nanoparticles of 20 nm size were synthesized hydrothermally, and were mixed with cellulose binders. Porous films on FTO substrates were obtained using the doctor blade technique (Zehntner ZAA2300) and calcination at 450 °C for 30 min (1 °C/min ramp).

### 6.5 References

1. Yang, P.; Zhao, D.; Margolese, D. I.; Chmelka, B. F.; Stucky, G. D. *Nature* **1998**, *396*, 152-155.

2. Lee, J.; Orilall, C. M.; Warren, S. C.; Kamperman, M.; DiSalvo, F. J.; Wiesner, U. *Nature Mater.* **2008**, *7*, 222-228.
3. Boettcher, S. W.; Fan, J.; Tsung, C.-K.; Shi, Q.; Stucky, G. D. *Acc. Chem. Res.* **2007**, *40*, 784-792.
4. Wan, Y.; Yang, H.; Zhao, D. *Acc. Chem. Res.* **2006**, *39*, 423-432.
5. Sanchez, C.; Boissière, C.; Grosso, D.; Laberty, C.; Nicole, L. *Chem. Mater.* **2008**, *20*, 682-737.
6. O'Regan, B.; Gratzel, M. *Nature* **1991**, *353*, 737-740.
7. Zhang, Q.; Chou, T. P.; Russo, B.; Jenekhe, S. A.; Cao, G. *Angew. Chem. Int. Ed.* **2008**, *47*, 2402-2406.
8. Rajan, J.; Velmurugan, T.; Seeram, R. *J. Am. Ceram. Soc.* **2009**, *92*, 289-301.
9. Pinna, N.; Neri, G.; Antonietti, M.; Niederberger, M. *Angew. Chem. Int. Ed.* **2004**, *43*, 4345-4349.
10. Li, H.; Balaya, P.; Maier, J. *J. Electrochem. Soc.* **2004**, *151*, A1878-A1885.
11. Poizot, P.; Laruelle, S.; Grugeon, S.; Dupont, L.; Tarascon, J. M. *Nature* **2000**, *407*, 496-499.
12. Grosso, D.; Cagnol, F.; Soler-Illia, G. J. de A. A.; Crepaldi, E. L.; Amenitsch, H.; Brunet-Bruneau, A.; Bourgeois, A.; Sanchez, C. *Adv. Funct. Mater.* **2004**, *14*, 309-322.
13. Yang, P.; Zhao, D.; Margolese, D. I.; Chmelka, B. F.; Stucky, G. D. *Chem. Mater.* **1999**, *11*, 2813-2826.
14. Szeifert, J. M.; Fattakhova-Rohlfing, D.; Georgiadou, D.; Kalousek, V.; Rathouský, J.; Kuang, D.; Wenger, S.; Zakeeruddin, S. M.; Gratzel, M.; Bein, T. *Chem. Mater.* **2009**, *21*, 1260-1265.
15. Fattakhova-Rohlfing, D.; Szeifert, J. M.; Yu, Q.; Kalousek, V.; Rathouský, J.; Bein, T. *Chem. Mater.* **2009**, *21*, 2410-2417.

16. Niederberger, M.; Garnweitner, G. *Chem. Eur. J.* **2006**, *12*, 7282-7302.
17. Niederberger, M.; Bartl, M. H.; Stucky, G. D. *Chem. Mater.* **2002**, *14*, 4364-4370.
18. Niederberger, M.; Bartl, M. H.; Stucky, G. D. *J. Am. Chem. Soc.* **2002**, *124*, 13642-13643.
19. Niederberger, M.; Garnweitner, G.; Krumeich, F.; Nesper, R.; Colfen, H.; Antonietti, M. *Chem. Mater.* **2004**, *16*, 1202-1208.
20. Kotsokechagia, T.; Cellesi, F.; Thomas, A.; Niederberger, M.; Tirelli, N. *Langmuir* **2008**, *24*, 6988-6997.
21. Pinna, N.; Niederberger, M. *Angew. Chem. Int. Ed.* **2008**, *47*, 5292-5304.
22. Feldmann, C.; Jungk, H.-O. *Angew. Chem. Int. Ed.* **2001**, *40*, 359-362.
23. Feldmann, C. *Adv. Funct. Mater.* **2003**, *13*, 101-107.
24. Wang, C.; Deng, Z.-X.; Zhang, G.; Fan, S.; Li, Y. *Powder Technol.* **2002**, *125*, 39-44.
25. Yang, X.; Konishi, H.; Xu, H.; Wu, M. *Eur. J. Inorg. Chem.* **2006**, *2006*, 2229-2235.
26. Li, G.; Li, L.; Boerio-Goates, J.; Woodfield, B. F. *J. Am. Chem. Soc.* **2005**, *127*, 8659-8666.
27. Wang, C.; Deng, Z.-X.; Li, Y. *Inorg. Chem.* **2001**, *40*, 5210-5214.
28. Garnweitner, G.; Antonietti, M.; Niederberger, M. *Chem. Commun.* **2005**, 397-399.
29. Kominami, H.; Kato, J.; Takada, Y.; Doushi, Y.; Ohtani, B.; Nishimoto, S.; Inoue, M.; Inui, T.; Kera, Y. *Catal. Lett.* **1997**, *46*, 235-240.
30. Bartl, M. H.; Boettcher, S. W.; Frindell, K. L.; Stucky, G. D. *Acc. Chem. Res.* **2005**, *38*, 263-271.
31. Bilecka, I.; Djerdj, I.; Niederberger, M. *Chem. Commun.* **2008**, 886-888.
32. Grosso, D.; Soler-Illia, G. J. d. A. A.; Crepaldi, E. L.; Cagnol, F.; Sinturel, C.; Bourgeois, A.; Brunet-Bruneau, A.; Amenitsch, H.; Albouy, P. A.; Sanchez, C. *Chem. Mater.* **2003**, *15*, 4562-4570.

33. Crepaldi, E. L.; Soler-Illia, G. J. d. A. A.; Grosso, D.; Cagnol, F.; Ribot, F.; Sanchez, C. *J. Am. Chem. Soc.* **2003**, *125*, 9770-9786.
34. Choi, S. Y.; Mamak, M.; Speakman, S.; Chopra, N.; Ozin, G. A. *Small* **2005**, *1*, 226-232.
35. Fattakhova-Rohlfing, D.; Wark, M.; Brezesinski, T.; Smarsly, B. M.; Rathouský, J. *Adv. Funct. Mater.* **2007**, *17*, 123-132.
36. Brezesinski, T.; Wang, J.; Polleux, J.; Dunn, B.; Tolbert, S. H. *J. Am. Chem. Soc.* **2009**, *131*, 1802-1809.
37. Ren, Y.; Hardwick, L. J.; Bruce, P. G. *Angew. Chem. Int. Ed.* **2010**, *49*, 2570.
38. Wang, J.; Polleux, J.; Lim, J.; Dunn, B. *J. Phys. Chem. C* **2007**, *111*, 14925-14931.
39. Ito, S.; Murakami, T. N.; Comte, P.; Liska, P.; Grätzel, C.; Nazeeruddin, M. K.; Grätzel, M. *Thin Solid Films* **2008**, *516*, 4613-4619.



## **7. Low-Temperature Synthesis of Mesoporous Titania-Silica Films with preformed Anatase Nanocrystals**

*This chapter is based on the following publication:*

Dina Fattakhova-Rohlfing, Johann M. Szeifert, Qianqian Yu, Vit Kalousek, Jiri Rathouský, Thomas Bein, *Chemistry of Materials* **2010**, 21 (12), 2410-2417.

### **7.1 Introduction**

Crystalline nanoparticles are attractive building blocks for the solution-based preparation of nanostructured materials.<sup>1-4</sup> In principle, the assembly of nanoparticles controlled by structure-directing agents can enable the preparation of highly crystalline porous structures with defined morphology already at low temperatures.<sup>2,5-7</sup> The scope of possible systems can be extended even further when the nanocrystals are dispersed in different non-crystalline matrices, thus opening the way towards novel nanocomposite systems.<sup>8-15</sup> However, the use of nanocrystals as building blocks imposes certain requirements on their properties. Besides a well-defined size distribution, the nanocrystals should be easily dispersible and form non-agglomerated colloidal solutions.<sup>16</sup> Moreover, these solutions should be compatible with the structure-directing agent and the precursor for the non-crystalline component of the matrix.

Here we report the preparation of mesoporous titania-silica composites from crystalline titania nanoparticles and mesoporous amorphous silica. Such systems have been the subject of intensive research activity, as they may combine the properties of both components, thus extending their functionality beyond that of the pure materials.<sup>17-25</sup> Such a composite can benefit, for example, from the antibacterial and self-cleaning properties of crystalline titania,<sup>26</sup>

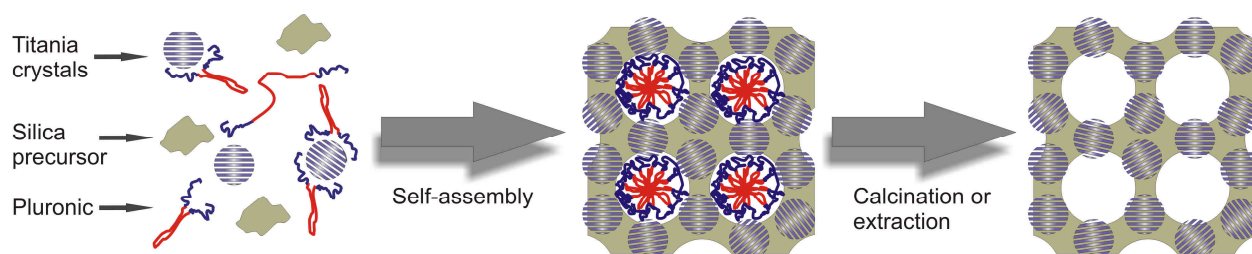
and the mechanical and thermal stability and excellent optical properties of periodic mesoporous silica in combination with a well-defined pore architecture.<sup>27</sup> Combining both components, novel materials can be obtained exhibiting, e.g., exceptional self-cleaning ability and high photocatalytic efficiency in gas phase reactions.

The preparation of mesoporous titania-silica coatings is a challenging task as the efficient performance of such films requires homogeneous distribution of both components, high loading and high crystallinity of the titania phase, and a controlled porosity exhibiting large accessible surface area, suitable pore size and connectivity. Moreover, the development of effective procedures for the preparation of highly crystalline titania-silica films at low temperatures is of great interest due to the possible use of thermally less stable substrates, higher energy efficiency, and simplified processing.

In view of these requirements, several routes towards the preparation of mesoporous titania-silica composites have been explored. The most commonly used techniques are based either on a self-assembly of sol-gel processed molecular precursors of TiO<sub>2</sub> and SiO<sub>2</sub> with a structure-directing agent,<sup>14,17-20,28,29</sup> or on grafting of titania precursors on the preformed mesoporous silica layers.<sup>23-25</sup> However, the titania phase in these composites is initially amorphous and has to be calcined at least at 400 °C in order to induce its crystallization. To overcome this problem, preformed titania nanocrystals have been combined with periodically organized mesoporous silica.<sup>13,21,22</sup> However, the reported methods deal with relatively large titania particles, whose size significantly exceeds that of the pore system. As a consequence, the crystals do not participate in the mesostructure formation and the potential advantage of the high surface-to-bulk ratio at the nanoscale cannot be fully exploited. To be compatible with the silica mesopore structure, the size of the titania crystals should be in the range of a few nanometers. Even if the preparation of colloidal solutions of such small nanoparticles has proven to be difficult due to their tendency towards irreversible agglomeration, recently a suitable synthetic technique has been developed.<sup>3,4,16,30-32</sup>

## 7. Synthesis of Mesoporous Titania-Silica Films

In this work we have used the so-called “brick and mortar” strategy<sup>9,10,33</sup> to prepare titania-silica composite films suitable for gas phase photocatalysis. Pre-formed titania nanocrystals were fused with surfactant-templated sol-gel silica, which acts as a structure-directing matrix and as a chemical glue (Scheme 7.1). Stable colloidal solutions of titania crystals 4-5 nm in size were obtained by a non-aqueous low-temperature route.<sup>30,31</sup> We found that the particles disperse easily in high concentration of up to 10 wt % in the presence of block-copolymers of the Pluronic family (PEO<sub>x</sub>-PPO<sub>y</sub>-PEO<sub>x</sub>) to form transparent colloidal solutions. The block copolymers of the polyether type are especially useful as they stabilize the particles by weakly bonding to the particle surface without covalent functionalization,<sup>32</sup> which could deteriorate their photocatalytic activity. At the same time, Pluronic acts as a structure directing agent in the film assembly. The sol-gel derived silica is especially suitable as a “mortar” as it condenses already at low temperatures, thus leading to the formation of mechanically stable continuous films of high optical quality.



**Scheme 7.1.** Formation of nanocomposite titania-silica mesoporous films using pre-formed titania nanocrystals stabilized by the Pluronic polymer, and amorphous sol-gel silica precursor.

The different chemical composition of “bricks” and “mortar” components in these nanocomposites makes them easily distinguishable, enabling deeper insights into the role of the individual synthesis parameters on the homogeneity of particle distribution and the morphology of the mesostructure. One of the important parameters is the nature of the structure-directing agent, because it influences both the solubilization of particles and their

self-assembly properties. We examined two Pluronic polymers with different lengths of hydrophilic polyethyleneoxide chains, namely Pluronic P123 ( $x, y = 20, 70$ ) and Pluronic F127 ( $x, y = 106, 70$ ). In order to make full use of the developed procedure, we have focused on the low-temperature processing of the films. For this purpose, two different strategies to remove the template were applied, namely calcination at the lowest possible temperature and template extraction. The calcination was deliberately performed at the lowest temperature of template combustion at 300 °C. Finally, the accessibility of the titania surface and its photocatalytic activity in the resulting composites was investigated in the photocatalytic oxidation of NO.

The following experiments have been performed as a joint project: The composite films were synthesized and characterized using X-ray diffraction, electron microscopy, and Raman spectroscopy by Dr. Dina Fattakhova-Rohlfing, Qianqian Yu, and Johann M. Szeifert. Krypton sorption and photocatalytic experiments were performed and evaluated by Vit Kalousek, and Dr. Jiri Rathouský at the J. Heyrovský Institute in Prague.

### 7.2 Results and Discussion

Completely crystalline titania nanoparticles serving as “bricks” were prepared by reacting titanium tetrachloride with benzyl alcohol at 40-150 °C.<sup>31</sup> Reaction time and temperature are the decisive parameters in the synthesis, resulting in anatase particles of 4-5 nm in size after treating the reaction mixture at 60°C for 24 hours (Figure 7.1b, Figure 7.2). A further increase in reaction time and temperature leads to particle agglomeration or particle growth.

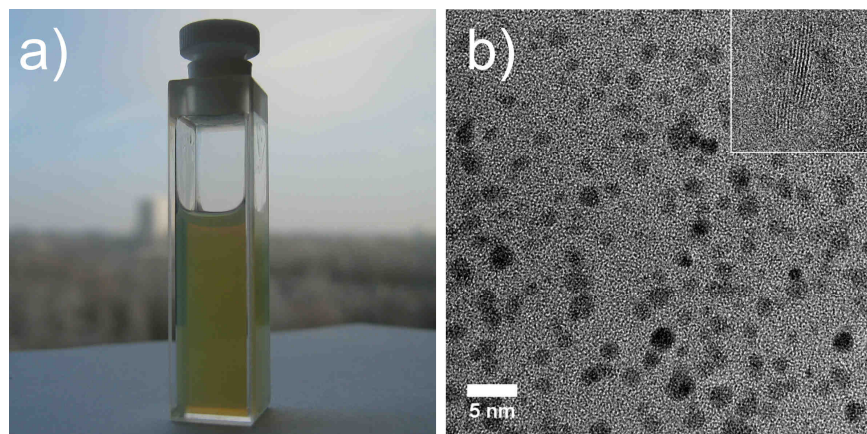


**Figure 7.1.** Colloidal solution (9 wt % in THF) of Pluronic - stabilized titania nanoparticles synthesized at 60 °C (a), and TEM image of the Pluronic - stabilized particles (b). The inset 5 nm x 5 nm in size shows the high resolution TEM (HR-TEM) of a single nanoparticle.

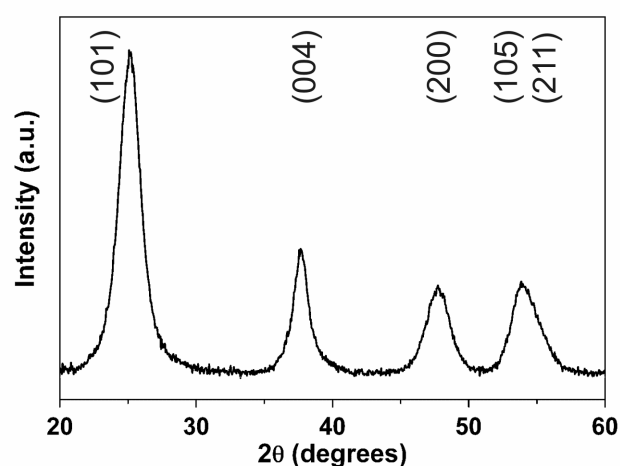


**Figure 7.2.** XRD pattern of titania nanoparticles synthesized at 60 °C corresponding to the crystalline structure of TiO<sub>2</sub> anatase. Particle size estimated according to Scherrer equation from the peak width broadening is 4.5 nm.

While the obtained particles are insoluble both in water and organic solvents, they redisperse easily at concentrations of up to 10 wt % in tetrahydrofuran in the presence of a suitable Pluronic block-copolymer (Figure 7.1a). The time needed to completely redisperse the particles depends on the type of Pluronic copolymer, being 2 and 12 hours for Pluronic P123

and F127, respectively. The nature of the interactions of the Pluronic polymers with the surface of titania particles is still unclear, although experiments with other surfactants suggest that the polyethylene oxide groups interact with the surface titanium atoms via multiple coordination bonds.<sup>34</sup> Apparently, the difference in hydrophilicity and the number of ethylene oxide groups in the polymer blocks have a decisive influence on their coordination and solvation behavior.

The established procedure for the preparation of the silica sol<sup>1,35</sup> had to be modified to make it compatible with the stability requirements of the titania colloids, especially the use of THF as a solvent and the low pH range at which titania colloids are stable. The optimized composition of silica sols contains TEOS as silica precursor, water as hydrolysis agent, HCl as a hydrolysis catalyst, and THF as a solvent in the molar ratio of 1.0 : 9.1 : 0.016 : 2.7. For the coating solutions, the amount of Pluronic was calculated as a weight ratio with respect to the total weight of metal oxides. The optimum amount regarding the complete redispersion of titania nanoparticles and the periodicity of the formed mesostructure was found to be 150 wt % and 100 wt % for Pluronic P123 and Pluronic F127, respectively.

For the preparation of the “brick and mortar” titania-silica nanocomposites, a certain amount of silica “mortar” was added to the copolymer-stabilized colloidal solution of nanocrystalline titania “bricks”. To investigate the influence of the particles on the development of the mesostructure, the ratio of “bricks” and “mortar” components was varied. The solutions were prepared in such a way that the relative amount of the copolymer with respect to the total amount of metal oxides was kept constant.

### 7.2.1 Films templated with Pluronic P123

X-ray diffractograms show that the addition of nanoparticles to the silica sol has a strong influence on the mesostructure of the formed films. The reference films prepared without

## 7. Synthesis of Mesoporous Titania-Silica Films

titania particles exhibit small angle XRD patterns corresponding to mesostructured domains with a periodicity  $d$  of 7 nm (Figure 7.3). When increasing the particle concentration, the mesostructure becomes less organized. Addition of more than 10 % of particles leads to the complete disappearance of the mesostructure ordering.

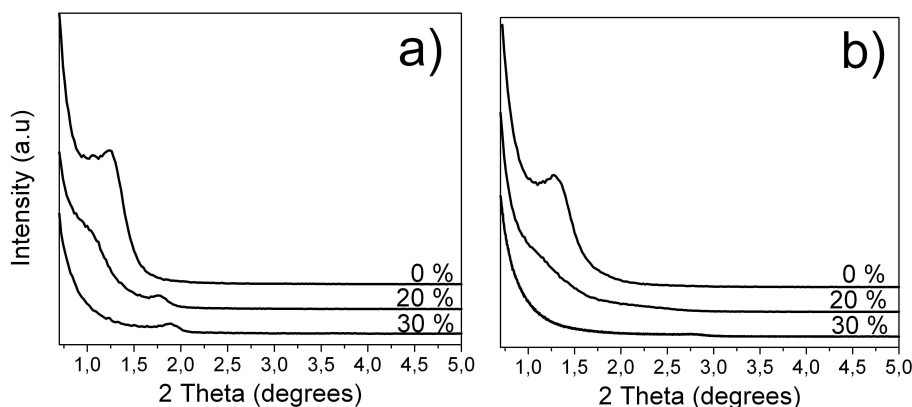


**Figure 7.3.** Diffraction patterns of the “brick and mortar” titania-silica films with different titania content prepared using Pluronic P123 after treatment at 100 °C (a) and 300 °C (b).

The morphology of the composite films and the distribution of both oxides were investigated with electron microscopy. The TEM images of the films containing 10 wt % nanoparticles reveal a porous mesostructure with inclusions of titania nanocrystals, which are identified as darker spots and whose lattice fringes are observed in HR-TEM (Figure 7.4a). According to Scanning Transmission Electron Microscopy in High Angle Annular Dark Field mode (STEM-HAADF) coupled with EDX analysis (Figure 7.4b, c), the film’s morphology is inhomogeneous. Addition of even small amounts of nanoparticles leads to a microphase separation and coexistence of mesoporous domains and the non-porous agglomerates (Figure 2c). EDX analysis of the corresponding areas (Figure 7.4b) demonstrates that the domains with periodic mesoporosity (inset 1) are composed almost solely of silica, while the non-organized agglomerates of particles (inset 2) contain a high concentration of titania.

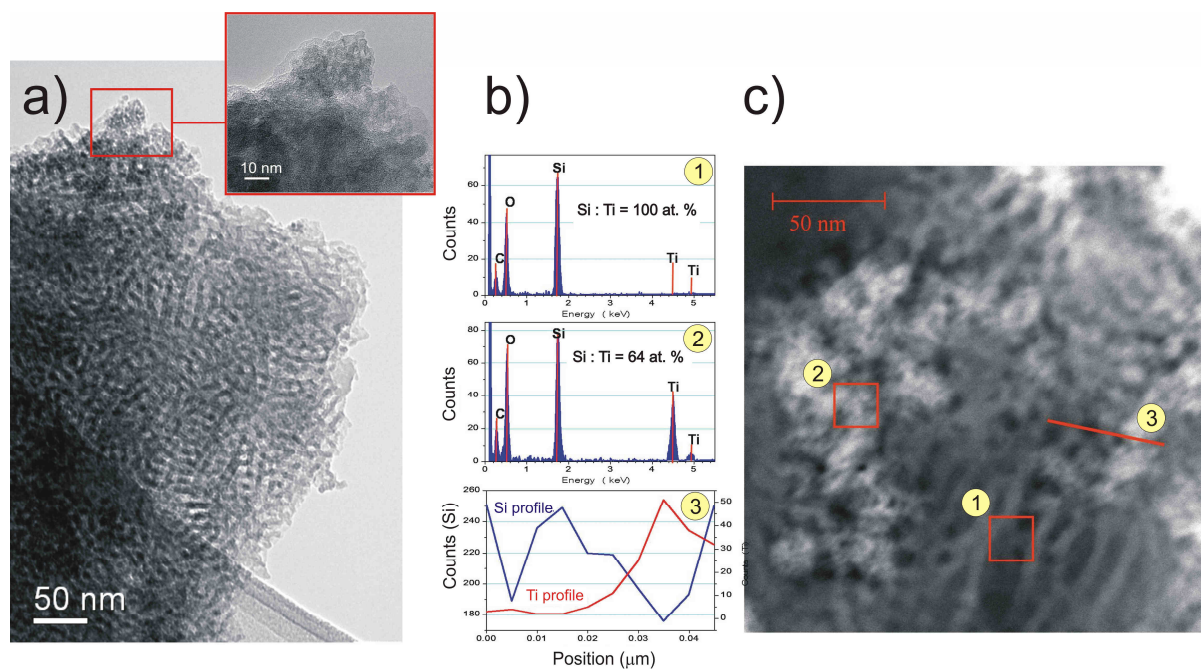


**Figure 7.4.** Electron microscopy of the titania-silica film templated with Pluronic P123 and containing 10 % particles after calcination at 300°C: a) TEM image demonstrating the mesoporous film structure with embedded titania nanocrystals, which are shown in the inset, c) STEM-HAADF image and b) EDX analysis of the selected areas marked in (c).

To sum up, the addition of the colloidal titania nanoparticles to the silica sol-gel precursor templated with Pluronic P123 as a structure-directing agent has a strong influence on the self-assembly and the meso-organization of the films. Only at very low concentrations, the particles can be incorporated into the mesoporous silica matrix with a homogeneous distribution in the bulk of the film (Figure 7.4a). Higher particle concentrations beyond 20 % lead to strong distortion or complete disorder of the mesoporous structure (Figure 7.5). Therefore, Pluronic P123 is not a suitable stabilizing agent for achieving a homogeneous distribution of nanoparticles within the silica phase. As high particle concentrations can be important for certain applications, the influence of a different template on the dispersibility of the particles and their final distribution in the films was investigated.

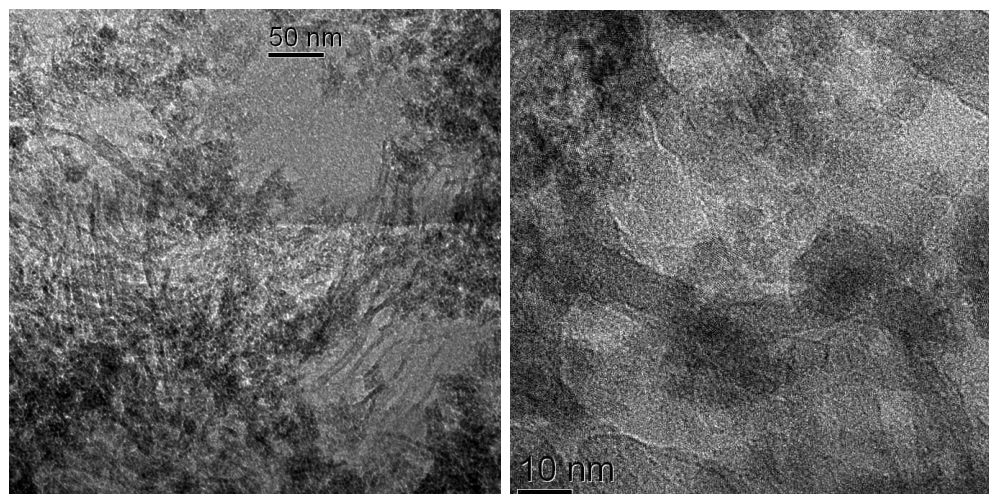


**Figure 7.5.** TEM images of the sample containing 30 % particles after calcination at 300 °C. The major part of the films does not show periodicity, however, small domains of silica featuring a filament-like morphology can be observed.

### 7.2.2 Films templated with Pluronic F127

#### *Mesostructure characterization*

In contrast to Pluronic P123, the use of the larger and more hydrophilic Pluronic F127 block copolymer permits the preparation of composite titania-silica mesoporous architectures that can accommodate a larger amount of nanocrystals without any significant perturbation of the mesostructure periodicity. Even for films with a particle content of up to 30 wt %, the diffraction signals at small angles are still observed, indicating the presence of a periodic mesostructure (Figure 7.6).

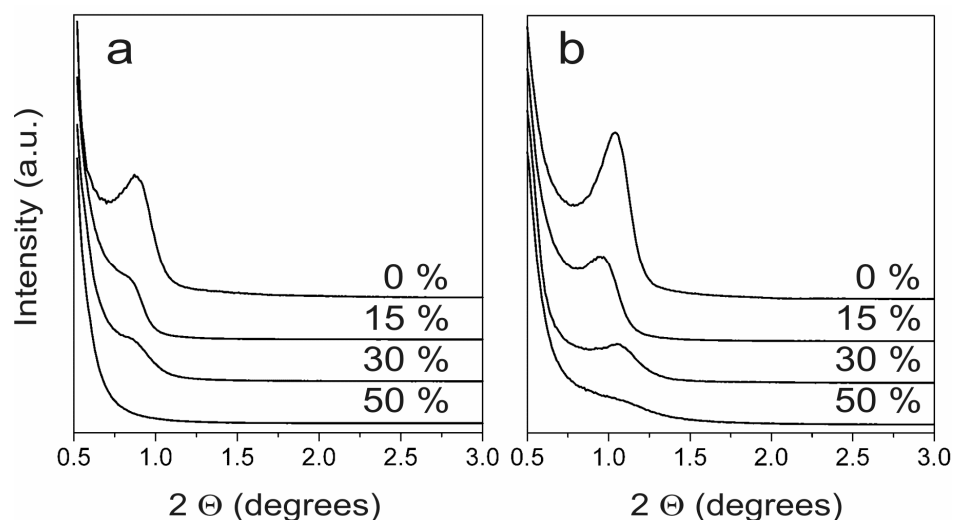


**Figure 7.6.** Small-angle XRD patterns of titania-silica “brick and mortar” films with various particle contents templated with Pluronic F127 after treatment at 100 °C (a) and 300 °C (b). The presence of the diffraction peak at low angles for the composite films with different particles content demonstrates the preservation of the pore ordering after particles addition, although the continuous decrease in the diffraction peak demonstrates the decrease in the pore structure periodicity with the increasing particles content.

TEM images of the films with different particle concentrations calcined at 300°C are shown in Figure 7.7. The pure silica films feature a periodic mesoporous structure with ellipsoidal pores 8.5 x 5.5 nm in size and periodic distances of 13 by 10 nm as derived from the Fourier transform of the images (inset). The addition of particles leads only to some slight deterioration of the mesostructure periodicity and an increase in the pore size ranging from 9 to 11 nm. The titania crystals form small agglomerates of 5 to 14 nm in diameter, which are homogeneously embedded within the pore walls throughout the complete volume of the films. The pores have a spherical rather than ellipsoidal shape, probably due to the presence of nanocrystals in the walls that might reduce the pore shrinkage during calcination.

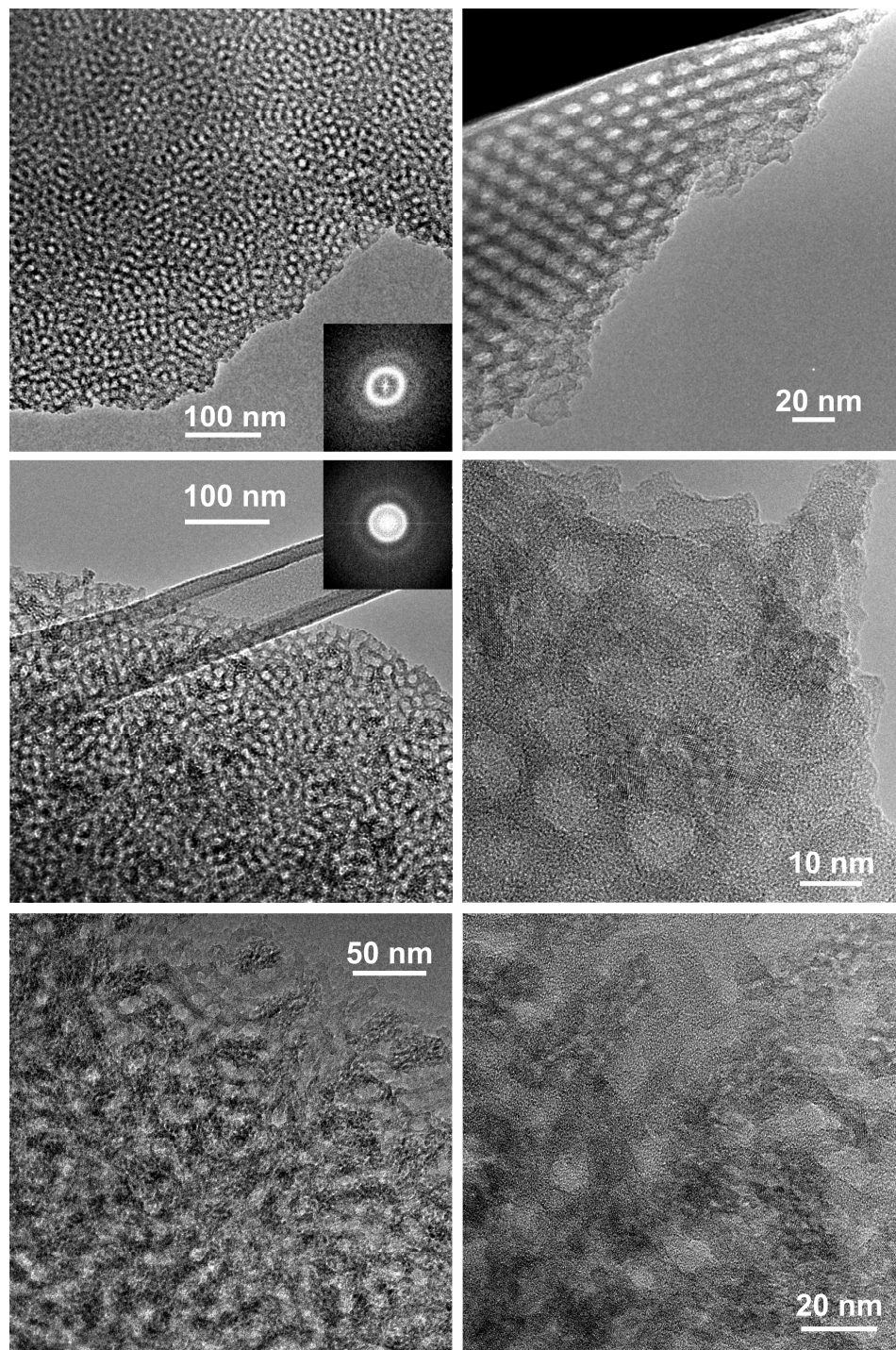


**Figure 7.7.** TEM images of titania-silica “brick and mortar” films templated with Pluronic F127 containing 0 wt % particles (first row), 15 wt % particles (second row) and 30 wt % particles (last row) after calcination at 300 °C. The insets show the Fourier transform of the same picture revealing the periodic mesopore structure.

Obviously, Pluronic F127 is much more suitable for the self-assembly of titania nanoparticles with silica precursor compared to the smaller and more hydrophobic Pluronic P123. The mesostructure is able to include up to 30 wt % of particles without significant changes.

### *Crystallinity and porosity of low-temperature processed films*

The crystalline anatase phase in the films can be easily detected by its Raman modes at  $144\text{ cm}^{-1}$  ( $E_g$ ),  $398\text{ cm}^{-1}$  ( $B_{1g}$ ),  $518\text{ cm}^{-1}$  ( $A_{1g}$ ) and  $639\text{ cm}^{-1}$  ( $E_g$ ).<sup>36,37</sup> As seen in the Raman spectra, the intensity of titania vibrational modes increases linearly with the particle content in the precursor solution (Figure 7.8A).

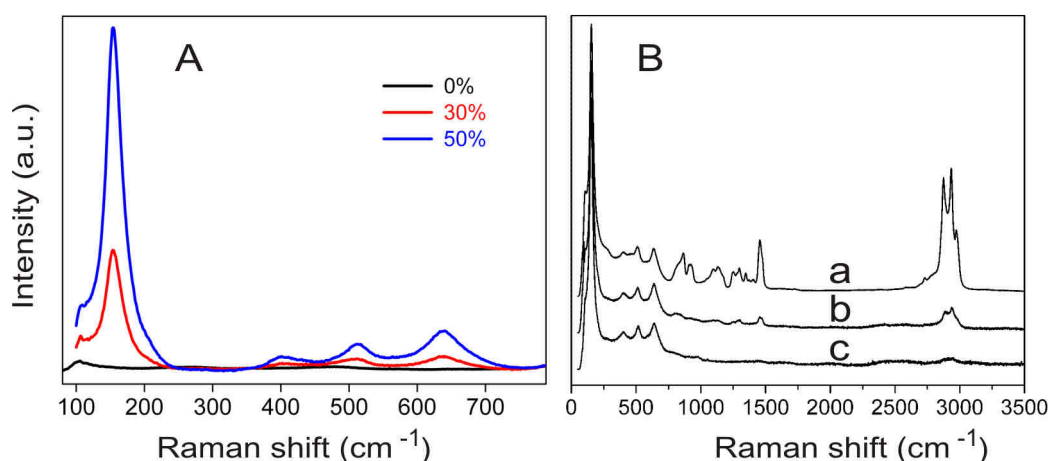


**Figure 7.8.** A) Raman spectra of titania-silica “brick and mortar” films templated with Pluronic F127 and containing various amount of particles. The spectra were normalized to the intensity of the C-H stretching vibrations of Pluronic.<sup>38</sup> B) Raman spectra of composite titania-silica films with 30 wt % of nanoparticles templated with Pluronic F127 and subjected to different post-synthesis treatments: non-treated (a), treated at  $100\text{ }^{\circ}\text{C}$  and extracted with EtOH under reflux (b) and calcined at  $300\text{ }^{\circ}\text{C}$  (c).

The Pluronic F127 template was removed either by calcination at  $300\text{ }^{\circ}\text{C}$  or by extraction with EtOH at  $80\text{ }^{\circ}\text{C}$ . The efficiency of the template removal in both cases was also followed

## 7. Synthesis of Mesoporous Titania-Silica Films

by Raman spectroscopy. The Raman spectra of differently treated films with identical composition were normalized using the anatase band at  $144\text{ cm}^{-1}$ , assuming that the amount and size of titania crystals are maintained after calcination. Figure 7.8B shows that the C-H stretching vibrations of Pluronic polyalkyleneoxide moieties in the range of  $2700\text{--}3100\text{ cm}^{-1}$  observed in the freshly deposited film vanish after its calcination at  $300^\circ\text{C}$  due to the combustion of the template. The intensity of these peaks also drastically decreases after extraction of films with EtOH under reflux for 4 hours, and further decreases after prolonged extraction for 16 hours, demonstrating the efficiency of this procedure for the removal of the template.

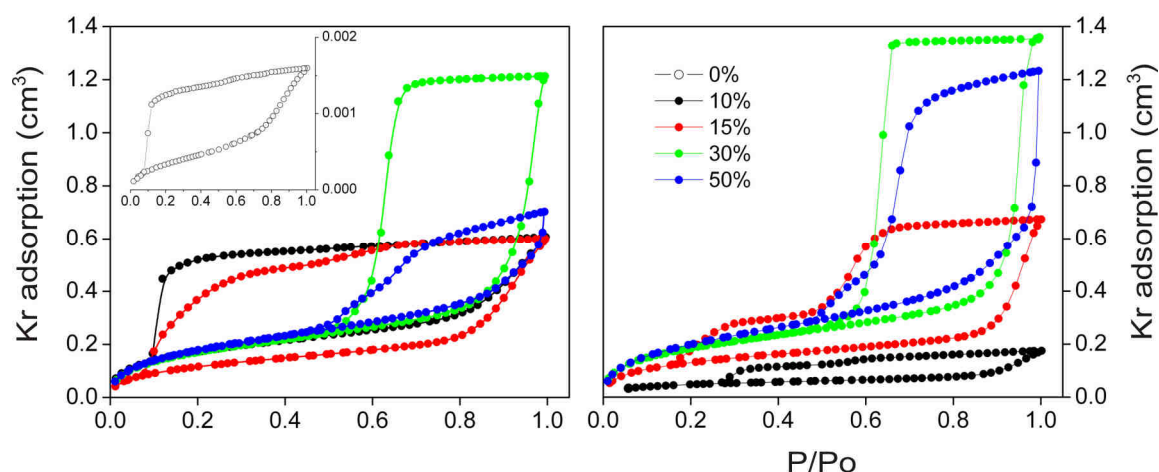


**Figure 7.9.** Adsorption isotherms of Kr at 77 K on titania-silica “brick and mortar” films templated with Pluronic F127 and containing various amounts of particles: calcined at  $300^\circ\text{C}$  (left) and treated at  $150^\circ\text{C}$  followed by extraction with EtOH under reflux (right). The inset shows an adsorption isotherm for a film containing 0 % of titania nanocrystals.

The textural properties of the films containing different amounts of titania particles, de-templated either by calcination or extraction, were quantitatively studied by Kr adsorption at 77 K (Figure 7.9, Table 7.1). The concentration of nanoparticles in the films calcined at  $300^\circ\text{C}$  has a decisive effect on the porosity. The films prepared without any  $\text{TiO}_2$

## 7. Synthesis of Mesoporous Titania-Silica Films

---

nanoparticles exhibit very small surface area and pore volume (Figure 7.9, inset), which we attribute to pore blocking preventing the access of adsorbate molecules at the very low temperature of the adsorption experiment. Apparently, the voids in the film (see the TEM image in Figure 7.7) are linked only via narrow pores (microporous defects or cracks), thus replicating the space occupied by the spherical micelles embedded within the unperturbed siliceous framework. The samples containing 10-15 % of TiO<sub>2</sub> nanoparticles have a much larger specific surface area and pore volume, with a smaller degree of pore blocking as follows from the shape of the hysteresis loop. The presence of the TiO<sub>2</sub> nanoparticles appears to open the continuous siliceous framework and facilitate the access of krypton. Furthermore, TiO<sub>2</sub> nanoparticles may act as oxidation catalyst, accelerating the complete removal of the template. The porosity of the films containing 30 % of nanoparticles is well-developed, featuring very narrow pore size distribution, very large pore volume and the absence of pore blocking. The narrowness of the pore size distribution follows from the steepness of the adsorption and desorption branches, however, at this point it is difficult to determine the actual pore size distribution due to the properties of Kr far below its triple point.

The increase in particle content to 50 % leads to a deterioration of the mesoporous system, which is characterized by a wider pore-size distribution and smaller pore volume, the large specific surface area being, however, preserved. Extracted films prepared without particles do not show mesoporous sorption characteristics, probably due to the fact that the pores are still partially filled with the template, which cannot be completely removed by extraction. This was confirmed by the observation that calcination at 400 °C leads to a substantial gain in surface area and pore volume (Table 7.1, Figure 7.5). Films containing 10-15 wt % of nanoparticles are characterized by two steps on their desorption branch, which corresponds to a bimodal pore system. Characteristically, the calcined and extracted samples containing 30 wt % of nanoparticles are practically identical with respect to their porosity. This supports the hypothesis that the structure of the solid phase is strongly affected by the presence of

## 7. Synthesis of Mesoporous Titania-Silica Films

nanocrystals such that extraction is sufficient for the removal of the polymer. The extracted films containing 50 wt % of nanoparticles exhibit a pore volume 70 % larger than the calcined ones, which could be attributed to a substantial shrinkage of the silica matrix upon treatment at higher temperatures.

TiO <sub>2</sub> , wt %	Treatment	S <sub>spec</sub> , cm <sup>2</sup> /cm <sup>2</sup>	V <sub>spec</sub> , mm <sup>3</sup> /cm <sup>2</sup>	Character of porosity, D, nm
0 %	calc	17.4	0.0020	pore blocking
	extr	~ 0		
	extr+calc 400°C	264.9	0.0197	voids + micropores
20 %	calc	213.5	0.0202	pore blocking
	extr	59.3	0.0059	bimodal
30 %	calc	167.0	0.0229	less pore blocking
	extr	166.8	0.0232	bimodal
50 %	calc	230.0	0.0425	7.4
	extr	236.3	0.0465	7.9
70 %	calc	240.4	0.0246	wide pore size distribution
	extr	258.0	0.0413	6.4

**Table 7.1.** Textural parameters and porosity of films calcined at 300°C or treated at 150°C with subsequent extraction with EtOH, respectively. S<sub>spec</sub>, V<sub>spec</sub>, BET surface area and pore volume are related to the geometric size of the support, respectively; D=4V/S, effective pore size calculated from the pore volume and surface area.

### *Titania accessibility and photocatalytic activity*

In order to assess the functionality of titania crystals in the composite films, the activity of composite films was tested in the photocatalytic oxidation of NO. This reaction was selected for two reasons. First it is of environmental importance as one of the technologies for the removal of NO, which is present in the range of several hundred ppb in the atmosphere of large cities. Second, it has been suggested as an ISO standard for testing the photocatalytic activity of materials in the gaseous phase. The adsorbed NO molecules react first with OH<sup>•</sup> or

$\text{HO}_2^\bullet$  radicals to form adsorbed  $\text{HNO}_2$ , which is further photooxidized to  $\text{NO}_2$ .  $\text{NO}_2$  is either desorbed or converted to  $\text{HNO}_3$ . The degree of conversion to  $\text{HNO}_3$  depends on the residence time of  $\text{NO}_2$  in the adsorbed state and is substantially enhanced by the porosity of the employed photocatalyst. Large-surface mesoporous films containing crystalline  $\text{TiO}_2$  are especially effective when the photodecomposition mechanism requires adsorption of species prior to reaction on the surface. The amount of adsorbed substances is increased due to the large surface area, which enhances their decomposition.

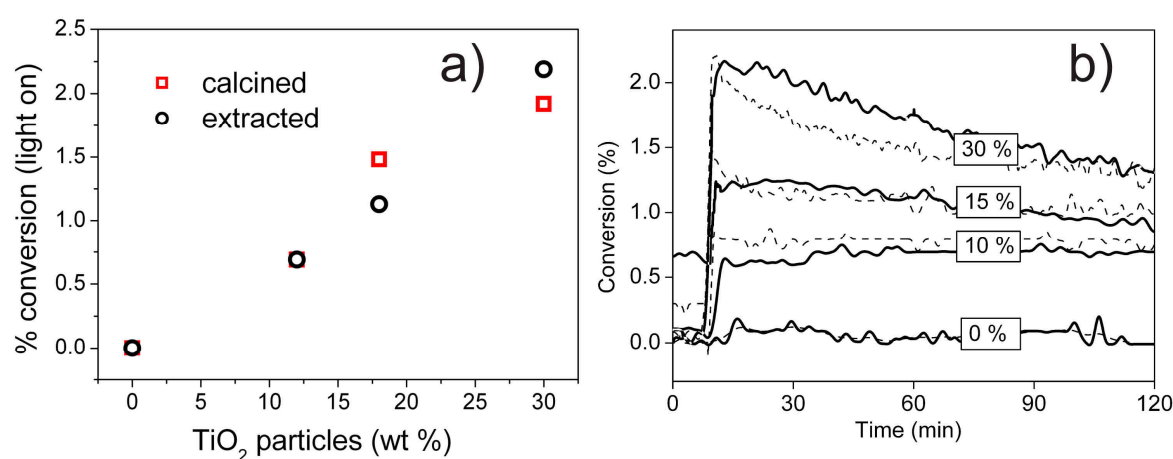


**Figure 7.10.** Photocatalytic activity of extracted (black) and calcined (red) titania-silica films with different particle content in the photocatalytic oxidation of NO measured after switching on the light (time = 5 min) (a) and the corresponding photocatalysis measurement curves of extracted (solid lines) and calcined (dashed lines) samples (b).

For the photooxidation of NO, both extracted and calcined films were tested. Here we selected the films with the organized periodic mesostructure, that is, those with a titania particle content up to 30 %. While films of pure silica are inactive, the activity of those containing  $\text{TiO}_2$  nanocrystals increases almost linearly with the  $\text{TiO}_2$  content (Figure 7.10), approaching the conversion efficiency of 3.9-4 % for the films composed solely of titania particles taken as a reference. This linearity confirms the homogeneous distribution of the

## 7. Synthesis of Mesoporous Titania-Silica Films

---

particles and their good accessibility for molecules from the gas phase. We also note that the activities of low-temperature extracted films are as high as those of calcined films. This opens up new perspectives for the preparation of crystalline photocatalytic coatings at low temperatures, which would make even plastic substrates acceptable for this application. Further increases of the photocatalytic activity of those films are expected for thicker films and for films with particle contents over 50 wt %.

Conversion (%)	Calcined				Extracted			
	0 %	10 %	15 %	30 %	0 %	10 %	15 %	30 %
Particle content								
light on	0.00	0.69	1.48	1.92	0.00	0.69	1.13	2.19
after 2h	0.00	0.89	0.99	0.99	0.00	0.69	0.79	1.29

**Table 7.2.** Efficiency of NO conversion in photocatalytic measurements for calcined and extracted films with various particle content measured directly after switching on the light (time = 5 min) and after 2 hours of illumination.

### *Possible self-assembly mechanism of the composite titania-silica mesostructures*

The obtained experimental data demonstrate that the composite titania-silica films with organized mesoporous architecture can be assembled from the Pluronic-stabilized nanoparticles and hydrolyzed silica precursor. We now address the question of how this meso-organization takes place. In a classical evaporation-induced self-assembly (EISA) process, the mesostructure formation is directed by the micelles of a surfactant, which self-assemble in the presence of inorganic precursor into supramolecular periodic structures. In contrast, in the “brick and mortar” procedure used here, the surfactant molecules are at least partially bound to the nanocrystals’ surface, thus lowering the concentration of free surfactant

in solution and altering the conditions for the micelle formation. Therefore, several different ways of interaction between particles, silica precursor and template have to be considered for the final EISA step.

We can hypothesize two extreme cases for the self-assembly process. In the first case, the surfactant-stabilized particles act themselves as the structure-building blocks and arrange in a liquid-crystalline periodic structure, which is impregnated by the silica oligomers. In the second case, addition of silica precursor leads to partial or complete desorption of the surface-bound template due to replacement by hydrolyzed silica, and a self-assembly of liberated surfactant molecules with inorganic components takes place in a classical EISA process. Although experimental proof on the different routes of self-assembly could not yet be obtained, the structural resemblance of the pure silica sample with the composite films gives evidence that their formation mechanism does not differ significantly. Another point is that no formation of periodic structure is observed for the polymer-stabilized particles without silica component. We therefore propose that the mesostructure formation follows rather the second case and that it involves several dynamic equilibrium steps such as adsorption/desorption of surfactant on/from titania or silica surface, reversible interactions between titania and silica components, or participation of partly particle-bound template in micelle formation. These equilibrium steps should be influenced by the surface chemistry of titania particles and the nature of the surfactant, as was demonstrated for two different types of Pluronic molecules.

### **7.3 Conclusion**

The “brick and mortar” approach utilizing Pluronic-stabilized crystalline titania nanoparticles and amorphous sol-gel derived silica precursors enables the fabrication of composite titania-

silica films with periodic mesoporous architecture. The nature of the Pluronic surfactant plays the decisive role in the mesostructure formation. The structure formation is greatly disturbed due to the presence of particles when Pluronic P123 is utilized as the structure-directing agent. In contrast, the use of larger and more hydrophilic Pluronic F127 enables the preparation of composite titania-silica mesoporous architectures which can accommodate up to 50 wt % of nanocrystals without significant deformation of the mesostructure periodicity. Films with a high degree of crystallinity can be obtained at temperatures as low as 100-150 °C, and the surface of the titania particles is not deactivated with respect to their photocatalytic activity by the surrounding silica matrix or by covalently attached ligands. This makes the “brick and mortar” approach very promising for the preparation of crystalline functional coatings under very mild conditions that are even acceptable for plastic substrates, and opens new perspectives for the fabrication of novel mesoporous crystalline composite materials.

### 7.4 Experimental Section

#### Preparation of titania nanoparticles and titania-silica films

Titanium dioxide nanoparticles were synthesized following a modified procedure by Niederberger et al.<sup>31</sup> Titanium tetrachloride (1.5 mL, 13.7 mmol) was dissolved in toluene (10 mL) and added to benzyl alcohol (30 mL, 290.8 mmol) under continuous stirring. The solution was kept at 60 °C for 20 h, then cooled down to room temperature. The particles were separated by centrifugation at 50000 rcf for 30 minutes and used without further treatment. As such, the particles contain about 55 wt % of benzyl alcohol according to thermogravimetric analysis; this was taken into account for the adjustment of the TiO<sub>2</sub>-content. In a typical synthesis, a solution of Pluronic P123 (PEO<sub>20</sub>PPO<sub>70</sub>PEO<sub>20</sub>, 0.6 g) or Pluronic F127 (PEO<sub>106</sub>PPO<sub>70</sub>PEO<sub>106</sub>, 0.55 g) in THF (5 ml) was added to non-washed

## 7. Synthesis of Mesoporous Titania-Silica Films

---

particles previously separated by centrifugation and stirred overnight until the particles were homogeneously redispersed. Subsequently, the desired amount of silica sol-gel (SG, see below) solution was added followed by stirring for several minutes. The final solutions were transparent or translucent, being of yellow to orange color. If the final solution was not transparent, then some amount of concentrated hydrochloric acid was added dropwise until the solution turned transparent. The SG solution was prepared by adding hydrochloric acid (0.1 M, 11 mL, 1.1 mmol) to tetraethyl orthosilicate (15 mL, 67.25 mmol) in 15 ml THF under continuous stirring and was stirred for 15 hours at room temperature. The composition of the solutions with different  $\text{TiO}_2/\text{SiO}_2$  ratios is listed in Table 7.3 (the values in brackets correspond to the amount of pure oxide).

$\text{TiO}_2/\text{MO}_2$ , wt %	Amount of nanoparticles/ $\text{TiO}_2$	Amount of SG (ml) / $\text{SiO}_2$ (g)
0	0	5.6 ml (0.55 g)
10	0.11 g (0.05 g)	4.5 ml (0.44 g)
15	0.16 g (0.07 g)	3.9 ml (0.38 g)
30	0.27 g (0.12 g)	2.8 ml (0.28 g)
50	0.38 g (0.17 g)	1.7 ml (0.17 g)

**Table 7.3.** Composition of the solutions used for the dip-coating of thin films

The films were deposited by dip-coating at  $23 \pm 2$  °C and a relative humidity of  $45 \pm 10$  % at a withdrawal rate of 1.8 mm/s, and either calcined at 300 °C (with a ramp of  $0.6$  °C  $\text{min}^{-1}$ ) for 30 minutes or treated at 100-150°C for 15 hours for their subsequent extraction with ethanol. The extraction was performed at 80°C under reflux for 4 to 18 hours. The thickness of the obtained films was ca. 300 nm as was measured by profilometry (Dektak 150, Veeco Instr.).

### **Characterization of the films**

High Resolution Transmission Electron Microscopy (HRTEM) and Scanning Transmission Electron Microscopy in High Angle Annular Dark Field mode (STEM-HAADF) was performed using a FEI Titan 80-300 equipped with a field emission gun operated at 300 kV. The particulate samples were prepared by evaporating a drop of a diluted solution of particles with small amounts of Pluronic P123 in THF on a Plano holey carbon coated copper grid. HRTEM of films was carried out by scraping the thin-film samples off the substrate onto a holey carbon coated copper grid. The film thickness was measured by profilometry (Dektak). The porosity of the films was determined by the analysis of adsorption isotherms of Kr at the boiling point of liquid nitrogen (approx. 77 K) using an ASAP 2010 apparatus (Micromeritics). Krypton sorption experiments were performed and evaluated by Dr. J. Rathouský and V. Kalousek at the J. Heyrovský Institute, Prague. Raman spectra were recorded with a LabRAM HR UV-VIS (Horiba Jobin Yvon) Raman microscope (Olympus BX41) with a Symphony CCD detection system using a HeNe laser at 632.8 nm. The spectra were taken from material removed from the substrate. X-ray diffraction was carried out in reflection mode using a Scintag XDS 2000 (Scintag Inc.) with Ni-filtered CuK $\alpha$ -radiation.

The experimental set-up for the photocatalytic tests consisted of a gas supply part, the photoreactor, and a chemiluminescent NO-NO<sub>x</sub> gas analyzer. (Horiba ambient monitor APNA-360). The gaseous reaction mixture was prepared by mixing streams of dry air (1500 mL/min), wet air (1500 mL/min, relative humidity of 100 %) and 50 ppm NO/N<sub>2</sub> (approx. 60 mL/min), in order to obtain a final concentration of NO of 1 ppm at a relative humidity of 50 %. The photoreactor was illuminated by four 8 W black lights, thus achieving a UV light intensity of 1 mW/cm<sup>2</sup>. Prior to the photocatalytic tests, the photoreactor was purged with the NO/water vapor/air mixture without illumination until a steady NO concentration was achieved at the outlet. 100 % NO conversion is equivalent to a photonic efficiency of  $\xi=0.14$  % assuming a mean irradiation wavelength of 350 nm. All photocatalytic experiments

were performed and evaluated by Dr. J. Rathouský and V. Kalousek at the J. Heyrovský Institute, Prague.

### 7.5 References

1. Sanchez, C.; Boissiere, C.; Grosso, D.; Laberty, C.; Nicole, L. *Chem. Mater.* **2008**, *20*, 682-737.
2. Antonietti, M.; Niederberger, M.; Smarsly, B. *Dalton Trans.* **2008**, 18-24.
3. Djerdj, I.; Arcon, D.; Jaglicic, Z.; Niederberger, M. *J. Solid State Chem.* **2008**, *181*, 1571-1581.
4. Pinna, N.; Niederberger, M. *Angew. Chem. Int. Ed.* **2008**, *47*, 5292-5304.
5. Lee, D.; Rubner, M. F.; Cohen, R. E. *Nano Lett.* **2006**, *6*, 2305-2312.
6. Page, M. G.; Nassif, N.; Borner, H. G.; Antonietti, M.; Cölfen, H. *Cryst. Growth Des.* **2008**, *8*, 1792-1794.
7. Niederberger, M.; Cölfen, H. *Phys. Chem. Chem. Phys.* **2006**, *8*, 3271-3287.
8. Agrios, A. G.; Cesar, I.; Comte, P.; Nazeeruddin, M. K.; Grätzel, M. *Chem. Mater.* **2006**, *18*, 5395-5397.
9. Arumugam, P.; Xu, H.; Srivastava, S.; Rotello, V. M. *Polymer Int.* **2007**, *56*, 461-466.
10. Boal, A. K.; Ilhan, F.; DeRouchey, J. E.; Thurn-Albrecht, T.; Russell, T. P.; Rotello, V. M. *Nature* **2000**, *404*, 746-748.
11. Liu, R.; Ren, Y.; Shi, Y.; Zhang, F.; Zhang, L.; Tu, B.; Zhao, D. *Chem. Mater.* **2008**, *20*, 1140-1146.
12. Rajeshwar, K.; de Tacconi, N. R.; Chenthamarakshan, C. R. *Chem. Mater.* **2001**, *13*, 2765-2782.

13. Penard, A. L.; Gacoin, T.; Boilot, J. P. *Acc. Chem. Res.* **2007**, *40*, 895-902.
14. Boettcher, S. W.; Fan, J.; Tsung, C.-K.; Shi, Q.; Stucky, G. D. *Acc. Chem. Res.* **2007**, *40*, 784-792.
15. Mackenzie, J. D.; Bescher, E. P. *Acc. Chem. Res.* **2007**, *40*, 810-818.
16. Kotsokechagia, T.; Cellesi, F.; Thomas, A.; Niederberger, M.; Tirelli, N. *Langmuir* **2008**, *24*, 6988-6997.
17. Husing, N.; Launay, B.; Doshi, D.; Kickelbick, G. *Chem. Mater.* **2002**, *14*, 2429-2432.
18. Calleja, G.; Serrano, D. P.; Sanz, R.; Pizarro, P. *Microp. Mesop. Mater.* **2008**, *111*, 429-440.
19. Dong, W. Y.; Sun, Y. J.; Lee, C. W.; Hua, W. M.; Lu, X. C.; Shi, Y. F.; Zhang, S. C.; Chen, J. M.; Zhao, D. Y. *J. Am. Chem. Soc.* **2007**, *129*, 13894-13904.
20. Zhang, X.; Zhang, F.; Chan, K. Y. *Appl. Catal. A-Gen.* **2005**, *284*, 193-198.
21. Inumaru, K.; Kasahara, T.; Yasui, M.; Yamanaka, S. *Chem. Comm.* **2005**, 2131-2133.
22. Allain, E.; Besson, S.; Durand, C.; Moreau, M.; Gacoin, T.; Boilot, J. P. *Adv. Funct. Mater.* **2007**, *17*, 549-554.
23. Reddy, E. P.; Sun, B.; Smirniotis, P. G. *J. Phys. Chem. B* **2004**, *108*, 17198-17205.
24. López-Muñoz, M.-J.; Grieken, R. v.; Aguado, J.; Marugán, J. *Catal. Today* **2005**, *101*, 307-314.
25. van Grieken, R.; Aguado, J.; López-Muñoz, M. J.; Marugán, J. *J. Photochem. Photobiol. A: Chem.* **2002**, *148*, 315-322.
26. Gaya, U. I.; Abdullah, A. H. *J. Photochem. Photobiol. C-Photochem. Rev.* **2008**, *9*, 1-12.
27. Dunn, B.; Zink, J. I. *Acc. Chem. Res.* **2007**, *40*, 747-755.
28. Ogawa, M.; Ikeue, K.; Anpo, M. *Chem. Mater.* **2001**, *13*, 2900-2904.
29. Wu, C.-W.; Kuwabara, M. *J. Inorg. Organomet. Polym.* **2003**, *13*, 131-141.

30. Niederberger, M.; Garnweitner, G.; Pinna, N.; Neri, G. *Progress Solid State Chem.* **2005**, *33*, 59-70.
31. Niederberger, M.; Bartl, M. H.; Stucky, G. D. *Chem. Mater.* **2002**, *14*, 4364-4370.
32. Polleux, J.; Pinna, N.; Antonietti, M.; Hess, C.; Wild, U.; Schlögl, R.; Niederberger, M. *Chem. Eur. J.* **2005**, *11*, 3541-3551.
33. Boal, A. K.; Gray, M.; Ilhan, F.; Clavier, G. M.; Kapitzky, L.; Rotello, V. M. *Tetrahedron* **2002**, *58*, 765-770.
34. Yang, P. D.; Zhao, D. Y.; Margolese, D. I.; Chmelka, B. F.; Stucky, G. D. *Nature* **1998**, *396*, 152-155.
35. Zhao, D.; Yang, P.; Melosh, N.; Feng, J.; Chmelka, B. F.; Stucky, G. D. *Adv. Mater.* **1998**, *10*, 1380-+.
36. Baddour-Hadjean, R.; Bach, S.; Smirnov, M.; Pereira-Ramos, J. P. *J. Raman Spectr.* **2004**, *35*, 577-585.
37. Smirnov, M.; Baddour-Hadjean, R. *J. Chem. Phys.* **2004**, *121*, 2348-2355.
38. Guo, C.; Liu, H.; Wang, J.; Chen, J. *J. Coll. Interf. Science* **1999**, *209*, 368-373.

## **8. All-Inorganic Core-Shell Silica-Titania Mesoporous Colloidal Nanoparticles Showing Orthogonal Functionality**

*This chapter is based on the following publication:*

Valentina Cauda, Johann M. Szeifert, Karin Merk, Dina Fattakhova-Rohlfing, Thomas Bein, *Journal of Materials Chemistry*, accepted.

### **8.1 Introduction**

Colloidal mesoporous silica (CMS) nanoparticles are of great interest as potential candidates for applications in gas-sensing,<sup>1</sup> host-guest chemistry and drug delivery.<sup>2-3</sup> The functionality of the CMS is caused by their large surface area and a mesoporous structure with tunable pore size, which makes them ideal hosts for the accommodation of various guest species. Most of the intended applications require silica nanoparticles with specific organic or inorganic functionalization, thus providing properties not obtainable from pure silica materials.<sup>4</sup> A special advantage of mesoporous silica nanoparticles is their chemical versatility and solution processability, making it possible to selectively functionalize different locations on the nanoparticle, for example inner pore volume and outer particle surface.<sup>5-6</sup> By using different functional groups, even nanoparticles with site-specific orthogonal functionality can be obtained.<sup>7</sup> In most cases, however, this extended functionality comes at the cost of limited thermal or chemical stability.

We propose the combination of two metal oxides such as silica and titania as an alternative approach toward the generation of core-shell nanoparticles with orthogonal chemical functionality. Titanium dioxide is commonly used as an inexpensive, non-toxic pigment.

## 8. Core-Shell Silica-Titania Mesoporous Nanoparticles showing Orthogonal Functionality

---

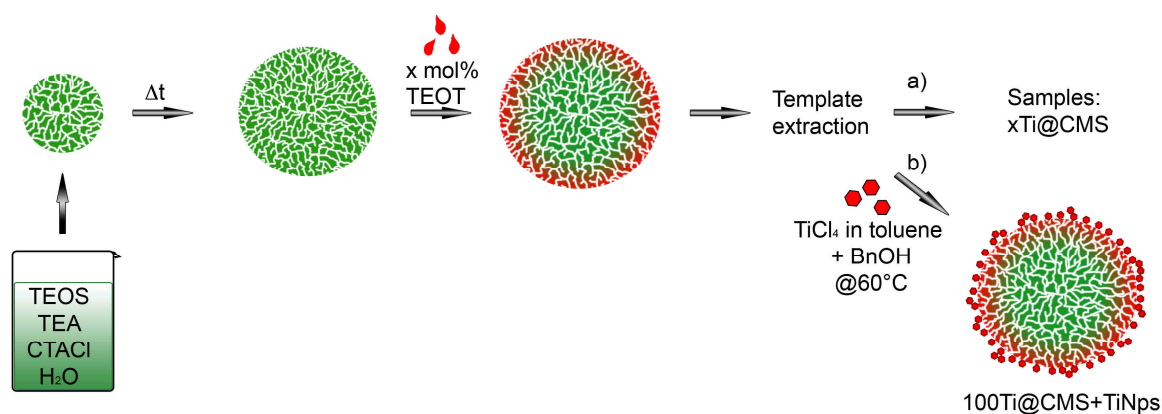
Additionally, its semiconducting properties are used in applications including non-silicon solar cells, photocatalysis and energy storage, respectively.<sup>8</sup> Although both silica and titania are chemically related and form solid solutions, titania exhibits different functionality and chemical reactivity. In contrast to silica, the titania surface shows a higher stability in basic media and has a strong affinity to acidic groups such as carboxylic or phosphonic acids, which is often used for the grafting of acid-containing moieties.<sup>9</sup> Previous examples of the spatially resolved combination of both materials are related to the deposition of a thin titania-shell on non-porous silica nanoparticles<sup>10-11</sup>, thus obtaining a good spatial definition of titania in highly dispersed colloids. Recently, silica-titania hollow nanoparticles were fabricated to study the cellular uptake and cytotoxicity in living cancer cells for drug delivery applications.<sup>12</sup> Other combinations of silica and titania in the form of thin films or bulk materials have been investigated with a view on different applications, including photocatalysis,<sup>13-14</sup> catalysis,<sup>15</sup> and optical devices<sup>16-18</sup> for chemical sensing.

Mesoporous titania-silica composites are primarily synthesized following two synthetic strategies. The first approach is the mixing of the two sol-gel precursors, or silica sol-gel and titania nanoparticles and subsequent surfactant-assisted assembly into a mesoporous structure.<sup>13-15,19</sup> This procedure is useful for obtaining well-ordered structures, especially in thin films, however, no spatially selective functionalization can be achieved. The second pathway involves the templated self-assembly of bulk mesoporous silica followed by post-modification using a titania precursor, resulting in a mostly amorphous TiO<sub>2</sub> shell.<sup>20-21</sup> These composite materials feature the chemical reactivity of titania coupled with a high surface area and good thermal stability. However, the post-synthetic coating of the bulk mesoporous silica often covers the pore openings, resulting in limited accessible pore volume. Furthermore, control over the spatial distribution of the two oxides is not possible in this case. The above-mentioned synthetic methods commonly rely on a final calcination step to achieve

## 8. Core-Shell Silica-Titania Mesoporous Nanoparticles showing Orthogonal Functionality

crystallization of titania. Such a calcination step would preclude the synthesis of colloidal systems due to irreversible agglomeration and loss of dispersibility.

Here we report the low-temperature preparation of colloidal mesoporous silica-core/titania-enriched shell nanoparticles with spatially resolved functionality. Instead of incorporating Ti atoms throughout the whole CMS nanoparticle, titania is selectively introduced at the outer shell of the mesoporous silica nanoparticles by a delayed co-condensation approach, in analogy to the site-selective functionalization previously reported by us<sup>5-6</sup> (Scheme 8.1).



**Scheme 8.1.** Synthetic pathway for the titania-shell colloidal mesoporous silica (CMS) nanoparticles. A delayed co-condensation approach is used to first synthesize the mesoporous silica core (in green) and then enrich the outer surface (in red) with the titania-phase, followed by template extraction. (a) Depending on the molar amount of TEOT added (with respect to the initial amount of silica) different  $x\text{Ti@CMS}$  samples are obtained. (b) The sample with the highest amount of Ti,  $100\text{Ti@CMS}$  (see Table 8.1), was used to nucleate anatase nanocrystallites (TiNPs) on the outer shell, increasing the orthogonality of the system (abbreviations: see Experimental Section).

Different Si/Ti ratios in the nanoparticle shells were obtained by changing the titania precursor stoichiometry. Furthermore, crystalline titania shells were also obtained via

## 8. Core-Shell Silica-Titania Mesoporous Nanoparticles showing Orthogonal Functionality

---

nucleation of anatase on the amorphous titania shell from a benzyl alcohol reaction system.<sup>22-</sup>

<sup>23</sup> This non-aqueous approach avoids the use of high temperature treatments, which would lead to irreversible particle aggregation. As a proof of principle addressing the spatially selective reactivity we present the selective adsorption of the carboxylate-containing ruthenium dye N3<sup>24-25</sup> and its fluorescence quenching upon specific adsorption to the titania-sites.

Key features of these titania-enriched shell mesoporous silica nanoparticles include their spatially-resolved, thus “chemically orthogonal” functionality, the biocompatibility of the two inorganic oxides, and their high porosity and nanoscopic size. These features can be attractive for drug delivery applications, bio-imaging and diagnostics. In addition, the titania-containing shell is expected to protect the mesoporous silica core against degradation by biological fluids due to its higher chemical stability.

The following experiments have been performed as a joint project between Dr. Valentina Cauda, Karin Merk, and Johann M. Szeifert in the group of Prof. Dr. Thomas Bein. The responsibilities were shared as follows: Dr. Valentina Cauda and Karin Merk contributed by synthesizing the mesoporous silica particles and characterization using sorption, zeta potential measurements, UV-Vis, and fluorescence spectroscopy. Functionalization of the silica particles with titanium dioxide, and X-ray diffraction analysis was done by Johann M. Szeifert. Dr. Valentina Cauda and Johann M. Szeifert were both responsible for the conceptual design of the experiments and the final interpretation of the data.

### 8.2 Results and Discussion

#### Mesoporous nanoparticle characterization

A solution of TEOS and triethanolamine (TEA) in water with the template, cetyltrimethylammonium chloride (CTAC), leads to the growth of a CMS nanoparticle. After 20 min the titania source (TEOT) is added to the uncompleted CMS synthetic mixture, leading to a co-condensation of silica and titania precursors. We anticipate that the resulting colloidal nanoparticles consist of a mesoporous silica core and a titania-enriched mesoporous silica shell. By varying the added amount of TEOT, different Si/Ti ratios in the resulting nanoparticle shells were obtained. Furthermore, a precursor solution for the synthesis of crystalline titania nanoparticles (TiNPs) of about 4 nm in diameter in benzyl alcohol<sup>22</sup> is added to the titania-shell CMS nanoparticles having the highest content of titania.

The UV-Vis spectra of the titania-enriched shell CMS samples in Figure 8.1a show an absorption band in the region of 220-240 nm. This absorption results from a ligand-to-metal charge transfer from oxygen to Ti(IV) as reported for titania incorporated in a silica network.<sup>15,17</sup> In particular, greater amounts of TEOT added to the reaction mixture result in a higher Ti-content of the samples and higher absorbance. In contrast, the pure silica nanoparticles (sample CMS, curve A) show negligible absorption in the measured UV-Vis range. These results suggest the incorporation of Ti atoms into the silica nanoparticles according to the Ti/Si ratio of the reactants.

Sample	Molar ratio <sup>a</sup> TEOT/TEOS	Total amount of TEOT [mmol]	BET surface area [m <sup>2</sup> /g]	Pore size [nm]	Pore volume [cm <sup>3</sup> /g]
<b>CMS</b>	0	0	1056	3.8	0.89
<b>10Ti@CMS</b>	0.1	0.92	1009	3.8	0.77
<b>50Ti@CMS</b>	0.5	4.61	1187	3.7	0.88
<b>80Ti@CMS</b>	0.8	7.38	963	3.8	0.72
<b>100Ti@CMS</b>	1	9.22	1115	3.7	0.87
<b>100Ti@CMS + TiNPs</b>	1 + 1 TiNPs <sup>b</sup>	9.22 (+ 9.22 TiCl <sub>4</sub> )	1279	4.2	1.15

**Table 8.1.** List of samples with molar ratio and molar amount of TEOT added in the synthetic mixture and their structural parameters.

<sup>a</sup> Total molar ratio of TEOT added vs. initial amount of TEOS in the synthesis solution.

<sup>b</sup> The quantity 1 TiNPs refers to a molar ratio of 1:1 between TiCl<sub>4</sub> and the initial amount of TEOS.

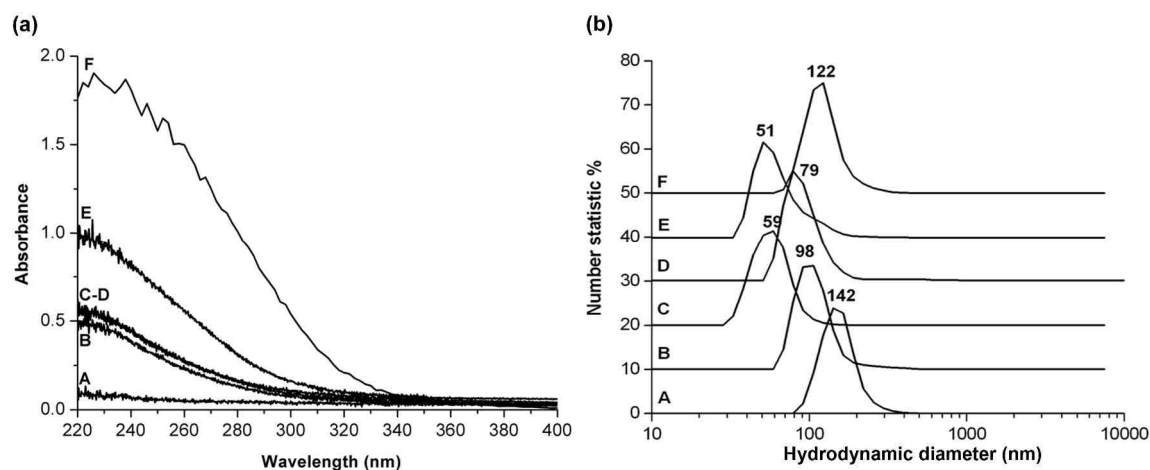


**Figure 8.1.** (a) UV-Vis spectra and (b) dynamic light scattering data of the samples: A: CMS; B: 10Ti@CMS; C: 50Ti@CMS; D: 80Ti@CMS; E: 100Ti@CMS; F: 100Ti@CMS+TiNPs. For clarity, the DLS curves are shifted along the y-axis by 10 units each.

Dynamic light scattering (DLS) curves (Figure 8.1b) show that the dispersed particles have a nanoscopic size in all samples. We note that with increasing titania content in the external shell the CMS particle size is reduced. We attribute this behaviour to a more negative surface charge as the Ti-content in the shell increases. This could be determined by zeta-potential measurements, which show a constant slight decrease of the zeta-potential values as the content of Ti in the CMS-shell increases (Figure 8.2).

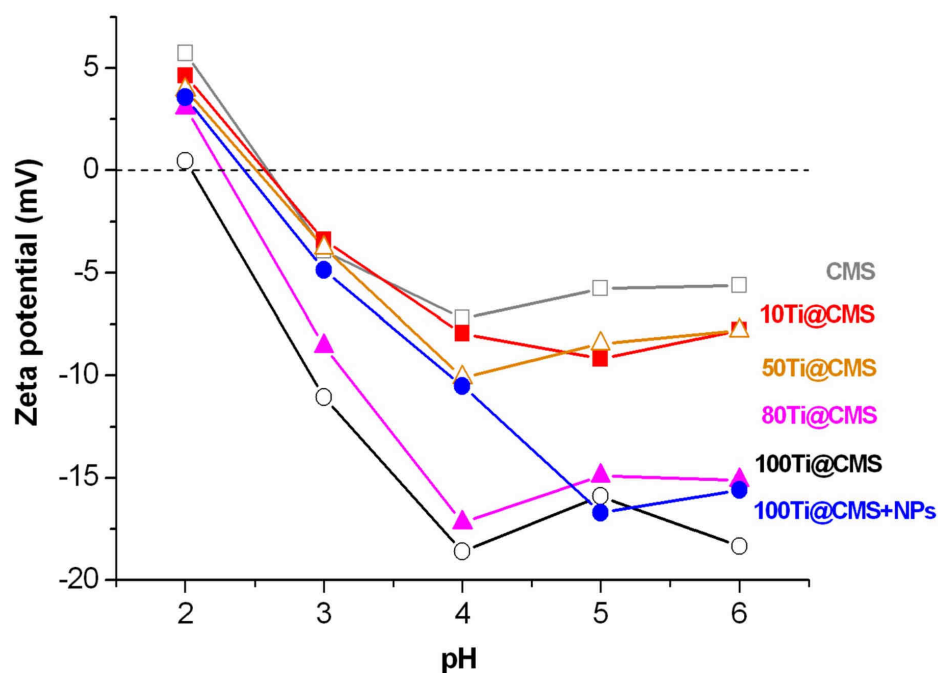


**Figure 8.2.** Z-potential measurements of the xTi-shell containing CMS nanoparticles (red filled squares: 10Ti@CMS; orange empty triangles: 50Ti@CMS; magenta filled triangles: 80Ti@CMS; black empty circles: 100Ti@CMS; blue filled circles: 100Ti@CMS+NPs) compared with the pure silica CMS nanoparticles (grey empty squares).

The pure silica sample exhibits zeta-potential values slightly closer to neutrality than the other Ti-containing samples. Their negatively charged surface results in a high repulsion between the nanoparticles in solution, and as a consequence in the small effective particle size and high colloidal stability of the Ti-shell CMS nanoparticles, as shown with Dynamic Light Scattering (DLS) measurements (see Figure 8.1a). This leads, on the one hand, to a higher repulsion and thus a lower tendency to agglomeration, and, on the other hand, to different sizes of the solvation shells and the corresponding changes in hydrodynamic radius. Interestingly, the sample 100Ti@CMS+TiNPs shows a larger mean particle size than the sample 100Ti@CMS, which we attribute to the presence of the anatase nanocrystals on the titania-shell surface. It is likely that this size difference is caused not only by the dimensions

of the titania nanocrystals, but also by the different surface charge and thus a different hydrodynamic radius in solution.

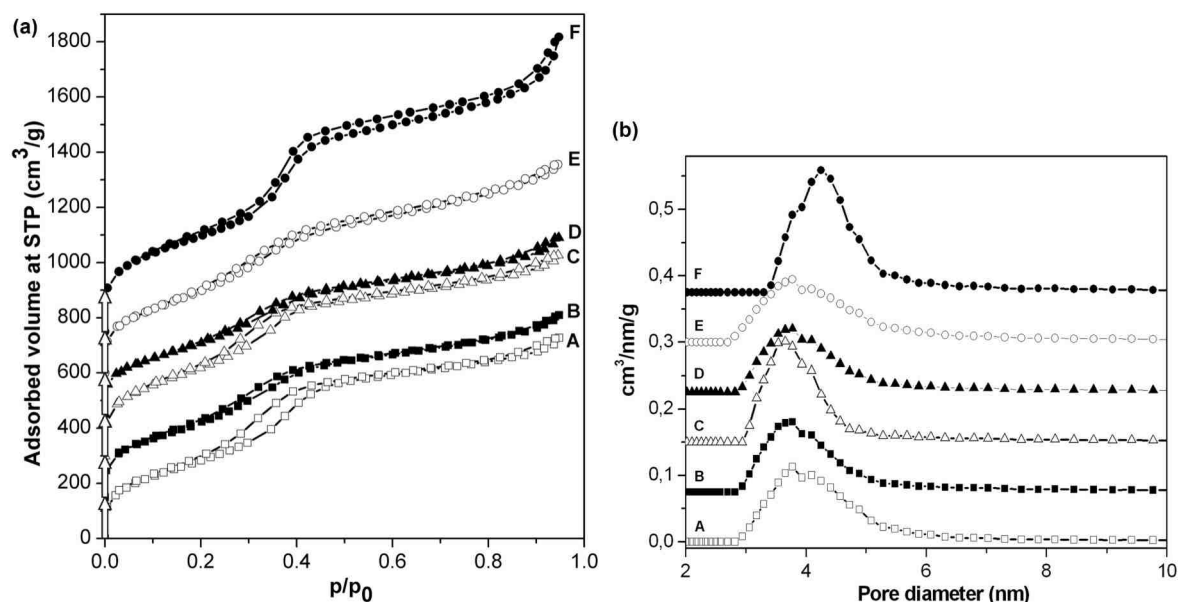


**Figure 8.3.** (a) Nitrogen sorption measurements and (b) DFT pore size distributions of the titania-shell CMS nanoparticles in comparison to the unmodified silica-CMS. A: CMS; B: 10Ti@CMS; C: 50Ti@CMS; D: 80Ti@CMS; E: 100Ti@CMS; F: 100Ti@CMS+TiNPs. For clarity reasons, the isotherms are shifted along the y-axis by 150 units each and the DFT pore size distributions are offset by 0.075 units.

Nitrogen sorption measurements of all samples (Figure 8.3a) exhibit type IV isotherms typical for mesoporous materials, with pore filling steps at around  $p/p_0 = 0.3 - 0.4$ . The isotherms of the titania-enriched shell samples show no significant changes with respect to the pure mesoporous silica nanoparticles (BET surface areas and pore volumes, see Table 8.1), concluding that the titania inclusion in the silica shell does not affect the mesoporous features of the nanoparticles. All the particles show a pore size of around 3.7-3.8 nm obtained by a DFT method and uniform pore size distributions (Figure 8.3b) except for 100Ti@CMS+TiNPs, having a slightly larger pore size of about 4.2 nm. Since the pore sizes

## 8. Core-Shell Silica-Titania Mesoporous Nanoparticles showing Orthogonal Functionality

of the xTi@CMS samples do not decrease with respect to the pure CMS nanoparticles, we conclude that the addition of titania precursor leads to an enrichment of titanium dioxide species only at the outer shell of the mesoporous nanoparticles.

Small-angle X-ray scattering shows the first order (100)-like reflection at  $2\theta = 1.98^\circ$  for all titania-shell nanoparticles and the pure silica sample (Figure 8.4a). The absence of higher order reflections indicates a worm-like mesoporous structure of the titania-shell CMS particles.

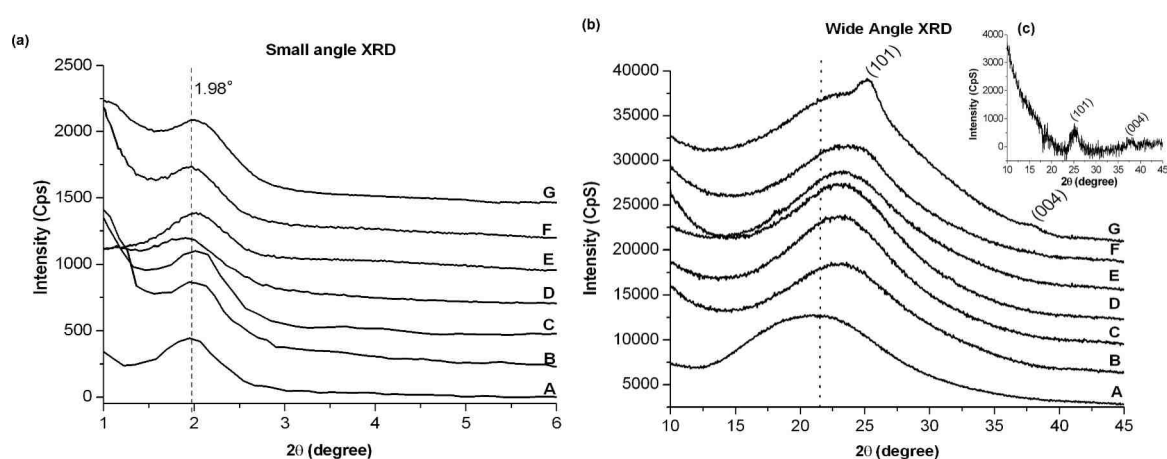


**Figure 8.4.** (a) Small angle and (b) wide angle X-ray diffraction pattern of the titania-shell CMS nanoparticles; (c, inset) WAXS pattern of the sample 100Ti@CMS+TiNPs after subtraction of the 100Ti@CMS pattern. A: CMS; B: 10Ti@CMS; C: 50Ti@CMS; D: 80Ti@CMS; E: 100Ti@CMS; F: 100Ti@CMS+TiNPs; G: 100Ti@CMS+TiNPs after calcination at 450 °C. For clarity reasons, the small angle XRD patterns are shifted along the y-axis by 100 units each (the pattern B by 400 units) and the wide angle XRD data are offset by 2500 units.

Wide-angle X-ray scattering (WAXS) for the CMS sample (Figure 8.4b, trace A) shows the broad feature centered at  $22^\circ$  attributed to amorphous silica. This reflection shifts gradually to a higher angle ( $24^\circ$ ) as the titania content at the outer shell of the samples increases (traces

## 8. Core-Shell Silica-Titania Mesoporous Nanoparticles showing Orthogonal Functionality

---

from B to E). This behavior is attributed to the shorter Ti-O-Ti and Ti-O-Si bonds with respect to the Si-O-Si bonds.<sup>26-27</sup> The sample 100Ti@CMS+TiNPs (trace F) shows an additional shoulder in the WAXS pattern at about 25° that is attributed to the (101) reflection of anatase (see also Figure 3c, in which the contribution of the amorphous part is subtracted). This becomes more evident upon additional calcination of sample 100Ti@CMS+TiNPs at 450 °C (Figure 3b, trace G), showing the (101) and (004) reflections of the crystalline anatase phase. The retention of the worm-like mesoporous structure upon calcination was also assessed by SAXS (Figure 8.4a, trace G). However, after such thermal treatment the dried particles are no longer colloiddally dispersible.

The presence of anatase nanocrystalline clusters in sample 100Ti@CMS+TiNPs even without calcination is observed with transmission electron microscopy (HRTEM, Figure 8.5g). In this micrograph dark spots, resulting from the higher contrast due to Ti compared to Si, are clearly observed at the edge of the CMS nanoparticles (in grey). Correspondingly, scanning transmission electron microscopy (STEM, Figure 8.5i) shows a brighter region attributed to Ti oxide at the CMS surface. Electron diffraction patterns (Figure 8.5l) and a high-resolution TEM image (HRTEM, Figure 8.5h) clearly show nanocrystalline clusters, assigned to the anatase phase, at the outer surface of the CMS nanoparticles.

TEM images of the other colloidal 10Ti@CMS and 100Ti@CMS nanoparticles (Figures 8.5a and 8.5d, respectively) show monodispersed, highly porous particles with worm-like mesoporous structure. The presence of the titania-enriched shell is almost negligible for the 10Ti@CMS sample (Figures 8.5a and b), whereas for sample 100Ti@CMS it is indicated by dark spots in the TEM image (Figure 8.5d) and bright clusters in STEM mode (Figures 8.5e). We conclude that the incidence of such contrast variations due to titanium enrichment increases as the amount of titania-precursors in the synthesis increases. Moreover, as already observed in the WAXS measurements, the electron diffraction patterns of samples 10Ti@CMS and 100Ti@CMS (Figures 8.5c and f, respectively) show only amorphous phases.

## 8. Core-Shell Silica-Titania Mesoporous Nanoparticles showing Orthogonal Functionality

The results of Energy Dispersive Spectroscopy (EDS) and elemental analysis (ICP) shown in Table 8.2 demonstrate that the Ti/Si ratio in the nanoparticles is significantly lower than the molar ratios of TEOT/TEOS precursors in the particle synthesis.

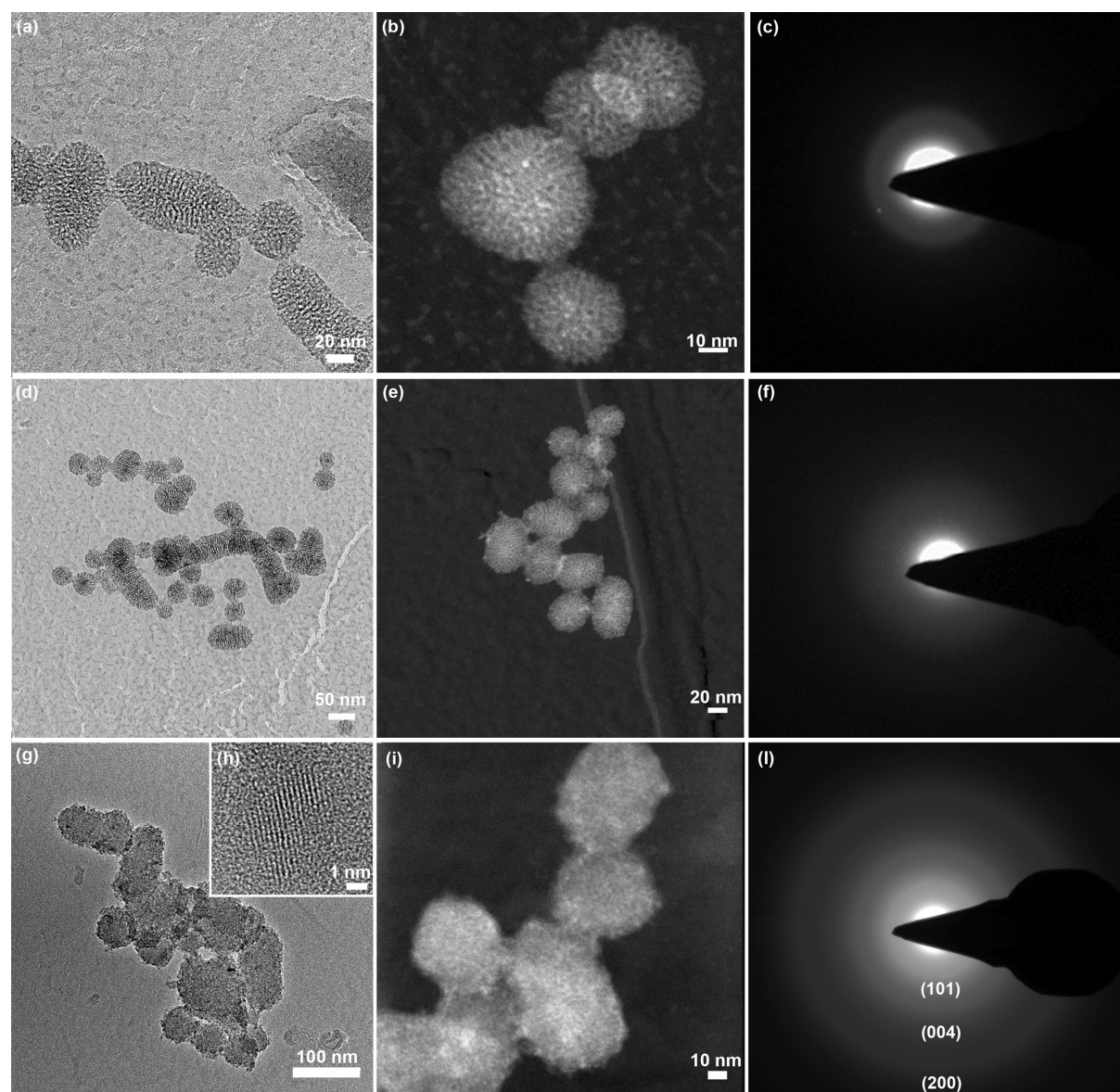


**Figure 8.5.** Transmission electron micrographs (TEM, left column), scanning transmission electron micrographs (STEM, central column), and electron diffraction patterns (right column) of the samples (a-c) 10Ti@CMS; (d-f) 100Ti@CMS; (g-l) 100Ti@CMS+TiNPs. Figure (h) represents the lattice fringes showing the crystallinity of the  $\text{TiO}_2$  nanoparticles at the edge of the CMS nanoparticles depicted in micrograph g.

## 8. Core-Shell Silica-Titania Mesoporous Nanoparticles showing Orthogonal Functionality

---

This indicates that the incorporation of titania into the shell of the mesoporous nanoparticles is kinetically limited and that some of the TEOT is hydrolyzed and polymerized not only on the particle surface but also in solution, forming soluble species which are removed during the washing step. The formation of anatase nanocrystals strongly increases the fraction of Ti obtained on the sample 100Ti@CMS+TiNPs. This trend is also confirmed by the elemental analysis (ICP) results (see the comparison between the Ti/Si ratios calculated from EDS and ICP results).

Sample	Ti/Si (from EDS)	Ti/Si (from ICP)
CMS	-	-
10Ti@CMS	0.020	0.009
100Ti@CMS	0.031	0.016
100Ti@CMS + TiNps	0.199	0.134

**Table 8.2.** Relative ratio of titanium to silicon obtained by EDS and elemental analysis (ICP) on different x-titania-shell CMS nanoparticles and the reference pure silica nanoparticles.

### N3-dye measurements

The results discussed above clearly indicate that an amorphous titania phase is formed through the delayed co-condensation approach on the mesoporous silica core. Moreover, the titania-enriched shell is able to serve as preferential nucleation site for the nanocrystalline anatase clusters. In this way, the sol-gel approach leads to fully inorganic silica-core titania/silica-shell mesoporous nanoparticles, which can exhibit an orthogonal chemical functionality, i.e., a spatially-resolved affinity to different chemical species.

## 8. Core-Shell Silica-Titania Mesoporous Nanoparticles showing Orthogonal Functionality

As a proof of principle we have examined the orthogonal functionality of such titania-enriched shell CMS nanoparticles by adsorption of a ruthenium-centered polypyridyl dye, N3. This complex possesses four carboxyl groups and is expected to preferentially bind to the titania-phase of the nanoparticles.<sup>18</sup> Specifically, we have examined both 100Ti@CMS samples, with and without the anatase nanocrystallites, and compared the results to the pure silica CMS nanoparticles. The N3-dye solutions were measured by UV-Vis spectroscopy before and after the uptake into the xTi@CMS and CMS samples (Figure 8.5a).

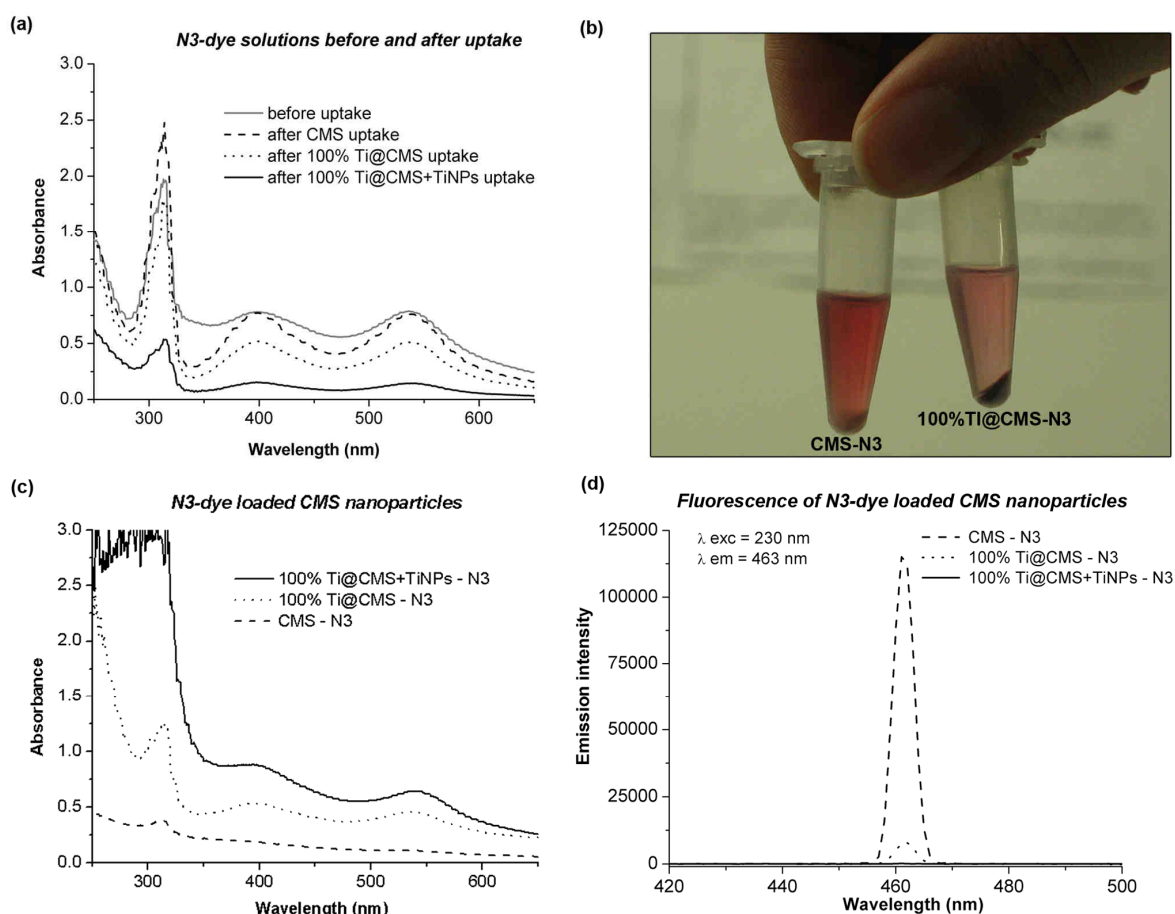


**Figure 8.6.** N3-dye adsorption experiments on the samples: CMS (dashed line), 100%Ti@CMS (dotted line) and 100%Ti@CMS+TiNPs (solid line). (a) UV-Vis absorption spectra of the N3 solutions before (solid line in gray) and after uptake in different sample solutions; (b) photograph of the reference sample CMS and of the 100%Ti@CMS after N3

## 8. Core-Shell Silica-Titania Mesoporous Nanoparticles showing Orthogonal Functionality

---

uptake with the supernatant solution analyzed in Figure 8.6a. (c) UV-Vis absorption spectra of the nanoparticles as colloidal solution in water after N3-dye adsorption; (d) Fluorescence spectra of the same colloidal nanoparticle solution, clearly showing the emission quenching of the N3 adsorbed on the sample 100%Ti@CMS+TiNPs.

After the adsorption step, the UV-Vis spectra of the solutions show the remaining amount of the dye that is not adsorbed into the samples. The N3-solution after the uptake into the 100Ti@CMS+TiNps shows the lowest absorbance (solid line), whereas the dye solution of the reference CMS nanoparticles shows the highest absorbance (dash line) in comparison to the initial N3-solution before the uptake (gray line). The colloidal suspensions of the N3-loaded nanoparticles were washed and centrifuged several times in order to desorb any physisorbed N3-dye and were then measured again by UV-Vis spectroscopy (Figure 8.6c). The highest adsorption levels are obtained for the 100Ti-containing shell CMS nanoparticles with the anatase nanocrystallites (100Ti@CMS+TiNps, solid line), whereas the lowest dye loadings were recorded for the reference CMS nanoparticles (dashed line). These results are also clearly visible in the photograph in Figure 8.6b, showing the nanoparticles after the centrifugation at the end of the dye-adsorption step. The sample 100Ti@CMS has assumed a darker color than the CMS sample, leaving the supernatant solution less colored with respect to that of the reference CMS sample. In conclusion, UV-Vis spectroscopy indicates a strong interaction of the N3-dye with the surface titania-phase of the CMS nanoparticles. Despite the high porosity of the mesoporous silica core, the pure CMS particles do not reach the same adsorption values as the samples with the titania-shell. This affinity between the N3-molecules and the titania-phase is increased when anatase nanocrystallites are attached to the titania-shell on the particles' surface.

## 8. Core-Shell Silica-Titania Mesoporous Nanoparticles showing Orthogonal Functionality

---

To further elucidate the localization of the N3-molecules on the titania part of the core-shell nanoparticles, the fluorescence emission of the N3-loaded nanoparticles was recorded (Figure 8.6d). It is known that the strong bond between the titania surface and the ruthenium complex enables the titania to quantitatively quench the fluorescence emission of the dye.<sup>28</sup> Strikingly, no fluorescence was detected for the N3-loaded 100Ti@CMS+TiNPs sample, and only a weak emission at 463 nm was recorded for the 100Ti@CMS, without the anatase nanocrystallites. In contrast, the reference CMS sample, showing very low levels of dye adsorption, exhibits a very intense fluorescence emission. These results show that the N3-dye molecules are selectively adsorbed at the titania shell on the CMS nanoparticles and not into the highly porous silica mesostructure of the core. In particular, the presence of anatase nanocrystallites at the titania-enriched shell of CMS nanoparticles leads to the highest dye adsorption values and the best selectivity for dye adsorption, as demonstrated by the complete quenching of its fluorescence emission.

### 8.3 Conclusion

We report on the synthesis of fully inorganic colloidal mesoporous nanoparticles with a silica-core and a titania/silica-shell. In order to obtain the selective inclusion of titania into the outer shell of mesoporous silica nanoparticles, a delayed co-condensation method using TEOT as titania precursor was applied. By varying the amount of TEOT added in the synthetic step, we show enrichment of an amorphous titania phase in the outer-shell at the particles' surface. After template extraction, the CMS nanoparticles containing the highest amount of Ti in the shell (100Ti@CMS sample) were used to nucleate titania nanocrystallites from a  $\text{TiCl}_4$  solution in benzyl alcohol at 60 °C. The presence of nanocrystalline anatase clusters could be

## 8. Core-Shell Silica-Titania Mesoporous Nanoparticles showing Orthogonal Functionality

---

observed on the surface of the colloidal 100Ti@CMS+TiNPs nanoparticles by HRTEM and STEM.

All titania-enriched shell CMS nanoparticles show a wormlike mesoporous structure, high surface area and pore volume, and a nanoscopic particle size similar to pure silica CMS nanoparticles.

To examine the orthogonal functionality of these fully inorganic silica-core titania-shell mesoporous nanoparticles, the adsorption and retention of a ruthenium-centered polypyridyl dye (N3) was investigated. UV-Vis and fluorescence spectroscopy indicate a strong interaction of the N3-dye only with the titania-phase at the outer shell of the CMS nanoparticles, thus demonstrating the selective adsorption of N3-molecules on the titania-phase and not into the highly porous silica core. We envision the use of such multiple core-shell inorganic nanoparticles in applications such as targeted drug delivery where colloidal stability and orthogonal functionality of both oxides are desired. Generalizing, this could also include access to different all-inorganic core-shell mesoporous nanoparticles offering orthogonal functionalities with the benefit of much higher thermal and chemical stability, as well as novel functionalities (catalytic, optical, magnetic...) not accessible with organic moieties.

### 8.4 Experimental Section

#### Synthesis of the mesoporous nanoparticles

The pure silica CMS nanoparticles (sample CMS) were synthesized by Dr. Valentina Cauda and Karin Merk according to a procedure described elsewhere.<sup>4</sup> Briefly, 1.92 g tetraethylorthosilicate (TEOS; 9.22 mmol; Fluka, >98 %) and 14.3 g triethanolamine (TEA;

## 8. Core-Shell Silica-Titania Mesoporous Nanoparticles showing Orthogonal Functionality

---

95.6 mmol; Aldrich, 98 %) were heated at 90 °C for 20 min without stirring in a polypropylene reactor (sol. 1). Thereafter, a second solution (sol. 2) of 2.41 mL cetyltrimethylammonium chloride (CTAC; 1.93 mmol; Fluka, 25 % in H<sub>2</sub>O) and 21.7 g (1.21 mol) bi-distilled water from a Millipore system (Milli-Q Academic A10) was prepared. It was heated at 60 °C for 20 min and then added to the sol. 1. The resulting mixture with a molar ratio of 1.0 TEOS: 0.2 CTAC: 10.37 TEA: 130.15 H<sub>2</sub>O was stirred at 500 rpm RT overnight. The nanoparticles were then isolated by centrifugation (19.000 rpm, 43.146 RCF, 20 min) and re-suspended in absolute ethanol.

The titania-enriched shell nanoparticles were synthesized by a procedure similar to our previously developed delayed co-condensation approach.<sup>5,6</sup> After combining sol. 1 and sol. 2, the mixture was stirred at 500 rpm for 20 minutes. Then a certain amount *x* of tetraethylorthotitanate (TEOT, Aldrich, > 98%), was divided into 20 portions and added at 30 second intervals giving a total molar ratio TEOT/TEOS of 0.1; 0.5; 0.8; 1.0, respectively (sample codes *x*Ti@CMS, see Table 8.1). The mixture was then stirred at 500 rpm at room temperature overnight. The template was extracted by heating the samples in a solution of 2.0 g (25.0 mmol) ammonium nitrate in 100 mL absolute ethanol for 45 min under reflux. After centrifugation (19.000 rpm, 43.146 RCF, 30 min) and re-suspending in absolute ethanol, a second extraction step with 10 mL of concentrated hydrochloric acid and 90 mL of absolute ethanol was carried out under reflux for 45 min. Afterwards, the colloidal mesoporous nanoparticles were again separated by centrifugation and redispersed in absolute EtOH.

The template was extracted by heating the samples in a solution of 2.0 g (25.0 mmol) ammonium nitrate in 100 mL absolute ethanol for 45 min under reflux. After centrifugation (19.000 rpm, 43.146 RCF, 30 min) and re-suspending in absolute ethanol, a second extraction step with 10 mL of concentrated hydrochloric acid and 90 mL of absolute ethanol was carried out under reflux for 45 min. Afterwards, the colloidal mesoporous nanoparticles were again

## 8. Core-Shell Silica-Titania Mesoporous Nanoparticles showing Orthogonal Functionality

---

separated by centrifugation and redispersed in 5 mL of absolute EtOH. To determine the concentration of nanoparticles, a known volume of colloidal solution was dried at 60 °C and the residue weighed.

The sample 100Ti@CMS was further used as a starting material for the growth of titania nanocrystallites at the outer surface of the mesoporous nanoparticles.<sup>22</sup> For this purpose, a solution of titanium tetrachloride (Aldrich, 1.0 mL, 9.22 mmol) in toluene (6.7 mL, in a ratio  $\text{TiCl}_4$  : toluene = 1 : 0.15) was added to water-free benzyl alcohol (Aldrich, 13.3 mL, 139.4 mmol, at a ratio  $\text{BnOH}$  : toluene = 3 : 2) under continuous stirring and then poured into the template-extracted 100Ti@CMS colloidal suspension (9.22 mmol of the silica content) in absolute EtOH under continuous stirring. The mixture was kept at 60 °C overnight to induce the formation of crystalline  $\text{TiO}_2$  nanoparticles (thus the sample name 100Ti@CMS+TiNPs) and afterwards washed twice with abs. EtOH by centrifugation (19.000 rpm, 43.146 RCF, 20 min). All the samples were washed with bi-distilled water for 2 h and redispersed in absolute EtOH before characterization. In order to determine the concentration of the particles in the colloidal suspension, the solvent of a known suspension volume was evaporated at 60 °C and the remaining sample was weighed. The dried sample 100Ti@CMS+TiNPs was also calcined at 450 °C for 4 h (at a ramp of 1 °C/min) in air.

### Characterization techniques

Dynamic light scattering (DLS) and zeta-potential measurements were carried out with a Malvern Zetasizer-Nano instrument with a 4 mW He-Ne laser ( $\lambda = 633$  nm) and an avalanche photodetector. DLS measurements were performed on diluted ethanolic suspensions (at a conc. of 1 mg/mL), whereas for the determination of the zeta potential profiles, one drop of the ethanolic suspension (~3 % wt.) was mixed prior to measurement with 2 mL commercial Hydrion Buffer solutions, having pH values of 2, 3, 4, 5 and 6, respectively. UV-Vis

## 8. Core-Shell Silica-Titania Mesoporous Nanoparticles showing Orthogonal Functionality

measurements were performed on a UV-Vis spectrophotometer (Hitachi U-3501) with ethanolic suspensions of the nanoparticles (conc. 1.15 mg/mL) in a 1 mm path length cuvette. X-ray diffraction was carried out in reflection mode using a Bruker D8 Discover with Ni-filtered  $\text{CuK}_\alpha$ -radiation and a position-sensitive detector (Vantec). Nitrogen sorption measurements were performed on all samples with a Quantachrome Instruments NOVA 4000e at 77 K. Pore size distribution and volume were calculated with a NLDFT equilibrium model of  $\text{N}_2$  on silica. The pore volume was determined up to a pore size of 8 nm in order to eliminate the contribution of interparticle textural mesoporosity. The specific surface area was estimated using a BET model. For Transmission Electron Microscopy (TEM) and Scanning Transmission Electron Microscopy (STEM) a Titan 80-300 microscope operating at 300 kV equipped with a high-angle annular dark field (HAADF) detector was used and a drop of the diluted colloidal suspension was dried on a carbon-coated copper grid. Fluorescence measurements were performed on a PTI spectrofluorometer with a photomultiplier detection system (model 810/814) and a xenon arc lamp. For all samples a 1 cm quartz cuvette with a volume of 3 mL was used.

### **N3-dye adsorption**

The amount of 5 mg of samples CMS, 100Ti@CMS and 100Ti@CMS+TiNPs respectively was added to 500  $\mu\text{L}$  of cis-Bis(isothiocyanato)bis(2,2'-bipyridyl-4,4'-dicarboxylato) ruthenium(II) (99% Aldrich, N3 hereafter) in water (0.6 mM) and stirred in the dark for 1 hour. Then the particles were separated by centrifugation (20.000 rpm, 15 min) and washed 3 times with bi-distilled water for 1 h each. Finally, the N3-loaded samples were dispersed in water at a conc. of 1.15 mg/mL. The UV-Vis spectra of the N3-solution before and after adsorption, and of the colloidal suspensions of N3-loaded samples were recorded. For the

fluorescence measurements, 100  $\mu$ L of N3-loaded nanoparticle suspension was diluted in 3 mL water (0.038 mg/mL).

## 8.5 References

1. J. Kobler and T. Bein, *ACS Nano*, **2008**, *11*, 2324-2330.
2. A. Schlossbauer, J. Kecht and T. Bein, *Angew. Chem., Int. Ed.*, **2009**, *48*, 3092-3095.
3. V. Cauda, C. Argyo, A. Schlossbauer and T. Bein, *J. Mater. Chem.*, **2010**, *20*, 4305-4311.
4. J. Kobler, K. Möller and T. Bein, *ACS Nano*, **2008**, *2*, 791-799.
5. V. Cauda, A. Schlossbauer, J. Kecht, A. Zürner and T. Bein, *J. Am. Chem. Soc.*, **2009**, *131*, 11361-11370.
6. J. Kecht, A. Schlossbauer and T. Bein, *Chem. Mater.*, **2008**, *20*, 7207-7214.
7. M. C. Lechmann, D. Kessler and J. S. Gutmann, *Langmuir*, **2009**, *25*, 10202-10208.
8. M. H. Bartl, S. W. Boettcher, K. L. Frindell and G. D. Stucky, *Acc. Chem. Res.*, **2005**, *38*, 263-271.
9. M. K. Nazeeruddin, A. Kay, I. Rodicio, R. Humpbry-Baker, E. Müller, P. Liska, N. Vlachopoulos and M. Graetzel, *J. Am. Chem. Soc.*, **1993**, *115*, 6382-6390.
10. J. W. Lee, M. R. Othman, Y. Eom, T. G. Lee, W. S. Kim and J. Kim, *Microporous Mesoporous Mater.*, **2008**, *116*, 561-568.
11. D.-W. Lee, S.-K. Ihm and K.-H. Lee, *Chem. Mater.*, **2005**, *17*, 4461-4467.

12. W. K. Oh, S. Kim, M. Choi, C. Kim, Y. S. Jeong, B.-R. Cho, J.-S. Hahn and J. Jang, *ACS Nano*, **2010**, DOI:10.1021/nn100561e.
13. R. Abe, K. Hara, K. Sayama, K. Domen and H. Arakawa, *J. Photochem. Photobiol. A*, **2000**, *137*, 63-69.
14. Q. Li, Z. Jin, Z. Peng, Y. Li, S. Li and G. Lu, *J. Phys. Chem. C*, **2007**, *111*, 8237-8241.
15. G. A. Eimer, S. G. Casuscelli, G. E. Ghione, M. E. Crivello and E. R. Herrero, *Appl. Catal., A*, **2006**, *298*, 232-242.
16. J. Kobler, B. V. Lotsch, G. A. Ozin and T. Bein, *ACS Nano*, **2009**, *3*, 1669-1676.
17. Y. Li and S.-J. Kim, *J. Phys. Chem. B*, **2005**, *109*, 12309-12315.
18. T. Fernandez, U. K. Samersen, X. Joseph and N. V. J. Unnikrishnan, *J. Mater. Process. Technol.*, **2008**, *202*, 528-535.
19. D. Fattakhova-Rohlfing, J. M. Szeifert, Q. Yu, V. Kalousek, J. Rathouský and T. Bein, *Chem. Mater.*, **2009**, *21*, 2410-2417.
20. D. R. Sahu, L. Y. Hong, S.-C. Wang and J.-L. Huang, *Microporous Mesoporous Mater.*, **2009**, *117*, 640-649.
21. L. Zhao, J. Yu and B. Cheng, *J. Solid State Chem.*, **2005**, *178*, 1818-1824.
22. J. M. Szeifert, J. M. Feckl, D. Fattakhova-Rohlfing, Y. Liu, V. Kalousek, J. Rathouský and T. Bein, *J. Am. Chem. Soc.*, **2010**, *132*, 12605-12611.
23. G. Garnweitner, M. Antonietti and M. Niederberger, *Chem. Commun.*, **2005**, *3*, 397-399.
24. M. Grätzel, *Acc. Chem. Res.*, **2009**, *42*, 1788-1789.
25. A. Hagfeldt and M. Grätzel, *Acc. Chem. Res.*, **2000**, *33*, 269-277.

## 8. Core-Shell Silica-Titania Mesoporous Nanoparticles showing Orthogonal Functionality

---

26. X. Orignac, H. C. Vasconcelos and R. M. Almeida, *J. Non-Cryst. Solids*, **1997**, *217*, 155-161.
27. W. Dong, Y. Sun, C. W. Lee, W. Hua, X. Lu, Y. Shi, S. Zhang, J. Chen and D. Zhao, *J. Am. Chem. Soc.*, **2007**, *129*, 13894-13904.



## 9. Conclusion and Outlook

This thesis focused on developing surfactant-templated mesoporous titania-based morphologies for applications in the fields of energy conversion and storage, and photocatalysis. The main objective was to improve the physical characteristics of the walls of the mesoporous materials by controlling their crystallinity and chemical composition, which is crucial for their performance.

The synthetic approach towards crystalline mesoporous coatings of TiO<sub>2</sub> is based on using preformed, crystalline nanoparticle precursors of about 4 to 5 nm in size in a novel “brick and mortar” strategy. The pre-formed titania nanocrystalline “bricks” are fused with surfactant-templated sol-gel titania “mortar”, which acts as a structure-directing matrix and as a chemical glue, leading to a striking synergy in the interaction of crystalline and amorphous components, and to a significant increase in crystallinity upon thermal treatment. By tuning the fraction of “bricks”, a variety of mesostructures with different physical characteristics can be obtained, which are efficient in dye-sensitized solar cells and photocatalysis due to a favorable combination of crystallinity and porosity (cooperation with the groups of Prof. M. Grätzel, EPF Lausanne, dye-sensitized solar cells, and Dr. J. Rathouský, J. Heyrovský Institute, Prague, photocatalysis). Furthermore, it was shown that the general limitation of low film thicknesses that are typical for surfactant-templated titania films can be overcome using the “brick and mortar” approach. Films made by sequential deposition of multiple layers exhibit very high surface area, which scales linearly with the thickness, and roughness factors of up to 1600 cm<sup>2</sup>/cm<sup>2</sup> can be reached. Applied in dye-sensitized solar cells, the films feature a remarkably high performance level of over 7 % efficiency already at thicknesses below 4 μm due to their high surface area and dye adsorption capacity.

Applied in more stable DSCs using ionic liquid electrolytes (cooperation with the group of Prof. M. Grätzel, EPF Lausanne), the high surface area proved to be especially beneficial, and films of only 2  $\mu\text{m}$  thickness reached conversion efficiencies of over 6 %, which is close to the maximum performance for these devices. However, the existence of charge transport-limitations in thicker films of this type indicate that further experiments regarding the optimization of pore size and film thickness are needed in order to reach even higher maximum conversion efficiencies.

The scope of our general strategies employing crystalline titania nanoparticles could be further extended by down-sizing the dimensions of the nanocrystalline building blocks. A new non-aqueous sol-gel protocol using *tert*-butyl alcohol and  $\text{TiCl}_4$  widens the available size range of  $\text{TiO}_2$  nanoparticles at its lower end by producing ultrasmall and highly soluble anatase nanoparticles of around 3 nm. The extremely small size of the nanoparticles allows the direct surfactant-templated self-assembly of periodic mesoporous structures without the need for additional amorphous sol-gel precursors. These mesoporous titania films exhibit high surface areas of up to 300  $\text{m}^2/\text{g}$ , and the advantages of this large interface and the nanocrystalline walls were demonstrated by the drastic acceleration of electrochemical lithium insertion kinetics.

The benefits of using pre-formed nanocrystalline titania precursors (“bricks”) for surfactant-templated mesoporous materials can also be exploited for synthesizing titania-silica composite materials. In combination with silica sol-gel precursors as “mortar”, periodically porous films containing a high degree of crystalline titania homogeneously distributed in silica mesostructures were obtained. The mesoporous nanocomposite coatings can be processed at low temperatures on a wide range of substrates and feature photocatalytically active sites for the photooxidation of NO (cooperation with Dr. J. Rathouský, J. Heyrovský Institute, Prague).

A different porous morphology of a titania-silica composite was achieved by synthesizing colloidal mesoporous silica (CMS) nanoparticles with a thin titania-enriched outer shell using a delayed co-condensation approach (cooperation with Dr. Valentina Cauda). These colloidal all-inorganic nanoparticles exhibit a spatially resolved functionality, which can be exploited for example for selective adsorption and fluorescence of dye molecules. The introduction of crystallinity by growing nanocrystalline anatase clusters on the titania shell leads to a further enhancement of the selectivity of this orthogonal functionality.

To summarize, the strategy described in this thesis to improve the physical properties of the walls of surfactant-based mesoporous materials by incorporating preformed crystalline nanoparticles leads to a significantly enhanced control over their crystalline and chemical characteristics. As a result, the materials' applicability and performance in solar cells, energy storage, and photocatalytic devices was found to be greatly improved.



## 10. Curriculum Vitae

### Persönliche Angaben

---

Geburtsdatum, -ort      26.08.1981, Peißenberg  
Nationalität              Deutsch

### Ausbildung

---

09/1987 – 07/1991      **Josef-Zerhoch Grundschule**, Peißenberg  
09/1991 – 07/2000      **Gymnasium Weilheim**, Weilheim  
Abschluss: Allgemeine Hochschulreife  
10/2001 – 09/2004      **Ludwig-Maximilians-Universität**, München  
Studium der Chemie und der Biochemie  
Abschluss: Bachelor of Science  
03/2004 – 09/2006      **Bayerische Elite-Akademie**, München  
Förderinstitution der bayerischen Wirtschaft und Universitäten,  
Zusatzstudium, Projektarbeit zum Thema: „Change Management –  
Kritische Einflussfaktoren und Steuerungsmethoden für den Erfolg  
von Veränderungs-Prozessen in Organisationen“  
10/2004 – 09/2007      **Ludwig-Maximilians-Universität**, München  
Studium der Chemie, Abschluss: Master of Science Chemie  
05/ 2005 – 07/2005      **University of British Columbia**, Vancouver (Kanada)  
Visiting Scholar, Forschungspraktikum in anorganischer Chemie  
12/2007 –                **Ludwig-Maximilians Universität**, München  
Promotionsstudium Chemie, Betreuer: Prof. Dr. Thomas Bein  
Thema: „Mesoporous Titania Materials – Tuning and Optimizing  
Nanostructures and Porous Morphologies“  
09/2008 –                **Center for Nanoscience (CeNS)**, München  
Internationales Doktoranden Kolleg – NanoBioTechnologie (IDK-  
NBT), Elite-Netzwerk Bayern  
10/2007 –                **Fernuniversität Hagen**, Hagen  
Bachelorstudiengang Wirtschaftswissenschaften (Teilzeit)

### Zivildienst

---

09/2000 – 07/2001      **Ökumenische Sozialstation**, Peißenberg  
Individuelle Schwerstbehindertenbetreuung

### **Berufliche Erfahrung**

---

07/2003 – 12/2003	<b>Munich Biotech AG</b> , Neuried Praktikum und Werkstudent im Bereich Analytik
04/2004 – 02/2005 04/2006 – 07/2007	<b>Ludwig-Maximilians-Universität</b> , München Übungsleiter der Mathematik am Department Chemie
10/2005 – 12/2005	<b>Wacker Chemie GmbH</b> , München Praktikum im Bereich Marketing Cystein
01/2006 – 03/2006	<b>Südchemie Catalysts Japan</b> , Toyama (Japan) Praktikum im Bereich Forschung und Entwicklung
12/2007 –	<b>Ludwig-Maximilians Universität</b> , München Wissenschaftlicher Mitarbeiter

### **Weitere Fähigkeiten**

---

Sprachen	<b>Deutsch</b> (Muttersprache), <b>Englisch</b> (verhandlungssicher), <b>Französisch</b> (gute Kenntnisse), <b>Italienisch</b> (gute Kenntnisse), <b>Spanisch</b> (Grundkenntnisse), <b>Japanisch</b> (Grundkenntnisse)
----------	---

## 11. Publications and Presentations

### 11.1 Publications

1. “Brick and mortar” strategy for the formation of highly crystalline mesoporous titania films from nanocrystalline building blocks  
J. M. Szeifert, D. Fattakhova-Rohlfing, D. Georgiadou, V. Kalousek, J. Rathouský, D. Kuang, S. Wenger, S. M. Zakeeruddin, M. Grätzel and T. Bein, *Chemistry of Materials* **2009**, *21* (7), 1260-1265.
2. Low-temperature synthesis of mesoporous titania-silica films with pre-formed anatase nanocrystals  
D. Fattakhova-Rohlfing, J. M. Szeifert, Q. Yu, V. Kalousek, J. Rathouský, and T. Bein, *Chemistry of Materials* **2009**, *21* (12), 2410-2417.
3. Ultrafast terahertz photoconductivity in nanocrystalline mesoporous TiO<sub>2</sub> films  
H. Němec, P. Kužel, F. Kadlec, D. Fattakhova-Rohlfing, J. M. Szeifert, T. Bein, V. Kalousek, and J. Rathouský, *Applied Physics Letters* **2010**, *96* (6), 062103.
4. Ultrasmall titania nanocrystals and their direct assembly into mesoporous structures showing fast lithium insertion  
J. M. Szeifert, J. M. Feckl, D. Fattakhova-Rohlfing, Y. Liu, V. Kalousek, J. Rathouský, and T. Bein, *Journal of the American Chemical Society* **2010**, *132*, 12605.
5. Niobium Doped Titania Nanoparticles: Synthesis, Assembly into Mesoporous Films and Electrical Conductivity  
Y. Liu, J. M. Szeifert, J. M. Feckl, B. Mandlmeier, J. Rathouský, O. Hayden, D. Fattakhova-Rohlfing, and T. Bein, *ACS Nano* **2010**, *4* (9), 5373.
6. All-Inorganic Core-Shell Silica-Titania Mesoporous Colloidal Nanoparticles Showing Orthogonal Functionality  
V. Cauda, J. M. Szeifert, K. Merk, D. Fattakhova-Rohlfing, and T. Bein, *Journal of Materials Chemistry* **2011**, *accepted*.
7. Tuning the light absorption of Cu<sub>1.97</sub>S nanocrystals in supercrystal structures  
I. Kriegel, J. Rodríguez-Fernández, E. Da Como, A. A. Lutich, J. M. Szeifert, and J. Feldmann, *Chemistry of Materials* **2011**, *23* (7), 1830.
8. Formation of interpenetrating hierarchical titania structures by confined synthesis in inverse opal  
B. Mandlmeier, J. M. Szeifert, D. Fattakhova-Rohlfing, and T. Bein, *submitted*.
9. Multilayered High Surface Area “Brick and Mortar” Mesoporous Titania Films as Efficient Anodes in Dye-Sensitized Solar Cells  
J. M. Szeifert, D. Fattakhova-Rohlfing, J. Rathouský, and T. Bein, *submitted*.

## 11.2 Poster Presentations

1. Crystalline mesoporous titania films through surfactant-assisted assembly of ultrasmall and dispersible anatase nanocrystals.  
J. M. Szeifert, J. M. Feckl, D. Fattakhova-Rohlfing, Y. Liu, and T. Bein,  
22. Deutsche Zeolith-Tagung, **2010**, München.
2. Highly crystalline mesoporous titania films for photovoltaic applications based on self-assembled nanocrystalline building blocks.  
J. M. Szeifert, J. M. Feckl, D. Fattakhova-Rohlfing, D. Georgiadou, V. Kalousek, J. Rathouský, D. Kuang, S. Wenger, S. M. Zakeeruddin, M. Grätzel and T. Bein,  
Materials for Energy Conference, **2010**, Karlsruhe.
3. Highly crystalline mesoporous titania films for photovoltaic applications based on self-assembled nanocrystalline building blocks.  
J. M. Szeifert, J. M. Feckl, D. Fattakhova-Rohlfing, J. Rathouský, and T. Bein,  
23. Deutsche Zeolith-Tagung, **2011**, Erlangen.

## 11.3 Oral Presentations

1. Highly crystalline mesoporous TiO<sub>2</sub> films assembled from crystalline nanoparticles.  
J. M. Szeifert, D. Fattakhova-Rohlfing, J. Rathouský, and T. Bein,  
Nanoporous Materials V, **2008**, Vancouver.
2. „Brick and Mortar“ Strategy for the Formation of Highly Crystalline Mesoporous Titania Films for Photovoltaic Applications.  
J. M. Szeifert, D. Fattakhova-Rohlfing, J. M. Feckl, V. Kalousek, J. Rathouský, D. Kuang, S. Wenger, S. M. Zakeeruddin, M. Grätzel, T. Bein,  
MRS Spring Meeting, **2010**, San Francisco.